Tectonics as recorded by thermochronometry, deformed datums, and submarine landscapes in western North America

Philip Schoettle-Greene

A dissertation
submitted in partial fulfillment of the
requirements for the degree of

Doctor of Philosophy

University of Washington

2021

Reading Committee:
Alison R. Duvall, Chair
Juliet Crider
Harold Tobin

Program Authorized to Offer Degree:
Earth and Space Sciences

University of Washington

Abstract

Tectonics as recorded by thermochronometry, deformed datums, and submarine landscapes in western North America

Philip Schoettle-Greene

Chair of the Supervisory Committee:
Associate Professor Alison R. Duvall
Department of Earth and Space Sciences

Since the Mesozoic, the west coast of North America has experienced near continuous right-lateral shear. Over this time, a series of exotic crustal terranes accreted to and translated along the expanding westward edge of the continent. In this dissertation, I use low-temperature thermochronomtery, geologic map interpretation, geophysics, and geomorphic analysis, to explore the effects of this tectonic regime on deformation and landscape development. First, I determine the geologic history of the Wallowa and Bald Mountain Batholiths of Northeast Oregon to better understand whether the mountains they underlie formed in response to Miocene lithospheric delamination. I find that both batholiths were exhumed to the near surface during early to mid-Cretaceous terrane amalgamation and accretion. Multiple subsequent phases of localized uplift in the Cenozoic led to the mountainous landscape seen today. Building on this research, I use the distribution of the Miocene Columbia River Flood Basalt, in conjunction with crustal thickness estimates, to investigate the crustal structure responsible for Miocene to present strain partitioning in the Pacific Northwest, USA. From this analysis, I find that CRB deformation is correlated with crustal thickness, with less deformed regions having thinner crust. Turning to the north, I use low-temperature thermochronometry to estimate the timing of exhumation of the island archipelago Haida Gwaii. I determine that exhumation began with the passage of the Yakutat terrane, not as

a result of transpression-induced subduction initiation as hypothesized in previous studies. Finally, I analyze the morphology of the seafloor along the Queen Charlotte Fault for the impact of tectonics. I find that transpression between the Pacific and North American plates determine the morphology of continental slope channel networks and whether the continental shelf is actively accumulating sediment. Across each of these studies, there is a common conclusion that the landscapes we observe today record multistage geologic histories.

TABLE OF CONTENTS

LIST OF FIGURES

LIST OF TABLES

ACKNOWLEDGMENTS

The work presented in this dissertation would not have been possible without the many people who helped me along the way. From Cody and Kristin, who worked as assistants in white-out smoke conditions during my first time doing field work, to Nate who was always down to take a trip to the Wallowas, the following chapters reflect the efforts of so many. I benefited greatly from conversations and comradeship with Sarah, Seth, Sean, Erich, Paul, and Tamara in the Duvall group. Same goes for all of Supergroup. Thanks to all the folks who I lunched with on the Ave over the years. This one is for you. Extra special thanks to Sean whose quick wits and wine saved my life twice, once on a freezing mountaintop in New Zealand and once during a particularly wet day in Haida Gwaii. Thanks to my folks for putting up with my pretensions over the years. I am also indebted to the folks at GeoSep services. Paul, Jim, Charlie, and Victora you guys always made my time in Idaho a pleasure. To everyone who graced the Kitty Kat Palace with their presence, you made Seattle everything it could have been. Andrea, you've made it all better.

I am indebted to the governmental bodies that permitted my research: The Haida Nation, Parks Canada, and USFS. To the Nations that I failed to ask for permission - the Nez Perce, Shoshone-Bannok, and Skidegate Band of the Haida Nation - I apologize and acknowledge that I am still actively working to unlearn my colonial mindset.

Alison has been the best advisor I could have wished for. From accommodating my spotty service in the Toronto Harbor when applying for the PhD, to entertaining my unannounced visits to her office, Alison has always supported my intellectual development and been a friend during my time at UW.

DEDICATION

To Gainor, Phil, Phil, John, and Connie

Chapter 1

INTRODUCTION

I would like to begin this dissertation by recognizing the First Nations in the regions I study. While only a small gesture, I have tried to ask permission for field work and accept when it is not granted. More generally, I think it is important as a geologist to be aware of the connection between my work and colonialism. At its core, geology belongs to a scientific tradition grounded in Christian Western European ways of knowing. I hope that moving forward we recognize this history and work towards greater equity in our discipline as well as outside academia.

While the chapters of my dissertation do not directly address colonialism nor do they present indigenous geologies, this way of thinking has grounded my research on processes whose scale, both in time and space, I cannot fathom. I have studied crystals that can only be seen beneath a microscope, the elevation of geologic contacts measured over tens of thousands of kilometers, and the landscape beneath the ocean to try and further my understanding of the region I have lived in for the past 6 years. In this dissertation, I attempt to share what I have learned.

In Chapter 2, I use apatite (U-Th-Sm)/He and zircon (U-Th)/He thermochronometry to determine the thermal history of the Mesozoic Bald Mountain and Wallowa batholiths in the Blue Mountains Province of Northeast Oregon. I pair this analysis with map interpretation of the distribution of Miocene Columbia River Basalt to explore the history of mountain building in the Blue Mountains Province. I find that both plutons record Cretaceous cooling during terrane amalgamation and accretion to North America. However, Cenozoic cooling histories are different between the two batholiths. These differences reflect localized deformation associated with the accretion of Siletzia and the eruption of Columbia River Basalt.

This project is in collaboration with Peter Crowley, Amherst College Professor of Geology, who collected and analyzed bedrock samples from the Wallowa Batholith for apatite and zircon (U-Th)/He thermochronometry in the late 1990's.

In Chapter 3, I present a compilation of elevation measurements of Columbia River Basalt unit contacts and use this compilation to explore the importance of crustal structure on deformation in the Pacific Northwest, USA. I find that crustal thickness is correlated with the locus of Miocene to present deformation. This chapter is part of ongoing work that began in a seminar series hosted by Leif Karlstrom, Associate Professor at the University of Oregon, in 2020. The project is a collaboration with Jonathan Perry-Houts, who graduated with a PhD from the University of Oregon in 2018, and Gene Humphreys, Emeritus Professor at the Univerity of Oregon.

In Chapter 4, I use apatite (U-Th-Sm)/He, apatite fission track, and zircon (U-Th)/He thermochronometry to determine the thermal history of bedrock from the island archipelago Haida Gwaii. I find that bedrock began to cool, presumably due to exhumation, in the Miocene during translation of the Yakutat terrane outboard of Haida Gwaii. This falsifies a prevalent hypothesis that uplift and exhumation of Haida Gwaii began as a result of late Miocene subduction initiation. This chapter was published in Geology in 2020 (Schoettle-Greene et al., 2020). The work was a collaboration with Alison Duvall, Eric Morley, former undergraduate at the University of Calgary, William Matthews, Assistant Professor at the University of Calgary, Ann Blythe, Associate Professor at Occidental College, and Sean LaHusen, USGS. Morley and Matthews analyzed four bedrock samples from Haida Gwaii for apatite (U-Th-Sm)/He thermochronometry. Blythe analyzed five bedrock samples for apatite fission track thermochronometry.

In Chapter 5, I examine the morphology of continental slope channels and the continental shelf edge along the Queen Charlotte Fault. I explore the role of tectonics in dictating the morphology of the submarine landscape observed today. I find that both the continental shelf edge and continental slope channels are modified by tectonics. Both the shelf edge and slope channels are influenced by uplift and translation of the Pacific Plate. This project

developed during an internship at the USGS Pacific Coastal and Marine Science Center in 2020. Interpretation and analysis was made in collaboration with Daniel Brothers, Research Geophysicist at the USGS, and Nathaniel Miller, Research Geophysicist at the USGS.

Chapter 2

TIMING OF EXHUMATION AND VOCANISM RECORDED IN THE THERMAL HISTORY OF THE WALLOWA AND BALD MOUNTAIN BATHOLITHS, BLUE MOUNTAINS PROVINCE, OREGON

ABSTRACT

The Mesozoic and Cenozoic history of the Cordillera in the north-western United States is characterized by terrane accretion and translation, shortening, and post-orogenic collapse. This history has complicated the record of paleogeography and inspired debate over the antiquity of present-day topography. As a result, this region is host to a variety of geodynamic hypotheses posited to explain topography. In this study, we determine the thermal history of the Wallowa and Bald Mountain batholiths in the Blue Mountains Province of northeastern Oregon. Our goal is to explore hypotheses regarding the uplift of the Wallowa Mountains, an enigmatic range often cited as the product of lithospheric delamination-induced uplift. We analyze the distribution of Columbia River Basalt, use low-temperature apatite and zircon (U-Th)/He thermochronometry, and conduct a literature review to develop a regional landscape history for the Blue Mountains Province. We find that low-temperature thermochronometry data from the Wallowa and Bald Mountain batholiths record independent cooling histories. Thermochronometry from the Bald Mountain Batholith records early to mid-Cretaceous cooling to near surface temperatures, limited reheating to the Eocene, and a pulse of exhumation after 50 Ma. After accounting for the thermal perturbation from Miocene dike intrusion in the Wallowa Batholith, we interpret Wallowa Batholith thermochronometry to show cooling in the mid-Cretaceous to near surface temperatures followed by slow cooling through the Cenozoic. We propose these differences result from the local tectonic and volcanic episodes. While both plutons record rapid cooling associated with

Mesozoic terrane accretion and amalgamation, cooing coinciding with the accretion of Siletzia is only recorded in the Bald Mountain Batholith. On the other hand, the distribution of Columbia River Basalt suggests a recent, Miocene to present, phase of uplift of the Wallowa Batholith that is not recorded by thermochronometry. Together with regional constraint, we conclude that the Cenozoic landscape history of the Wallowa Mountains is unique relative to surroundings, lending support to the hypothesis that they are the product of Miocene or younger uplift. [1]

2.1 Introduction

The Blue Mountains Province of northeastern Oregon and western Idaho is underlain by a number of exotic ocean island arc terranes that accreted to North America during the Mesozoic. The region is characterized by isolated fault-bound uplifts which expose Mesozoic and older units above denuded Eocene Clarno volcanics, Miocene Columbia River Basalt (CRB), and sediment filled grabens and half grabens (Figure 2.1). The origin of these isolated mountains is a matter of debate, with most prior studies focused on the Wallowa Mountains, a domal uplift intruded by the Miocene Chief Joseph Dike Swarm. It has been proposed that lithospheric delamination during intrusion of the Chief Joseph Dike Swarm led to uplift of the Wallowa Mountains (Figure 2.1; Hales et al., 2005; Darold & Humphreys, 2013). However, extension of an orogenic plateau, hypothesized to have developed across eastern Oregon and Idaho during Cretaceous and early Cenozoic shortening (Fayon et al., 2017), could also explain their genesis (Kahn et al., 2020).

A thorough understanding of regional topographic evolution is needed to critically appraise hypothesized delamination below the Wallowa Mountains. Mantle lithosphere delamination remains an enigmatic albeit often cited mechanism for volcanism and vertical deformation in orogenic (DeCelles et al., 2009) and post-orogenic (Bird, 1979; Ducea & Saleeby, 1998; Hales et al., 2005) settings. However, an inability to directly observe the

[1] In collaboration with Alison Duvall and Peter Crowley. Manuscript in revision, Tectonics

mantle, the filtering of subcrustal forces through a structurally heterogenous crust, and the presence of preexisting topography makes identifying the topographic signature of delamination non-trivial (e.g., Valera et al., 2011). Therefore, a careful analysis of the tectonic and topographic history of the Blue Mountains Province can help rule out other drivers for uplift and lend support to hypothesized delamination.

In this contribution, we examine the tectonics and geomorphology of the Blue Mountains Province from the late Jurassic to present using low-temperature thermochronometry, map interpretation, and a synthesis of available studies. We analyze 44 bedrock samples using apatite (U-Th)/He (AHe) thermochronometry and 7 samples using zircon (U-Th)/He (ZHe) thermochronometry collected from the Wallowa and Bald Mountain batholiths which underlie the Wallowa and Elkhorn mountains, respectively (Figure 2.1).

2.1.1 Geologic Background

The 140-160 Ma Bald Mountain Batholith and 120-140 Ma Wallowa Batholith were intruded into the Blue Mountains Province during the early stages of accretion to North America along the Salmon River Suture Zone (Figure 2.1; Schwartz et al., 2014). Assembled prior to collision with North America, the Blue Mountains Province is comprised of the volcanic island arc assemblages of the Wallowa and Olds Ferry terranes and a subduction-accretionary prism complex known as the Baker terrane (LaMaskin et al., 2011).

Following accretion, transpression along the right-lateral Western Idaho Shear Zone (WISZ) translated the Blue Mountains Province into the Syringa embayment (Figure 2.1; Schmidt et al., 2017). After translation, the Blue Mountains Province sat in the forearc of the Farallon/Kula subduction zone during the Laramide orogeny. Previous studies suggest that much of the Blue Mountains Province was tectonically quiescent during this period (Gaschnig et al., 2017; Kahn et al., 2020).

After the Eocene accretion of the oceanic plateau Siletzia to North America, volcanism recommenced in the Blue Mountains Province with the eruption of the Clarno volcanics (Figure 2.1). This was followed by the Miocene eruption of $\sim$160,000 km^3 of Grande Ronde

and Imnaha CRB from the Chief Joseph Dike Swarm in the eastern Blue Mountains Province (Hooper et al., 1984; Reidel, Camp, Tolan, & Martin, 2013; Kasbohm & Schoene, 2018; Morriss et al., 2020). Volcanism continued following the eruption of CRB in the Powder River volcanic field on the northwestern flank of the Wallowa Mountains (Figure 2.1; Ferns & McClaughry, 2013). At the same time, widespread diffuse extension in the Blue Mountain Province on NNW-SSE oriented normal faults led to down-dropping of the La Grande Graben since at least ∼9 Ma (Figure 2.1; VanTassell et al., 2001; Ferns et al., 2010).

The genesis of a present-day landscape of rugged, fault bound mountain ranges in the Blue Mountains Province adjacent the regional uplift of central Idaho is not well understood. Whether the development of these ranges is distinct (Hales et al., 2005) or represents a continuum of crustal deformation from west to east (Kahn et al., 2020) remains a matter of debate.

2.2 Methods

To further elucidate the tectonic, geomorphic, and thermal evolution of the Blue Mountains Province, we interpolate a structure contour of the CRB basal unconformity and present new apatite and zircon low-temperature thermochronometry data from the Wallowa and Bald Mountain Batholiths.

2.2.1 Interpolation of the CRB Basal Unconformity

Eruption of the Imnaha and Grande Ronde members of CRB ca. 16-17 Ma led to the burial of much of the study area beneath up to 1 km of basalt (Camp & Hooper, 1981). To estimate the topography of this buried landscape and provide constraint on the degree of post-Miocene regional topographic change, we interpolated a structure contour of the basal unconformity between the CRB and older bedrock. Using the Oregon state digital geologic map (OGDC-6, accessed December 2019), as well as regional USGS reconnaissance maps (Swanson et al., 1981), we sampled the elevation of the basal CRB contact. With additional information from modeled CRB basal depth in Washington (Burns et al., 2011),

we used the spline with barriers function in ArcGIS v. 10.7 to interpolate a surface through these contacts. We incorporated the Wallowa Fault and the fault bounding the southwestern Wallowa Mountains (Figure 2.1), as discontinuities in the interpolation scheme.

2.2.2 Low-temperature Thermochronometry

To determine the timing of tectonic, topographic, and thermal events in the Wallowa and Elkhorn Mountains region, we analyzed bedrock samples from the Wallowa and Bald Mountain Batholiths using the apatite (U-Th)/He and zircon (U-Th)/He methods.

Apatite (U-Th)/He Thermochronometry

Apatite (U-Th)/He thermochronometry (AHe) utilizes the temperature dependence of radiogenic He diffusion in apatite crystals to constrain the timing of cooling from 120-30°C (Farley, 2000; Flowers et al., 2009; Gautheron et al., 2013; Ault et al., 2019). The temperature at which helium is quantitatively retained varies depending on the diffusion kinetics of the apatite crystal which are affected, in turn, by radiation damage due to alpha ejection (Flowers et al., 2009). Radiation damage is estimated with the proxy $eU = U + 0.235Th$ which predicts a given crystal's potential for damage if held below the crystal lattice annealing temperature. Increasing damage and, by proxy, eU will mean lower helium diffusion rates and a higher closure temperature. eU variability in a dataset can produce substantial date dispersion if samples cool slowly or are reheated after cooling to low temperatures (Flowers et al., 2007, 2009; Ault et al., 2013).

We acquired new AHe data for 98 apatite crystals from 20 bedrock samples collected from the Wallowa and Bald Mountain batholiths of eastern Oregon. These data complement legacy data, including 39 AHe dates from 24 samples. Samples were collected across the Wallowa Mountains at a variety of elevations and on a single transect up the Anthony Lake road in the Elkhorn Mountains (Figure 2.1). Single apatite crystals were selected for analysis based on size, lack of inclusions, and euhedral crystal shape. The more recently collected apatite samples (sample prefix WM) were analyzed for U, Th, Sm, and He content at the

Caltech Noble Gas Lab. Legacy AHe data (sample prefix WB) used aliquots of 1-5 apatite grains from each sample and were analyzed at Washington State University.

Zircon (U-Th)/He Thermochronometry

Zircon (U-Th)/He thermochronology (ZHe) uses the temperature dependent retentivity of helium in zircon crystals to constrain the timing of crystal cooling from 220-140°C (Reiners, Farley, & Hickes, 2002; Guenthner et al., 2013). Radiation damage also plays a role in determining the temperature at which helium is quantitatively retained within a zircon crystal but the correlation is more complicated than with apatite. For zircon, radiation damage may reduce helium diffusivity, increasing the effective closure temperature, much like apatite. Given sufficient damage, however, helium diffusivity increases, decreasing the effective closure temperature (Guenthner et al., 2013). We present ZHe dates for aliquots of 1-5 grains from 7 samples in the Wallowa Batholith. All zircons were analyzed at Washington State University.

2.2.3 Thermal Modeling of Thermochronometry Data

To better understand the thermal history of the Wallowa and Bald Mountain Batholiths, we use the thermal modeling softwares QTQt (Gallagher, 2012) and HeFTy (Ketcham, 2005) to estimate viable time-temperature histories constrained by our data. QTQt uses a Bayesian Monte-Carlo Markov chain method to determine time-temperature histories that reproduce thermochronometry data (Gallagher, 2012). This technique estimates thermal histories by satisfying geochemical constraints provided by individual apatite and zircon crystals, the spatial relationship between samples if more than one sample is modeled, and any known temperature constraints independent of the thermochronometry dataset. HeFTy allows for forward modeling of thermal histories and the estimation of apatite and zircon dates given published diffusion kinetics (Ketcham, 2005).

2.3 Results

2.3.1 Interpolation of the CRB Basal Unconformity

The interpolated basal unconformity of the CRB in northeastern Oregon ranges from 0 to 2900 m elevation (Figure 2.2 A). We crop the interpolated surface to the southwest of the Wallowa Mountains where no Imnaha or Grande Ronde basalt are mapped and the interpolation is unconstrained (Figure 2.2 A). In the Wallowa Mountains region, where Imnaha basalt is found on many mountain summits, the surface is better constrained. Here, the basal unconformity is characterized by a domal high over the Wallowa Mountains (Figure 2.2). Local relief on the surface is minimal and lows are seen along the Snake and Grande Ronde rivers. Greatest local structural relief on the surface is found across the Wallowa Fault, where the unconformity drops >2 km across the fault.

Swath profiles over the Wallowa Mountains further reveal patterns in present-day topography and the CRB basal unconformity (Figure 2.2 A-A', B-B'). Both the basal unconformity and present-day topography are broadly upwarped when viewed in the swath parallel to the Wallowa Fault (Figure 2.2 A-A'). The local relief of the unconformity surface is at maximum ∼700 m and the greatest variance is found on the southeast flank of the Wallowas. This may reflect local relief in Miocene topography. A profile across the Wallowa Fault and Mountains reveals a plateau-like topography to the interpolated unconformity and present-day topography (Figure 2.2 B-B'). The plateau top is seen to dip gently to the south west.

CRB is thickest on the northwestern flank of the Wallowa Mountains, where the Minam and Lostine valleys expose ∼800m of basalt (Figure 2.2 A-A'). This contrasts with the other flanks of the Wallowa Mountains, where the unconformity surface and present topography are roughly coincident (Figure 2.2 A-A', B-B'). The dip of individual CRB flows are parallel to the interpolated unconformity on the northwest flank of the Wallowas (Figure 2.2 A-A'), suggesting basalt did not onlap topography (Figure 2.2 A-A'). On the southeast flank, flow dips are slightly steeper than the interpolated unconformity. This may reflect CRB onlap onto a topographic high east of the Wallowa Mountains.

2.3.2 Low-temperature Thermochronometry

We present 137 AHe and 7 ZHe dates from 44 bedrock samples collected from the Wallowa and Bald Mountain Batholiths (Figure 2.3; Table 2.1; Appendices B.1, D.1). Wallowa Batholith sample elevation varies from 1227 to 2874 m. Samples were collected 2 to 2735 m from Miocene dikes mapped at 1:24,000 scale (Table 2.1; Morriss et al., 2020). Samples from the Bald Mountain Batholith were collected from 1153 to 2499 m elevation. No Miocene dikes have been mapped with confidence within the Elkhorn Mountains so distance to the nearest dike was not calculated.

AHe dates range from 15 to 129 Ma, and ZHe dates range from 20 to 133 Ma. AHe data from the Wallowa Batholith are bimodally distributed with a sharp peak at 10 to 20 Ma at the time of Chief Joseph dike intrusion and a more diffuse peak between 90 to 100 Ma (Figure 2.4 A). In contrast, the majority of AHe data from the Bald Mountain Batholith are between 40-60 Ma, with three dates in the 80-100 Ma range. ZHe data cluster between 110-130 Ma, with two dates between 20 to 100 Ma (Figure 2.4 C).

All AHe samples with date averages >100 Ma as well as the oldest ZHe date are recorded in samples from the Pole Bridge pluton and Sawtooth Stock of the northwest Wallowa Batholith. Samples collected from the Hurricane Divide and Craig Mountain plutons have ZHe dates between 100 to 110 Ma and AHe dates from 15 to 100 Ma. Average AHe data from the Needle Point pluton range from 71 to 84 Ma. Samples with AHe dates ∼15-20 Ma are found throughout the Wallowa Batholith (Figure 2.3). Two ZHe dates between 20 to 100 Ma were recorded in samples from the Pole Bridge pluton.

Sample eU Variability

AHe data eU values from the Wallowa and Bald Mountain Batholiths vary from 8 to greater than 250 ppm. This broad range is expected to result in significant variation in the temperature sensitivity of individual apatite grains. Viewed in bulk, the AHe data show a positive date-eU correlation (Figure 2.4 B), consistent with the log-normal relationship

described by previous workers (Shuster et al., 2006; Flowers et al., 2009). This date-eU correlation indicates radiation damage has played a role in determining the effective closure temperature of samples. Inconsistent with this trend, however, are 24 AHe dates from the Wallowa Batholith between 15-20 Ma (Figure 2.4 B). These dates overlap the timing of the Chief Joseph Dike Swarm and may reflect thermal resetting by the dikes. Similarly, Wallowa Batholith AHe dates at eU values less than 150 ppm are scattered. If all apatite grains experienced the same thermal history, this scatter would not be observed, suggesting some samples may have been partially reset by the Chief Joseph Dike Swarm. Bald Mountain Batholith AHe dates plot in a date-eU space with few Wallowa Batholith dates, suggesting the batholiths do not share a common thermal history (e.g., Flowers et al., 2007).

The five Wallowa Batholith plutons sampled in this study show distinct AHe eU values (Figure 2.3, 2.4 B, Table 2.1). AHe eU values for the Pole Bridge pluton average 53±16 ppm, the Hurricane Divide pluton averages 114±70 ppm, the Sawtooth Stock has an average eU of 104±58, the Craig Mountain pluton averages 25±12 ppm, and Needle Point pluton samples average 86±33 ppm. Samples from the Bald Mountain Batholith have eU values ranging from ∼15-111 ppm (Table 2.1). Sample WM08, shows a distinct date-eU relationship indicating radiation damage effects on He diffusivity played a role in the observed date dispersion (>30%) for this sample (Appendix A.1, Figure A.1).

ZHe eU values range from 47 to 330 ppm (Figure 2.4 D). This is a small range in eU for zircon relative to other locations (e.g., Orme et al., 2016), and is not expected to produce significant variability in the temperature sensitivity of samples. Two younger ZHe dates are not consistent with the date-eU trend observed in other samples. These ZHe dates come from samples with AHe dates at ∼17 Ma and likely reflect He loss due to reheating during Chief Joseph Dike intrusion. The paucity of ZHe dates does not allow us to determine pluton-specific trends in eU.

Thermochronometry Data Relative to Elevation and the CRB Basal Unconformity

It is common for low temperature thermochronometry dates to show a relationship with elevation, reflecting a geothermal gradient through which samples were advected during exhumation (e.g., Stüwe et al., 1994). We plot AHe and ZHe dates from the Wallowa and Bald Mountain batholiths, colored by the pluton sampled, against present-day elevation (Figure 2.5 A) as well as depth relative to the CRB basal unconformity (Figure 2.5 B). Coloring by pluton both allows for the interrogation of eU effect on sample date, given the characteristic eU values for each pluton (Figure 2.4 B; Table 2.1), as well as spatial trends in sample date (Figure 2.3). Plotting sample dates relative to the CRB basal unconformity corrects for hypothesized surface upwarping after eruption of the CRB (Figure 2.2). Pinning sample elevations to regional unconformities has helped elucidate trends in other studies' thermochronometry datasets (e.g., M. K. Clark et al., 2010; Zapata et al., 2019).

Bald Mountain Batholith AHe dates are anti-correlated with elevation. This may be due to the higher eU values for apatites from the lowest sample. However, if the >2 km elevation difference between the bottom and top samples is reflective of the vertical distance between samples during exhumation, a very low geothermal gradient would be needed even after accounting for eU variation. Alternatively, reduction in topographic relief may result in date-elevation profile inversion (Braun, 2002). While we cannot exclude this possibility, an explanation more consistent with warped CRB north of these samples (Figure 2.2), is that the present difference in elevation is the product of more recent deformation that we are unable to correct for.

Trends are difficult to interpret from the Wallowa Batholith data. Samples with AHe dates between 15-20 Ma are found at all elevations and likely reflect heating during Chief Joseph Dike intrusion (Figure 2.5 A). Excluding dates between 15-20 Ma, both the Hurricane Divide and Pole Bridge Pluton data show a rapid drop in age at low elevations, in a manner like that observed in exhumed partial retention zones (e.g., Wolf et al., 1998). Samples from the Needle Point Pluton do not show a trend with elevation and neither do ZHe data.

When plotted relative to the CRB basal unconformity, trends in the data remain opaque. Samples with AHe dates between 15-20 Ma cluster near the elevation of the unconformity and at depths greater than 600 m. A negative date-depth trend is observed in samples from the Needle Point Pluton. This trend is not observed clearly in any of the other plutons although the youngest dates for the Hurricane Divide and Pole Bridge plutons, excluding those that are coincident with the Chief Joseph Dikes, are found at 600 m depth or greater (Figure 2.5 B).

Chief Joseph Dike Distribution and Thermochronometer Dates

The lack of clear trends in the data relative to elevation and depth suggest thermochronometry from the Wallowa Batholith may record a more complicated thermal history than monotonic exhumation through a geothermal gradient. A probable candidate for complicating samples' thermal history is a thermal pulse during intrusion of the 15-17 Ma Chief Joseph dikes. A total of 2340 dike segments associated with this volcanic episode have been mapped in the Wallowa Batholith, exceeding 10 dikes km^{-2} across much of the pluton (Appendix A.1 Figure A.2; Morriss et al., 2020). Previous studies have found that reheating during intrusion of these dikes may result in the complete diffusion of helium from apatite and zircon grains (Reiners, 2005b; Karlstrom et al., 2019), and the 24 AHe dates between 15-20 Ma we present provide further evidence for complete He loss during Chief Joseph dike intrusion. Chief Joseph dike reheating is also recorded to drive partial helium loss from apatite and zircon (Reiners, 2005b; Karlstrom et al., 2019), which may be the cause of the date dispersion and resulting obfuscation of trends relative to elevation and depth that we observe (e.g., Figure 2.5 A, B).

To better constrain the impact of dike-induced reheating on our dataset, we examine the distribution of mapped dikes in the Wallowa Batholith relative to sample locations (Figure 2.5 C, D; Morriss et al., 2020). We find that mapped dike density varies across the Wallowa Batholith, increasing to the south and reaching a maximum of 24 dikes km^{-2} in the Craig Mountain pluton (Appendix A.1, Figure A.2). Many samples collected in this area are <1

km from 30-65 dikes (Figure 2.5 C; Table 2.1). Across the Wallowa Batholith, the density of dikes within 1 km of a sample varies from 0 to 65 (Figure 2.5 C; Table 2.1). Distance to the nearest dike ranges from 2 m to ∼3 km (Figure 2.5 D; Table 2.1).

Neither distance from the nearest dike nor the local dike density show a clear correlation with AHe date (Figure 2.5 C, D). Samples within 100 m of mapped dikes cover the range of recorded AHe dates, and no correlation between eU and greater propensity for fully reset dates is observed (Figure 2.5 C; Table 2.1). This lack of correlation is most likely due to the incomplete mapping of dikes (Morriss et al., 2020), varying scales of thermal perturbation from individual dikes (Petcovic, 2003; Karlstrom et al., 2019), local reheating superimposed on a regional increase to ambient temperature during dike intrusion (Karlstrom et al., 2019), as well as depth-dependent hydrothermal fluid flow around dikes (Bindeman et al., 2020). Our inability to correlate mapped dikes with scatter in AHe sample dates suggests that reheating during the intrusion of Chief Joseph dikes was heterogenous.

2.3.3 Time-temperature History Models

Using QTQt (Gallagher et al., 2012), we model Wallowa and Bald Mountain batholith AHe and ZHe datasets separately given the absence of mapped dikes in the Bald Mountain Batholith. Bald Mountain Batholith AHe data were modeled as a single group in an elevation transect. Wallowa Batholith AHe and ZHe data were subdivided into samples that have AHe dates between 15-20 Ma, coincident with the timing of Chief Joseph Dike activity, and samples that have AHe dates older than 20 Ma. Samples in these groups were individually modeled using QTQt. QTQt model results were then used to constrain a forward modeling exploration of the effect of Miocene reheating by the Chief Joseph dikes on AHe dates using HeFTy.

Bald Mountain Batholith Time-temperature History

First, we modeled the three samples collected from the Bald Mountain Batholith using QTQt (Figure 2.6). A 600° temperature constraint was provided for the timing of batholith

emplacement at 150±10 Ma and three AHe date errors were resampled. The model was run for 500,000 burn-in and 100,000 post burn-in steps which allowed convergence on a solution. Model results reproduce the AHe data well and successfully account for the date-eU relationship in sample WM08 (Figure 2.6; Appendix A.1, Figure A.1). Independent modeling of only WM08 suggests that it exerts a dominant influence on the model outcome, producing a similar time-temperature history even in the absence of WM07 and WM06. This corroborates our inference that these samples share a common thermal history and their present elevation offset is due to recent deformation not recorded by the thermochronometers.

The model estimates cooling to near-surface temperatures in the mid-Cretaceous. This is followed by slow reheating or isothermal holding until ∼50 Ma, after which the samples are estimated to cool to the present. From 110 Ma, the samples are estimated to be no greater than 80°C, with a narrow temperature range of 60-80°C estimated at ∼50 Ma. The intersample temperature range is small (∼10°C) for most of the model run. If the present-day elevation range of samples represents the long-term range, this would imply a geothermal gradient of ∼5°C, which is unreasonable given the tectonic and magmatic history of this region. Instead, the present-day elevation range of samples is likely the product of recent deformation of the Bald Mountain Batholith. Given that no Chief Joseph dikes are mapped or were identified in the field near these samples, we assume the data were not affected by Miocene or younger heating due to magmatism.

Reset Samples from the Wallowa Batholith

Next, we modeled six samples from the Wallowa Batholith that have AHe dates coincident with the Chief Joseph Dike Swarm using QTQt (Figure 2.7). We assume that all samples experienced complete He loss due to Miocene reheating and begin the models at 17 Ma with a constrained temperature range of 100-200°C from 15 to 17 Ma. Each model was run for 50,000 burn-in and 10,000 post burn-in steps which allowed convergence on a solution.

Results from fully reset AHe samples show rapid cooling to near-surface temperatures by ∼14 Ma. Two samples from the Pole Bridge Pluton cool later than others but are constrained

by a single AHe date each (Figure 2.7), limiting the conclusions that can be drawn from these results. Although modeled samples were collected from near the CRB basal unconformity to as much as 1 km depth below the unconformity (Table 2.1), predicted time-temperature histories are similar.

Wallowa Batholith Samples not Fully Reset by Chief Joseph Dikes

Many of these samples may have experienced reheating and partial He loss rather than full resetting during Chief Joseph Dike intrusion. This may result in model time-temperature histories that are not geologically accurate. To address this issue, we avoided modeling groups of data where a common thermal history must be assumed. Instead, we individually modeled 34 samples from the Wallowa Batholith with AHe dates >20 Ma using QTQt. We applied a crystallization age temperature of 600°C for each model given the pluton sampled. Each model was run for 50,000 burn-in and 10,000 post burn-in steps which allowed the statistics to converge on a solution.

We present the maximum, minimum, and average times at which each model estimates cooling to 60°C in order of increasing eU (Figure 2.8). If all samples experienced the same thermal history, then this approach would correct for eU and every sample would estimate a similar time for cooling below 60°C. Given that samples were collected over a variety of elevations, some variability in the timing of cooling below 60°C is expected, but the lack of depth or elevation correlation with AHe date suggests this variability was minimal (Figure 2.5 A, B).

The average time of cooling below 60°C shows scatter across samples and plutons, with a median of 80 Ma (Figure 2.8). However, if the 95% credibility time-temperature envelope is accounted for, 75% of samples, across all plutons and eU values, allow for cooling below 60°C by 90 Ma. Therefore, despite possible helium loss due to dike reheating, data from the Wallowa Batholith continue to record a thermal history associated with Cretaceous cooling to near surface temperatures.

Samples with the lowest eU values in the Craig Mountain pluton tend to show younger

times of cooling below 60°C. Given the lower effective closure temperature because of low eU and the high density of dikes in the Craig Mountain pluton (Appendix A.1, Figure A.2), this trend is most likely due to partial helium loss during Miocene dike intrusion.

Forward Modeling Exploration of Reheating During Dike Intrusion

To further understand this dataset and whether the younger cooling times from the Craig Mountain pluton reflect He loss during intrusion of the Chief Joseph dikes, we took the constraints provided by the inverse models and used them to guide forward models exploring the impact of dike reheating (Figure 2.9). First, we forward modeled synthetic AHe dates given eU from 1-300 ppm for two simple time-temperature histories for the Wallowa and Bald Mountain batholiths based on inverse model results (Figure 2.9 A). For the Wallowa Batholith forward model, we assume all samples cool to between 20 to 60°C at 90 Ma, cooling to 12-30°C by 17 Ma and then cooling to a uniform temperature of 10°C at present. For the Bald Mountain Batholith, we use the inflections at 130 Ma and 50 Ma in the average time-temperature paths estimated by the inverse model to constrain the forward model (Figure 2.6). Two features are worth noting from this experiment: the time-temperature histories for the Wallowa and Bald Mountain Batholiths are distinct and the Wallowa Batholith model does not adequately predict the range of measured AHe dates.

We modify the thermal model from A to include a transient phase of reheating between 15 to 17 Ma, to determine the temperature increase needed to reproduce the AHe date range observed in the Wallowa Batholith (Figure 2.9 B). The modeled samples are reheated to a maximum of 60, 80, 100, and 120°C at 16.5 Ma, cooling to 20°C at 15 Ma. These model results show that all AHe dates younger than those estimated given the simple cooling history in Figure 2.9 A, can be explained by transient heating to $\leq$120°C. Furthermore, if fully reset samples are excluded, transient heating to 60°C produces estimated dates that best fit the data in aggregate.

2.4 Discussion

Since emplacement between 120 and 160 Ma at depths of ∼4-7 km (Schwartz et al., 2014; Žák et al., 2015), the thermal histories of the Wallowa and Bald Mountain batholiths have been linked to the local effects of regional tectonics and volcanism. Below, we explore these thermal histories in the context of regional constraint on orogeny and landscape evolution. We argue that the Blue Mountains Province has undergone three major phases of uplift and deformation since the Cretaceous, each associated with a distinct shift in regional tectonics.

2.4.1 Bald Mountain Batholith Time-temperature History

The thermal history estimated by modeling Bald Mountain Batholith samples indicates the batholith was exhumed to the near surface by the mid-Cretaceous. During this time, the terranes of the Blue Mountains Province were amalgamating and accreting to North America. The next major phase of cooling began at 50 Ma coincedent with a Pacific basin-wide tectonic reorganization (e.g., Seton et al., 2015). Locally, this timing coincides with the accretion of Siletzia (Wells et al., 2014), and cessation of the Laramide Orogeny (DeCelles, 2004). Estimated cooling just predates local geologic constraint on surface exposure of the batholith, including sediments with Eocene age detrital zircons found in contact with the Bald Mountain Batholith as well as overlying volcanic units associated with the Tower Mountain Caldera dated to 22-32 Ma (Figures 2.1, 2.3, 2.6; Reiners, 2005a; Seligman et al., 2014). Given these constraints, the timing of Cenozoic cooling to surface temperatures of the Bald Mountain Batholith is bracketed between 50 and 22-32 Ma.

Cenozoic cooling of the Bald Mountain Batholith may have been associated with deformation and exhumation following the accretion of Siletzia. The Columbia Embayment, north of the Bald Mountain Batholith may have experienced a period of rifting and extension during this time (Catchings & Mooney, 1988). Additionally, the geochemistry of Eocene and Oligocene volcanic units in the Blue Mountains Province have been interpreted as showing evidence for lithospheric delamination (Seligman et al., 2014).

2.4.2 Wallowa Batholith Time-temperature History

The time temperature history of the Wallowa Batholith recorded by our data reflects mid-Cretaceous cooling to near surface temperatures and transient reheating during the intrusion of the Chief Joseph dikes. Time-temperature histories constrained by samples fully reset by the Chief Joseph dikes estimate cooling to the near surface by 14 Ma. This cooling is most likely due to heat loss following the cessation of dike activity, not exhumation. AHe date-eU relationships indicate ambient temperature of the Wallowa Batholith may have increased to 60°C during dike intrusion as suggested by prior modeling efforts (Karlstrom et al., 2019). Given the shallow depth of samples below the CRB basal unconformity (Figure 2.5 B; Table 2.1), AHe data do not have the resolution to record the timing of cooling related to exhumation since the Miocene. However, the thermal histories of samples not fully reset by the Chief Joseph dikes as well as the distribution of CRB across the Wallowa Mountains suggest the Wallowa Batholith had not experienced uplift and mountain building since the mid-Cretaceous

Reheating due to burial beneath an estimated 800 m of CRB is not clearly observed in the dataset. We speculate that the lack of resetting from CRB of samples in the Wallowa Batholith could be the result of groundwater flow through the CRB as is observed in the Columbia Basin (Burns et al., 2015). If upwarping of the Wallowa Mountains occurred shortly after CRB eruption, then meteoric water could have penetrated through extensional fractures in the basalt and limited an increase to the geothermal gradient.

In the southeastern Wallowa Batholith, samples with AHe dates averaging ∼20-30 Ma despite no locally mapped dikes and hundreds of meters distance between sample sites (Figure 2.3; Table 2.1), may have been partially reset by burial. Kahn et al. (2020) record similar AHe dates from a sample nearby. They also report full resetting of AHe data from the Snake River north of the Wallowa Batholith which they interpret to result from CRB burial.

The preponderance of inverse model results for samples not fully reset by the Chief Joseph dikes show cooling to near surface temperatures occurred in the mid-Cretaceous (Figure

2.8). This result is similar to the Mesozoic cooling recorded by the Bald Mountain Batholith (Figure 2.6) and likely reflects uplift and deformation during terrane amalgamation and accretion to North America. If a geothermal gradient of 20-30°C is assumed, cooling below 60°C by 90 Ma would suggest an average late Cretaceous through Cenozoic exhumation rate of 0.02-0.03 mm yr^{-1}. This contrasts with the estimated thermal history for the Bald Mountain Batholith which resolves a period of rapid Eocene cooling event equivalent to an exhumation rate up to 0.19 mm yr^{-1}.

Samples from the Craig Mountain pluton record a slightly later time of cooling than samples from other plutons (Figure 2.8). This could reflect a true difference in the exhumation history of theses samples resulting from differential exhumation rates during orogenic decay (e.g., Reiners, 2003). Numerical modeling of the exhumation of batholiths suggests that isostasy alone will result in heightened rates of exhumation in the cores of batholiths even after tectonically driven uplift ceases (Braun et al., 2013). Such a process could be responsible for the later cooling in the Craig Mountain pluton. Alternatively, the low eU of these samples may have made them more susceptible to He loss during dike intrusion. Given that the Craig Mountain pluton hosts the greatest density of mapped dikes (Appendix A.1, Figure A.2), it is most likely that partial He loss during Miocene reheating is responsible for the later cooling time estimated by these samples.

This dataset provides clear evidence for slow cooling of the Wallowa Batholith since the mid-Cretaceous. Assuming a conservative geothermal gradient of 20-30°C, cooling could be explained if all samples were 1.5-2.5 km below the surface at 90 Ma. We estimate ∼1 km of Miocene to present incision into the Wallowa Batholith, as evidenced by the depth below the CRB basal unconformity of river valleys (Appendix A.1, Figure A.3).

Less than 2.5 km exhumation from 90-17 Ma is suggestive of a post-orogenic landscape. Given the high elevation and relief of the Wallowa Mountains at present, slow exhumation through the Cenozoic supports the hypothesis that the Wallowa Mountains experienced renewed uplifted from the Miocene to present (Hales et al., 2005), but that resulting exhumation has not been large enough to be recorded by the AHe thermochronometer.

2.4.3 Mesozoic to Present Tectonics and Landscape Change in the Blue Mountains Province

In this section, we present a topographic history of the Blue Mountains Province from the Mesozoic to present by synthesizing our data from this study with previous regional studies. To aid in describing this history, we provide a map-view cartoon depiction of the major geologic events from the Mesozoic to the Miocene in the Blue Mountains Province and surroundings (Figure 2.10). The Wallowa and Bald Mountain batholiths as well as pertinent plate boundaries were rotated to satisfy paleomagnetic constraints from Wilson and Cox (1980), Gromme et al. (1986), Housen (2005), Housen (2018), and Tikoff et al. (2019). All rotations made are clockwise and involve 21° from 90-120 Ma, 30° from 70-90 Ma, 7° from 17-32 Ma, and 7° from 15 Ma to present. Rotations prior to 55 Ma involve all depicted features. For rotations after 55 Ma, the pole of rotation for the Blue Mountains Province is assumed to be fixed in the Riggins group at the Salmon River Suture Zone.

Mesozoic: Exhumation of the Wallowa and Bald Mountain batholiths likely began immediately following emplacement as a result of deformation associated with the late stages of terrane amalgamation and suturing to North America (Figure 2.10 A; Schwartz et al., 2011, 2014; Žák et al., 2015). Both the Wallowa and Bald Mountain batholiths lay along strike of the continental boundary from 120-160 Ma (Figure 2.10 A), however cleavage and foliation in the Wallowa and Baker terranes suggests shortening from 140-160 Ma was oriented roughly parallel to the plate boundary and between terranes (Schmidt et al., 2017; Žák et al., 2015). Removing subsequent rotation, the 040/320 Wallowa Fault and Wallowa-Baker terrane boundaries were oriented favorably for reverse motion during middle Cretaceous inter-terrane convergence (Figure 2.10 A). The Bald Mountain Batholith was emplaced during the final phases of intra-terrane convergence at the suture between the Baker and Wallowa terranes (Figure 2.10 A; Schwartz et al., 2014). The Wallowa Batholith was subsequently intruded into Wallowa terrane crust thickened by terrane amalgamation (Žák et al., 2015).

From 120-140 Ma the Blue Mountains Province records increasing influence of pure-shear deformation at the plate boundary with the development of the Salmon River Suture Zone

(McKay et al., 2017). By 125 Ma, shortening in the Wallowa Batholith area was oriented perpendicular to the North American plate boundary (Figure 2.10 A; Žák et al., 2015). After 120 Ma, transpression, mostly taken up by the WISZ and regions to the east (Kahn et al., 2020), further deformed the Blue Mountains Province (Schmidt et al., 2017; Braudy et al., 2017). While thermal models for the Bald Mountain Batholith do not suggest an increase in exhumation rate over this time (Figure 2.6), data from the Wallowa Batholith constrain cooling to below 60°C by 90 Ma (Figure 2.8). Although the majority of deformation associated with the WISZ occurred within and east of the Salmon River Suture Zone (Lund & Snee, 1988; Giorgis et al., 2005; Kahn et al., 2020), deformation rates remained elevated in the Blue Mountains Province, resulting in rapid cooling of the Seven Devils Mountains east of the Wallowa Batholith (Morriss 2021, personal comm., Kahn et al., 2020), and deformation in the Syringa Embayment (Lund et al., 2008; Schmidt et al., 2017). The Wallowa Batholith may have continued to be uplifted and exhumed during this time.

The topography of the Blue Mountains Province ca. ∼90 Ma was likely mountainous, with increasing topographic relief in the Syringa Embayment and adjacent the WISZ (Figure 2.10 B). This is evidenced by a regional west to east trend in decreasing ZHe cooling age presented by Kahn et al. (2020). Transpression in the WISZ led to extreme shortening and exhumation of a mid-Cretaceous volcanic arc at the North America plate boundary (Figure 2.10 B; Giorgis et al., 2005). Shortening migrated inboard North America, thickening the crust east of the WISZ (Fayon et al., 2017). South of the Wallowa Batholith, topography was more subdued, dropping below sea level in the Ochoco basin, presently ∼150 km from the Bald Mountain Batholith. Rivers flowing from highlands in the north fed sediment to the Ochoco basin and other forearc basins during this time (Figure 2.10 B; Surpless & Beverly, 2013; Dumitru et al., 2013).

By the end of transpression on the WISZ ca. 90 Ma, the Wallowa Batholith had exhumed to the near surface (Figures 2.8, 2.10 B). From 90 to 55 Ma the Wallowa Batholith gradually cooled during a period of orogenic decay. The Bald Mountain Batholith may have been buried over this time, leading to subtle reheating (Figure 2.6). Elsewhere in the Blue

Mountains Province there is evidence for late-Cretaceous and Cenozoic deformation. North of the Wallowa Batholith, the dextral-oblique Mt Idaho and Limekiln structural zones in the Syringa Embayment may have remained active until ∼70 Ma (Schmidt et al., 2017). In the WISZ and to the east, exhumation rates remained elevated through the early Cenozoic (Giorgis et al., 2005; Fayon et al., 2017), likely driven by ongoing deformation, volcanism, and topographic growth. By 55 Ma, interior Idaho west of the WISZ had developed into an elevated plateau (Figure 2.10 C; Fayon et al., 2017). The western flank of this plateau likely did not extend west of the area adjacent the WISZ, where thermochronometry data record steady cooling to surface temperatures from 70-40 Ma (Kahn et al., 2020).

Paleogene: Accretion of Siletzia east of the Blue Mountains Province ca. 50-55 Ma (Wells et al., 2014) marks the onset of the next major phase of topographic development in the Blue Mountains Province (Figure 2.10 C). Coincident with accretion of Siletzia was the cessation of arc magmatism in the Northern Cordillera (Gehrels et al., 2009; Gaschnig et al., 2010), and the end of the Laramide Orogeny (Humphreys, 1995; DeCelles, 2004). Rollback of subducted oceanic lithosphere to the west and south (Humphreys, 1995), may have led to the widespread volcanism of the Challis episode in Idaho (43-51 Ma; Janecke & Snee, 1993; Gaschnig et al., 2010, 2011; Chetel et al., 2011) and possibly the Clarno volcanics in Oregon (39-54 Ma; Retallack et al., 2000). Accretion of Siletzia also coincided with rifting in the Columbia Embayment (Catchings & Mooney, 1988). Large rivers transported sediment from the rapidly exhuming interior of Idaho to the west (Sweetkind & Blackwell, 1989; Foster & Raza, 2002; Fayon et al., 2017), depositing cobble-sized clasts of quartzite across the Blue Mountains Province (Figure 2.10 C; Allen, 1991; Reiners, 2005a). These rivers were likely destined for the 45-52 Ma Herren formation of central Oregon (Jijina et al., 2019), the Columbia Embayment (Campbell, 1989), and the Tyee basin of western Oregon (Dumitru et al., 2013).

Thermochronometry from the Bald Mountain Batholith indicates a phase of accelerated cooling after 50 Ma, at approximately the same time as is observed in Idaho (Figure 2.6; Sweetkind & Blackwell, 1989; Foster & Raza, 2002; Fayon et al., 2017). Cooling may have

been driven by exhumation resulting from uplift in response to slab breakoff and delamination during Siletzia accretion. Lithospheric delamination has been proposed as a driver for the Clarno volcanics found adjacent the Bald Mountain Batholith as well as the Challis volcanics in Idaho (Seligman et al., 2014; Schmandt & Humphreys, 2011). Alternatively, exhumation and cooling may have been related to significant extension hypothesized north of the KBML (Figure 2.1; Catchings & Mooney, 1988).

Volcanism, while widespread in the Blue Mountains Province after 55 Ma, did not extend into the Syringa Embayment and Wallowa Batholith region (Figures 2.1, 2.10 C). Together with the steady cooling predicted from Wallowa Batholith thermochronometry (Figure 2.8), this suggests that these areas were exempt from the tectonics responsible for volcanism and cooling in the Bald Mountain Batholith and areas west. By 32 Ma, west flowing rivers had been disrupted by Clarno volcanism and concomitant deformation, leading to regional drainage reorganization (Figure 2.10 C; Ferns et al., 2010; Seligman et al., 2014).

Neogene to Present: At the time of CRB eruption ca. 17 Ma, the Blue Mountains Province and surroundings could be broadly divided between areas that experienced volcanism and deformation following the accretion of Siletzia ∼55 Ma (Figure 2.10 C; Wells et al., 2014), and those that did not. Topographic differences between these domains appear to have influenced the distribution of CRB (Figures 2.2, 2.10 D). CRB did not flow over the Bald Mountain Batholith region, nor did it extend past the WISZ to the east. It did inundate mountains with ∼1 km local relief in the Syringa Embayment and south of the Wallowa Batholith (Fitzgerald, 1982). These observations suggest the area from the Wallowa Batholith north into the Syringa Embayment were topographically depressed relative to surroundings.

Uplift of the south and eastern portions of the study area began during the earliest phases of CRB eruption, leading to northwestward offlap of Grande Ronde R2 and N2 members (Figure 2.10 D; Camp, 1995). Uplift was aided by deformation on discreet structures from the Wallowa Batholith, south (Camp & Hooper, 1981; Reidel, Camp, Tolan, & Martin, 2013). Although our data do not directly constrain the onset of Miocene to present uplift in the

Wallowa Mountains, the lack of Grande Ronde N2 and later flows on all but the northwest flank of the range indicate uplift began by the end of Grande Ronde eruption. Deformation during this time may reflect isostatic responses to loading by CRB as well as delamination of underplated oceanic lithosphere and lower crust (Hales et al., 2005; Camp & Hanan, 2008; Perry-Houts & Humphreys, 2018; Castellanos et al., 2020).

Structural relief on the warped basal unconformity of the CRB over the Wallowa Batholith is evidence for 1-2 km of uplift since the Miocene (Figure 2.2). Adding an estimated CRB thickness of 800 m, average erosion rates since 16 Ma range from 0.05-0.13 mm yr^{-1}. This is equivalent to a ∼2-4x increase in rate compared to the late Cretaceous and Cenozoic average. This rate increase is similar in magnitude to the Cenozoic exhumation rates estimated for the Bald Mountain Batholith following a the accretion of Siletzia. It is possible that in both cases, removal of underplated oceanic lithosphere drove uplift (Darold & Humphreys, 2013; Seligman et al., 2014). At present, a high velocity mantle anomaly extending to depths > 250 km below the Wallowa Batholith is observed and has been interpreted as a remnant of such a foundering/delamination event (Figure 2.10, Wallowa Anomaly; Hales et al., 2005; Darold & Humphreys, 2013; Gao, 2015; Stanciu et al., 2016).

Crustal deformation continued after CRB eruption. Extension in the La Grande Graben began by 9 Ma or earlier (Figure 2.10 E; VanTassell et al., 2001), and volcanism on the La Grande-Owyhee eruptive axis continued to the Quaternary (Ferns & McClaughry, 2013). Many of the structures active from the Miocene to present in the Blue Mountains Province likely exploited pre-existing weaknesses derived from Mesozoic deformation (e.g., Tikoff et al., 2001; Schmidt et al., 2017).

2.5 Conclusions

New geologic map interpretations and low-temperature thermochronology data from the Blue Mountains Province reveal multipart thermal and exhumation history for the Wallowa and Bald Mountain Batholiths. Exhumation of the Wallowa and Bald Mountain Batholiths began following emplacement during Blue Mountains Province terrane amalgamation and

slowed by ∼90 Ma. At this time, both the Wallowa and Bald Mountain Batholiths were likely <2-3 km from the surface. The Bald Mountain Batholith experienced a phase of rapid cooling in the Eocene, potentially linked to accretion of Siletzia. No similar cooling history is recorded in the Wallowa Batholith. During Miocene CRB eruption, pre-existing topography dictated basalt flow directions, inundating the denuded Wallowa Batholith but not the uplifted Bald Mountain Batholith. Miocene to present deformation, while not recorded by thermochronometers due to the limited amount of recent exhumation (<2 km), is evidenced by warping and faulting of CRB across the Wallowa Mountains.

2.6 Figures and Tables

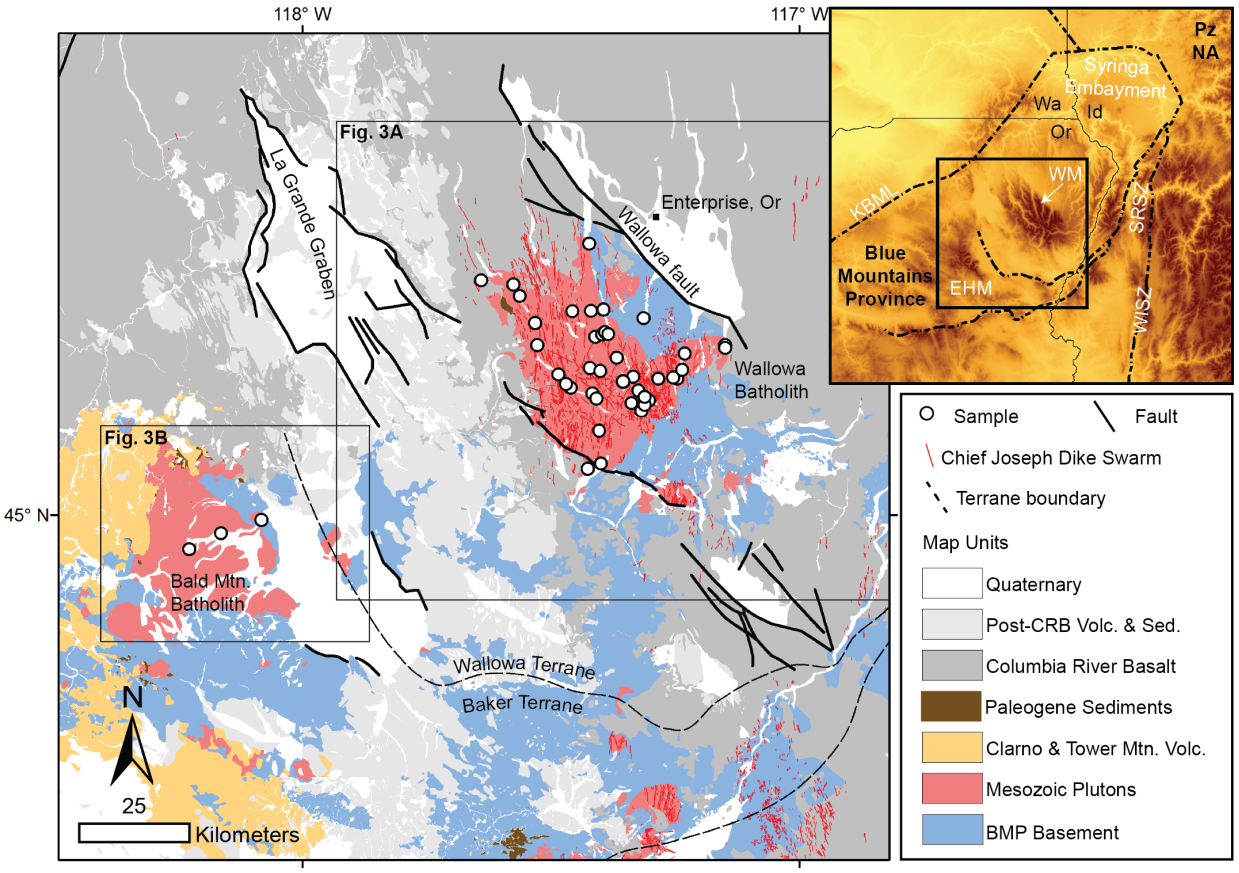

Figure 2.1: Map of the study area showing surface geology, major faults, sample locations, and terrane boundaries. Inset figure shows regional topography with major lithotectonic terrane boundaries. Pz NA – Paleozoic North America; EHM – Elkhorn Mountains; WM – Wallowa Mountains; KBML – Klamath-Blue Mountains Lineament; SRSZ – Salmon River Suture Zone; WISZ – Western Idaho Shear Zone.

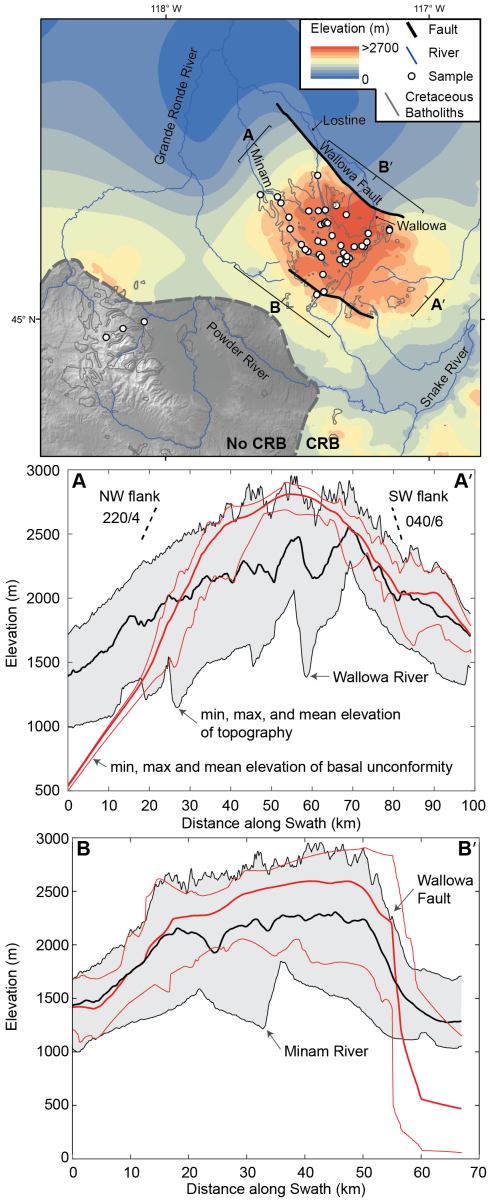

Figure 2.2: Interpolated structure-contour of the Columbia River Basalt basal unconformity overlain on outline of Wallowa batholith and major rivers (upper panel). Swath profiles A-A' and B-B' (lower two panels) show present-day topography and basal unconformity parallel and perpendicular to Wallowa fault, respectively. Dashed lines in panel depicting A-A' swath show strike and dip of basalt flows.

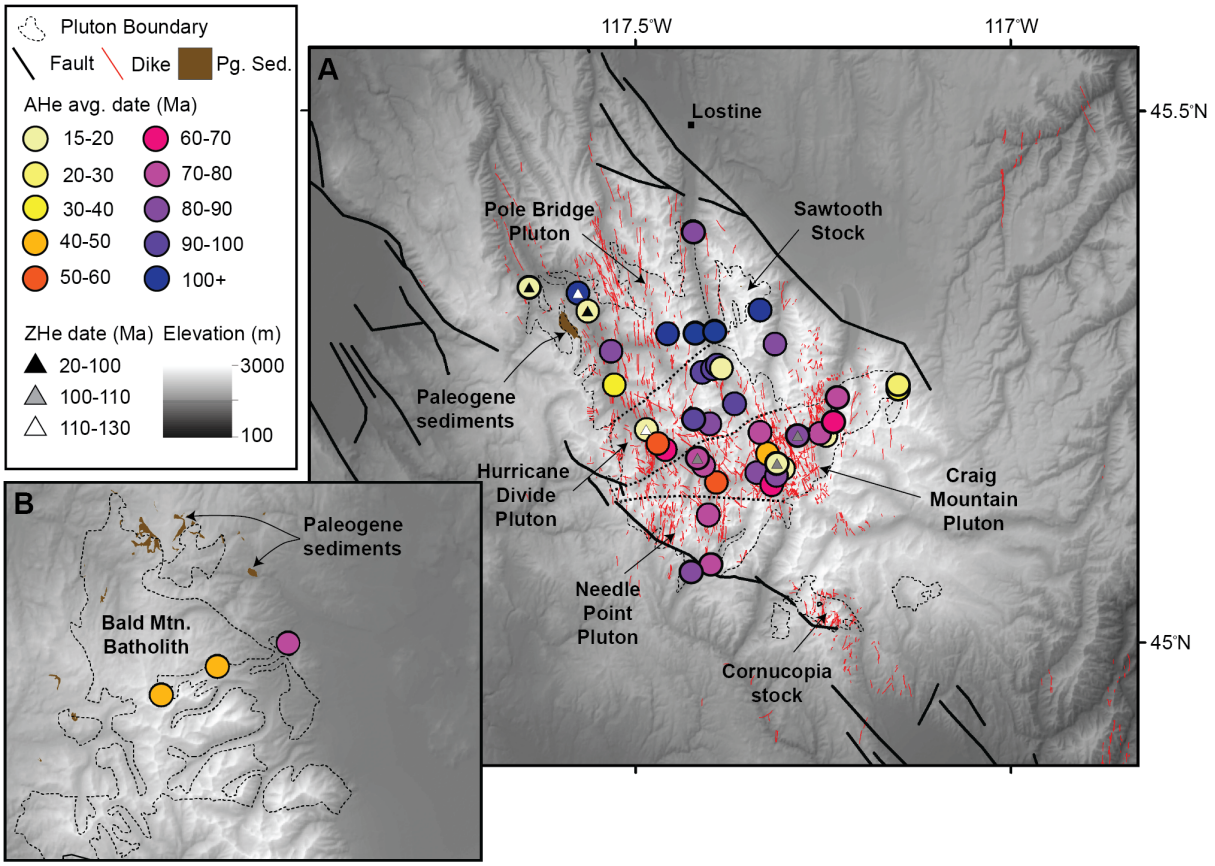

Figure 2.3: Low-temperature thermochronometry sample average dates overlain on present day topography with outlines of major plutonic bodies, Chief Joseph Dikes, and the location of Paleogene sedimentary deposits, in the Wallowa (A) and Elkhorn (B) Mountains.

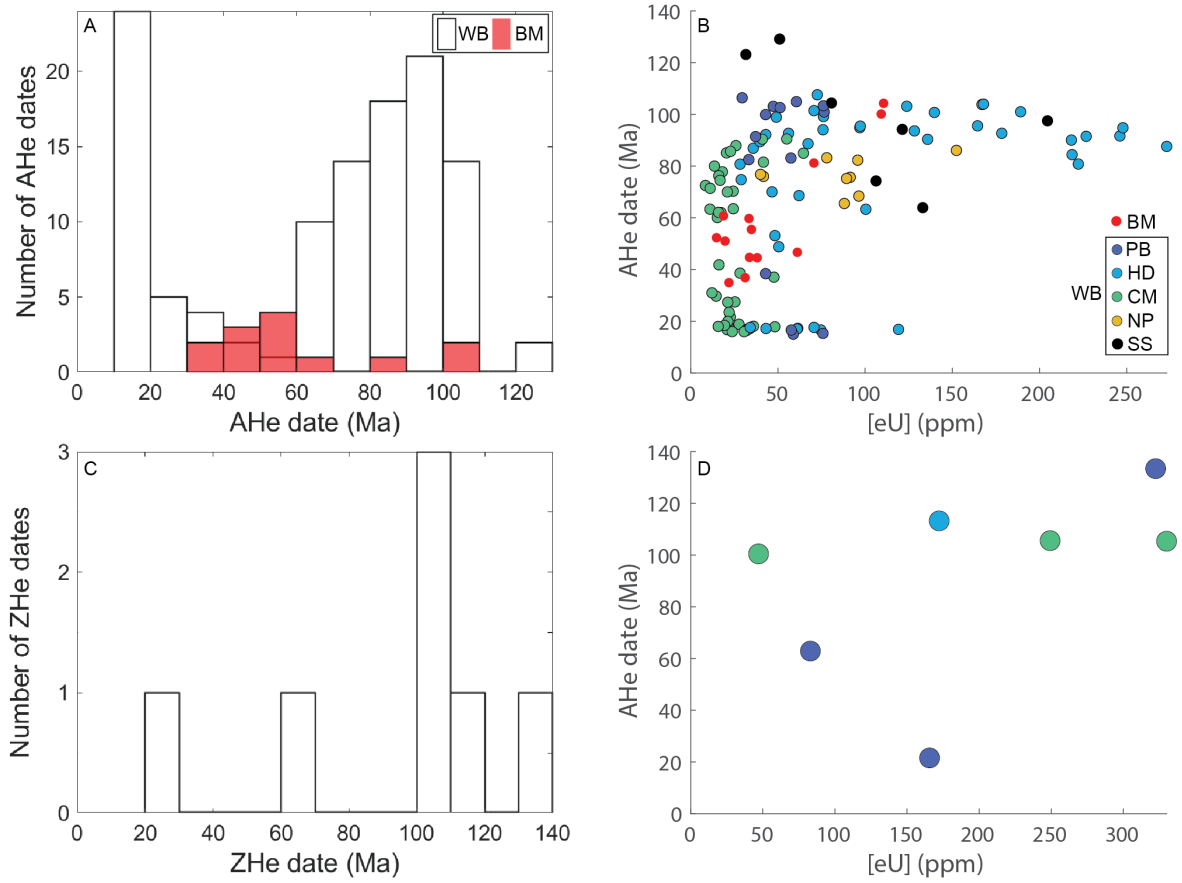

Figure 2.4: Histogram of AHe data from the Wallowa and Bald Mountain Batholiths. B. AHe dates from the Wallowa and Bald Mountain Batholiths plotted against eU. C. Histogram of ZHe data from the Wallowa Batholith. D. ZHe dates from the Wallowa Batholith plotted against eU. PB – Pole Bridge Pluton; HD – Hurricane Divide Pluton; CM – Craig Mountain Pluton; NP – Needle Point Pluton; SS – Sawtooth Stock; BM – Bald Mountain Batholith; WB – Wallowa Batholith.

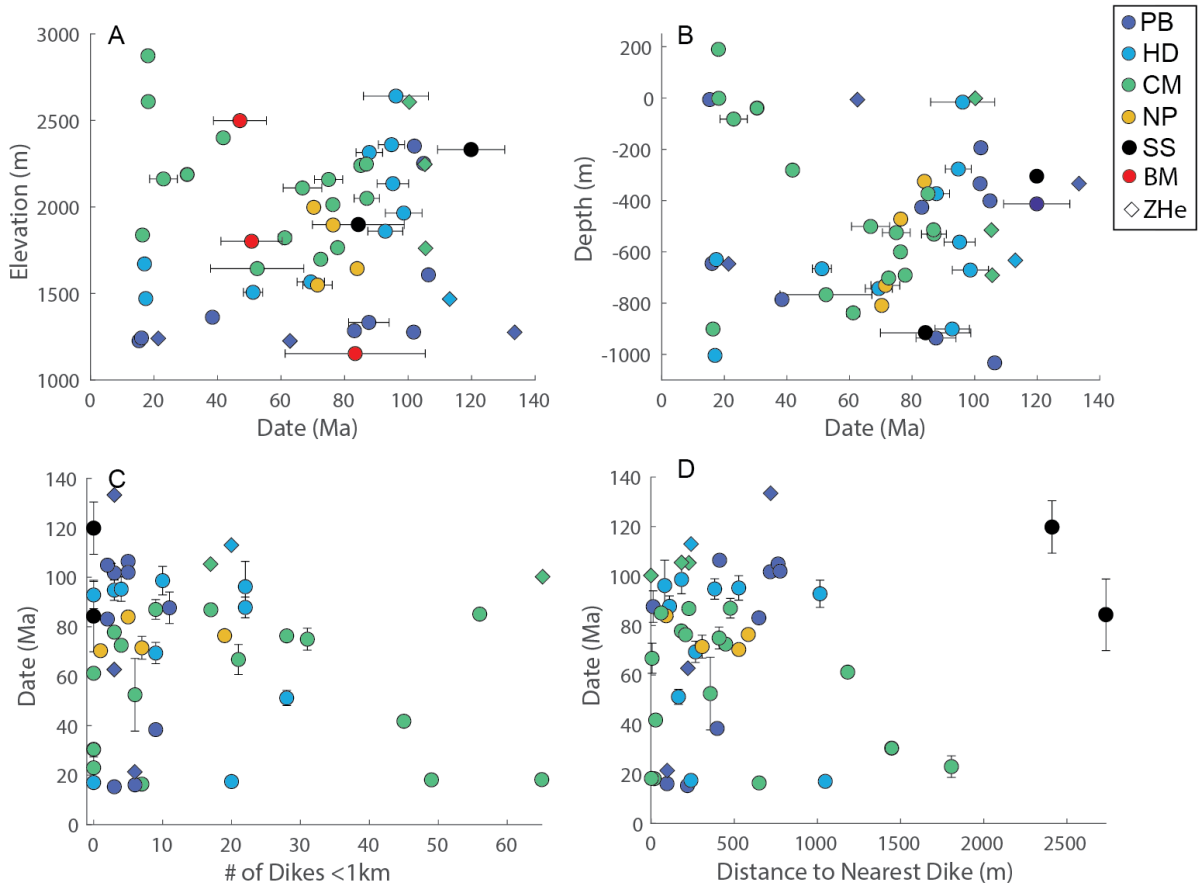

Figure 2.5: A. Date-elevation plot of samples from the Wallowa and Bald Mountain Batholiths, B. Date-depth below CRB basal unconformity plot of samples from the Wallowa Batholith, C. Date vs. distance to the nearest dike and D. Date relative to number of dikes within 1 km. WB – Wallowa Batholith; PB – Pole Bridge Pluton; HD – Hurricane Divide Pluton; CM – Craig Mountain Pluton; NP – Needle Point Pluton; SS – Sawtooth Stock; BM – Bald Mountain Batholith.

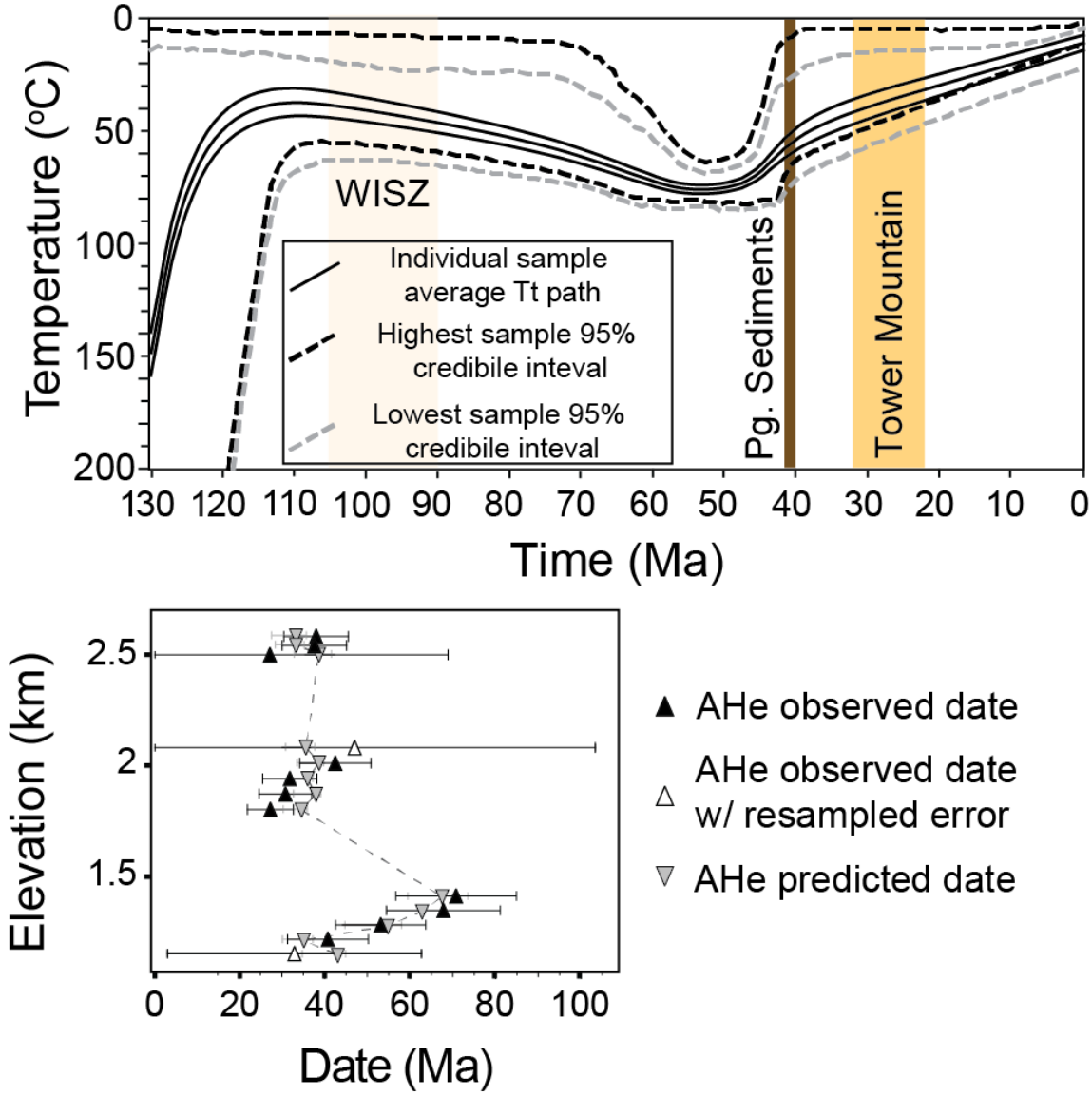

Figure 2.6: Time-temperature plot and estimated AHe dates from modeled Bald Mountain Batholith samples. Time of peak WISZ activity, age of youngest zircons in Paleogene sediments in contact with the batholith as well as timing of Tower Mountain volcanism shown.

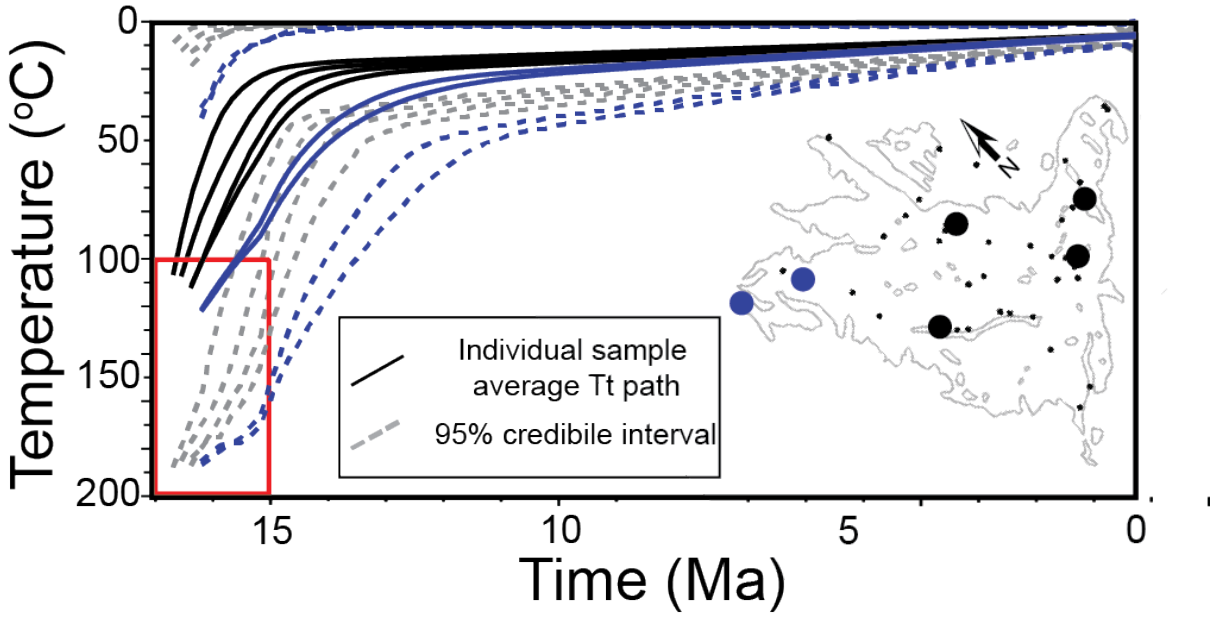

Figure 2.7: Time-temperature plot of model results for samples with 15-20 Ma AHe dates with inset map of Wallowa Batholith showing sample locations.

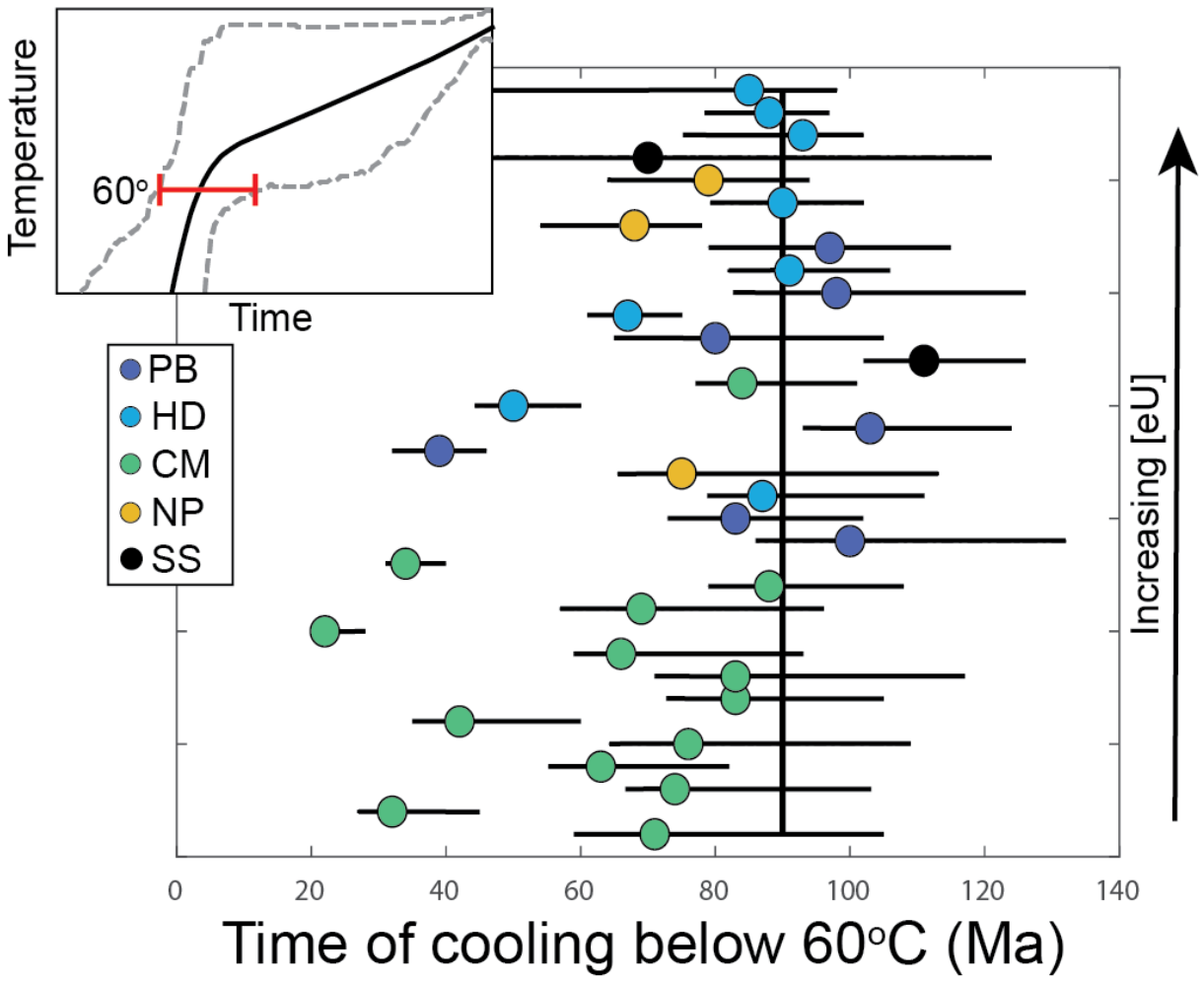

Figure 2.8: Estimated time of cooling below 60°C for 34 samples from the Wallowa Batholith, stacked in order of increasing eU. PB – Pole Bridge Pluton; HD – Hurricane Divide Pluton; CM – Craig Mountain Pluton; NP – Needle Point Pluton; SS – Sawtooth Stock.

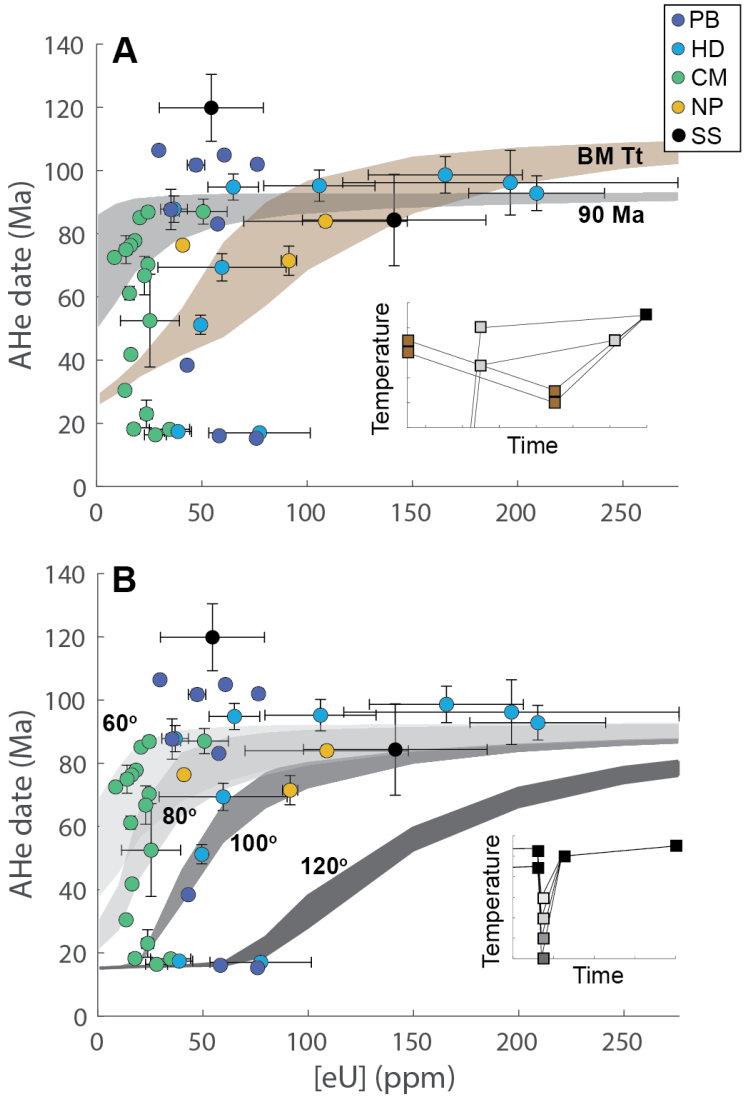

Figure 2.9: Forward modeling experiments exploring the effect of eU on sample AHe dates compared to observed AHe dates from the Wallowa Batholith. A. Bald Mountain Batholith cooling model compared to steady cooling from 90 Ma. Shaded region denotes synthetic AHe date range from model. B. The effect of Miocene reheating on the age distribution given the steady cooling model from A. Temperatures are peak temperature during Miocene reheating.

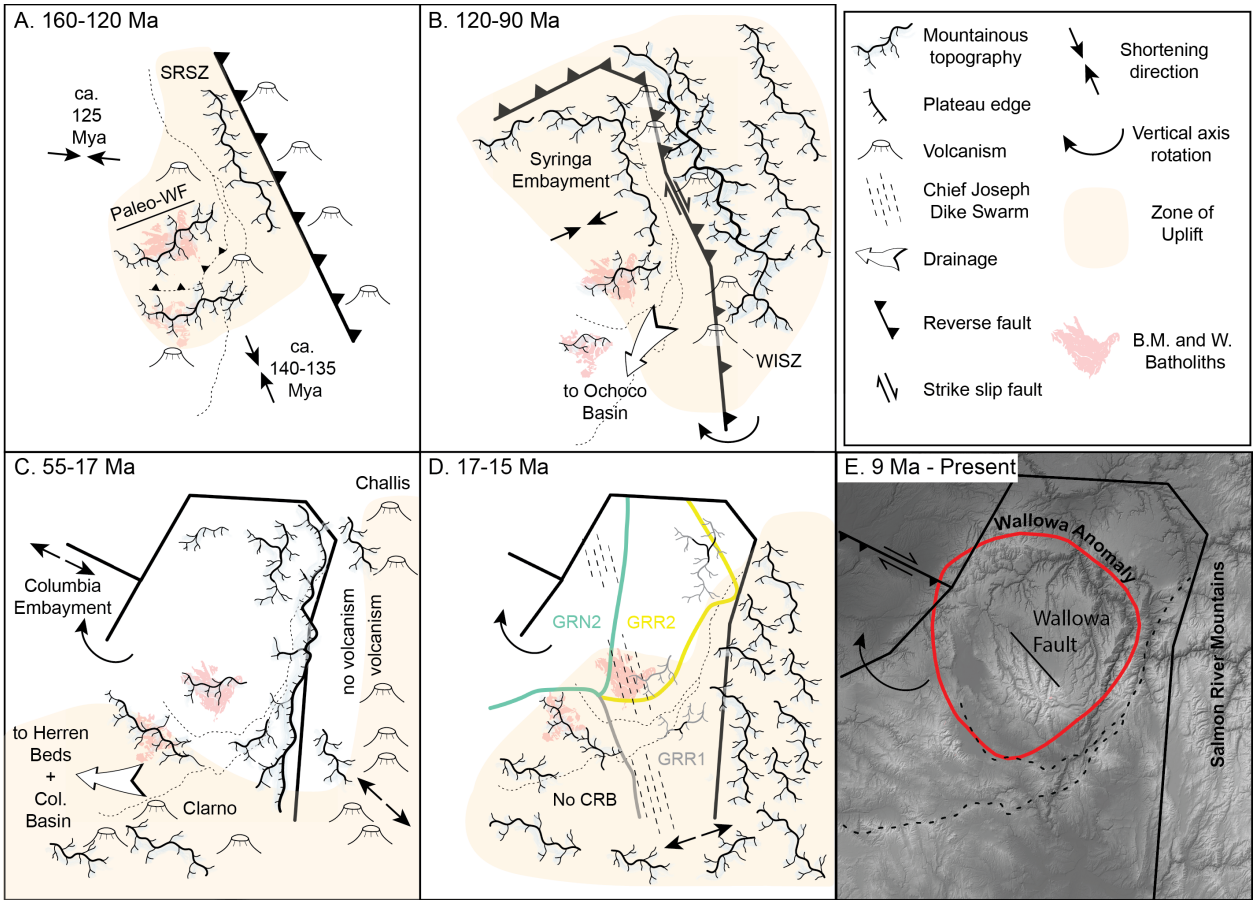

Figure 2.10: Proposed Mesozoic to present tectonic, volcanic, and topographic history for the Blue Mountains Province and surroundings. Boundary between Baker, Wallowa, and Old's Ferry terranes marked as dotted line. Boundary of Paleozoic North America shown as weighted black line. SRSZ – Salmon River Suture Zone; WISZ – Western Idaho Shear Zone; WF – Wallowa Fault; GRR1-R2-N2 – Grande Ronde Reverse 1, Reverse 2, and Normal 2 members.

Table 2.1: AHe and ZHe data from the Wallowa and Bald Mountain Batholiths

Sample	Lithology	Longitude (W)	Latitude (N)	No. Grains or Aliquots	Corrected Ahe Date (Ma)	1σ (Ma)	eU (ppm)	1σ (ppm)	Elevation (m)	Depth (m)	no. CJD	Dike proximity (m)
WM06	Bald Mt Batholith	118.228	44.951	3	47.05	8.33	18.80	3.65	2499	0	0	7536
WM07	Bald Mt Batholith	118.164	44.974	5	50.73	9.66	31.04	7.3	1802	0	0	6843
WM08	Bald Mt Batholith	118.083	44.993	5	83.33	22.07	77.27	32.56	1153	0	0	11432
WM21	Craig Mountain pluton	117.150	45.242	5	22.97	4.36	23.66	2.8	2162	-82	0	1805
WM22	Hurricane Divide pluton	117.411	45.255	5	94.78	4.13	64.89	12.04	2360	-277	3	382
WM23	Hurricane Divide pluton	117.397	45.258	5	95.2	4.96	105.79	26.42	2135	-562	4	527
WM24	Hurricane Divide pluton	117.391	45.261	5	92.83	5.5	209.03	32.25	1860	-901	0	1015
WM25	Hurricane Divide pluton	117.385	45.258	5	17.01	0.43	77.37	24.09	1671	-1004	0	1047
WM27	Hurricane Divide pluton	117.460	45.182	4	69.36	4.31	59.52	30.43	1567	-743	9	267
WM28	Craig Mountain pluton	117.392	45.151	5	52.49	14.68	25.29	14.04	1644	-767	6	356
WM29	Hurricane Divide pluton	117.422	45.210	5	96.17	10.24	196.51	79.63	2641	-16	22	82
WM30	Hurricane Divide pluton	117.401	45.206	4	87.79	4.18	36.72	6.33	2315	-373	22	111
WM31	Craig Mountain pluton	117.303	45.164	5	18.1	1.28	34.61	9.56	2874	190	49	19
WM35	Craig Mountain pluton	117.338	45.160	4	86.99	3.97	50.62	11.35	2050	-531	9	476
WM39	Craig Mountain pluton	117.246	45.195	5	16.37	0.45	27.90	5.2	1838	-901	7	649
WM42	Hurricane Divide pluton	117.368	45.225	4	98.62	5.77	165.62	36.59	1965	-671	10	183
WM51	Needle Point pluton	117.399	45.073	4	71.48	4.62	91.33	3.66	1549	-731	7	307
WM52	Needle Point pluton	117.426	45.066	3	83.95	1.75	108.71	38.83	1644	-325	5	90
WM53	Sawtooth Stock	117.314	45.281	4	84.33	14.45	141.30	43.59	1898	-916	0	2735
WM54	Sawtooth Stock	117.334	45.313	3	119.85	10.58	54.45	24.72	2332	-304	0	2410
WB005	Craig Mountain pluton	117.231	45.231	1	70.3	0.7	24.34	-	1998	-809	1	527
WB009	Craig Mountain pluton	117.150	45.238	2	30.44	0.92	13.40	1.7	2188	-39	0	1446
WB010	Pole Bridge pluton	117.423	45.386	1	83.1	1	57.45	-	1285	-426	2	648
WB017	Pole Bridge pluton	117.394	45.293	1	106.4	1.2	29.49	-	1608	-1033	5	412
WB034	Pole Bridge pluton	117.641	45.334	1	15.3	0.1	75.85	-	1227	-6	3	218
WB101	Pole Bridge pluton	117.576	45.329	3	101.74	1.74	47.17	4.13	1277	-334	3	716
WB104	Pole Bridge pluton	117.563	45.312	2	16.06	1.13	58.23	0.82	1243	-645	6	96
WB109	Pole Bridge pluton	117.532	45.274	2	87.65	6.38	35.27	2.75	1333	-936	11	12
WB112	Pole Bridge pluton	117.528	45.243	1	38.4	0.5	42.96	-	1363	-786	9	397
WB118	Hurricane Divide pluton	117.485	45.201	2	17.40	0.28	38.64	6.4	1471	-630	20	239
WB121	Hurricane Divide pluton	117.470	45.188	2	51.19	3.04	49.38	1.56	1507	-666	28	164
WB130	Craig Mountain pluton	117.417	45.174	1	77.8	0.7	18.15	-	1765	-691	3	182
WB131	Craig Mountain pluton	117.409	45.167	1	72.5	0.8	8.43	-	1698	-702	4	448
WB139	Needle Point pluton	117.403	45.120	2	76.40	0.57	40.88	1.22	1896	-472	19	584
WB141	Craig Mountain pluton	117.318	45.149	2	66.75	4.60	22.71	2.39	2110	-501	21	6
WB143	Craig Mountain pluton	117.312	45.158	1	85.1	0.9	20.50	-	2240	-373	56	60
WB146	Craig Mountain pluton	117.324	45.178	1	41.8	0.4	16.21	-	2400	-281	45	27
WB149	Craig Mountain pluton	117.312	45.169	2	18.20	0.28	17.60	2.59	2609	-1	65	2

WB152	Craig Mountain pluton	117.284	45.195	2	86.86	1.71	24.38	2.19	2248	-514	17	227
WB154	Craig Mountain pluton	117.254	45.197	1	76.3	0.8	16.08	-	2014	-600	28	207
WB158	Craig Mountain pluton	117.236	45.208	2	61.18	2.08	15.59	0.47	1822	-838	0	1182
WB166	Pole Bridge pluton	117.420	45.291	1	104.9	0.9	60.59	-	2252	-401	2	763
WB250	Pole Bridge pluton	117.457	45.291	2	101.98	1.69	76.29	0.34	2352	-194	5	775
WB267	Craig Mountain pluton	117.334	45.198	3	74.96	4.43	13.88	2.85	2159	-525	31	409

				No. Aliquots	Corrected Zhe Date (Ma)	1σ (Ma)	eU (ppm)	1σ(ppm)				
WB034	Pole Bridge pluton	117.641	45.334	1	62.60	0.6	82.96	-	1227	-6	3	218
WB101	Pole Bridge pluton	117.576	45.329	1	133.40	1.3	322.47	-	1277	-334	3	716
WB104	Pole Bridge pluton	117.563	45.312	1	21.40	0.1	165.31	-	1243	-645	6	96
WB118	Hurricane Divide pluton	117.485	45.201	1	113.10	1.1	172.44	-	1471	-630	20	239
WB130	Craig Mountain pluton	117.417	45.174	1	105.50	1.0	249.35	-	1765	-691	3	182
WB149	Craig Mountain pluton	117.312	45.169	1	100.30	1.0	47.03	-	2609	-1	65	2
WB152	Craig Mountain pluton	117.284	45.195	1	105.30	1.0	330.09	-	2248	-514	17	227

Table 2.1: Measurements for thermochronometry samples from the Wallowa and Bald Mountain Batholiths

Chapter 3

SPATIAL TRENDS IN THE MIOCENE TO PRESENT DEFORMATION OF THE COLUMBIA RIVER BASALT

ABSTRACT

The Miocene Imnaha, Grande Ronde, Wanapum, and Saddle Mountains formations of the Columbia River Basalt cover much of central Washington, northern Oregon, and eastern Idaho. In their transit from eruptive centers in eastern Oregon to the Pacific Ocean, these basalts crossed a crustal mosaic of terranes accreted to North America since the Mesozoic. Strength and structural differences between these terranes are often invoked in discussions regarding present-day strain partitioning in the Pacific Northwest although questions remain regarding the relative importance and location of crustal and lithospheric boundaries. The wide distribution of Columbia River Basalt makes it an excellent datum for tracking deformation and exploring how it relates to crustal and lithospheric structure. To examine the role of lithospheric strength in partitioning Miocene to present upper crustal deformation, we compiled and digitized mapped contacts of Columbia River Basalt units from previous mapping efforts by state and national geologic surveys. The resulting dataset was used to interpolate elevation surfaces for contacts between members of the Columbia River Basalt and the basal unconformity below the basalts. From these surfaces, we estimate the thickness and volume of Columbia River Basalt, as well as local structural relief of inter-unit contacts, used as a proxy for post-depostion deformation. We compare these measurements to crustal thickness estimates and mapped terrane boundaries. After correcting for post Eocene deposition, the thickest Columbia River Basalt is found to overlie the thinnest crustal basement. Structural relief of Columbia River Basalt unit contacts is greatest in the Blue Mountains and the eastern flank of the Cascades and Yakima Fold Belt. The lowest structural relief is

found in the northeastern Columbia Plateau, where crust is estimated to be thinnest. We explore multiple hypotheses for why this region is less deformed, all of which share in common the interpretation that the boundary of this domain is defined by a change in lithospheric strength. [1]

3.1 Introduction

The Columbia River Basalt (CRB) is the youngest continental flood basalt province on Earth and remains widely preserved across the Columbia Plateau in the US Northwest. More than 95% of CRB was erupted during an 800 kyr period in the early Miocene (Kasbohm & Schoene, 2018), flowing from the Chief Joseph Dike Swarm in eastern Oregon, Washington, and western Idaho (Figure 3.1;] Waters, 1961; Swanson et al., 1975; Morriss et al., 2020) across a landscape formed on a crustal and lithospheric mosaic established after the Eocene accretion of the oceanic plateau Siletzia (Figure 3.1; Schmandt & Humphreys, 2011; Wells et al., 2014). Given the short duration of eruption and broad distribution, the CRB is an excellent datum for tracking Miocene to present deformation (e.g., Beeson & Tolan, 1990; Hales et al., 2005; Kelsey et al., 2017) and estimating pre-Miocene topography in the US Northwest (e.g., S. Smith, 2005; S. G. Mitchell & Montgomery, 2006; Kahn et al., 2020).

Since the onset of eruption, CRB has recorded crustal deformation in the Northwest. Hypothesized drivers for this deformation include clockwise rotation of crustal blocks (Wells et al., 1998; McCaffrey et al., 2007; Wells & McCaffrey, 2013; McCaffrey et al., 2013), oroclinan bending (Finley et al., 2019), formation of the Explorer plate and related changes to the Juan de Fuca subduction zone (Staisch et al., 2018), lower crustal flow (Castellanos et al., 2020), delamination of continental (Reiners, Ehlers, et al., 2002; Hales et al., 2005; Camp & Hanan, 2008) and oceanic (Darold & Humphreys, 2013) lithosphere, uplift of the Idaho Batholith (Hooper & Camp, 1981), and lower crustal eclogitization (Perry-Houts & Humphreys, 2018). In many of these models, lithospheric structure is explicitly hypothesized

[1] In collaboration with Jonathan Perry-Houts and Eugene Humphreys. Manuscript in preparation with planned submission to Geosphere.

to localize deformation. Furthermore, kinematic block models constrained by gps geodesy (McCaffrey et al., 2007, 2013) imply the crust in the Northwest is currently deforming through rotation of a number of microplates or crustal blocks. Together, both present-day observations and theories of Miocene to present deformation suggest variation in lithospheric structure play a fundamental role in how the Northwest deforms.

Despite the hypothesized importance of lithospheric structure in the Northwest, blanketing of pre-Miocene units with CRB and younger volcanic and sedimentary rocks in the Cascades volcanic arc and backarc has prevented the clear interpretation of crustal boundaries. For example, the location of the boundary of Paleozoic (Cratonic) North America, while well constrained along the Western Idaho Shear Zone and in northernmost Washington, is not known beneath the CRB (Figure 3.1). Additionally, the western boundary of the Blue Mountains terranes is commonly mapped along a steep isostatic gravity gradient known as the Klamath-Blue Mountains Lineament (Riddihough et al., 1986), but, in the Cascadia backarc, a change in bedrock geology has not been observed across this hypothesized boundary. Further complicating an understanding of the lithospheric architecture of this region is the history of subduction and terrane accretion spanning the Mesozoic and Cenozoic. Underplating during this time may have introduced vertical heterogeneity in the lithosphere not readily evident in surface bedrock geology. For example, the eastern extent of the Siletzia terrane, while relatively well constrained in the upper crust by aeromagnetic data (Wells et al., 2014), may be underplated beneath the Cascadia backarc as far east as central Idaho (Schmandt & Humphreys, 2011; Gao et al., 2011). The Olympic-Wallowa Lineament (OWL), a zone of upper crustal deformation that runs oblique to much of the topographic grain of the Northwest (Raisz, 1945), may also mark a lithospheric boundary from the Cascade Mountains to the Blue Mountains (Blakely et al., 2011; Reidel, Camp, Tolan, Kauffman, & Garwood, 2013; Reidel et al., 2020).

In this study, we compare the spatial distribution of CRB deformation to mapped crustal boundaries, models of crustal thickness, and upper mantle topography. Through this comparison, we explore the role of lithospheric structure in localizing deformation in the US

Northwest.

3.1.1 Using CRB as a Datum

Our analysis of the CRB in the context of deformation relies on the assumption that inter-unit CRB contacts were originally approaching horizontal over long distances. This allows the interpretation of these contacts as a Miocene horizontal datum. We believe this assumption is valid given the rapid eruption of CRB (Kasbohm & Schoene, 2018), wide aerial extent of individual flows (Reidel, Camp, Tolan, & Martin, 2013) and the low viscosity of CRB lavas (Ho & Cashman, 1997). In some locations, CRB flows pinch out against folds and faults that were actively deforming during CRB eruption (Reidel, Camp, Tolan, Kauffman, & Garwood, 2013), which may undermine our assumption of initially horizontal contacts. However, we believe the rate and volume of CRB emplacement overwhelmed local deformation in most places.

If we assume that inter-unit CRB contacts were originally horizontal, it is easy to envision possible contact types (Figure 3.2). Inter-unit contacts can be horizontal relative to an undulating CRB basal unconformity contact, reflecting onlap and burial of pre-CRB topography. Inter-unit contacts can be deflected from horizontal into folds and they can be offset by faults (Figure 3.2). In these cases, structural relief of the contact can be interpreted as a proxy for Miocene to present crustal deformation (e.g., Kelsey et al., 2017).

3.2 Methods

We compiled mapped contacts of Imnaha, Grande Ronde, Wanapum, and Saddle Mountains basalt from published datasets (Table 3.1). Picture Gorge, Prineville and Steens basalt, which account for 16.6% of CRB volume (Reidel, Camp, Tolan, & Martin, 2013), were not included in this compilation. Surface geology was extracted from Oregon and Washington state digital geology compilations, as well as georeferenced maps published by the Idaho Geological Survey (IGS), United States Geological Survey (USGS), and Oregon Department of Geology and Mineral Industries (DOGAMI). Map resolutions range from 1:250,000 to

1:24,000 and in most cases we used the highest resolution available. In Washington, the 1:100,000 resolution digital map compilation was used in place of the 1:24,000 resolution compilation. This choice was made because the 1:24,000 compilation does not provide complete coverage and map units are often not mapped to the resolution of CRB members. However, future work incorporating these higher resolution maps would improve the accuracy of the dataset. Subsurface geology was constrained by a USGS borehole compilation as well as reports on exploratory wells in the Columbia Basin (Campbell, 1989; Lingley, 1995; Reidel et al., 2006).

Contacts between Imnaha, Grande Ronde R1, N1, R2, N2, Wanapum Lower and Upper, Saddle Mountains Lower and Upper, and interbedded sediments were extracted (Figure 3.3). Contacts between these units and pre-Miocene as well as younger Miocene-Pliocene age volcanic units were also extracted. Contacts with Quaternary units were not included. When contacts were not mapped to the resolution of individual CRB units, the highest resolution distinction was used. For subsurface data where CRB was only mapped to the formation level, the stratigraphically highest CRB unit was assumed to define the contact.

Extracted contacts were sampled for elevation every 500 m from a 90 m SRTM DEM in ArcGIS. The endpoints of contact lines were also sampled to include contacts less than 500 m long. Depths of contacts in boreholes were corrected for surface elevation to reflect contact elevation. The resulting sampled elevations were then subdivided into simplified contacts that represent the base of the CRB and the top of each CRB unit as defined by a contact with a pre-Quaternary unit. The spline with barriers function in ArcGIS was used to interpolate a surface for each contact defined by these data. This technique produces a surface of minimum curvature by deforming an originally uniform surface through iteratively decreasing grid size. For each iteration, the surface is deformed based on the average value of points within the grid cell and the weighted summation of the 12 neighboring cells. Lines or polygons can be incorporated as barriers to the spline interpolation.

We chose a grid resolution of 1 km^2 for the splined surfaces and did not include barriers. While the surface will conform to abrupt elevation changes when they are constrained by

data, not including barriers may result in unrealistically smooth changes in elevation across faults. To account for increasing potential for error in surface interpolation where constraint is lacking, resulting surfaces were cropped to always be within 12.5 km of a point marking the elevation of the contact. The less well constrained surface was cropped to be within 25 km of a known location of CRB.

3.2.1 Further Constraints Used in Contact Surface Interpolation

Further constraint based on context was incorporated into the spline interpolation for the base and composite top of the CRB. Because these surfaces define the maximum and minimum elevations of CRB at any point if CRB has not been overturned, other contact elevations can be used as an additional constraint. For example, if the interpolated base of CRB is higher than observed CRB at a given location, then the interpolation is incorrect. We correct for this by incorporating contacts lower than the initial interpolation of the basal unconformity of the CRB into a subsequent interpolation, effectively pinning the surface to the maximum constrained depth of a CRB contact.

This correction is conservative as it does not assume the thickness of CRB at any location but it does introduce error into the surface interpolation. Because we pin the basal unconformity to an intra-CRB contact and not the maximum constrained depth of CRB, the basal unconformity interpolation underestimates the true depth of the basal unconformity. This correction could be improved by incorporating constraint from boreholes that extend below the lowest intra-CRB contact but do not reach the basal unconformity. The maximum depth of these boreholes is a better estimate of the depth of the basal unconformity than the approach we take. Unfortunately, the borehole data compilation we use does not contain information regarding the maximum depth of the borehole in an easily accessible manner. Future work could involve compiling borehole depths to better constrain maximum CRB depth.

We only correct the basal unconformity interpolation using the aforementioned technique. If a similar approach was taken for an inter-unit CRB contact, the resulting surface could no

longer be interpreted as an originally horizontal datum. The basal unconformity cannot be interpreted as originally horizontal given onlap and burial of pre-CRB topography (Figure 3.3)

For the top of the CRB, all interpolated contact surfaces were mosaiced with an extracted DEM of the surface exposure of CRB. This mosaic took the highest elevation value across a grid with 1 km^2 cell size. The resulting mosaiced upper CRB surface reflects both surface and subsurface constraints on the top of the CRB.

3.2.2 Terrane Boundaries

Terrane boundaries used in this analysis were compiled and simplified from USGS and Yukon Geological Survey maps (Lund et al., 2015, Yukon Geological Survey 2020), with corrections made given geologic constraints. The boundary of Siletzia was taken from the USGS terrane map (Lund et al., 2015), whereas the boundary between Paleozoic North America and accreted terranes in northern Washington was taken from the Yukon Geologic Survey Map (Yukon Geological Survey 2020). We chose to compile multiple sources for terrane boundaries because of observed discrepancies between surface geology and previously mapped terrane boundaries. Specifically, the USGS terrane map did not adhere to constraints from mapped bedrock units and isostatic gravity anomalies. The Blue Mountains terrane boundary was modified to better fit geologic constraints along the Western Idaho Shear Zone (WISZ) and to follow the Klamath-Blue Mountains gravity lineament (KBML; Appendix A.2, Figure A.4; Riddihough et al., 1986). The Blue Mountains terrane boundary was drawn through sheared plutons in the WISZ and on the North American side of the Riggins Group (Appendix A.2, Figure A.4), a metamorphic unit associated with accretion of the Blue Mountains terranes. The KBML was chosen at the steepest gradient in the free air gravity anomaly (https://mrdata.usgs.gov/gravity/isostatic/). To try to limit over-interpreting the gravity anomaly map, we aimed to make the terrane boundary as linear as possible. The Paleozoic-Mesozoic crustal terrane boundary is not constrained on the Palouse Slope where it is buried by CRB and we did not extend this boundary below the CRB.

3.2.3 Structural Relief of CRB Contacts

We calculate local structural relief for each CRB member contact and the CRB basal unconformity using a grid with 25 km spacing. We use contact-elevation points as opposed to interpolated surfaces to limit analysis to constrained data. Local structural relief is measured as the difference between the median of contact elevation values exceeding the 95th percentile and the median of values below the 5th percentile in each grid cell. We chose this approach as opposed to taking the minimum and maximum elevation values to reduce the influence of spurious elevation points at either extreme. The resulting relief estimates are a measure of the elevation range of a given contact over 50 km^2.

3.2.4 Uncertainty in the Dataset

Uncertainty in the estimated CRB contact elevations arises primarily from mapping resolution. For much of the study area 1:100,000 scale maps were used (Table 3.1). 1:100,000 and 1:24,000 scale maps in Washington can show very different geologic interpretations, with inter-map contact locations kilometers apart. Inaccurate contact mapping will have a disproportionate effect on elevation estimates in regions with high relief, where small horizontal differences in contact locations result in large elevation differences. Georeferencing errors may also introduce uncertainty, however the magnitude of this uncertainty is almost certainly less than the mapping uncertainty. Similarly, the 90 m resolution of the sampled DEM also introduces uncertainty, but is most likely smaller than that arising from map scale. Given these known issues with the data, this dataset is not recommended for use at scales below which a 1:100,000 resolution map would be suitable. Future work will include updating the CRB contact compilation with higher resolution data.

3.2.5 Crustal Thickness Corrections in the Columbia Basin

We take three crustal thickness models (Schmandt et al., 2015; Shen & Ritzwoller, 2016; Ma & Lowry, 2017) available from IRIS (Trabant et al., 2012) and correct them for the thick-

ness of CRB and pre-CRB sediments in the Columbia Basin to explore crustal structure as it relates to Miocene to present deformation. Each of these models uses receiver function data in conjunction with other constraints to estimate crustal thickness. Data was collected by USarray, FlexArray, and other seismic networks. Specific methodologies can be found in the source papers (Schmandt et al., 2015; Shen & Ritzwoller, 2016; Ma & Lowry, 2017). We use a CRB isopach developed in this study to correct for CRB thickness and a sediment isopach compiled from well and geophysical data to correct for pre-CRB sedimentation (Appendix A.2, Figure A.5; Campbell, 1989).

3.3 Results

The total compiled length of CRB contacts is 78,902 km, spanning 8° longitude and 3° latitude. Combining points sampled from these contacts with subsurface constraints, there are a total of 208,229 latitude and longitude points where elevation and contact type are known for CRB. Point density is variable across the study area, with a maximum of 2,800 points per 25 km^2. This dataset is available in an online tool made by collaborator Jonathan Perry-Houts (https://jperryhouts.github.io/CRB-Explorer/) and can be found in a digital data repository (Appendix E). As the dataset is updated, it will be uploaded to *https://github.com/PSGreene/Columbia-River-Basalt-Contacts*.

3.3.1 Interploated CRB Surfaces

Below, we briefly review the interpolated surfaces and note first-order observations of deformation. Interpolated surfaces for intra-CRB contacts are semi-transparent where no contact constraint is within 12.5 km. Areas where constraint is within 12.5 km are outlined in black and are opaque. Major rivers and mapped crustal boundaries are included to aid in comparison between figures and topography. All surfaces are overlain on a regional greyscale DEM for reference.

Elevation of the CRB Basal Unconformity

The CRB basal unconformity shows the greatest total relief of all interpolated contact surfaces. It is found to range over 6 km of elevation, rising from -3275 m in the center of the Columbia Basin to 3000 m in the Blue Mountains (Figure 3.4). The basal unconformity is at highest elevations on the eastern flank of the Cascades and in the Blue Mountains.

Elevation of the Top of the CRB

The top of CRB mostly reflects surface elevation across the study area and erosion of CRB. Only in the Columbia Basin and parts of the Blue Mountains is CRB covered by considerable overburden. Much like the basal unconformity, the top of CRB is highest in the Blue Mountains and on the eastern flank of the Cascades (Figure 3.4). Elevations are lowest in the Columbia Basin and on the Siletzia terrane.

Elevation of the Top of Imnaha Basalt

The Imnaha flows comprise ∼5.3% of the total CRB volume (Reidel, Camp, Tolan, & Martin, 2013) and erupted between ∼16.6-16.5 Ma (Kasbohm & Schoene, 2018).

Imnaha basalt is mapped only in the eastern portion of the study area (Figure 3.5). The contact is interpolated across a 2800 m elevation range. Highest elevations are estimated in the Wallowa Mountains (1) and lowest elevations are estimated in the Lewiston Basin (2). The course of the Salmon River turns abruptly northward to follow a north-south low in the Imnaha basalt surface (3). The Snake River tracks along the flank of an NNE-SSW striking upwarp that includes the Seven Devils Mountains, Cuddy Mountain, and Sturgill Peak (4).

Elevation of the Top of Grande Ronde Basalt Units

The Grande Ronde flows are the most extensive and voluminous of all CRB. They represent ∼72% of the total CRB volume (Reidel, Camp, Tolan, & Martin, 2013) and erupted between 16.59-16.06 Ma (Kasbohm & Schoene, 2018).

Grande Ronde R1 exposure is limited to the eastern portion of the study area mostly on the Blue Mountains terrane and is interpolated over an elevation range of 2200 m (Figure 3.6). Lowest elevations are found in the Lewiston Basin (2) and highest elevations are observed on the western flank of the Seven Devils Mountains (4) and northeastern flank of the Elkhorn Mountains (5). A pronounced low is observed on the north-south segment of the Salmon River (3), like that seen in the Imnaha surface. The Stites basin is also apparent in the interpolated surface (6; Camp & Hooper, 1981). The anticline-syncline pair associated with the Blue Mountains Anticline is also observed (7).

Grande Ronde N1 basalt is the first found west of the Columbia Basin on the eastern flank of the Cascade Mountains (Figure 3.6). Exposure is limited, however, so we review only the surface east of the basin. The surface ranges from 0 to 2100 m elevation. The Grande Ronde N1 surface resolves subsidence in Lewiston Basin (2), the low on the north-south segment of the Salmon River (3), subsidence in the Stites basin (6), as well as the Blue Mountains Anticline (7). Highest elevations are observed on the western flank of the Seven Devils Mountains (4) An abrupt decrease in elevation northwest of the Limekiln fault is also apparent (Arrows).

Grande Ronde R2 basalt is extensively exposed on the eastern flank of the Washington Cascades and east of the Columbia Basin in the Blue Mountains (Figure 3.6). It ranges in elevation from 0 to 2100 m. Highest elevations are recorded east of Mt. Rainier (8) and lowest elevations are found in the Lewiston Basin (2) and directly east of the Columbia River Gorge (9). In the Columbia River Gorge, the surface is interpolated at $\sim$1 km elevation. The Blue Mountains Anticline is clearly observed (7). The surface is up-warped against the Elkhorn Mountains (5), and between the Wallowa and Seven Devils Mountains.

The N2 member of Grande Ronde basalt has the most extensively constrained surface of all the CRB members (Figure 3.6). Relatively complete constraint is found through the Columbia basin, the northwestern flank of the Blue Mountains, the Cascade Mountains, and at the outlet of the Columbia River. The surface is interpolated from -750 m to 2100 m elevation. It is lowest in the central Columbia Basin and highest on the western flank of the

Wallowa Mountains (1). The surface decreases in elevation to the north across the OWL. The elevation of the surface is remarkably continuous in the northeastern Columbia Basin (11), dipping gently to the southwest. The surface is up-warped on the eastern flank of the Washington Cascades (8) and a low-elevation saddle (900 m) is observed at the Columbia River Gorge (9). Deformation of the surface is seen in the Yakima Fold Belt (10), Blue Mountains Anticline (7), and the Coulee Monocline (12). Lower elevations in the Lewiston Basin are also observed (2).

Elevation of the Top of Wanapum Basalt Units

The Wanapum flows comprise ∼5.8% of the total CRB volume (Reidel, Camp, Tolan, & Martin, 2013) and erupted between 16.06-15.9 Ma (Kasbohm & Schoene, 2018).

The top of Lower Wanapum basalt is discontinuously constrained from the Blue Mountains to the outlet of the Columbia River (Figure 3.7). High elevations are observed in the Yakima Fold Belt (10) and along the Blue Mountains Anticline (7). Lowest elevations are observed along the Columbia River at the eastern edge of the Columbia River Gorge. A low is also observed in the Lewiston Basin (2). The surface dips gently to the southwest in the northeastern Columbia Basin (11).

The top of Upper Wanapum basalt is mostly observed in the Columbia Basin, along the northern edge of the Blue Mountains and north (Figure 3.7). Elevations are highest in the Yakima Fold Belt (10), the Blue Mountains Anticline (7), and the northeast Columbia Basin. Lowest elevations are observed immediately north of the OWL. The surface drops in elevation in the Lewiston (2) and Stites basins (6).

Elevation of the Top of Saddle Mountains Basalt Units

The Saddle Mountains flows comprise ∼1.1% of the total CRB volume and erupted over a 9 myr period from 15-6 Ma (Reidel, Camp, Tolan, & Martin, 2013). Saddle Mountains basalt is the last of CRB basalts and a hiatus in deposition after cooling makes constraining an uneroded upper Saddle Mountains Basalt surface difficult. Similarly, more care must be

taken in interpreting elevations of the Lower Saddle Mountains contact because of erosional hiatuses between flows. This undermines the assumption that the top contact of the Lower Saddle Mountains unit was initially horizontal.

The top of Lower Saddle Mountains basalt is constrained in the Yakima Fold Belt and the northwestern and northeastern parts of the Blue Mountains (Figure 3.8). Highest elevations are seen on the limbs of the Blue Mountains Anticline (7) and in the Yakima Fold Belt (10). The surface drops in elevation in the Columbia Basin and the Stites Basin (6).

3.3.2 Combined Thickness of CRB

To estimate the thickness of CRB, we subtracted the the interpolated basal unconformity from the top of CRB (Figure 3.9). The resulting CRB isopach estimates the thickness of the Imnaha, Grande Ronde, Wanapum, and Saddle Mountains Basalt. CRB thickness as great as 3800 m is estimated in the central Columbia Basin adjacent the OWL, thinning radially from this location. Estimated thickness varies considerably in the Blue Mountains and southwest of the OWL.

3.3.3 CRB Surface Relief

Assuming CRB flow tops were initially horizontal, the structural relief of inter-unit CRB contacts across the study area reflects post-emplacement vertical deformation (Figure 3.2). The structural relief of the basal unconformity also provides valuable information, reflecting the combination of pre-Miocene topography onlapped by CRB and post CRB deformation (Figure 3.2).

For most contacts, structural relief is greatest on the eastern flank of the Cascades and in the Blue Mountains (Figure 3.10). Greatest structural relief is found in the basal unconformity and Imnaha contacts in the Blue Mountains. Local relief is lowest in the northeast Columbia Basin. Structural relief is also low on the Siletzia terrane. Regions of high structural relief can be correlated with features observed in interpolated surfaces (Figures 3.4-3.8).

To account for post-Miocene erosion of individual CRB units which would lead to an underestimate of structural relief, we extract the maximum structural relief measured across all inter-unit contacts (Figure 3.11). Deformation is greatest in the Blue Mountains and the western flank of the Cascade Mountains, including the Yakima Fold Belt. Structural relief is <400 m in the northeastern Columbia Plateau on the Palouse Slope. It is also minimal on the Siletzia terrane.

3.3.4 Crustal Thickness Estimates in the Columbia Basin

Crustal thickness models for the Columbia Basin show a present-day tabular zone of thinner crust, north-northeast of the OWL (Figure 3.12 A-C) Crust is thinnest north of the deepest mapped CBR. A zone of low structural relief (Figure 3.11), is generally found over this thin crust. A crustal thickness gradient is observed north of the OWL and adjacent the border of the Blue Mountains. Correcting crustal thickness for CRB thickness (Figure 3.12 D-F), the deepest part of the Columbia Basin overlies a gradient in crustal thickness. This gradient generally tracks along the OWL in the Columbia Basin and the western margin of the Blue Mountains terranes. Subtracting the thickness of Eocene and younger sedimentary units below the CRB in the Columbia Basin provides an approximation of the thickness of crystalline basement in the Columbia Basin (Figure 3.12 H-J). For all three crustal thickness models, this correction results in the thinnest crust centered below the deepest part of the Columbia Basin. Crust is still observed to thicken south of the OWL and is thin beneath the low structural relief zone.

3.4 Discussion

In this section we discuss various implications of the distribution and deformation of CRB. We begin with a short comparison between our interpolation effort and previous work. Then we examine our observations of CRB deformation in the context of mapped terrane boundaries, crustal thickness estimates (Schmandt et al., 2015; Shen & Ritzwoller, 2016; Ma & Lowry, 2017), and upper mantle tomography (Schmandt & Humphreys, 2011). We find

that the least deformed portions of CRB overly crust that is thinner relative to surroundings, the deepest CRB overlies thin crystalline basement, and the OWL is coincident with a steep pre-CRB crustal thickness gradient.

3.4.1 Comparison with Other CRB Interpolation Efforts

Our results compare favorably to previous mapping efforts. Reidel et al., (2013) estimate a combined area of Imnaha, Grande Ronde, Wanapum, and Saddle Mountains Basalt of 210,000 km^2 and a volume of 173,376 km^3. The area (255,000 km^2) and volume (181,767 km^3) estimates from this study are larger than these estimates. This difference may result from the buffer we applied to the distribution of CRB when interpolating surfaces as well as the largely unconstrained thickness of basalt in south-central Washington and north-central Oregon. Burns et al. (2011) estimate a considerably smaller area (109,000 km^2) and volume (142,000 km^3), despite including the Picture Gorge Basalt in their analysis. This discrepancy may be due to their omission of CRB west of the Cascades and in the Weiser Embayment south of the Wallowa Mountains.

3.4.2 CRB Deformation in the Northeastern Columbia Plateau

Using the structural relief of CRB contacts as a proxy for Miocene to present deformation, it is apparent that the CRB has been variably deformed across the Northwest (Figure 3.11). Specifically, deformation is significant everywhere save the Palouse Slope in the northeastern Columbia Plateau and on the Siletzia terrane. Whereas the coherent structure of the Siletzia terrane may resist internal deformation (Wells et al., 1998), a hypothesis corroborated by geodetically constrained block models (McCaffrey et al., 2013), it is less clear why the Palouse Slope shows little evidence for Miocene to present deformation. This trend could be explained by the Palouse Slope having stronger or weaker lithosphere than surroundings.

Prior studies hypothesize that the Palouse Slope is underlain by strong cratonic basement which resists deformation (Camp & Hanan, 2008; Blakely et al., 2014). While cratonic lithosphere may exist in the region north of the Blue Mountains in Idaho, where bedrock

exposure of the craton boundary is observed (Appendix A.2, Figure A.4), a paucity of constraint from limited boreholes that penetrate crystalline basement make it difficult to map out the location of the craton beneath the CRB (Figure 3.1 Reidel, Camp, Tolan, Kauffman, & Garwood, 2013). Therefore it is difficult to test this hypothesis with available data. Furthermore, the crust is thin beneath much of the Palouse Slope west of Idaho (Figure 3.12), and was likely thinned during a phase of Eocene extension (Catchings & Mooney, 1988), as is observed adjacent the Columbia Plateau (Parrish et al., 1988; Janecke & Hammond, 1997). Even if the crust beneath the Coulumbia Plateau was originally of cratonic affinity, Eocene crustal thinning suggests it has been significantly modified.

Another argument for strong lithosphere beneath the Palouse Slope is a hypothesized remnant oceanic underplate linked to the accretion of Siletzia (Gao et al., 2011). McCaffrey et al. (2013) further propose underpltaed Siletzia could explain a lack of internal deformation recorded by gps from eastern Oregon, south of the region we identify as not having been deformed. Underplated oceanic lithosphere beneath the northeastern Columbia Plateau, while a provocative theory, is corroborated by limited evidence. Specifically, it relies on the interpretation that high velocity anomalies in the upper mantle (Figure 3.13) are remnants of subducted oceanic lithosphere recently decoupled from beneath the North American plate (Schmandt & Humphreys, 2011; Gao et al., 2011). These high velocity anomalies surround the less deformed portion of CRB and are presumed to have been recently attached to an oceanic underplate beneath the Palouse Slope (Figure 3.13; Gao et al., 2011). Numerical modeling of the longevity of stalled slabs in the upper mantle indicates the longest period of time they can remain coupled to the lithosphere is $\sim$28 myr (Burkett & Gurnis, 2013), far shorter than the $\sim$50 myr since Siletzia accretion.

An alternative explanation for the distribution of deformation recorded by CRB is that the lithosphere beneath the Palouse Slope could be considerably weaker than surroundings. Weak lithosphere would prevent rigid body rotation in response to regional clockwise rotation (McCaffrey et al., 2013) and localize deformation at the boundaries between rigid and weak crustal domains. Crustal thickness estimates suggest a thickness gradient on the southern

and eastern margins of the Palouse Slope (Figure 3.12), which could correlate to a change in crustal strength. This change in crustal thickness is spatially correlated with deformation in the Yakima Fold Belt and Blue Mountains Anticline (See Figure 3.6 for example). Both of these regions could have deformed in response to rotation of stronger crust into the boundary of a weak crustal domain beneath the Palouse Slope.

3.4.3 Coincidence of the Columbia Basin With Thin Crust

In the Columbia Basin, adjacent the Palouse Slope, there is evidence for a phase of rapid subsidence during the peak eruption of CRB (Reidel et al., 1989). CRB is found at depths greater than 3 km below sea level in the Columbia Basin (Figures 3.4, 3.9). Boreholes reveal terrestrial sediments below (Campbell, 1989), and interbedded between, CRB in the Columbia Basin, which suggest subsidence was contemporaneous with CRB eruptions (Reidel et al., 1989). The Columbia Basin sits above the thinnest crust observed east of the Cascades (Figure 3.12), which may help explain the subsidence. Recent work proposes subsidence was driven by a positive feedback between loading driven depression of the crust from CRB flows and a concomitant lower crustal mineralogic phase change to eclogite, increasing crustal density and further promoting subsidence (Perry-Houts & Humphreys, 2018). Active source (Catchings & Mooney, 1988), as well as surface wave and receiver function (Gao et al., 2011) studies suggest that the crust of the Columbia Basin may be underlain by a mafic underplate, which could be susceptible to eclogitization. This underplate may have formed during an Eocene phase of extension (Campbell, 1989), associated with the northward translation of terranes from the KBML (Wyld et al., 2006).

Accounting for CRB thickness and Eocene and younger sediments, crust is thinnest beneath the Columbia Basin (Figure 3.12 G-I). This is consistent with prior workers interpretation of the Columbia Basin as an extensional rift (Catchings & Mooney, 1988). Furthermore, it suggests the distribution of CRB was strongly affected by a crustal framework established following Eocene deformation.

3.4.4 The OWL

In our examination of crustal thickness, we find that the OWL east of the Cascades correlates with a crustal thickness gradient (Figure 3.12). This is most explicit when the thickness of CRB is removed (Figure 3.12 D-F). Accounting for sub-CRB sediments, thin crust extends south of the OWL but the southern boundary of thin crust continues to parallel the OWL (Figure 3.12 G-I). These observations suggest that the OWL does indeed mark a crustal-scale boundary between thick crust to the south and thin crust to the north. Determining the origin of this boundary is beyond the scope of this paper.

3.5 Conclusions

Contacts of the CRB record spatially heterogeneous deformation of the Pacific Northwest from the Miocene to present. This deformation appears to be modulated by differences in lithospheric strength. CRB is little deformed on the Palouse Slope which is underlain by thinned crust that may be weaker than surroundings or strengthened by underplated oceanic lithosphere. In either case, deformation is localized at the boundaries of the Palouse Slope in the Yakima Fold Belt and Blue Mountains Anticline, where crustal blocks associated with the Blue Mountains and northern Oregon translate northward. The Columbia Basin formed at the southeastern margin of this less deformed region over thin crust likely extended during the Eocene.

3.6 Figures and Tables

ID	Source	Organization	Location	Type	Mapping Resolution	Georeferenced?
1	OGDC v6	DOGAMI	Or	digital map compilation	variable - highest available	yes
2	GMS115	DOGAMI	Or	bedrock geology map	1:24,000	no
3	DS-18 v 3.1	WADNR	Wa	digital map compilation	1:100,000	yes
4	p1666	USGS	Id	digital map compilation	variable - highest available	yes
5	GM 48	IGS	Id	bedrock geology map	1:100,000	no
6	GM 28	IGS	Id	bedrock geology map	1:100,000	no
7	GM 29	IGS	Id	bedrock geology map	1:100,000	yes
8	GM41	IGS	Id	bedrock geology map	1:100,000	no
9	DWM-92	IGS	Id	bedrock geology map	1:100,000	yes
10	DWM-93	IGS	Id	bedrock geology map	1:100,000	no
11	M-7	IGS	Id	bedrock geology map	1:50,000	no
12	DWM-105	IGS	Id	bedrock geology map	1:24,000	no
13	GM-50	IGS	Id	bedrock geology map	1:100,000	yes
14	TR-11	GRC/IGS	Id	reconaissance map	1:125,000	no
15	81-797	USGS	Or, Id, Wa	reconaissance map	1:250,000	no
16	2010-5246	USGS	Or, Id, Wa	borehole record	N.A.	yes
17	Lingley 1995	-	Wa	borehole record	N.A.	no
18	Reidel 2006	-	Wa	borehole record	N.A.	no
19	Reidel 2002	-	Wa	borehole record	N.A.	no

Table 3.1: Sources for CRB contact compilation

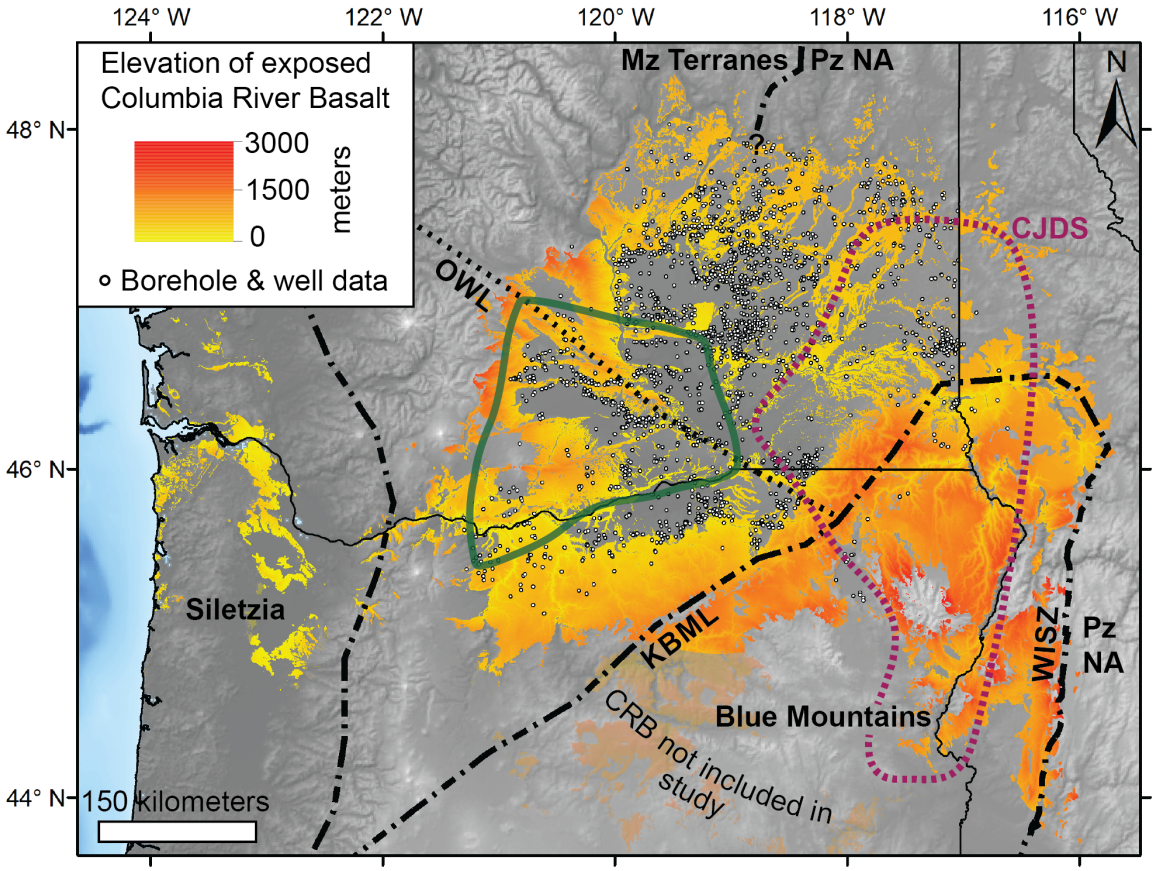

Figure 3.1: Elevation of exposed CRB with locations of boreholes and wells that intersect CRB in the subsurface overlain on a greyscale DEM of Washington, Idaho, and Oregon. The region where CRB is found east of the Cascade Mountains is commonly referred to as the Columbia Plateau. Picture Gorge member of CRB is transparent and was not included in this study. Major crustal boundaries marked with thick dash-dot line. Olympic Wallowa Lineament (OWL) marked with dotted line. Green line outlines Yakima Fold Belt. Schematic outlines of Chief Joseph Dike Swarm shown by magenta dashed line. Mz – Mesozoic; Pz – Paleozoic; NA – North America; KBML – Klamath-Blue Mountains Lineament; WISZ – Western Idaho Shear Zone; CJDS – Chief Joseph Dike Swarm.

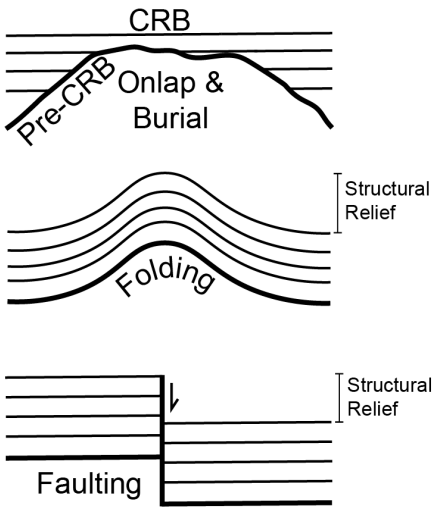

Figure 3.2: Schematic representation of CRB contact interaction with pre-existing topography and the effects of Miocene to present deformation.

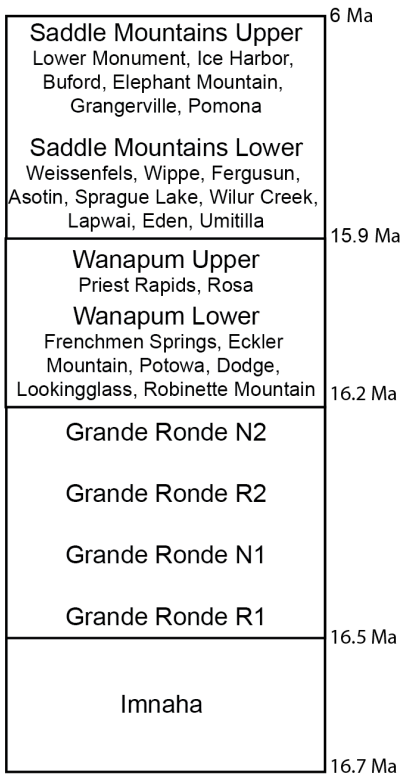

Figure 3.3: Simplified stratigraphy used in Columbia River Basalt map compilation. Dates marking age range of basalt map units from Kasbohm and Schoene (2018).

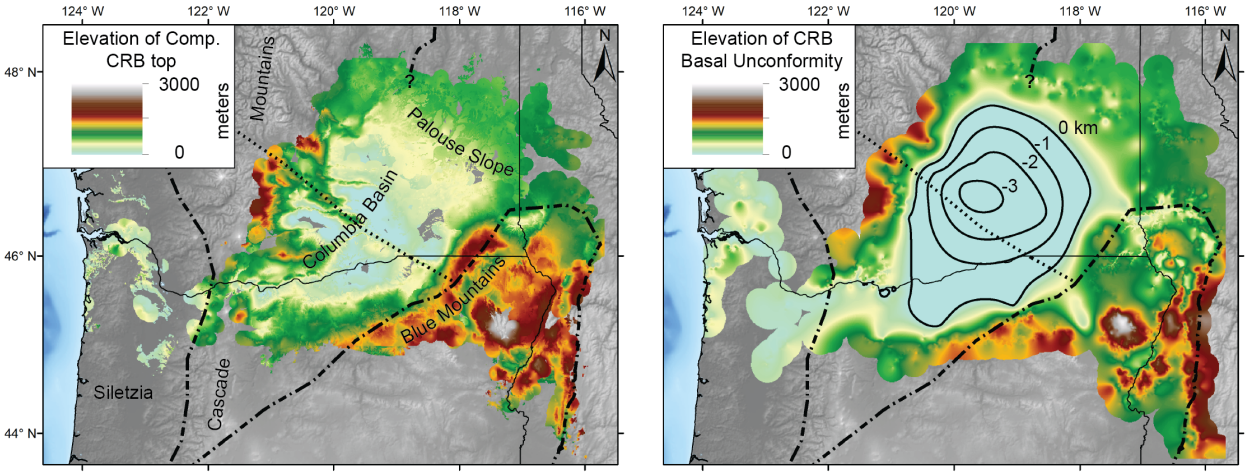

Figure 3.4: Elevation of the top and bottom of CRB interpolated from contact and borehole elevation constraints. Contours in basal unconformity surface show depths below the color range of the figure. Major terrane boundaries shown as dashed lines. Olympic-Wallowa Lineament is marked by dotted line.

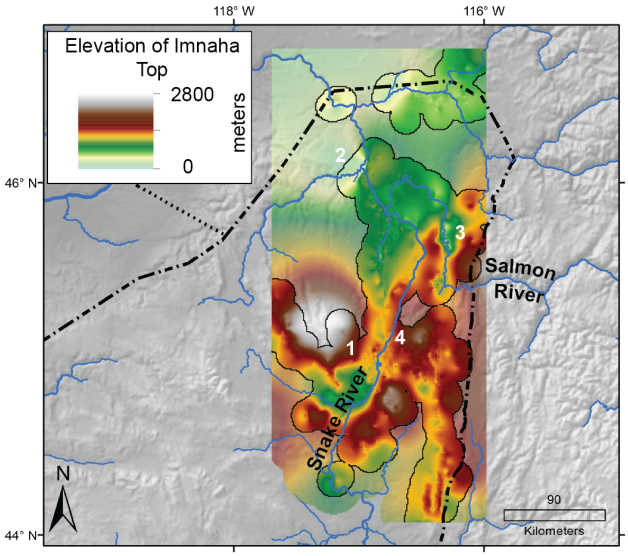

Figure 3.5: Elevation of the interpolated contact between Imnaha Basalt and younger units. Major terrane boundaries shown as dashed lines. Olympic-Wallowa Lineament is marked by dotted line. Numbers are referred to in the text.

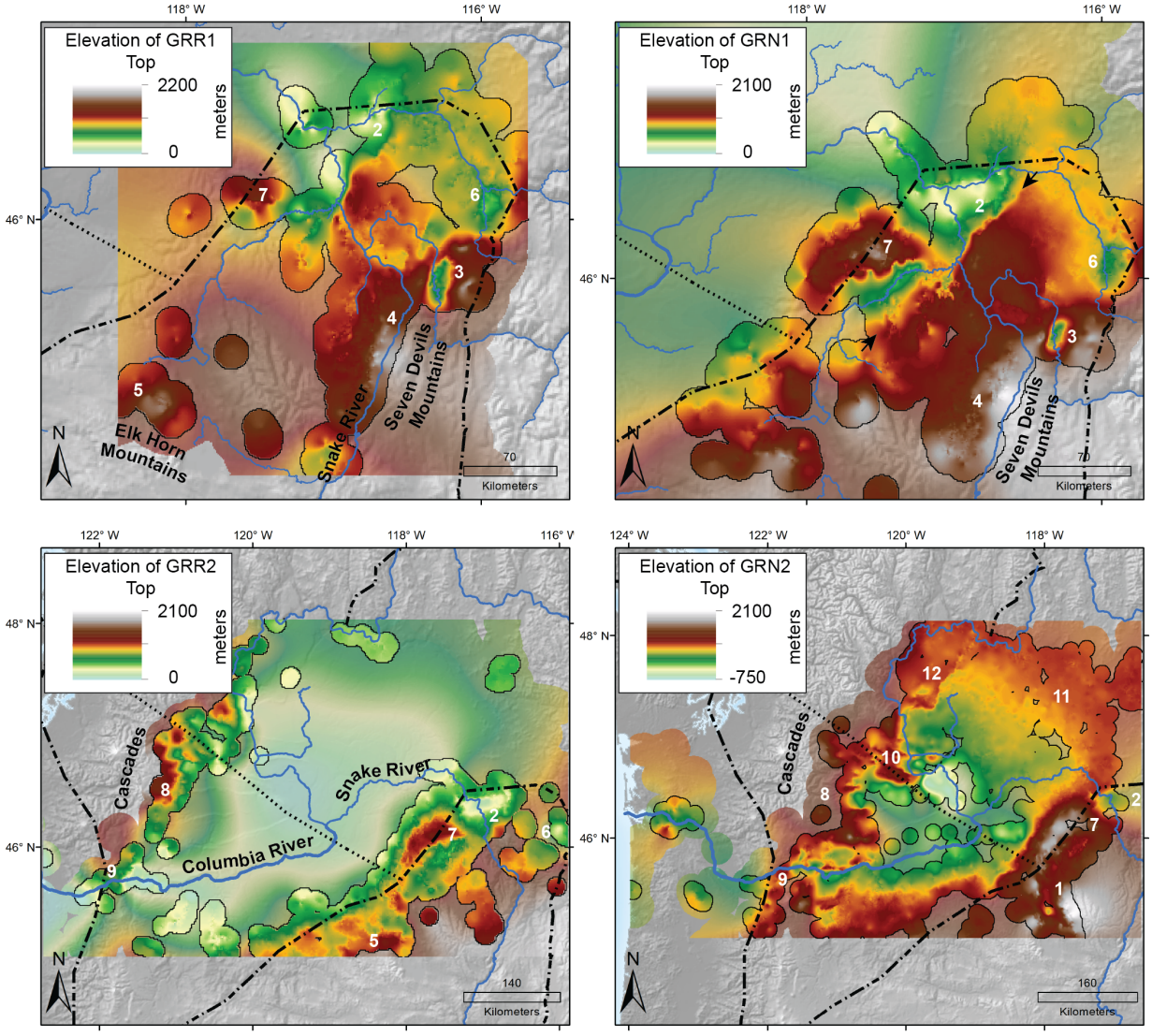

Figure 3.6: Elevation of the contact between Grande Ronde R1, N1, R2, and N2 units and younger units. Major terrane boundaries shown as dashed lines. Olympic-Wallowa Lineament is marked by dotted line. Numbers are referred to in the text. Arrows in the Grande Ronde N1 panel show the location of the Limekiln Fault.

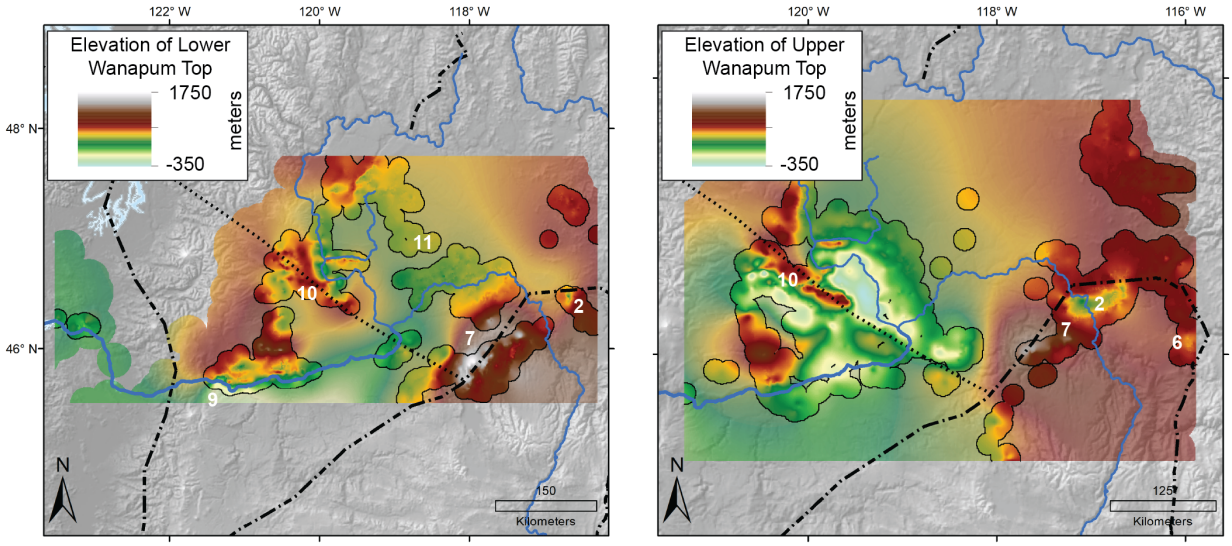

Figure 3.7: Elevation of the contact between Wanapum Lower and Upper units and younger units. Major terrane boundaries shown as dashed lines. Olympic-Wallowa Lineament is marked by dotted line. Numbers are referred to in the text.

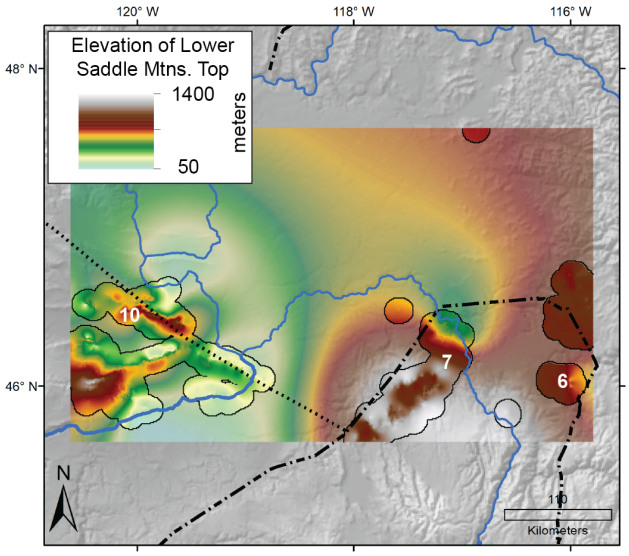

Figure 3.8: Elevation of the contact between the Lower Saddle Mountains unit and younger units. Major terrane boundaries shown as dashed lines. Olympic-Wallowa Lineament is marked by dotted line. Numbers are referred to in the text.

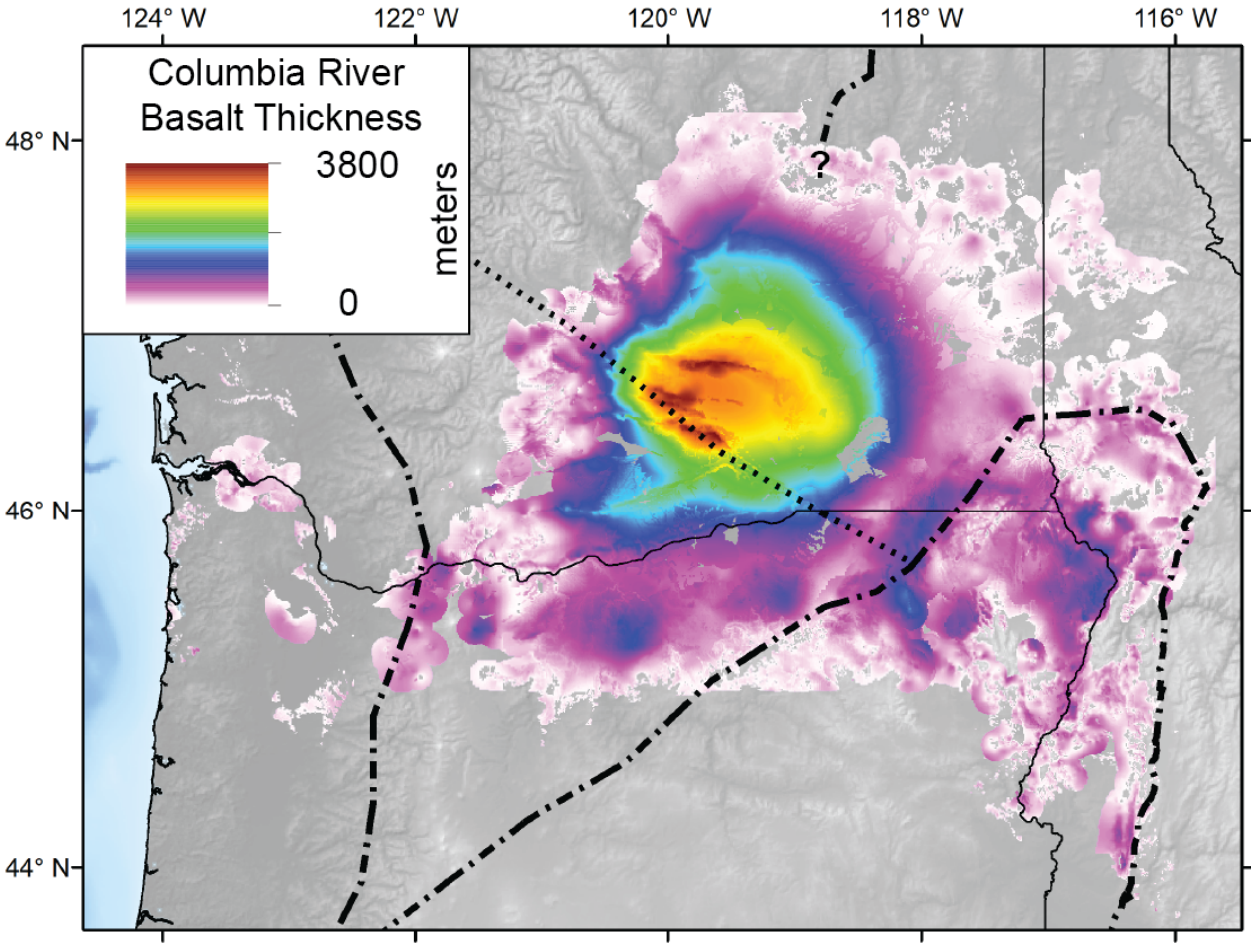

Figure 3.9: Estimated thickness of CRB. Major terrane boundaries shown as dashed lines. Olympic-Wallowa Lineament is marked by dotted line.

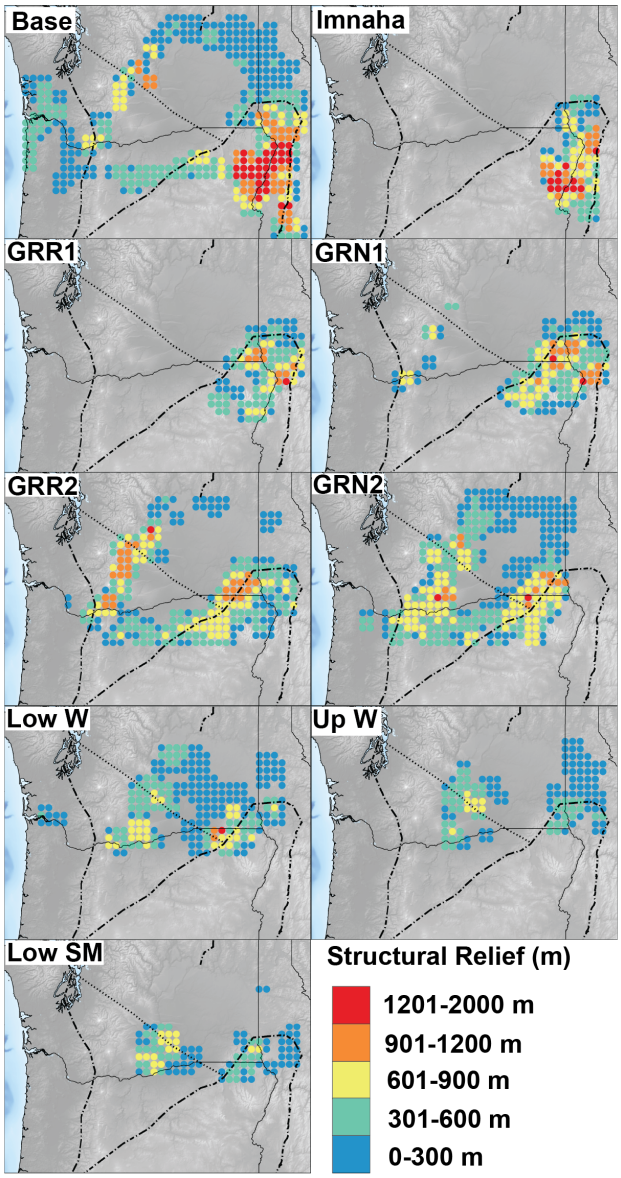

Figure 3.10: Local structural relief estimates of each mapped CRB unit contact. Major terrane boundaries shown as dashed lines. Olympic-Wallowa Lineament is marked by dotted line. Base – Basal contact of CRB; W – Wanapum Basalt; SM – Saddle Mountains Basalt.

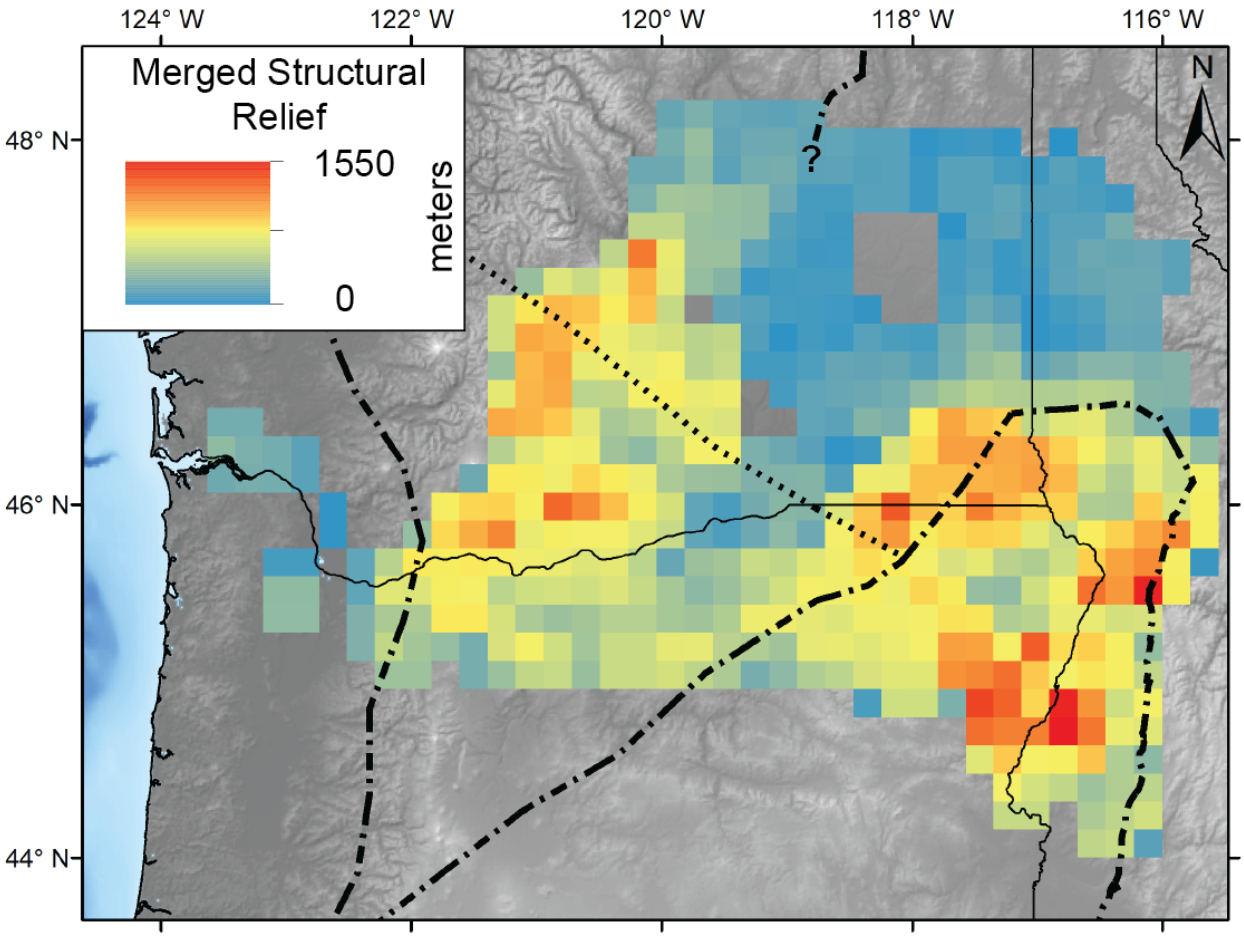

Figure 3.11: Merged structural relief of all inter-unit CRB contacts. Major terrane boundaries shown as dashed lines. Olympic-Wallowa Lineament is marked by dotted line.

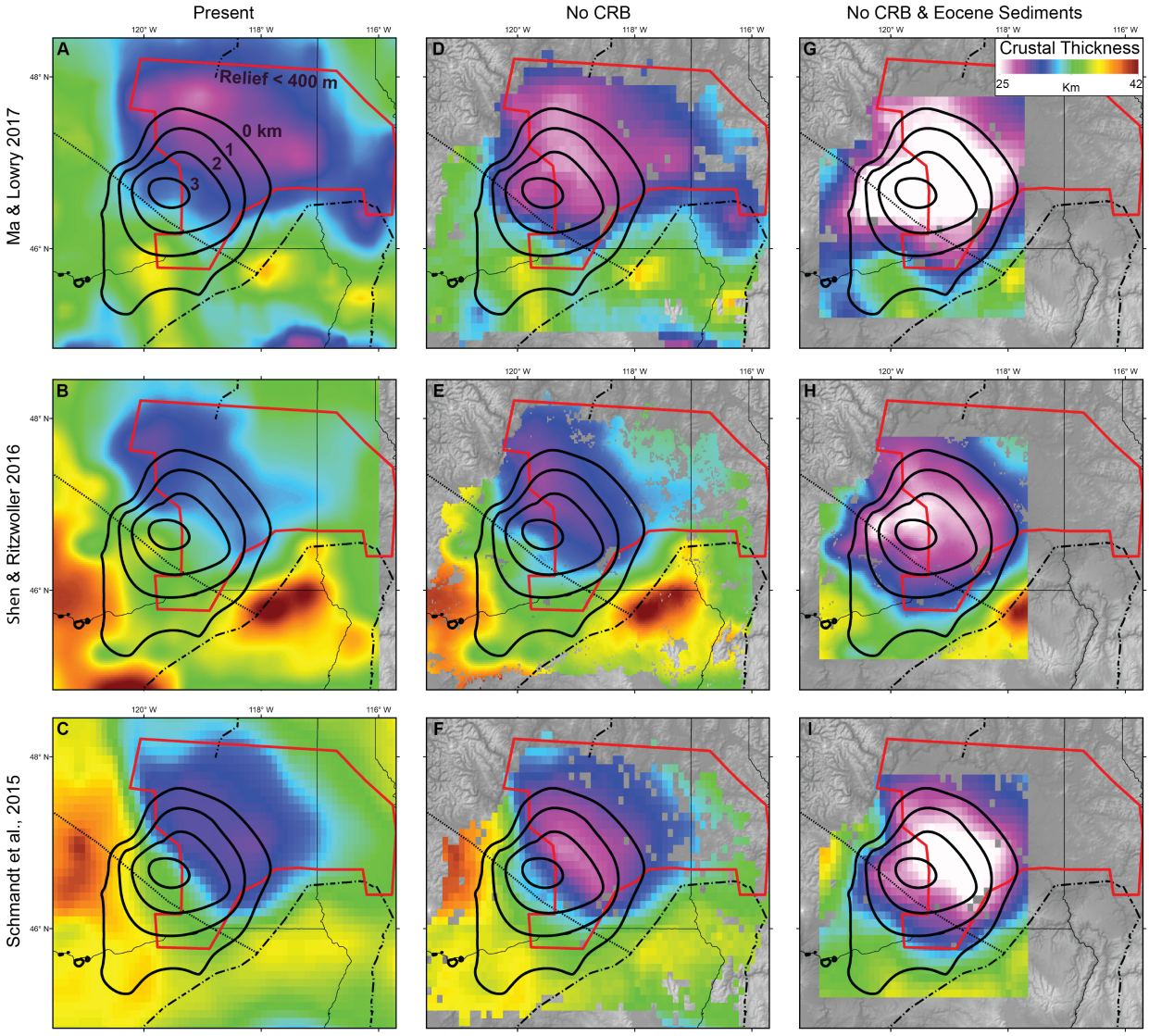

Figure 3.12: Crustal thickness estimates with 1 km contours of CRB basal unconformity below 0 km elevation. Red polygon outlines region of low CRB structural relief from Figure 3.11. Major terrane boundaries shown as dashed lines. Olympic-Wallowa Lineament is marked by dotted line. Present crustal thickness (A, B, C), crustal thickness with CRB thickness removed (D, E, F), and crustal thickness with CRB thickness and sub-CRB Eocene sediment thickness removed (G, H, I). Panels A, D, G – Crustal thickness model of Ma and Lowry (2017); Panels B, E, H – Crustal thickness model of Shen and Ritzwoller (2016); Panels C, F, I – Crustal thickness model of Schmandt et al. (2015).

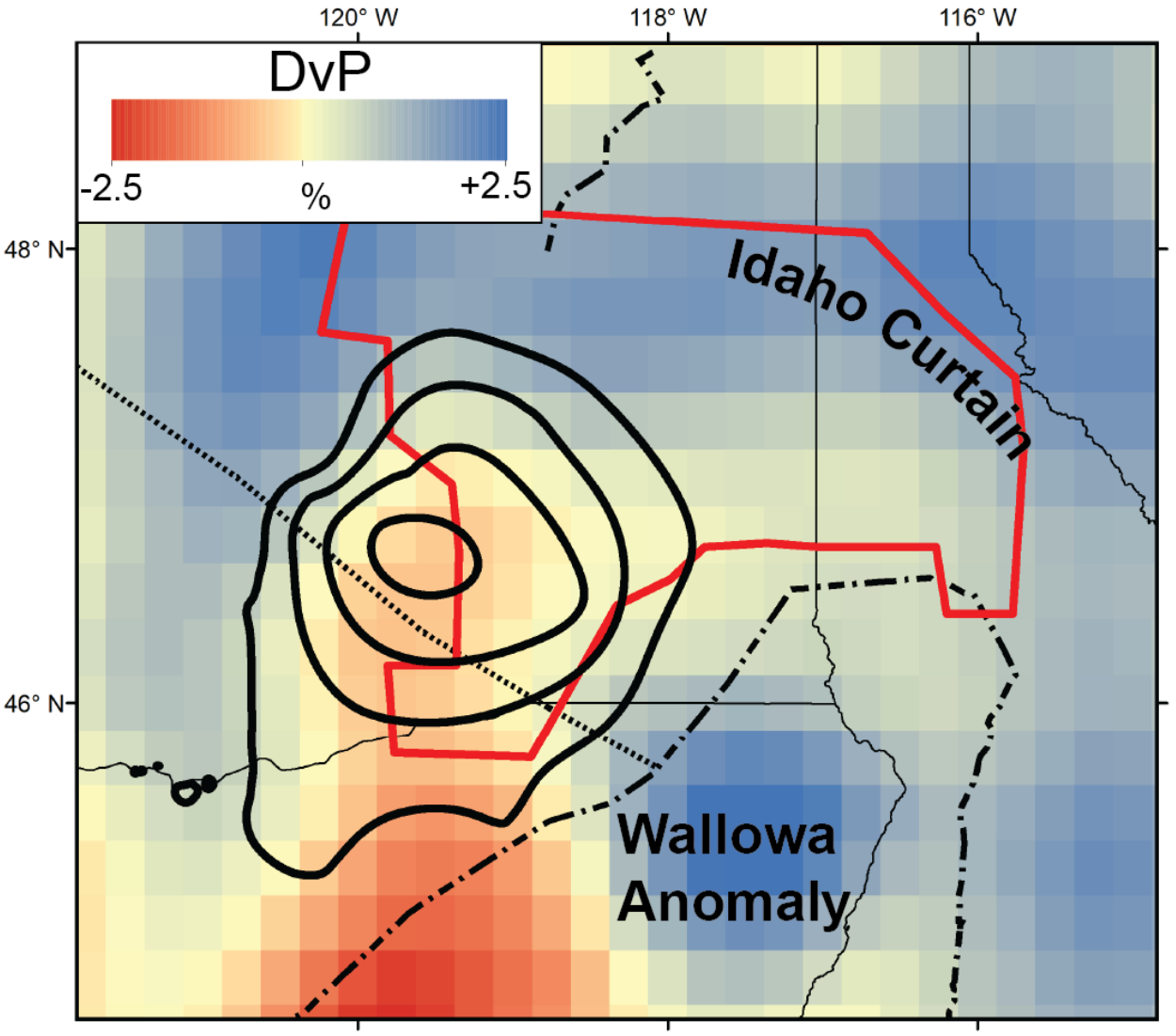

Figure 3.13: DvP velocity at 195 km depth below CRB (Schmandt & Humphreys, 2011). High velocity anomalies (Wallowa Anomaly and Idaho Curtain) have been interpreted as remnant sub-vertical oceanic lithosphere in the upper mantle (Schmandt & Humphreys, 2011; Stanciu & Humphreys, 2020). One km contours of CRB basal unconformity below 0 km elevation. Red polygon outlines region of low CRB structural relief from Figure 3.11. Major terrane boundaries shown as dashed lines. Olympic-Wallowa Lineament is marked by dotted line.

Chapter 4

EXHUMATION IN HAIDA GWAII INITIATED BY TERRANE TRANSLATION AND CONTINUED VIA TRANSPRESSION ALONG THE SOUTHERN QUEEN CHARLOTTE FAULT, CANADA

ABSTRACT

The mountainous archipelago of Haida Gwaii abuts the transpressive Pacific/North America plate margin north of the Cascadia subduction zone. Topography on Haida Gwaii has been attributed to either dynamic uplift supported by subduction initiation or crustal shortening driven by shear adjacent the plate-bounding Queen Charlotte Fault. In order to resolve how interplate strain is accommodated, we obtained thermochronometry data from 20 bedrock samples on Haida Gwaii, including zircon (U-Th)/He, apatite (U-Th-Sm)/He, and apatite fission track dates. With dates ranging from 5 to 60 Ma, we interpret exhumation rates increasing in proximity to the Queen Charlotte Fault and leading to a maximum of 6 km of exhumation since 20 Ma. The onset of exhumation significantly predates the purported initiation of subduction, precluding a direct relationship between subduction initiation and the development of topography in the archipelago. Instead, exhumation onset correlates with passage of the Yakutat terrane, suggesting North America was deformed and Haida Gwaii uplifted during terrane translation. Steady or slightly decreasing exhumation rate since the Miocene is at odds with estimated increases to interplate convergence over this time, ruling out crustal shortening in Haida Gwaii as the only response to transpression between North America and the Pacific. From this, we conclude plate convergence is accommodated through basin inversion and internal shortening in the North American and Pacific plates as well as

potential underthrusting of the Pacific plate beneath North America. [1]

4.1 Introduction

The Queen Charlotte Fault (QCF), a dextral transform between the Pacific and North American plates, runs for more than 800 km offshore British Columbia to Southeast Alaska. Formed in the wake of the Yakutat terrane as it translated northward since the late Oligocene (ten Brink et al., 2018), this fault juxtaposes oceanic against continental lithosphere, a setting where transpression may lead to strain partitioning at the plate boundary and the initiation of subduction (Gurnis et al., 2019). At the latitude of the southern QCF and the island archipelago Haida Gwaii (Figure 4.1), the Pacific and North American plates converge up to 20 mm yr^{-1} and subduction may be initiating (Hyndman, 2015; DeMets & Merkouriev, 2016).

The 2012 M7.8 thrust earthquake adjacent central Haida Gwaii and the QCF provides some insight into strain accommodation along this plate boundary (Figure 4.1). Interpreted as occurring on a nascent subduction megathrust (Szeliga, 2013), this earthquake may validate the theory that Pacific-North America convergence is leading to subduction initiation (Hyndman, 2015). But, uncertainty in the extent of fault slip limits conclusions regarding the presence and geometry of subducted Pacific plate beneath North America (Lay et al., 2013). Additional evidence is needed to fully determine whether subduction is initiating.

A better understanding of the topographic development of Haida Gwaii may provide insight into the dynamics of transpression between the Pacific and North American plates. Models of subduction initiation show transient uplift of the overriding plate of up to 2 km adjacent a nascent subduction zone (Mao et al., 2017). The mountainous west coast of the archipelago, with peaks reaching as high as ∼1 km within 20 km of the plate boundary (Figure 4.1), appears consistent with model predictions for uplift driven by subduction initiation (Yorath & Hyndman, 1983). Additionally, the sub-aerial extent of Haida Gwaii is

[1] In collaboration with Alison Duvall, Ann Blythe, Eric Morley, William Matthews, and Sean LaHusen. Published, Geology (Schoettle-Greene et al., 2020)

roughly coincident with predicted Pacific plate underthrust extent since 6 Ma (ten Brink et al., 2018). These observations suggest a direct relationship between subduction initiation and topographic development in Haida Gwaii.

Topography on Haida Gwaii may have an alternate genesis, however. Transpression along the QCF could drive internal shortening of the North American and Pacific plates, leading to uplift of Haida Gwaii (Rohr et al., 2000). Seismic reflection profiles collected to the east, in the Oligocene-Miocene Queen Charlotte Basin (Figure 4.1), show the onset of basin inversion in the late Miocene (Rohr & Dietrich, 1992). On the Pacific plate, the Queen Charlotte Terrace, a 30 km wide wedge of deformed sediment and oceanic crust abutting the QCF, spans the extent of Haida Gwaii (Figure 4.1). Whether the Queen Charlotte Terrace is an accretionary prism (Hyndman, 2015) or the product of crustal shortening of the Pacific plate (Rohr et al., 2000), is a matter of debate.

To better understand the topographic development and, by extension, the nature of strain accommodation at this portion of the Pacific/North America plate boundary, we determine the exhumation history of Haida Gwaii using low temperature thermochronometry.

4.1.1 Background

Haida Gwaii is a remote and rugged 10,000 km^2 archipelago off the coast of central B.C., Canada (Figure 4.1). Previously named Xhaaydla Gwaayaay (Bringhurst, 2000), or the Islands on the Boundary Between Worlds, Haida Gwaii abuts the QCF at the boundary of the North American and Pacific plates (Figure 4.1). Generally, bedrock structural depth increases from north to south on Haida Gwaii, from Neogene volcanics in the north to exhumed Mesozoic Wrangellia terrane in the south (Haggart et al., 2004).

Offshore Haida Gwaii, oceanic lithosphere age varies from 15 Ma in the north to 8 Ma at the southern Queen Charlotte Terrace (Figure 4.1; Wilson, 2002). The triple junction between the Pacific, North American, and Juan De Fuca plates is defined by a region of distributed shear encompassing the Explorer plate (Dziak, 2006) and currently extends to the Tuzo Wilson Seamounts at the termination of the QCF south of Haida Gwaii (Figure

4.1; Rohr, 2015). This plate boundary is unstable, migrating northward from offshore the Brooks Peninsula on Vancouver Island since 2-4 Ma (Rohr & Tryon, 2010).

The rupture extent of the 2012 M7.8 thrust earthquake offshore Haida Gwaii provides evidence of present-day strain partitioning from 53-52°N between the dextral QCF and a subparallel east dipping thrust fault (Nykolaishen et al., 2015). Receiver function study (Gosselin et al., 2015), heat flow data (A. J. Smith, 2003), and a strong negative residual free-air gravity anomaly (ten Brink et al., 2018), all suggest the Pacific plate is underthrusting North America beneath Haida Gwaii. Convergence rate between the Pacific and North American plates, determined from the global plate circuit model of (DeMets & Merkouriev, 2016), is estimated to have increased from the Miocene to present, leading to a predicted total of 90-160 km of interplate shortening adjacent Haida Gwaii.

4.2 Methods

4.2.1 Low-Temperature Thermochronometry

In this study, we assess time-temperature histories of bedrock samples using the low temperature thermochronometers apatite (U-Th-Sm)/He (AHe), apatite fission track (AFT), and zircon (U-Th)/He (ZHe) and relate trends in cooling to erosion and rock uplift. As AHe records the time of cooling from 90-50°C (Flowers et al., 2009), AFT from 120-60°C (Ketcham et al., 1999), and ZHe 220-130°C (Guenthner et al., 2013), our data constrain cooling through the upper crustal geotherm.

20 bedrock samples were collected from across the archipelago of Haida Gwaii on two separate occasions in 2016 and 2017 (Figure 4.2). Samples with the prefix CD were collected in the summer of 2016 by C. Dorsey, J. Pickering, and M. Boivin from the University of Calgary. Samples with the prefix HG were collected in the summer of 2017 by P. Schoettle-Greene from the University of Washington. Sample BARRY was collected by L. Nykolaishen from the Geological Survey of Canada. Samples were excavated from >5cm depth so as to avoid possible reheating from forest fire and lightning strike (S. G. Mitchell & Reiners, 2003).

HG and BARRY apatite and zircons were separated at Geosep services in Moscow, Idaho, using standard magnetic and heavy liquid techniques. Mineral separation of CD samples was performed at the University of Calgary using standard magnetic and heavy liquid techniques. All samples were analyzed using AHe thermochronometry. Of these, six were selected for AFT and three for ZHe analysis.

(U-Th)/He Thermochronometry

Individual apatite and zircon grains were handpicked at the University of Washington and University of Calgary. P. Schoettle-Greene picked HG and BARRY samples using a Leica M205C binocular microscope using transmitted and polarized light. E. Morley picked CD samples at the University of Calgary under a reflected light microscope. Selected grains were screened for quality to ensure they were free from inclusions or other crystal defects and were of sufficient size. Between 12 and 3 individual grains were selected from each sample. Each grain was measured and photographed before being packed.

HG and BARRY apatite and zircon samples were packed in Pt tubes and sent to CU-TRaIL at the University of Colorado, Boulder for (U-Th)/He analysis. At CU-TRaIL each grain was heated with a 25W diode laser to allow for the diffusion of Helium through the crystal lattice. This procedure was repeated at least once to ensure the grain was completely degassed and determine the presence of inclusions. Helium concentration was measured on a mass spectrometer attached to the laser stage. After degassing, samples were dissolved in acid. Apatite was dissolved in HNO3 at 80°C and zircon with a multi-step acid-vapor dissolution using HF, HCl, and HNO3. Dissolved grains were spiked and analyzed for U, Th, and Sm content on an ICP-MS. From these data, cooling ages were calculated using the protocol of Ketcham (2011).

Apatite grains for CD samples were packed in Nb packets and degassed in an Alphachron 772 helium mass spectrometer. U and Th were measured using an inductively coupled plasma mass spectrometer at the University of Calgary using the protocol of the CPATT lab.

Apatite Fission Track Thermochronometry

Apatite fission track data was collected by A. Blythe at Oberlin College. Apatites were mounted in epoxy. Sample surfaces were ground and polished. Apatite mounts were etched in 5.5M HNO3 at 18°C for 22 seconds. An external detector (e.g., Naeser, 1979), consisting of low-U (<5 ppb) Brazil Ruby muscovite, was used for each sample. Samples were irradiated in the Oregon State Triga nuclear reactor. Following irradiation, the muscovites were etched in 48 % HF at 18°C for 30 min. Tracks were counted using a 100X dry lens and 1250X total magnification in crystals with well-etched, clearly visible tracks and sharp polishing scratches. A Kinitek stage and software written by Dumitru (1993) were used for analyses. Standard and induced track densities were determined on external detectors (geometry factor = 0.5), and fossil track densities were determined on internal mineral surfaces. Ages were calculated using zeta 359 ± 10 (AB) for dosimeter CN-5 (e.g., Hurford & Green, 1983). All ages are central ages, with the conventional method (Green, 1981) used to determine errors on sample ages. The chi-square test estimated the probability that individual grain ages for each sample belong to a single population with Poissonian distribution (Galbraith, 1981). The data were reduced with the program Binomfit (Brandon, 2002).

4.2.2 Pacific-North America Relative Plate Motion

To better understand the tectonic history of Haida Gwaii, we reconstruct relative plate motions between the Pacific and North American plates using the kinematic models of DeMets and Merkouriev (2016) and Doubrovine & Tarduno (2008), with the tectonic reconstruction software Gplates (Müller et al., 2018). The DeMets and Merkouriev (2016) kinematic model resolves plate motion to ∼20 Ma in high resolution (∼1 myr) increments whereas Doubrovine & Tarduno (2008) resolves plate motion to the Cretaceous albeit at much lower resolution. We chose to limit our reconstruction to the past 25 myr when it is generally agreed that the Pacific and North American plates were in contact in this region (Plafker, 1987; Hyndman & Hamilton, 1993).

4.3 Results

Average AHe dates range from ∼5-21 Ma, AFT dates range from ∼10-13 Ma, and ZHe from ∼27-59 Ma (Figure 4.2; Table 4.1). All AHe dates younger than 12 Ma were found in samples less than 35 km from the plate boundary as defined by the QCF (Figure 4.2; Appendix A.3, Figure A.6), while all AHe dates greater than 35 km from the plate boundary were 21-13 Ma. AFT dates are ∼12 Ma, within error, for all samples analyzed (Figure 4.2). The northernmost ZHe date is older by ∼20 Ma relative to the two southern ZHe dates (Figure 4.2).

4.3.1 Thermal Modeling

We performed inverse thermal history modeling of 11 samples using the software QTQt (v 5.7 Gallagher, 2012). QTQt uses a Bayesian transdimensional Markov Chain Monte Carlo method to invert thermochronometry data for time-temperature histories. A major advantage to QTQt over other thermal modeling software is its ability to model multiple thermochronometers within a single sample as well as groups of samples. Samples were selected for modeling if they had multiple thermochronometers, were collected from sedimentary rocks, or made up part of a vertical transect.

For 6 samples, we ran the model for 100,000 burn-in and 500,000 post burn-in steps. For samples with AHe, ZHe, and AFT thermochronometers, we ran models for 500,000 burn-in and 1,000,000 post burn-in steps. Inversions rejected more complex models that did not improve data fit. For sedimentary and igneous samples, we did not add a deposition crystallization age constraint as we found this constraint over-determines model outcomes. All samples use the RDAAM diffusion model for apatite (Flowers et al., 2009), ZRDAAM for zircon (Guenthner et al., 2013), and the fission track annealing model outlined by Ketcham et al., (2007). Errors on all helium dates were re-sampled to address uncertainty not accounted for in recorded analytical error (Gallagher, 2012). Interpretation of model results was based on the expected model, which is a mean model weighted by each model's posterior probability

and the 95% credible interval around the expected model (Gallagher, 2012). Detailed model parameters can be found in an online data repository (Appendix E).

Thermal modeling results show all samples were cooler than 65°C by 6 Ma (Appendix E). A maximum average temperature of 130°C is estimated at 20 Ma for the northernmost sample with AHe, AFT, and ZHe data (Figure 4.3 A).

4.4 Discussion

Low-temperature thermochronometry data from the archipelago of Haida Gwaii show distinct spatial and temporal trends in upper crustal cooling (Figures 4.2, 4.3). Specifically, we observe a doubling in Miocene-present cooling rate with proximity to the QCF, a slight decrease in cooling rate after 8-10 Ma in central and southern Haida Gwaii, and a northward progression of the timing of cooling onset (Figures 4.2, 4.3). We do not record an increase in cooling rate with the onset of glaciation such as that observed in the Coast Mountains to the east of the Queen Charlotte Basin (Farley et al., 2001).

Assuming a geothermal gradient of 20-30°C, thermochronometry data allow for early Miocene to present near-fault exhumation of 3-6 km at an average rate of 0.2-0.3 mm yr^{-1}. A lesser, albeit still substantial, 2-3 km of exhumation since the early Miocene is estimated at distances greater than 30 km from the plate boundary (Figure 4.2). This trend is roughly consistent along 200 km of the QCF.

Our results provide the first quantitative estimate of exhumation in Haida Gwaii and show that topography is likely older than the purported onset of subduction in the late Miocene (Figure 4.3; Hyndman, 2015; ten Brink et al., 2018). Instead, low temperature thermochronometry suggests exhumation began ∼15-20 Ma and continued at a steady or slightly slowing rate to the present (Figure 4.3). This timing of exhumation onset overlaps the passage of the Yakutat terrane (Figures 4.3, 4.4) and invites the interpretation that topography on Haida Gwaii began to form during terrane translation, not subduction initiation. Additionally, the phase of maximum deformation in the Queen Charlotte Basin, 21-24 Ma (Schumann et al., 2013), coincides with the passage of the Yakutat terrane (Figure 4.4;

Appendix E).

A parsimonious explanation for these observations is that both exhumation in Haida Gwaii and transtensional shear in the Queen Charlotte Basin were instigated by translation of the Yakutat terrane. Recent work proposes that as the Yakutat terrane moved north with the Pacific plate from offshore Vancouver Island to southern Alaska, interplate strain localized on the QCF, ending a phase of distributed deformation within the fossil forearc of North America (ten Brink et al., 2018). This hypothesis is supported by a late Oligocene phase of distributed shear leading to the formation of the Queen Charlotte Basin (Rohr & Dietrich, 1992), as well as a strong correlation between the current geometry of the plate boundary and the late Oligocene-present trajectory of the Yakutat terrane (Figure 4.4; DeMets & Merkouriev, 2016). Our thermochronometry data further supports this hypothesis. We argue that the opening of the Queen Charlotte Basin and exhumation in Haida Gwaii were a response to deformation of the western margin of North America driven by passage of the Yakutat terrane. We propose Haida Gwaii translated northward with the Yakutat terrane, much like a forearc sliver, driving the opening of the Queen Charlotte Basin in the late Oligocene, only to be deformed and abandoned in its current location in the early Miocene. This is consistent with prior models of Queen Charlotte Basin formation that emphasize right-lateral shear (Rohr & Dietrich, 1992), as well as measured offsets on the right-lateral Louscoone Inlet fault system in eastern Haida Gwaii (Lewis et al., 1991).

Following the onset of exhumation, our data show steady to slightly decreasing exhumation rate to present (Figure 4.3). This is surprising considering the estimated $\sim$2 cm yr^{-1} increase in convergence rate between the Pacific and North American plates since the Miocene at this latitude (DeMets & Merkouriev, 2016). While plate motion models may not accurately estimate regional kinematics (Brothers et al., 2020), interplate convergence could also be accommodated by more than crustal shortening and uplift in Haida Gwaii. Partial inversion of the Queen Charlotte Basin (Rohr et al., 2000), deformation of the Pacific plate in the Queen Charlotte Terrace (Figure 4.1; Rohr et al., 2000), and the localization of strain on a subduction fault (Lay et al., 2013; ten Brink et al., 2018), are also linked to interplate

convergence. Together, a variety of styles of strain accommodation mean exhumation rates in Haida Gwaii may not correlate directly with convergence rate.

While basin inversion in North America and deformation of the Pacific plate are well documented, they cannot account for the >100 km convergence estimated at the latitude of Haida Gwaii (Figure 4.4 DeMets & Merkouriev, 2016). Crustal shortening in the Queen Charlotte Basin (8-10 km) and the Queen Charlotte Terrace (6-20 km) can accomodate a maximum of 30 km convergence (Rohr et al., 2000). The resulting shortening deficit of ∼70 km is most easily resolved with subduction of the Pacific plate.

If subduction has initiated since the latest Miocene, it has not led to an increase in upper plate exhumation rate as recorded elsewhere (House, 2002; Sutherland et al., 2009). In fact, our data for central and southern Haida Gwaii suggest a minor decrease in exhumation rate over the past 8-10 myr (Figure 4.3 B, C). Furthermore, the lack of a Benioff zone associated with the estimated extent of underthrust slab (Figure 4.4), is difficult to reconcile with subduction initiation. These observations may be the result of the age of oceanic lithosphere offshore Haida Gwaii (Figure 4.1), as very young lithosphere has little elastic strength, requiring minimal upper plate uplift to maintain force balance during subduction, and thermal diffusion in the mantle could prevent underthrust lithosphere from maintaining a slab-like geometry (Gurnis et al., 2004). Furthermore, the earlier phase of topographic development in Haida Gwaii may obfuscate a signal linked to subduction initiation.

4.5 Conclusions

We estimate up to 6 km of Miocene to present exhumation on the archipelago of Haida Gwaii using low-temperature thermochronometry. Exhumation rates exceed 0.2 mm/yr within 30 km of the QCF, suggesting more pronounced deformation and uplift at close proximity to the plate boundary. Additionally, we find a time-transgressive onset to exhumation in Haida Gwaii that shortly postdates the opening of the Queen Charlotte Basin. Both events are correlated with the passage of the Yakutat terrane, suggesting terrane translation drove crustal deformation in North America. In spite of estimated increasing convergence

rate, thermochronometry data from Haida Gwaii show steady or slowing exhumation rate over the past 8-10 myr. We take this to indicate interplate convergence north of Cascadia has been accommodated to varying degrees by basin inversion in North America, shortening of the Pacific plate, and possibly, the initiation of subduction.

4.6 Figures and Tables

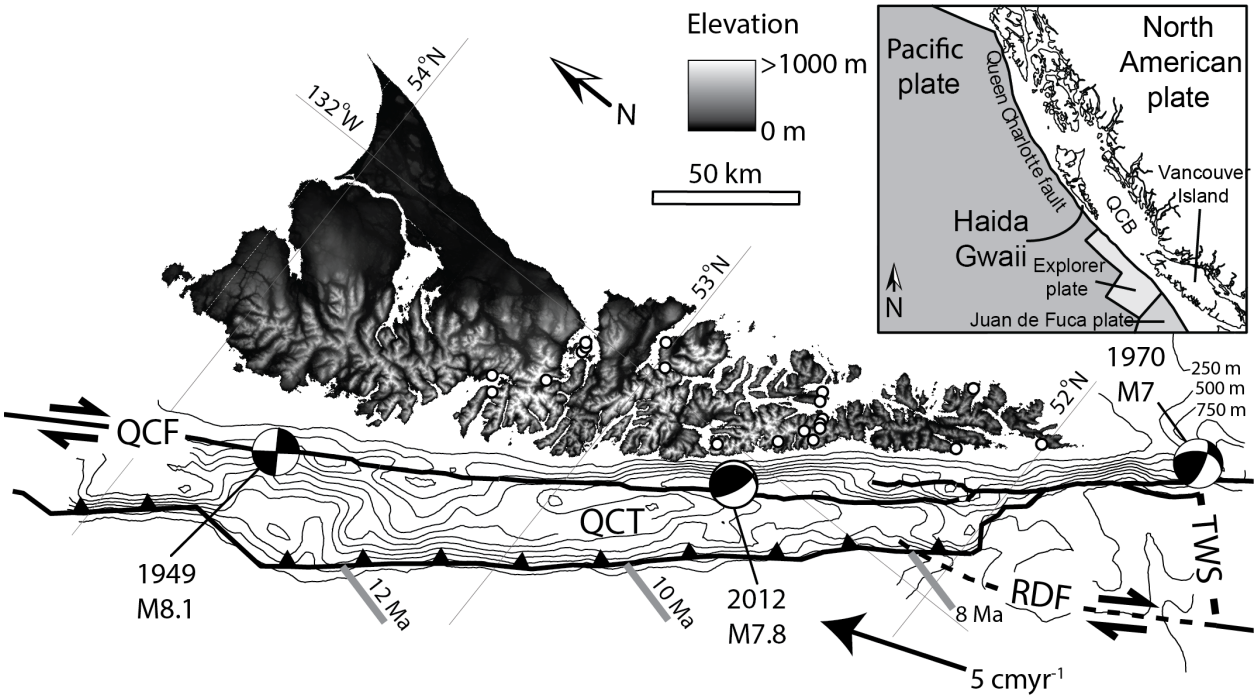

Figure 4.1: Regional map showing topography of Haida Gwaii (offshore western Canada), bathymetric contours at 250 m increments, sample locations (white circles), and pertinent tectonic features. Focal mechanisms for three historic $\geq$ M7 earthquakes (Rogers, 1986; Lay et al., 2013) show varying degrees of strain partitioning at the plate boundary. Pacific plate age is marked as grey lines extending off Queen Charlotte Terrace (Wilson, 2002). Relative plate motion vector is calculated from DeMets and Merkouriev (2016). Inset shows regional context. QCF – Queen Charlotte Fault; QCF – Queen Charlotte Terrace; QCB – Queen Charlotte Basin; TWS – Tuzon Wilson Seamounts; RDF – Revere Dellwood Fault.

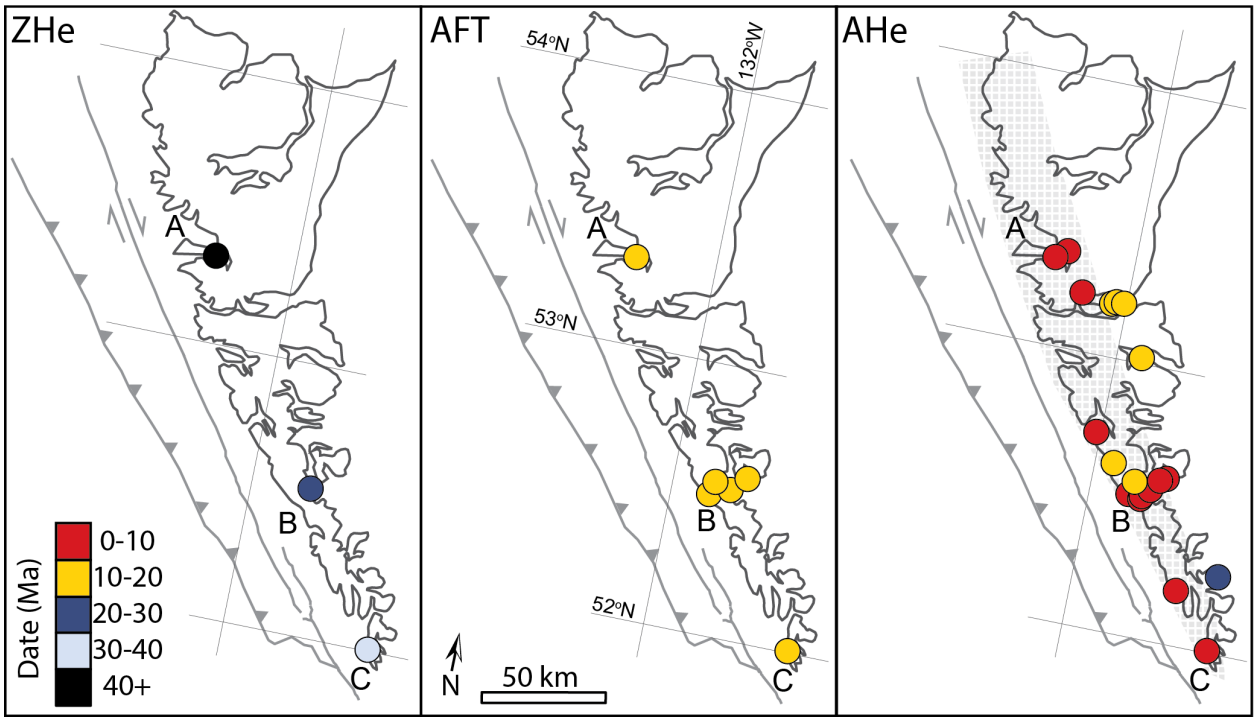

Figure 4.2: Thermochronometry samples from Haida Gwaii showing average AHe, AFT, and ZHe dates. A, B, C locations (northern, central, and southern Haida Gwaii, respectively) are sites from which samples were used for thermal modeling, results shown in Figure 4.3. Stippled region encompasses area of increased predicted exhumation rate.

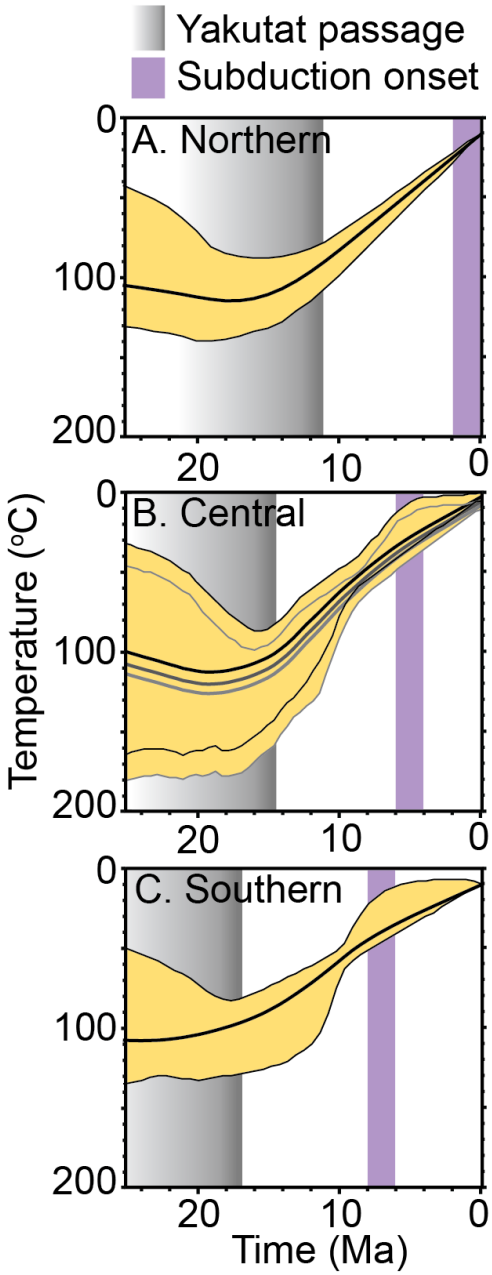

Figure 4.3: Thermal modeling results for samples from northern (A), central (B), and southern (C) Haida Gwaii. Yellow envelope marks 95% credibility interval and thick lines are expected time-temperature path with the thick black line marking the sample at highest elevation in (B). Timing of Yakutat passage is marked as is purported onset of subduction, given a 15° critical convergence obliquity (Trehu et al., 2015; ten Brink et al., 2018)

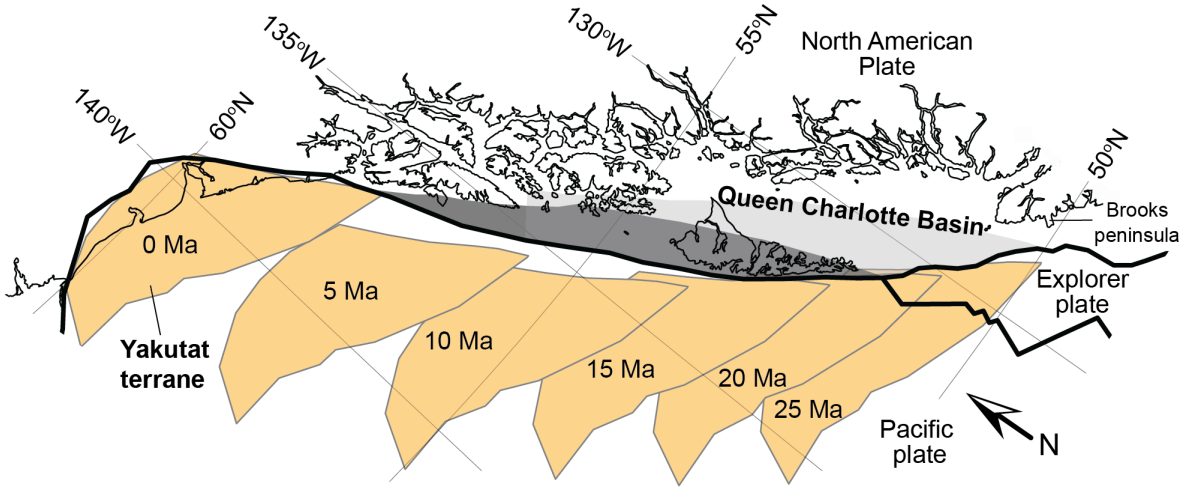

Figure 4.4: Plate reconstruction of unsubducted portion of the Yakutat terrane in 5 m.y. increments since 25 Ma. Maximum extent of the under-thrust Pacific plate assuming fixed plate boundary since 19 Ma is shown in grey; figure shows underthrust estimates for fixed triple junction either at Tuzo Wilson Seamounts (dark grey) or off Brooks Peninsula (light grey; Rohr and Tyron, 2010). Both DeMets and Merkouriev (2016) and Doubrovine and Tarduno (2008) kinematic models were used to reconstruct the Yakutat terrane position with software GPlates (Müller et al., 2018). Underthrusting estimates use DeMets and Merkouriev (2016) model.

Sample	Lithology	Longitude (W)	Latitude (N)	No. AHe	Corrected Ahe Date (Ma)	1σ (Ma)	eU (ppm)	1σ (ppm)	Elevation (m)
06CD16	Honna Sandstone	132.118	53.204	9	13.314	2.25	12.50	7.68	0
07CD16	Yakoun Sandstone	132.080	53.215	10	19.732	3.26	1.30	0.15	0
21CD16	Longarm Formation	132.319	53.226	2	8	1.73	23.30	10.72	0
29CD16	Honna Sandstone	132.149	53.230	12	17.05	5	11.20	14.15	0
BARRY	San Christoval Amphibolite	131.753	53.576	4	10.6	0.5	159.50	21.95	794
HG02	Burnaby Island Diorite	131.562	52.595	5	5.7	1.7	21.24	7.18	0
HG03	San Christoval Diorite	131.586	52.581	5	7.7	0.7	52.94	6.62	0
HG04	San Christoval Diorite	131.569	52.551	5	8.8	1	62.88	9.89	0
HG05	San Christoval Diorite	131.691	52.528	5	8.5	0.4	99.33	26.2	347
HG06	San Christoval Diorite	131.678	52.533	5	6.9	1.3	171.76	54.13	0.00
HG09	Kano Diorite	131.146	52.307	5	20.6	4.3	9.33	0.55	0
HG10	San Christoval Diorite	131.146	52.188	5	7	0.07	76.54	21.49	0
HG12	San Christoval Diorite	131.097	52.006	5	9.9	0.9	28.35	5.68	0
HG15	San Christoval Diorite	132.047	52.746	5	7.6	0.4	18.55	1.41	914
HG17	*Kano Diorite*	*131.927*	*52.989*	*3*	*25.33*	*1.38*	*23.88*	*14.14*	*0*
HG19	Honna Conglomerate	131.816	53.037	4	16.8	3.3	24.06	9.68	0
HG28	San Christoval Diorite	132.511	52.352	5	6.3	0.8	13.84	7.69	0
HG29	Burnaby Island Diorite	132.480	53.363	4	6.8	1.5	12.40	3.18	0
HG32	San Christoval Diorite	131.889	52.655	4	10.9	0.9	26.26	2.52	0
HG34	Kano Diorite	131.768	52.530	5	7	0.9	53.27	2.56	0.00
				No. AFT	Central age (Ma)	95% C.I. (Ma)	Mean track length in um (No. measured)		
BARRY	San Christoval Amphibolite	131.753	53.576	16	12.9	+3.7/-2.9	13.53±1.1 (9)	-	794
HG02	Burnaby Island Diorite	131.562	52.595	20	10	+5.1/-2.4	-	-	0
HG04	San Christoval Diorite	131.569	52.551	20	11.2	+3/-2.4	14.9±0.9 (4)	-	0
HG12	San Christoval Diorite	131.097	52.006	20	13.4	+3.4/-2.7	15±0.8 (4)	-	0
HG28	San Christoval Diorite	132.511	52.352	30	12.2	+7.2/-4.5	13.1±1.5 (4)	-	0
HG34	Kano Diorite	131.768	52.530	20	10.50	+3.3/-2.5	14.7±1 (5)	-	0
				No. Zhe	Corrected Zhe Date (Ma)	1σ (Ma)	eU (U+0.235*Th)	1σ (ppm)	
HG04	San Christoval Diorite	131.569	52.551	3	27.00	2.0	151.10	31.81	0
HG12	San Christoval Diorite	131.097	52.006	3	33.10	2.4	157.73	36.88	0
HG28	San Christoval Diorite	132.511	52.352	3	59.10	7.5	73.86	7.69	0

Table 4.1: AHe, AFT, and ZHe data from Haida Gwaii.

Chapter 5

SUBMARINE TECTONIC GEOMORPHOLOGY OF THE NORTH AMERICAN CONTINENTAL SHELF AND SLOPE ADJACENT THE QUEEN CHARLOTTE FAULT

ABSTRACT

The Queen Charlotte Fault is a submarine plate-bounding transpressive strike slip fault that for ∼800 km juxtaposes oceanic lithosphere of the Pacific plate with Mesozoic accreted terranes on the North American Plate. The seafloor expression of the Queen Charlotte Fault is characterized by conspicuous offset features and Pacific Plate shortening is shown by deformed sediments and oceanic crust in the Queen Charlotte Terrace. The effects of this deformation on submarine sediment routing from the continental shelf to the Pacific Plate remains an outstanding topic of study. Here, we examine the geomorphology of the continental shelf edge and submarine channels on the continental slope along the Queen Charlotte Fault to probe the record of submarine landscape processes and neotectonics. We find evidence for erosion and narrowing of the continental shelf offshore Haida Gwaii and northern Baranof Island, indicating the North American plate is deforming internally in these regions. Along the central Queen Charlotte Fault, the shelf edge appears to be subsiding and accumulating sediment. Continental slope channel gradients are shown to vary in response to sediment supply and seafloor obstructions resulting from uplift of the Queen Charlotte Terrace and translation of seafloor ridges on the Pacific Plate. Given sufficient sediment supply, these obstructions may drive progradation of the shelf edge seaward of the Queen Charlotte Fault. Together, our observations show that the continental shelf edge provides evidence for uplift and deformation of the North American margin, while deformation of

the Pacific Plate sets an important boundary condition for geomorphic development of the continental slope. [1]

5.1 Introduction

The North American and Pacific Plates are juxtaposed for more than 800 km along the transpressive dextral Queen Charlotte Fault (Figure 5.1). This fault is submarine for its entire length and formed in the wake of the northward translating Yakutat terrane since 19 Ma (Figures 4.4, 5.1 ten Brink et al., 2018). The fault offsets a seafloor topography developed in response to tectonics (Rohr et al., 2000; Trehu et al., 2015; Walton et al., 2015; Brothers et al., 2020), glacio-isostatic adjustment (Hetherington et al., 2004; Barrie et al., 2021), and periodic high-volume sediment input from the Cordilleran Ice Sheet (Barrie & Conway, 2013; Walton et al., 2014; Greene et al., 2019; Barrie et al., 2021; Zhang & Gulick, 2020). On a lithospheric scale, the Queen Charlotte Fault delineates a major discontinuity in the strength, composition, and thickness of the crust between the oceanic Pacific Plate and continental North American Plate (ten Brink et al., 2018; Walton et al., 2019). How and whether these differences affect deformation and geomorphic development remains unclear (Rohr et al., 2000; ten Brink et al., 2018; Walton et al., 2019; Barrie et al., 2021).

Using geomorphology to study tectonics has proven effective in terrestrial landscapes (e.g., Burbank & Anderson, 2011; Kirby & Whipple, 2012), but logistical and data constraints have limited study offshore. The recent acquisition of high resolution (30 m grid spacing) multibeam bathymetry along nearly the entire length of the Queen Charlotte Fault and adjacent continental slope and shelf edge (Brothers et al., 2020; Barrie et al., 2021), invites an examination of the tectonic influence on seafloor geomorphology along this margin. Recent work on the Queen Charlotte Fault suggests that deformation results in topographic scarps and offsets along strike of the Queen Charlotte Fault (Brothers et al., 2020). While along-strike trends in deformation rate and sediment input appear to relate to the gross morphology

[1] In collaboration with Daniel Brothers, Nathaniel Miller, Vaughn Barrie, and Alison Duvall. Manuscript in preparation with planned submission to Geosphere.

of the margin (Brothers et al., 2019), and plate boundary deformation and glacio-isostatic adjustment have been identified as locally affecting submarine canyon evolution and the morphology of the continental shelf (Harris et al., 2014; Barrie et al., 2021), a high-resolution analysis of margin-scale seafloor morphology on the continental slope and shelf has yet to be performed. In this paper, we survey the continental shelf and slope along the entire Pacific-North America margin defined by the Queen Charlotte Fault. We focus our analysis on the the impact of tectonics in determining the morphology of the continental shelf and submarine channels on the upper continental slope.

5.2 Background

5.2.1 Neotectonics of the Pacific-North American Plate Boundary

Historical seismicity, geodetic studies, and geomorphic mapping constrain the neotectonic history of the Pacific-North America Plate boundary offshore British Columbia and Southeast Alaska. Since 1900, this margin has hosted 5 major (Mw>7) earthquakes (Figure 5.1). All of them, save the 2012 Mw7.8 Haida Gwaii thrust earthquake, were predominantly strike-slip and occurred on the main strand of the Queen Charlotte Fault. Pacific-North America relative pate motion models predict a Holocene right-lateral slip rate of ∼45-50 mm yr^{-1} on the Queen Charlotte Fault (DeMets & Merkouriev, 2016; Brothers et al., 2020). Minor (<5 mm yr^{-1}) boundary parallel shear in the North American Plate is evidenced by GPS geodesy (Mazzotti et al., 2003; Elliott & Freymueller, 2020), suggesting much of the predicted boundary-parallel relative plate motion is indeed accommodated on the Queen Charlotte Fault (Brothers et al., 2020). Less clear, however, is the accommodation of interplate convergence, estimated to range from 15-20 mm yr^{-1} offshore southern Haida Gwaii to ∼6 mm yr^{-1} offshore Baranof Island (DeMets & Merkouriev, 2016; Elliott & Freymueller, 2020). The Queen Charlotte Terrace, an uplifted and faulted region extending from the Queen Charlotte Fault out to 30 km on the Pacific plate accomodates some of this convergence (Figure 5.1; Rohr et al., 2000; Trehu et al., 2015). GPS velocities suggest ∼5 mm

yr^{-1} shortening of the North American Plate within the Queen Charlotte Basin inboard of Haida Gwaii (Mazzotti et al., 2003), and exhumation rates from Haida Gwaii indicate the islands are being uplifted, possibly due to crustal shortening (Schoettle-Greene et al., 2020). North of Haida Gwaii, limited data prevent a similar determination of whether the North American plate is shortening.

The recent acquisition of high-resolution multibeam bathymetry along the Pacific-North America plate boundary has invited a closer look at the tectonic geomorphology of this region (Brothers et al., 2020). Analysis of bathymetry proximal to the Queen Charlotte Fault support the interpretation from geodetic studies that the majority of boundary-parallel plate motion is accounted for by slip on the fault (Brothers et al., 2020; Elliott & Freymueller, 2020). However, submarine geomorphology indicates that the Queen Charlotte Fault may experience far less convergence than relative plate motion models predict (DeMets & Merkouriev, 2016; Brothers et al., 2020). This may be due to effective regional strain partitioning in the Pacific and North American plates (Rohr et al., 2000; Mazzotti et al., 2003; Brothers et al., 2020; Elliott & Freymueller, 2020).

5.2.2 Surface Processes Along the Queen Charlotte Fault

Submarine surface processes are closely linked to terrigenous sediment input along the Queen Charlotte Fault (Barrie & Conway, 2002). Sediment input increased dramatically with the onset of northern hemispheric glaciation ca. 2.8 Ma and the development of the Cordilleran Ice Sheet (Sánchez-Montes et al., 2020; Zhang & Gulick, 2020). Glaciation, and concomitant sea level fall, resulted in a pronounced increase in sediment transport across the continental shelf to the Pacific Plate (Zhang & Gulick, 2020). This trend continues to present, with terrigenous sediment transport to the continental shelf edge and slope only occurring during sea level low stands (Barrie & Conway, 2002; Greene et al., 2019).

Prior to the development of the Cordilleran ice sheet, terrigenous sediment transport across the shelf and slope may have occurred in the region offshore Haida Gwaii, where the narrow shelf lacked accommodation space. To the north, off of Prince of Wales and southern

Baranof Island as well as in Dixon Entrance (Figure 5.1), sediment was likely trapped on the shelf in fault-bound basins up to 3 km deep (Bruns, 1988; Rohr & Dietrich, 1992). With the onset of continental glaciation, ice streams in Dixon Entrance and Chatham Straight transported sediment from the mainland directly to the continental slope off Prince of Wales Island (Figure 5.1; Carrara et al., 2007; Brothers et al., 2019; Zhang & Gulick, 2020). These ice streams served as point sources for sediment input to the continental shelf edge and slope, feeding the deep marine Baranof Fan via a succession of deep-sea channels including the currently active Horizon and Mukluk channels (Figure 5.1; Walton et al., 2014; Zhang & Gulick, 2020). The topography of Haida Gwaii shielded the shelf edge and slope from Cordilleran Ice Sheet-derived sediment, resulting in little sediment input during glaciation (Sutherland Brown, 1968; Greene et al., 2019).

Relative sea-level fall during glacial periods further promoted sediment transport to the continental slope by reducing the width of the continental shelf. During the last glacial maximum, relative sea level was 150-180 mbsl (Figure 5.1; Carrara et al., 2007; Shugar et al., 2014; Barrie et al., 2021), with potential for temporal and spatial variation driven by a migrating glacio-isostatic forebulge (Hetherington et al., 2004). While shelf width was nominally decreased offshore Haida Gwaii during sea level low stands, the shelf width west of Prince of Wales and Baranof Islands was greatly reduced.

With the retreat of the Wisconsin Cordilleran Ice Sheet 15-17 ka and rising sea level, the continental slope began to be cut off from terrigenous sediment supply (Barrie & Conway, 2002; Greene et al., 2019). By 12-13 ka, the continental slope was starved of sediment, with deposition relegated to fjords and on the upper continental shelf (Brothers et al., 2020). This resulted in the cessation of geomorphic surface processes that sculpt the seafloor (Brothers et al., 2020; Barrie et al., 2021). Therefore, outside of fault displacements and submarine landslides, the submarine geomorphology of the outer shelf and continental slope has most likely not evolved since the early Holocene.

5.2.3 Background on Submarine Geomorphology

The quantitative analyses of submarine geomorphology is an emerging discipline with recent advances made possible by the acquisition of high-resolution bathymetry (Lecours et al., 2016). Being in its infancy, many outstanding questions remain regarding the processes that sculpt the seafloor as well as the information that can be gleaned from seafloor morphology. Below, we review current understandings of continental shelf and submarine canyon development.

Morphology of the Continental Shelf and Shelf-break

The continental shelf is a shallow, gently sloping, submarine platform found adjacent most continents. It is commonly defined as extending from the shoreline to the shelf break, a major physiographic boundary associated with an increase in seafloor slope (Vanney & Stanley, 1983). Depending on tectonic setting, sediment input, and sea level history, shelf and shelf-break morphologies vary. If the shelf is subsiding, it can serve as a major sink for terrestrial sediment, with deposits often exceeding kilometers in thickness (Divins, 2003). Given sufficient sediment supply, the shelf will prograde and, in conjunction with oscillating sea level, may form a diffuse shelf-break as sediments are reworked and drape over the shelf-slope transition (Schlager & Adams, 2001). In tectonically active settings, basement rock may be exposed at the seafloor with little sediment deposition on the shelf (Helland-Hansen et al., 2012). This can result in an abrupt, structurally defined, shelf-break (Helland-Hansen et al., 2012).

Shelf-break depth is seen to vary considerably across the globe, with a range from 0 to ∼500 mbsl (Paris et al., 2016). The depth and locus of the shelf-break may be defined by a combination of sediment input (Olariu & Steel, 2009), subduction zone locking on convergent margins (Malatesta et al., 2021), crustal structure (Helland-Hansen et al., 2012), active faulting (Johnson et al., 2018), sea level lowstand depth (Dietz & Menard, 1951; Fraccascia et al., 2013), and wave base erosion (Iwasaki & Parker, 2020).

Submarine Channels on the Continental Slope

Channelized submarine sedimentary flows are recognized as important drivers of the morphological development of continental slopes (N. C. Mitchell, 2005), and serve to transport terrigenous sediment to abyssal depths (Shepard, 1981). Basal shear stress from flows may drive substrate erosion, resulting in the development of submarine canyons (Pratson & Coakley, 1996; N. C. Mitchell, 2005), a common feature on continental slopes (Harris & Whiteway, 2011). Canyons can be generally categorized as those that are shelf-sourced vs. those that are slope-sourced based on whether the canyon channel network has a direct link to the continental slope or if channel heads are found downslope of the shelf-break, respectively (Brothers et al., 2013). Differences in sediment sourcing and supply between these two categories of continental slope canyon are often reflected in channel morphology (Brothers et al., 2013).

An outstanding question in the study of submarine channels is how similar submarine channel-forming processes driven by sediment gravity flows are to fluvial processes in subaerial environments (N. C. Mitchell, 2005; Dobbs et al., 2019). This degree of similarity determines whether the approaches used to study subaerial rivers can be effectively applied to submarine settings. In subaerial settings, the stream incision law has long been applied to estimate the erosion rate, E, of channel networks:

$E = KQS^n$ (1)

Where K is the erodibility coefficient, Q is discharge, S is the channel slope, and n is an exponent that accounts for erosion process (Whipple & Tucker, 1999). Empirical measurement shows that Q is proportional to upstream catchment area, A, raised to the constant m (Leopold & Miller, 1962). This exponent accounts for scaling of channel width and discharge with increasing A (Whipple & Tucker, 1999). Following the replacement of Q with A^m, this equation is often rearranged to relate terrestrial channel slope to upstream catchment area:

$S = k_s A^\theta$ (2)

Where k_s and θ are the steepness index (K/E) and the concavity index (m/n) of the channel, respectively. In terrestrial channels, θ generally occupies a narrow range (0.4-0.6) and S decreases as A increases (Leopold & Miller, 1962; Whipple & Tucker, 1999).

Recent work suggests a slope-area relationship may also be present in submarine channels where turbidity current discharge, Q_t, erodes the thalweg (N. C. Mitchell, 2004, 2005; Brothers et al., 2013; Dobbs et al., 2019). However, there is no recorded empirical correlation between A and Q_t in submarine catchments and in-situ observation of turbidity currents is very rare (Paull et al., 2002, 2018). Analysis of continental slope canyons suggests using A as a proxy for Q_t in submarine channel networks may prove problematic if channels are shelf-sourced because of uncertainty in the magnitude of external sediment inputs from the shelf (Brothers et al., 2013). Furthermore the upslope extent of slope-sourced channel networks must be chosen manually, resulting in uncertainty in A. Finally, processes specific to submarine channel discharge including turbidity current entrainment of bed material and transformation between debris flows and turbidity currents may all complicate application of a slope-area scaling relationship to submarine channel networks (Ramsey et al., 2006; N. C. Mitchell, 2008).

While significant uncertainty in the processes responsible for submarine channel longitudinal profile form remain, channel gradient is understood to be of fundamental importance for sediment transport and deposition (Maier et al., 2017). High channel gradients may result in sediment bypass and bed erosion whereas downslope decreases in gradient result in sediment deposition (N. C. Mitchell, 2004; Stevenson et al., 2015; Maier et al., 2017; Pohl et al., 2020). The relationship between channel slope and sedimentation and erosion results in channel thalweg gradient evolving towards a state of dynamic equilibrium that is optimally suited for sediment bypass without bed erosion (Kneller, 2003; Georgiopoulou & Cartwright, 2013; Lai et al., 2016).

Submarine channel evolution in the context of tectonic perturbation is a relatively understudied subject (Huyghe et al., 2004; Mayall et al., 2010; I. R. Clark & Cartwright, 2009, 2011; Micallef et al., 2014; Maier et al., 2017). I. R. Clark and Cartwright (2009) propose

four main submarine channel responses to deformation: (1) Confinement, where the channel location is constrained by regional structure. (2) Diversion, where the channel is forced to bypass an obstruction to flow. (3) Deflection, where a channel migrates in response to a growing obstruction to flow and (4) Blocking, where an obstruction to flow causes reflection of individual flow events and sediment deposition. Micallef et al. (2014), in a study of Cook Canyon offshore New Zealand, propose that channel knickpoints form in response to uplift-driven changes to base level and translate up-channel in a manner similar to river slope-break knickpoints (Kirby & Whipple, 2012). Similarly, knickpoint propagation up submarine channels has been identified in the Niger Delta (Heiniö & Davies, 2007), and in repeat multibeam surveys in fjords offshore western Canada (Heijnen et al., 2020).

5.3 Methods

To better understand the interplay between crustal deformation and submarine geomorphology offshore northwest British Columbia and Southeast Alaska, examining both the Pacific and North American plates, we map the continental shelf-break and continental slope channels using multibeam bathymetry. We measure the depth below sea level of the shelf-break and gradient of continental slope channels to explore along strike trends in seafloor morphology.

The bathymetry data used were collected from 2009-2017 and gridded to 30 m resolution (see Barrie et al., (2021) and Brothers et al., (2020) for a full description of the dataset). Coverage of the edge of the shelf and slope is relatively complete, with minor gaps off of northern Haida Gwaii, central Prince of Wales Island, and northern Baranof Island.

5.3.1 Continental Shelf and Shelf-break

We map the shelf-break from multibeam bathymetry, estimate the depth of the mapped shelf-break, width of the shelf relative to the shore and sea level lowstand, and the average slope of the shelf. To map the shelf-break, we used the slope and curvature of the seafloor to determine the point at which the continental shelf transitions to the slope. The continental

shelf-break is generally marked by an increase in downslope curvature and slope. We mapped the shelf-break on the upslope edge of high curvature and, when the curvature of the shelf-break was less pronounced, we used a threshold seafloor slope of 2° to guide placement of the shelf-break. Mapping the shelf-break manually differs from that of previous workers who examined a global dataset and employed automated techniques (Olariu & Steel, 2009), but we find it to be most effective at accounting for the range of shelf-break morphologies observed. We were unable to map the shelf-break offshore northern Haida Gwaii and between Noyes Canyon and the Sumner Sea Valley due to limited multibeam bathymetry coverage. We also did not map the shelf-break at the outlet of the Chatham Sea Valley where a large pull-apart basin on the Queen Charlotte Fault has deformed the shelf edge (Figure 5.1).

Using the newly mapped shelf-break, we measured the depth of the shelf-break, distance to the present-day shore, and distance to the 175 mbsl lowstand. With these measurements, we calculated the average present-day and lowstand shelf slopes.

High resolution multichannel seismic-reflection profiles were examined proximal to the shelf edge to determine sub-seafloor structure and sedimentation processes. Profiles were collected in 2016 and 2017 aboard the R/V Norseman and R/V Ocean Starr using a sparker sound source and variable length hydrophone streamers. Reflection profiles resolve structures to ∼200 m depth below the seafloor and allow a determination of the sedimentary and tectonic regime at the shelf edge.

5.3.2 Continental Slope Channels

Submarine channel thalwegs were mapped from multibeam bathymetry using the flow routing algorithms in the Matlab software package TopoToolBox (Schwanghart & Scherler, 2014). The multibeam data were cropped above the continental shelf-break to slopes that exceeded 5°, limiting channels to the shelf-break and slope. Local sinks were filled to guarantee flow connectivity and channel heads were determined using a threshold upstream drainage area of 10^5 m^2. In terrestrial landscapes, a transition from hillslope to fluvial processes is commonly predicted at an upstream drainage area of $\sim 10^5$-10^6 m^2 (Montgomery &

Foufoula-Georgiou, 1993). This approach may be less applicable in submarine settings where drainage area estimated from a DEM does not necessarily correlate with discharge (Brothers et al., 2013). Because of this, we qualitatively reviewed extracted channels to determine whether they accurately predicted the location of seafloor channels. We found a critical upslope drainage area, while often successfully predicting channel thalwegs, does not accurately predict the onset of channelization nor does it accurately predict channel formation. To resolve these issues, the mapped channel network was manually edited to remove predicted channel heads not associated with obvious seafloor concavities indicative of channelization. Downstream cessation of channelization was ignored during editing. Channel networks were further parsed to only include those shallower than 1000 mbsl and those that had an upslope connection to the shelf-break. In places where the shelf-break was not mapped, channels were kept if the head of channel networks was observed in the available multibeam data.

5.4 Results

5.4.1 Continental Shelf and Shelf-break

We mapped a total shelf-break length of 902 km, covering much of the continental margin along the Queen Charlotte Fault (Figure 5.2). The shelf-break is shallowest near the northern extent of the map area and offshore central Haida Gwaii, deepening off southern Baranof Island, Prince of Wales Island, and south of Haida Gwaii. Mean shelf-break depth for the whole margin is 225 mbsl (1σ = 29 m, median = 221 mbsl; Table 5.1). The shelf-break parallels the Queen Charlotte Fault for most of its length, save for a 30 km embayment in the shelf at Noyes Canyon (Figure 5.2). The distance from the shelf-break to the Queen Charlotte Fault ranges from 37 km to 30 m (mean = 8.6 km, 1σ = 8.1 km, median = 7.4 km; Table 5.1). From central Baranof Island north, the continental shelf extends onto the Pacific Plate side of the Queen Charlotte Fault (Figure 5.2).

The width of the continental shelf as measured from the present shoreline to the shelf-break ranges from 264 m to 55 km (mean = 21.5 km, 1σ = 16.4 km, median = 20 km; Table

5.1). The mean slope of the shelf is 1.79° (1σ = 2.36°, median = 0.63°; Table 5.1). The narrowest shelf is observed offshore Haida Gwaii, and the widest shelf is observed offshore Prince of Wales Island and southern Baranof Islands (Figure 5.2).

Measuring the shelf from an estimated sea-level lowstand of 175 mbsl (Barrie et al., 2021), we find that shelf width ranges from 42 km to 0 km (mean=8.4 km, 1σ = 9.7 km, median = 4.6 km; Table 5.1). The mean slope of the lowstand shelf is 1.25° (1σ = 2.68°, median = 0.56°; Table 4.1). The lowstand shelf is narrowest offshore Haida Gwaii, with the shelf-break frequently located at the estimated lowstand shoreline (Figures 5.2, 5.3 A). Significant shelf narrowing is also observed offshore Mount Edgecumbe along the northern Queen Charlotte Fault and at the northernmost Queen Charlotte Fault just south of the Yakutat terrane (Figures 5.1, 5.2). The widest part of the lowstand shelf is observed at the outlet of the Dixon Sea Valley, north of Haida Gwaii (Figure 5.2).

Continental Shelf Segments

Based on trends observed in the bathymetry, we identify three distinct shelf segments along strike of the Queen Charlotte Fault (Figures 5.2). These segments are characterized by differences in slope, width, distance from the Queen Charlotte Fault, and the depth of the shelf-break (Table 5.1). Where data coverage allows, the transition between segments is observed to be gradational, reflecting the increasing influence of changing tectonic and sedimentary boundary conditions.

The northern continental shelf segment is found offshore central and northern Baranof Island (Figure 5.2 A). This segment is mapped from the Yakutat terrane to the southernmost shelf that extends onto the Pacific Plate. A transitional domain between this segment and the central segment extends south to the Chatham Sea Valley (Figure 5.2). This shelf segment is characterized by a shallow and abrupt shelf-break often defined by the Queen Charlotte Fault (Figures 5.2 A, 5.3 A; Table 5.1). In a number of locations, the shelf extends west of the Queen Charlotte Fault onto the Pacific Plate (Figures 5.2 A, 5.3 A). The shelf-break is more broadly convex where the shelf extends onto the Pacific Plate (Figure 5.3 A).

Active Holocene volcanism in the Mt. Edgecumbe volcanic field locally shallows the shelf and shelf-break (Figures 5.2 A, 5.3 A).

Given present-day sea level, the northern continental shelf segment is on average 21.1±4.2 km wide, with a slope of 0.61±0.11° (Table 5.1). The estimated lowstand shelf is on average 5.4±3.8 km wide, with a mean slope of 0.55±1.4° (Table 5.1). Average distance to the Queen Charlotte Fault is 1.7±1 km (Table 5.1). Shelf-break depth averages 220±30 m (median = 213 m; Table 5.1) and deepens along the southernmost portion of this shelf segment (Figures 5.2 A).

The central continental shelf segment is found offshore southern Baranof and Prince of Wales Islands (Figure 5.2 B). This shelf is deeper and wider on average than that found elsewhere along the Queen Charlotte Fault. The seafloor is relatively smooth at the shelf edge along the central segment, suggesting basement is not exposed (Figure 5.3 B). Bedforms we interpret to be sand ridges indicate submarine sediment transport across the shelf (Figure 5.3 B). North of the Chatham Sea Valley the shelf-break is nearly coincident with the Queen Charlotte Fault and is the most consistently deep shelf-break observed along the entire margin (Figure 5.2 B). At the outlet of the Chatham Sea Valley a step-over in the Queen Charlotte Fault results in deformation at the shelf edge and the formation of a pull-apart basin (Figure 5.2 B). The shelf extends onto the Pacific Plate immediately south of this pull-apart (Figure 5.2 A).

Shelf-indenting canyons are observed along the central shelf segment, with the most pronounced being the ∼25 km length Noyes Canyon (Figure 5.2 B, 5.3 B). Noyes Canyon forms on the Alexander terrane between the Wrangell and Chugach terranes (Figure 5.2). Tributary lengths along the canyon are asymmetric, with longer tributaries found along the southern part of the canyon (Figure 5.2 B).

The Chatham, Sumner, and Dixon sea valleys extend across the central continental shelf segment (Figure 5.2 B). These sea valleys hosted glacial ice streams, forming sediment fans at the outlets of the the Chatham Sea Valley, southern fork of the Dixon Sea Valley (Dobson et al., 1998), and, to a lesser extent, the Sumner Sea Valley. A transtensional step in the Queen

Charlotte Fault at the outlet of the Chatham Sea Valley results in a structurally controlled shelf-break that we do not include in our mapping (Figure 5.2 B). Incomplete multibeam coverage at the outlets of the Dixon and Sumner sea valleys limits our ability to completely map the depth of the shelf-break in these locations (Figure 5.2).

Given present-day sea level, the central continental shelf segment is on average 40.2±6.2 km wide, with a slope of 0.35±0.06° (Table 5.1). The estimated lowstand shelf is on average 17.9±9.6 km wide, with a mean slope of 0.27±0.17° (Table 5.1). Average distance to the Queen Charlotte Fault is 11.4±10 km (Table 5.1). Shelf-break depth averages 240±26 m (median = 239 m; Table 5.1) and is deepest along the southern and northern portions of this shelf segment (Figures 5.2 A).

The southern continental shelf segment is found offshore Haida Gwaii (Figure 5.2 C). The southern segment is the narrowest, shallowest, and steepest shelf along the Queen Charlotte Fault (Figure 5.2, Table 5.1). Across much of its length, it is characterized by rough bathymetric highs that extend above a gently dipping planar surface which ocean-bottom cores show to be a thin layer of sediment over basement (Figure 5.3 C; Barrie et al., 2021). An exception is observed offshore northern Graham Island, where the shelf appears to be depositional in origin (Figure 5.2 C). The shelf edge is frequently abrupt, with a linear to concave form of the uppermost continental slope. A coastal mountain range, with peaks up to 1100 m elevation, is found adjacent this shelf (Figure 5.3 C). North of Tasu Inlet, subaerial topography grades directly into the continental slope (Figure 5.3 A). Shelf-indenting submarine canyons are infrequently observed and are often associated with inlets (Barrie et al., 2021). Exceptions include a major shelf-indenting canyon offshore Kungit Island (Here named Kunghit Canyon) and smaller canyons offshore northernmost Graham Island.

Given present-day sea level, the southern continental shelf segment is on average 5.4±4.6 km wide, with a slope of 3.6±2.7° (Table 5.1). The estimated lowstand shelf is on average 1.4±2.1 km wide, with a mean slope of 2.42±3.65° (Table 5.1). The shelf-break is exclusively mapped on the North American plate side of the Queen Charlotte Fault, with an average distance to the fault of 9.5±5.8 km (Table 5.1). Shelf-break depth averages 213±26 m

(median = 213 m; Table 5.1) and, excluding a deeper segment in the northernmost Queen Charlotte Sound, is relatively consistent along strike (Figures 5.2 C, 5.3 C).

Multichannel Seismic Profiles From the Shelf Edge of the Central and Northern Continental Shelf Segments

Multichannel seismic reflection profiles from the central and northern shelf segments indicate long-term differences in shelf evolution along the Queen Charlotte Fault. Seismic reflection profiles along the northern shelf segment show evidence for internal deformation and complicated shelf sedimentation. Numerous locations reveal seaward-dipping reflectors truncated by a near surface unconformity (Figure 5.5 A, C; Walton et al., 2018). Sub-vertical faults inboard of the Queen Charlotte Fault are observed in some seismic profiles along the northern shelf segment (Figure 5.5 B). In some cases, folded reflectors we interpret as growth folds extend to the near surface, indicating ongoing fault activity (Figure 5.5 B). In line 54, sediment collects in a shelf-proximal valley between the continental shelf-break and a bathymetric high interpreted as a volcanic cone (Figure 5.5 B Prouty et al., 2020).

Profiles that cross parts of the shelf on the Pacific Plate side of the Queen Charlotte Fault generally show complicated stratigraphy (Figure 5.5 C). On the Pacific Plate, reflectors indicate the presence of buried bathymetric highs and filled shelf-proximal valleys (Figure 5.5 C). Inboard of the Queen Charlotte Fault, reflectors dipping steeply seaward are observed adjacent folded sub-horizontal reflectors (Figure 5.5 C). Steep reflectors trend towards horizontal at ∼250 ms. We interpret these reflectors as imaging a former shelf edge and perched apron deposit (e.g., Prather et al., 2012), which has been truncated by an unconformity near the seafloor. A second set of steep reflectors is imaged seaward and may represent another buried shelf edge.

Along the central segment of the shelf, seismic reflection profiles generally show evidence for sediment accumulation (Figure 5.4). North of the Chatham Sea Valley, in the transitional domain between the northern and central segments, three distinct buried shelf edges are observed in seismic profiles up to 7 km inboard of the present shelf-break (Figure 5.4 A).

At the outlet of the Sumner Sea Valley a mound with finely laminated seaward dipping reflectors is visible at the shelf edge (Figure 5.4 B). We interpret this feature to be an ice-contact fan associated with the terminus of a former glacial ice stream in the Sumner Sea Valley. Turbulent reflectors observed beneath the Sumner Sea Valley may reflect subglacial processes including soft-sediment deformation. South of the Sumner Sea Valley, erosional unconformities are rarely observed, with continuous reflectors seen to drape across the shelf-slope transition in many locations (Figure 5.4 C).

5.4.2 Submarine Channels on the Continental Slope

A total of 454 submarine channel networks were extracted from the shelf-break to 1000 mbsl (Figure 5.6). The drainage area of these networks varies from 0.2 to 157 km^2, with a median drainage area of 3 km^2. Net channel network lengths vary from 1.2 to 340 km, with a median network length of 7.6 km. Of the 454 mapped channel networks, 407 have a Strahler stream order (Strahler, 1957) >1 and 248 had channels with stream order >2.

Average channel thalweg gradient ranges from 3-29° (Figure 5.6). Gradient decreases with increasing stream order and is on average 2-30° for first order channels, 0-26° for second order channels, and 1-20° for third order and greater channels (Appendix A.4, Figure A.7). Similar trends in gradient are observed for each stream order south of the Chatham Sea Valley. For channel networks north of the Chatham Sea Valley, channel gradient decreases significantly when first order channels are excluded (Appendix A.4, Figure A.7). The lowest average gradients are observed at the outlets of the Chatham, Sumner, and Dixon sea valleys (Figure 5.6). Highest gradients are found offshore Haida Gwaii, Noyes Canyon, as well as locally offshore Baranof Island (Figure 5.6). High gradient channels offshore Haida Gwaii and adjacent Noyes Canyon are associated with lows in the seafloor expression of the Queen Charlotte Fault (Figure 5.6; Appendix A.4, Figure A.8).

We calculated θ for all mapped channel networks and found an average value of 0.18 ± 0.23 (Appendix A.4, Figure A.9). This value is consistent with prior work that suggests submarine channel θ values are consistently lower than the average value of 0.45 for subaerial channels

(Dobbs et al., 2019). Channel concavity is variable across the study area, with few clear spatial trends (Appendix A.4, Figure A.9). Using the mean value of 0.18 for θ, we calculated a normalized channel steepness, k_{sn}, for the channel networks (Appendix A.4, Figure A.10; Kirby & Whipple, 2012). This did not produce results significantly different from average channel gradient, suggesting that the normalization was ineffective. Because of this, as well as the lack of an empirical relationship between submarine channel gradient and catchment area, we chose to focus on average channel network gradient in place of k_{sn}.

Submarine Channel Network End-members

We identify four channel network end-members on the continental slope (Figure 5.7). Each is found in a characteristic tectonic and sedimentary environment along the margin. Channel networks with high sediment input, like those found at the outlets of the Chatham, Sumner, and Dixon sea valleys (Figure 5.6 B, D), are generally elongate, have low thalweg gradients, and often show low channel concavity values (θavg = 0.18 1σ = 0.18; Figure 5.7 A). Channel networks characterized by bedrock substrate and low sediment input, like those observed offshore central and southern Haida Gwaii (Figure 5.6 F, G, H), are steep, elongate, and have low concavities (θavg = 0.18 1σ = 0.26; Figure 5.7 B). Channel networks found on the Pacific plate, like those found offshore Baranof Island (Figure 5.6 A), generally have the greatest drainage density, are less elongate, and have higher concavities (θavg = 0.21 1σ = 0.21; Figure 5.7 C). Finally, some channel networks along the Queen Charlotte Fault are bisected by the fault itself (Figures 5.6, 5.7 D). These channel networks are frequently elongate to the south on the fault and have first order channels that are considerably steeper than higher order channels (Appendix A.4, Figure A.7). Where the channel network follows the Queen Charlotte Fault, thalweg gradient is low, resulting in a convexity in the longitudinal profile (θavg = 0.16 1σ = 0.18; Figure 5.7 D).

5.4.3 Along-strike Channel Network Observations

Continental slope channel gradient along the Queen Charlotte Fault is observed to correlate with proximity to sediment input, substrate, faulting, as well as deformation of the Pacific Plate adjacent the Queen Charlotte Fault. In the following section, we review observations of variable channel network morphology from north to south, highlighting areas where margin morphology shows a pronounced response to tectonics.

Continental Slope Channels North of the Chatham Sea Valley

Along the northern Queen Charlotte Fault submarine channels are slope-sourced and are often bisected by the fault or found exclusively on the Pacific Plate (Figure 5.6 A). Channel gradient is variable, reflecting disruption resulting from faulting as well as possible differences in substrate erodibility between the Pacific and North American plates. Along the northern-most portion of the continental slope, slope channels are seen to transit around seafloor obstructions on the Pacific Plate (Figure 5.8). Channels are steepest where they extend onto the North American Plate and decrease in slope when bypassing obstructions (Figure 5.8 B). Crescentic bedforms are observed in many of the channels along this region (Figure 5.8 A). Landslide scars are common here as well (Figure 5.8 A; Brothers et al., 2019). A shelf-proximal valley between a volcanic cone on the Pacific Plate and the shelf-break is unchannelized, potentially reflecting active sediment deposition (Figures 5.5 C, 5.8).

Continental Slope Channels Between the Chatham Sea Valley and Northern Haida Gwaii

Channels mapped between the Chatham and Sumner sea valleys generally have very low gradients and are slope-sourced (Figure 5.6 B). At the outlets of the sea valleys, channels form on top of sand fans (Dobson et al., 1998). Channels at the outlet of the Chatham Sea Valley and immediately south are entirely slope-sourced (Figure 5.9). The Queen Charlotte Terrace is uplifted in this area and forms a seaward sloping plateau with a steep western edge (Figure 5.9 A). Channels cross the Terrace, carving deep canyons into its western edge (Figure

5.9 B). Channels in these canyons show pronounced convexities and numerous knickpoints (Figure 5.9 B, C).

South of the Sumner Sea Valley, deformation in the Queen Charlotte Terrace becomes more broadly distributed west of the Queen Charlotte Fault (Figure 5.6 C; Trehu et al., 2015). As a result, uplift of the Pacific Plate adjacent the Queen Charlotte Fault is less pronounced, resulting in greater continental slope relief. Slope channel gradient is high in this region with both shelf-sourced and slope-sourced canyons. Noyes Canyon is the most prominent shelf-sourced canyon along this part of the continental slope (Figure 5.6 C-inset). Channels exiting the canyon turn to the north in order to bypass an uplifted pressure ridge on the Pacific Plate. From Noyes Canyon south, channels extend to the shelf-break. Channel gradients remain steep to the outlet of the Dixon Sea Valley.

At the outlet of the Dixon Sea Valley channel gradients are low and most channel networks are slope-sourced (Figure 5.6 D). Both the tectonic and sedimentary setting is similar to the outlets of the Chatham and Sumner sea valleys, with a sedimentary fan developing on and adjacent to an uplifted portion of the Queen Charlotte Terrace. Seismic reflection profiles across the Terrace indicate significant sediment accumulation (Trehu et al., 2015). In cases where channels do not over-top the terrace, they flow north to bypass the uplifted Pacific Plate.

Continental Slope Channels Offshore Northern Haida Gwaii

South from the Dixon Sea Valley and offshore northern Haida Gwaii, channels are significantly impacted by uplift of the Pacific Plate in the Queen Charlotte Terrace (Figure 5.6 E). Channel networks are frequently forced to elongate parallel to the Queen Charlotte Fault to bypass uplifted blocks in the Queen Charlotte Terrace. Periodic cross-cutting canyons serve as outlets for channels across the Terrace. Average channel gradient is low, reflecting the impact of channel elongation.

Along the southern-most portion of this region, a 42 km long uplifted block in the Queen Charlotte Terrace is observed to block slope channels, forcing them to re-route to cross-

cutting canyons north and south of the obstruction (Figures 5.6 E, 5.9). Slope channels flow perpendicular from the shelf edge to the Queen Charlotte Fault where they coalesce into a northern and southern trunk channel separated by a seafloor high (Figure 5.9). Channel gradient is highest near the shelf-break, decreasing to the fault-parallel channels. Numerous channel knickpoints, frequently associated with small pull-apart basins on the Queen Charlotte Fault, are observed in the channel network flowing south (Figures 5.9 B, 5.10). A subtle convexity is observed along the mainstem of the channels flowing north (Figures 5.9 B, 5.10).

Continental Slope Channels Offshore Central and Southern Haida Gwaii

Offshore central Haida Gwaii, channels steepen from the north to highs offshore Tasu Inlet, with gradient decreasing from the inlet, south (Figure 5.6 F). In the northern part of this region, channel substrate appears to be sediment and some channel networks are shelf-sourced. To the south, substrate transitions to a mixed bedrock-sedimentary slope and channels are slope-sourced. Faults along the southern part of the slope in this region disrupt channel networks, leading to channels with spatially variable gradient. Save channels draining sedimentary slopes in the north, channels are visible in the bathymetry up to the shelf-break.

A pressure ridge along the southern Queen Charlotte Fault uplifts the Pacific Plate and causes a decrease in the slope of submarine channels (Figure 5.6 G). Complicated deformation in this area results in small depocenters and abrupt changes in channel gradient. Channels in the northern part of this region bypass the pressure ridge by transiting north along-strike of the regional trend of the Queen Charlotte Fault. Channel networks situated adjacent the center of the pressure ridge carve cross-cutting valleys through the uplift.

Offshore Kunghit Island and southern-most Haida Gwaii, channel gradient is high and the shelf-sourced Kunghit Canyon extends to the 175 mbsl lowstand contour (Figure 5.6 H). Channels steepen south of Kunghit Canyon to the highest observed along the margin.

5.5 Discussion

Based on our analysis, we identify characteristic geomorphic responses to tectonics along the continental shelf and slope along the Queen Charlotte Fault. We begin by discussing our observations of the continental shelf in the context of regional tectonics. We then discuss along-strike submarine channel morphologies and their relationship to seafloor obstructions to flow on the Pacific Plate. We combine these analyses to develop a model for the geomorphic development of the Queen Charlotte margin.

5.5.1 Tectonic Controls on the Morphology of the Continental Shelf

Along-strike variation in the character of the continental shelf along the Queen Charlotte Fault is significantly influenced by tectonics. Specifically, our observations suggest that the North American plate along both the northern and southern segments of the shelf is actively deforming whereas the central segment is passively accumulating sediment. We interpret these trends to reflect both the young age of the plate margin along the northern segment as well as a higher convergence rate along the southern Queen Charlotte Fault. The accumulation of sediment along the central shelf segment may reflect efficient strain accomodation west of the Queen Charlotte Fault in the Pacific Plate.

The northern shelf segment lies adjacent the youngest section of the Queen Charlotte Fault, with Yakutat terrane passage occurring over the past ∼2 myr (Figure 4.4). As a result, this margin has had the least time to evolve geomorphically and largely retains a structurally controlled shelf break at the Queen Charlotte Fault (e.g., Helland-Hansen et al., 2012). Sediment is observed to accumulate locally (Figure 5.4 B), but the widespread presence of unconformities indicate much of this shelf segment is erosional (Figure 5.4 A, C). Furthermore, active faults in the North American Plate (Figure5.4 B; Walton et al., 2018), and volcanism adjacent Mt. Edgecumbe (Figure 5.2, 5.3), suggest interplate strain may not be fully localized on the Queen Charlotte Fault. This part of the margin is estimated to be in transtension (Brothers et al., 2020), which may explain growth folds and fanning reflectors in

a seismic reflection profile from the northern margin that indicate ongoing normal faulting in the North American Plate (Figure 5.4 B). Other explanations for deformation in the North American Plate could include the young age of the Queen Charlotte Fault relative to elsewhere along the margin and the recent passage of the Yakutat Terrane. Surveys of large-offset fault systems show a trend towards simplification with increasing cumulative slip (e.g., Perrin et al., 2016). Given that this part of the margin is newly developed, strain may not have fully localized on the Queen Charlotte Fault. Alternatively, faulting in the North American Plate could reflect ongoing adjustment to a change in boundary conditions following the passage of thickened oceanic crust in the Yakutat terrane. The transition from thickened crust to oceanic crust of regular thickness may have induced gravitational instability in the North American crust.

Deformation along the northern shelf segment is also directly linked to translation along the Queen Charlotte Fault. In numerous cases, the shelf has prograded onto the Pacific Plate (Figure 5.4 C), which causes it to be subsequently translated north. This dynamic has a lasting impact on the entire margin by producing shelf-proximal valleys which serve as sediment traps and present a barriers to sediment transport from the shelf to the deep ocean.

The continental shelf along the central segment shows evidence for sediment accumulation (Figures 5.2, 5.3, 5.5). This is a surprising observation given the overall transpressive nature of the plate boundary (DeMets & Merkouriev, 2016; Brothers et al., 2020), which would be predicted to lead to basin inversion on the North American Plate. It could be that convergence is fully accommodated by the Pacific Plate or far from the plate boundary in the North American Plate, allowing subsidence at the shelf edge. The Queen Charlotte Terrace is observed along much of this part of the margin and seismicity suggests it is actively deforming (Figure 5.2; Walton et al., 2019). If convergence is fully accommodated by the Pacific Plate adjacent the central shelf segment, North American Plate subsidence and sediment accumulation could occur despite regional transpression.

The morphology of the continental shelf along the southern segment is the product of

tectonically driven uplift of the North American margin. Uplift near the continental margin results in a steep and narrow continental shelf with exposed basement which reflects the balance between tectonically driven rock uplift and downcutting due to wave base erosion (e.g., Anderson et al., 1999). High rock uplift rates adjacent the shelf edge is shown by the exceedingly narrow and shallow shelf adjacent a 740 m high mountain peak north of Tasu Inlet, Haida Gwaii (Figure 5.3 C). Without high uplift rates, wave erosion would drive landward retreat of the shoreline and widening of the shelf as well as downcutting of the shelf-break. This region was host to a 2012 Mw 7.8 thrust earthquake which may reflect Pacific Plate underthrusting beneath North America (Figure 5.3 C; Lay et al., 2013), and interplate convergence rates up to 2.2 cm yr^{-1} are estimated here (DeMets & Merkouriev, 2016). Steady, moderate exhumation rates exceeding 0.2 mm yr^{-1} estimated from low-temperature thermochronometry on Haida Gwaii (Schoettle-Greene et al., 2020), further suggest this shelf segment is uplifting.

5.5.2 Tectonic and Sediment Input Controls on the Morphology of Continental Slope Channels

Continental slope channels along much of the margin show evidence for morphologic evolution in response to tectonic perturbation and sediment input. Tectonic influence is most clear when slope channel networks are directly cross-cut by the Queen Charlotte Fault (Figures 5.7 D, 5.8), however, seafloor obstructions to flow formed in response to uplift in the Queen Charlotte Terrace also significantly affect channel morphology (Figures 5.6, 5.10). In both cases, a reduction in channel gradient is seen as a result of elongation along the fault or around obstructions (Figures 5.7 D, 5.11). This likely leads to a reduction in the sediment transport capacity of channels and sediment aggradation. In cases where channels overtop the Queen Charlotte Terrace (Figure 5.9), they may be further perturbed by continued uplift of the Terrace. This may explain the channel profile convexity and distinct knickpoints observed in channels that flow over the terrace south of the Chatham Sea Valley (Figure 5.9).

At a margin-wide scale, gradient of continental slope submarine channel networks is

highest along the southern Queen Charlotte Fault and lowest at the outlets of shelf sea valleys (Figure 5.6). High gradient channel networks and shelf-sourced canyons are often associated with areas where the seafloor expression of the Queen Charlotte Fault is mapped at depths > 2 kmbsl. These deep reaches contrast with the frequently shallow surface expression of the Queen Charlotte Fault along strike (Figure 5.6; Appendix A.4, Figure A.8). Analog models of slope channel development suggest channels grade to changes in base level by steepening and headward erosion into the continental shelf (Lai et al., 2016). The coincidence of shelf-sourced canyons and high gradient channel networks with deeper surface expression of the Queen Charlotte Fault may reflect the importance of the fault in setting base level (Figure 5.6). In contrast, high rates of sediment input from tidewater glaciers at the outlets of sea valleys may result in largely aggradational channel systems which could overwhelm a fault-defined base level. Overtopping of the Queen Charlotte Terrace is frequently observed in these regions (Figures 5.6, 5.9).

The complex interplay between along-fault transport of seafloor obstructions and channel networks is an intriguing facet of the morphology of this margin (Figures 5.8, 5.10, 5.11). Northward translation of obstructions appear to result in migrating waves of sedimentation and erosion as channels are variably elongated and shortened (e.g., Figures 5.8, 5.10), similar to field observations (e.g., Walker & Allen, 2012) and numerical models (e.g., Goren et al., 2014; Duvall & Tucker, 2015; Harbert et al., 2018; Reitman et al., 2019) of terrestrial rivers. In the context of the Queen Charlotte Fault, where relative plate motion is upwards of 5 cm yr^{-1} (Demets and Merkouriev, 2016; Brothers et al., 2020), the rate of tectonic surface advection is far greater than submarine geomorphic processes during sea level highstands. Only during lowstands are channels active in a significant way (Brothers et al., 2018; Greene et al., 2018; Barrie et al., 2021), which means that the geomorphic evolution of the continental slope occurs over relatively short periods of time following 4-5 km of northward Pacific Plate translation. The punctuated nature of submarine geomorphic processes together with high rates of tectonic deformation results in a persistent state of submarine channel disequilibrium along the Queen Charlotte Fault.

5.5.3 A Model for the Morphological Development of the Continental Shelf and Slope Along the Queen Charlotte Fault

To summarize our observations, we present a conceptual model for the morphological development of the continental shelf and slope along the Queen Charlotte Fault (Figure 5.12). This model specifically focuses on the interaction between slope channels, barriers to flow, and progradation of the continental shelf. It is applicable to obstructions at the scale of translating seafloor ridges a kilometer in length with tens of meters of relief to crustal block uplifts tens of kilometers in length with hundreds of meters of relief in the Queen Charlotte Terrace.

As a starting condition, we envision a shelf and slope in a state of quasi-equilibrium where slope channels drain across the Queen Charlotte Fault with minor perturbation (Figure 5.12 A). If there is seafloor uplift on the Pacific Plate side of the fault or the translation of seafloor topography along the fault, slope channels may be deflected (Figure 5.12 B). Deflection will be dependent on the rate at which the obstruction grows and the erosive power of the submarine channel, in a manner equivalent to a rivers response to a growing fold (Burbank et al., 1996). Channel elongation to bypass these features results in a decrease in gradient and the onset of sediment deposition in a slope-proximal valley (Figure 5.12 B). This deposition will increase the slope of the seafloor in the direction of channel elongation, resulting in channels that run along strike of the fault to the edge of the seafloor obstruction. If uplift continues and/or barriers continue to be translated along the fault, channels may be completely obstructed, resulting in further sediment deposition (Figure 5.12 C).

Following the development of a seafloor obstruction to slope channels, we identify two end-member scenarios that reflect the interplay between sediment input and transport capacity around obstructions. When sediment supply far exceeds sediment transport capacity, the slope-proximal valley will fill with sediments and overtop in a manner equivalent to basin fill-and-spill (Figure 5.12 D; e.g., Sinclair & Tomasso, 2002). This can promote shelf progradation across the fault, resulting in shelf fragments that are translated along the fault.

Additionally, channel networks will be exclusive to the Pacific Plate given this scenario. Both Pacific Plate channels and shelf fragments are observed along much of the margin north of Noyes Canyon and channels are seen to overtop the Queen Charlotte Terrace at the outlet of the Dixon Sea Valley (Figures 5.2, 5.6). This is likely also the morphological pathway taken by the continental shelf and slope adjacent the Chatham Sea Valley, where the shelf-break is mapped on the Pacific Plate and channels overtop the Queen Charlotte Terrace (Figure 5.9). Furthermore, seismic reflection profiles across the northern Queen Charlotte Fault show shelf-proximal valleys that are in the process of being filled (Figure 5.4 B) as well as ones completely filled with sediment (Figure 5.4 C).

As an alternative, low sediment input or sufficient transport capacity of sediment will prevent infilling of the slope-proximal valley (Figure 5.12 E). Low sediment input will decrease the rate of valley infilling and, if sufficiently low, may never result in obstruction overtopping. Channel transport capacity may be increased if deflected slope channels are captured by canyons that cross-cut the seafloor obstruction. The resulting drop in channel base-level and concomitant increase in gradient will drive incision into sediments deposited during channel obstruction (Figure 5.12 E). Incision may manifest morphologically as knickpoints in the longitudinal profiles of channels. While channel deflection offshore Haida Gwaii provides the best example of this scenario (Figure 5.10), the process of fault-parallel channel elongation and capture is observed along much of the northern Queen Charlotte Fault (Figure 5.8), indicating this end-member may be the norm away from the Chatham, Sumner, and Dixon sea valleys, which serve as large point-sources of coarse-grained sediment.

This model helps explain the persistent co-location of the Queen Charlotte Fault and shelf edge from the Chatham Sea Valley, north. The youthfulness of this part of the margin (<5 myr; Figure 4.4), coupled with increased sediment input with the onset of Cordilleran Ice Sheet development at 2.8 Ma (Sánchez-Montes et al., 2020; Zhang & Gulick, 2020), has prevented significant headward erosion of slope channels into North America. Even in cases where headward erosion has occurred, northward translation of seafloor barriers to North American slope channels has promoted the progradation of the shelf and burial of

these channels. This process is actively occurring along the northernmost part of the margin where an infilling shelf-proximal valley is observed (Figures 5.4 B, 5.8), and evident in seismic reflection profiles crossing parts of the continental shelf that extend onto the Pacific Plate (Figure 5.4 C). ten Brink et al. (2018) previously suggested that increased sediment input was responsible for the shallow seafloor expression of the Queen Charlotte Fault in this region. Here, we build on this hypothesis by presenting a model that links slope channel deformation with shelf-forming processes and the shallowing of the Queen Charlotte Fault.

5.6 Conclusions

An analysis of the continental shelf edge and slope along the Queen Charlotte Fault reveals a primary tectonic imprint on the geomorphology of this margin. The depth of the shelf-break is seen to relate to deformation rates at the North American Plate edge, with a shallow shelf-break and eroded shelf edge observed offshore Haida Gwaii and a shallow, internally deformed, shelf offshore northern Baranof Island. This contrasts with the deep shelf-break and active sediment accumulation observed along much of the central Queen Charlotte Fault. Together, these observations indicate strain is accommodated within the North American Plate along the northern and southern Queen Charlotte Fault but not along the Central Queen Charlotte Fault. This may reflect both transpression as well as the age of the plate boundary.

Continental slope channels are indirectly influenced by variations in strain accommodation through obstructions to flow resulting from deformation of the Pacific Plate. Submarine channel gradient is decreased as channels are forced to bypass seafloor obstructions which results in sediment deposition and may lead to the progradation of the continental shelf. In cases where sediment supply is low, the rate of channel adjustment may be slower that the rate of base level change, resulting in the preservation of channels in the process of regrading to tectonically determined boundary conditions. Together, these observations show that transpression along the Pacific-North America plate boundary results in a persistent state of submarine landscape disequilibrium.

5.7 Figures and Tables

	mean shelf-break depth (m)	**1σ (m)**	**median (m)**	**mean distance to QCF (km)**	**1σ (km)**	**median (km)**
Full Margin	225	29	221	8.6	8.1	7.4
North	220	30	213	1.7	1	1.6
Central	240	26	239	11.4	10	10.5
South	213	26	213	9.5	5.8	7.9
	mean shelf width (km)	**1σ (km)**	**median (km)**	**mean slope (°)**	**1σ (°)**	**median (°)**
Shoreline						
Full Margin	21.5	16.4	20	1.79	2.36	0.63
North	21.1	4.2	21	0.61	0.11	0.59
Central	40.2	6.2	39.4	0.35	0.06	0.34
South	5.4	4.6	3.9	3.60	2.70	3.06
Lowstand						
Full Margin	8.4	9.7	4.6	1.25	2.68	0.56
North	5.4	3.8	5.3	0.55	1.40	0.43
Central	17.9	9.6	16	0.27	0.17	0.21
South	1.4	2.1	0.8	2.42	3.65	2.32

Table 5.1: Shelf and shelf-break measurements

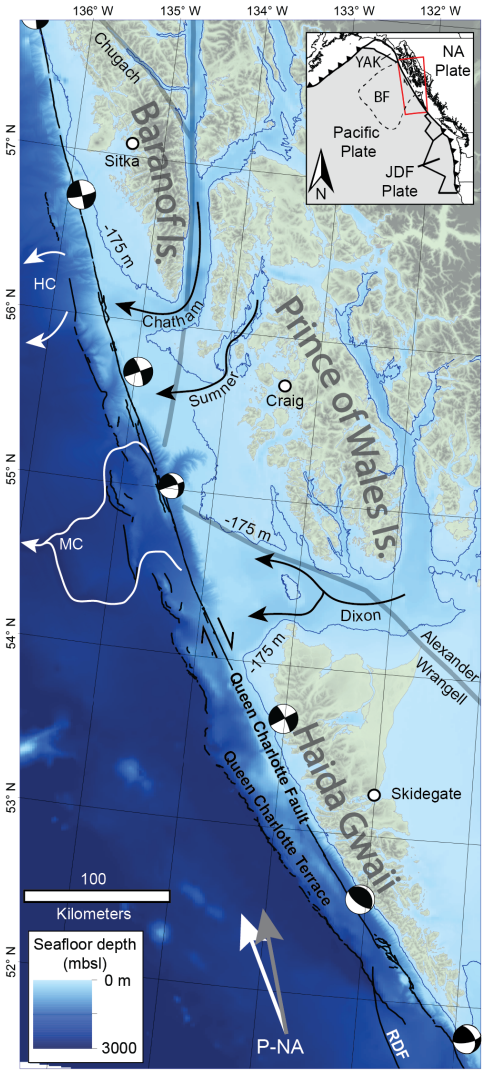

Figure 5.1: The study region, encompassing the Pacific-North American continental margin from 51.5-58° N. The three major island chains, Baranof, Prince of Wales, and Haida Gwaii, are underlain by the Chugach, Alexander, and Wrangell terranes, respectively. The Queen Charlotte Fault defines the plate boundary. Faults associated with the Queen Charlotte Terrace are found west of the Queen Charlotte Fault. Estimated sea level lowstand is marked with blue line. Pacific-North America relative plate motion vectors for Demets and Merkouriev 2016 (grey) and Brothers et al., 2020 (white). YAK – Yakutat terrane; NA – North America; JDF – Juan De Fuca Plate; BF – Baranof Fan; HC – Horizon Channel; MC – Mukluk Channel; P – Pacific Plate; RDF – Revere-Delwood Fault.

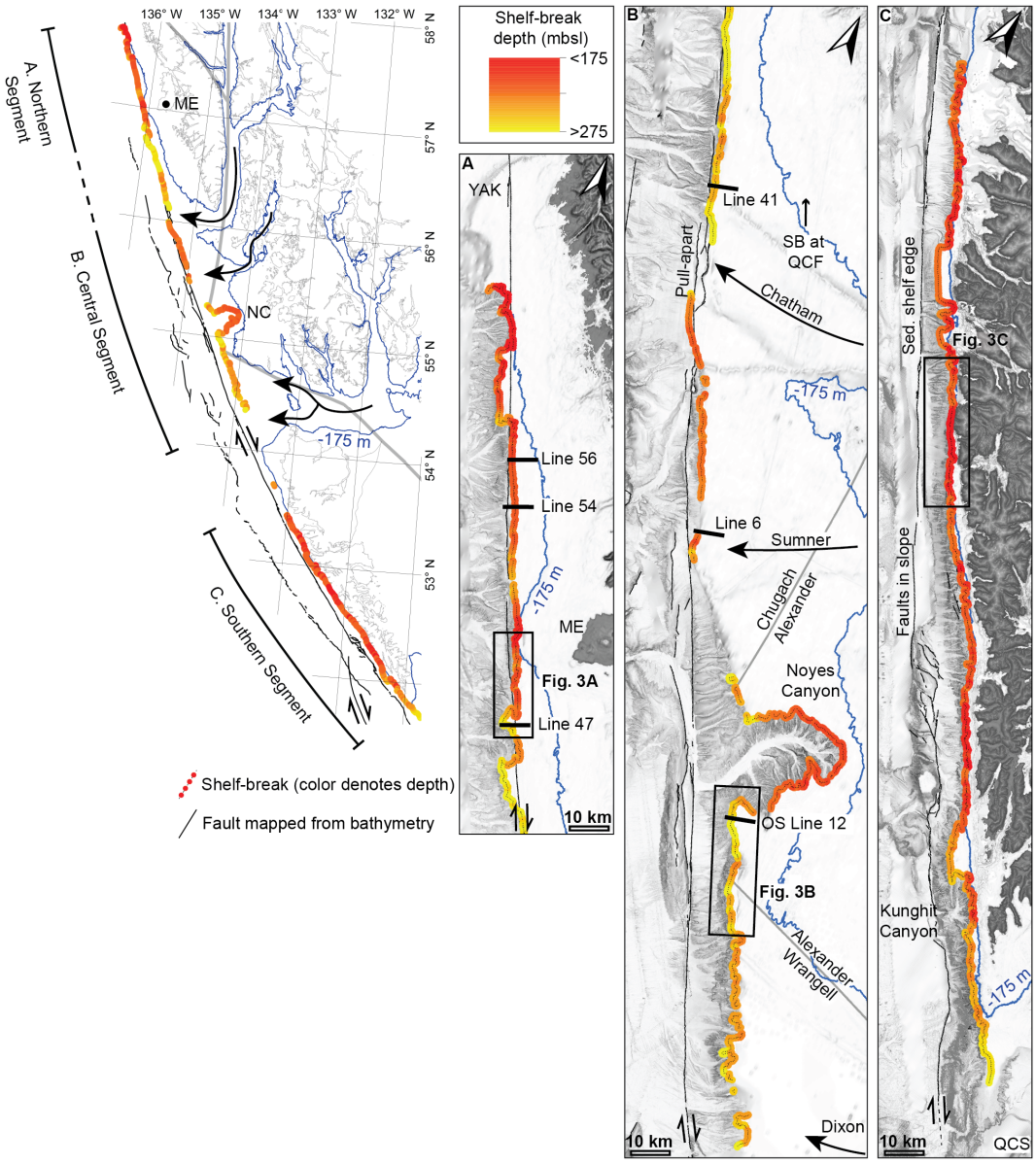

Figure 5.2: Depth of mapped shelf-break along the Queen Charlotte Fault. Overview map shows interpreted segments of the margin. Large arrows show locations of major continental shelf sea valleys. Panels A, B, and C show the northern, central, and southern segments, respectively. Seismic profile locations for figures 5.4 and 5.5 are labeled in panels A and B. Thick grey line marks terrane boundaries. Thin black lines mark faults mapped from bathymetry. NC – Noyes Canyon; ME – Mt. Edgecumbe; SB – Shelf-break; QCS – Queen Charlotte Sound; YAK – Yakutat terrane.

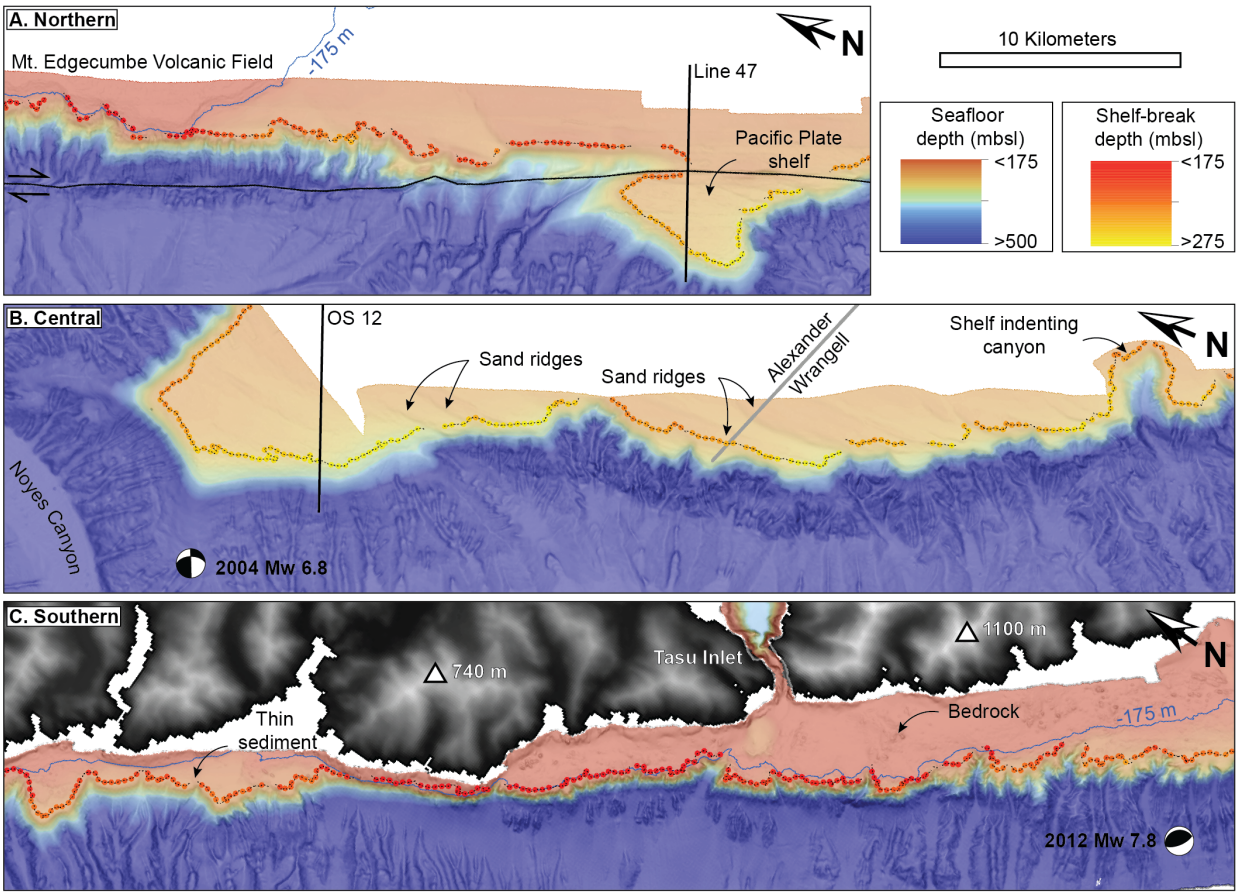

Figure 5.3: Characteristic shelf edge segments along the Queen Charlotte Fault. Depth of shelf-break drawn as colored dots on dashed line. (A) The shelf offshore norther Baranof Island. Tracks of seismic lines shown in Figure 5.4 shown. (B) The shelf offshore Prince of Wales Island. The focal mechanism for the 2004 Noyes Canyon (NC) earthquake is shown. Grey lines show terrane boundaries. (C) The shelf offshore Haida Gwaii. The focal mechanism for the 2012 Haida Gwaii earthquake is shown. Refer to Figure 5.2 for locations. All plots are parallel to the Queen Charlotte Fault.

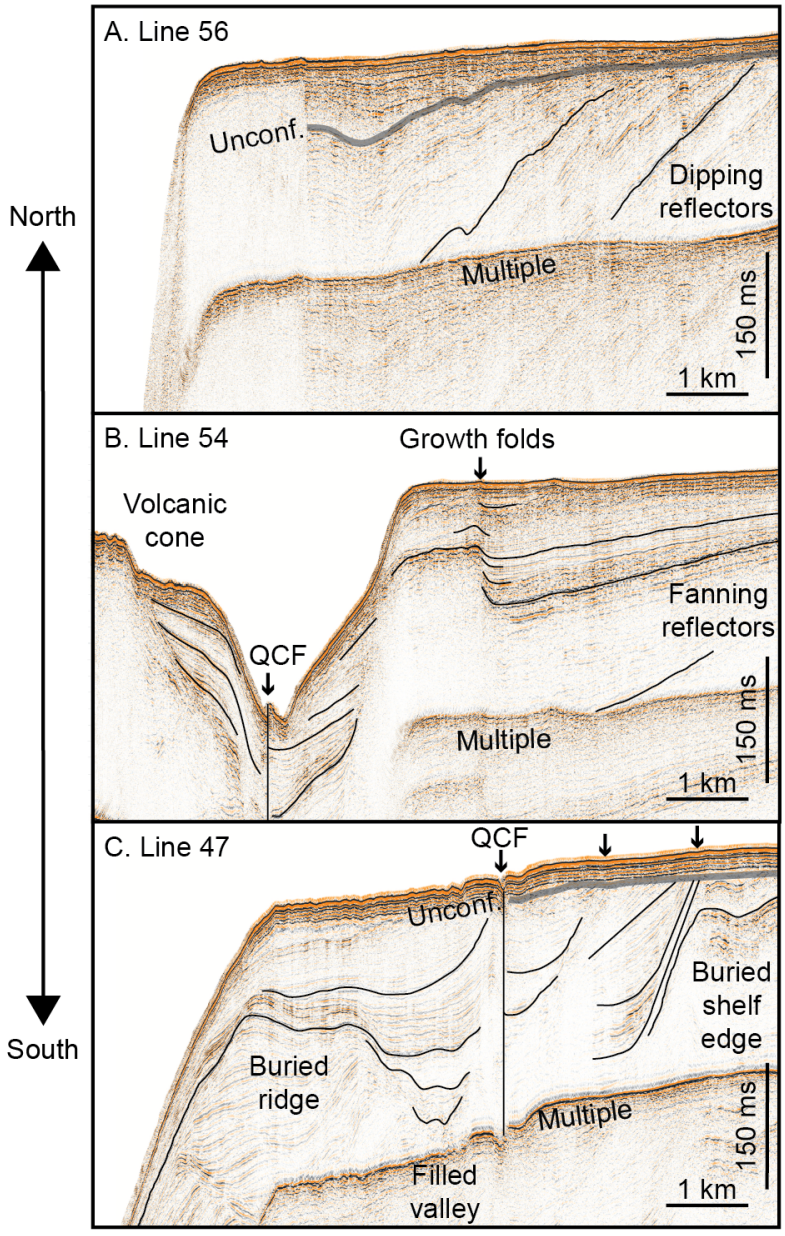

Figure 5.4: Multichannel seismic profiles from northern segment shelf edges. Arrows landward of the QCF in panel C point to truncated continental slope deposits.

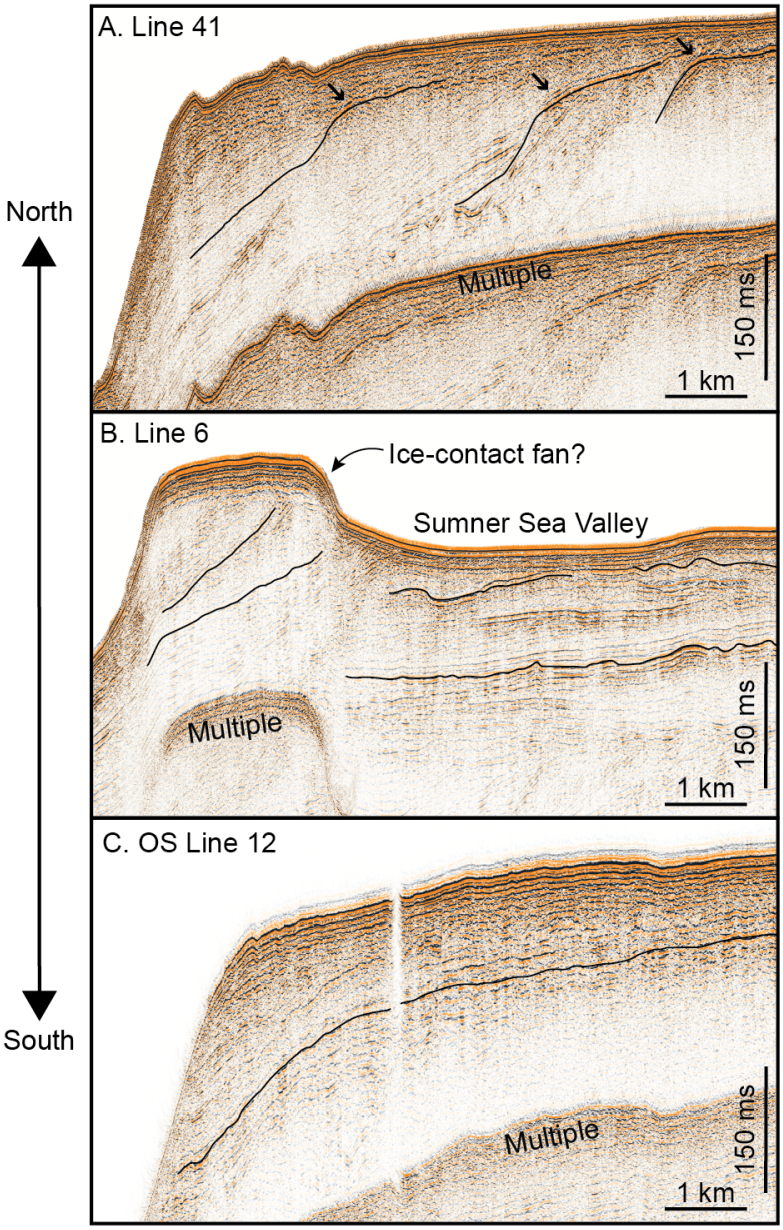

Figure 5.5: Multichannel seismic profiles from central segment shelf edges.

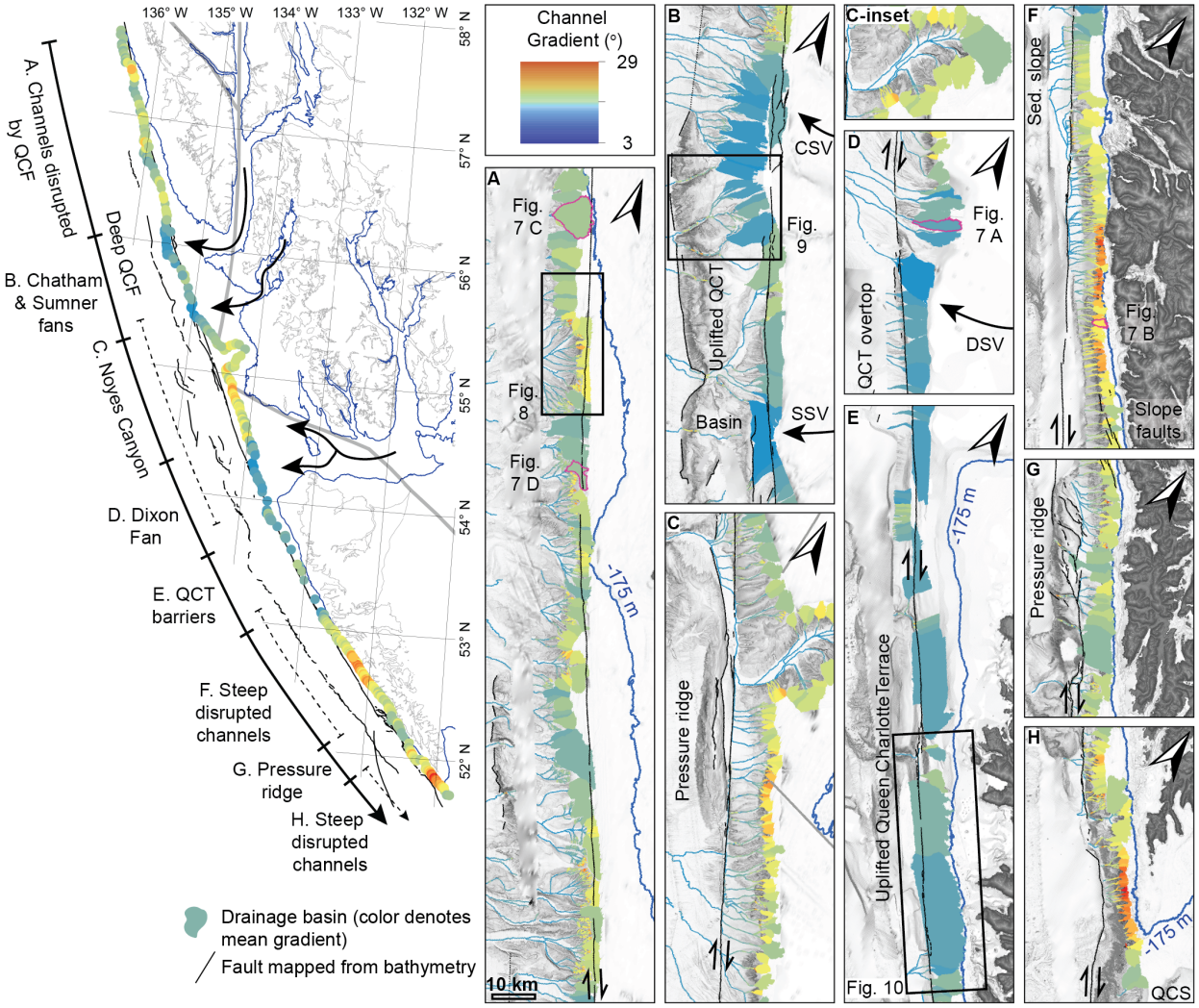

Figure 5.6: Average submarine channel gradient for channel networks mapped on the continental slope overlain on simplified tectonic and geographic map. Large arrows show locations of major continental shelf sea valleys. Panels A-H show subsections of continental slope channel networks from north to south. QCT – Queen Charlotte Terrace; QCS – Queen Charlotte Sound; CSV – Chatham Sea Valley; SSV – Sumner Sea Valley; DSV – Dixon Sea Valley.

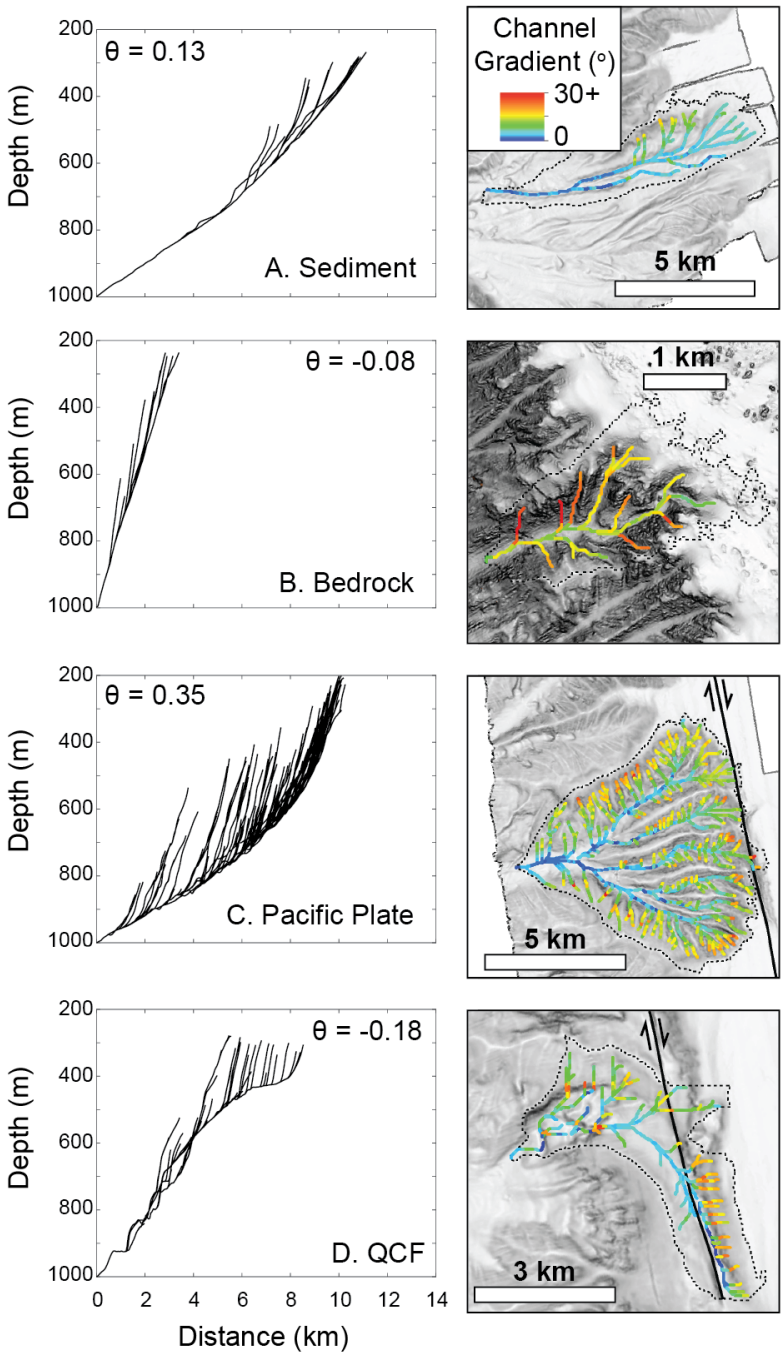

Figure 5.7: Plan and profile view of channel network end members on the Queen Charlotte Fault margin. North American Plate channel end-members: (A) sediment dominated end member, (B) bedrock dominated end-member. (C) Pacific Plate end-member. (D) Queen Charlotte Fault end-member. Refer to Figure 5.6 for locations.

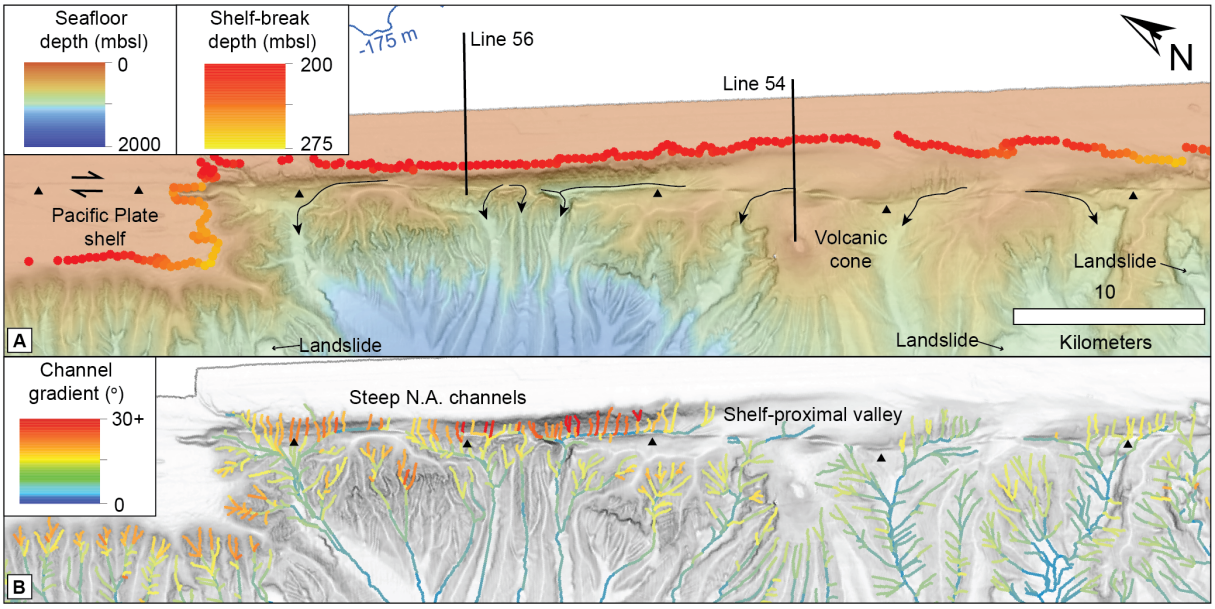

Figure 5.8: Interaction between the northern Queen Charlotte Fault and slope channels. (A) Bathymetry and shelf-break depth. Channel routing around obstructions on the Pacific Plate shown with arrows. Triangles point to surface expression of the Queen Charlotte Fault. Multichannel seismic lines from Figure 5.5 are marked. (B) Gradient of channel networks overlain on a slope map for the same area. Refer to Figure 5.6 A for locations.

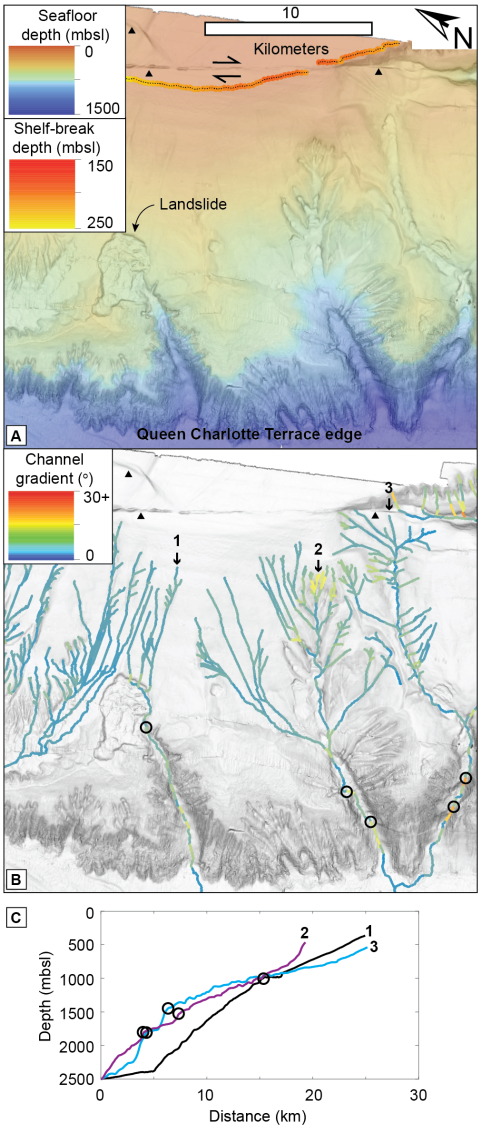

Figure 5.9: Location south of the Chatham Sea Valley where the Queen Charlotte Terrace is over-topped by submarine channels. (A) Bathymetry and shelf-break depth. Triangles point to scarp marking surface expression of the Queen Charlotte Fault. (B) Gradient of channel networks overlain on a slope map for the same area. Knickpoints are marked with open circles and black arrows point to channels plotted in panel C. (C) Longitudinal profiles of channels draining across the Queen Charlotte Terrace. Refer to Figure 5.6 B for location.

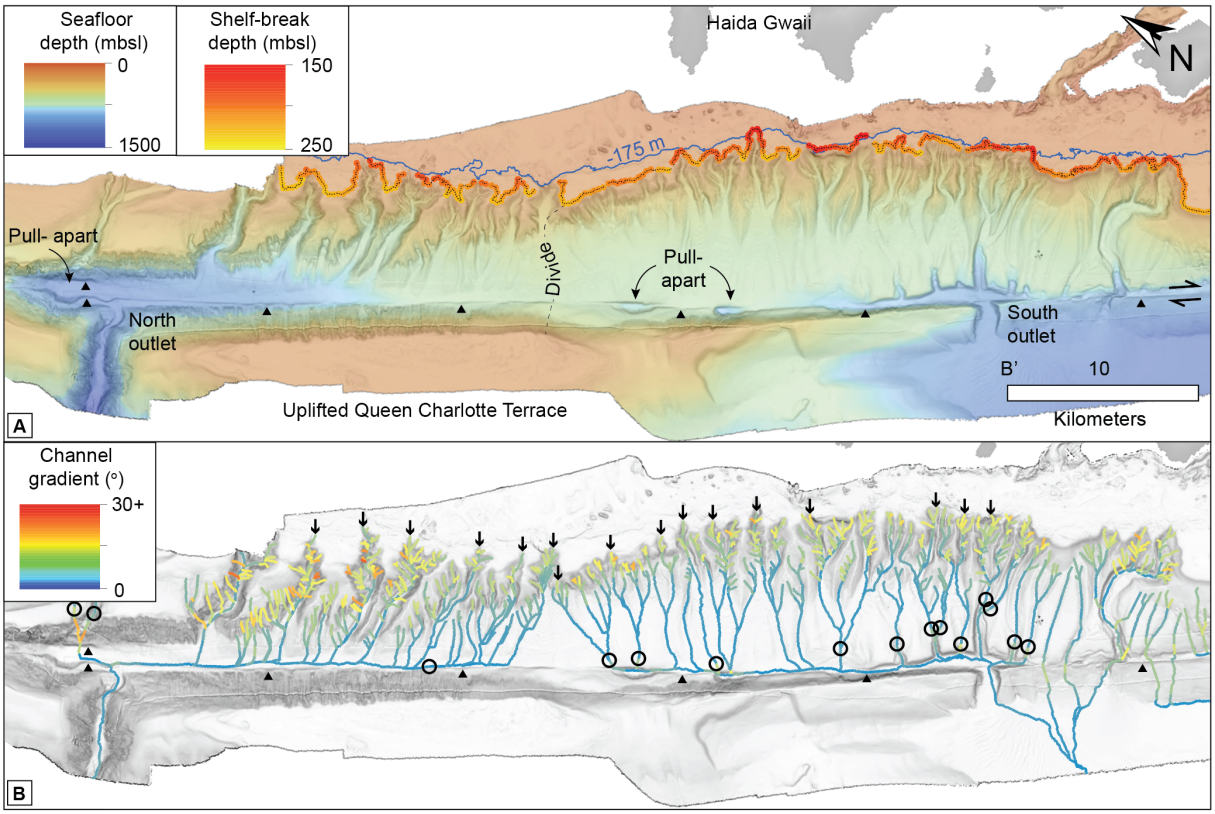

Figure 5.10: Location offshore southern Graham Island, Haida Gwaii where the uplifted Queen Charlotte Terrace blocks channel networks at the Queen Charlotte Fault. (A) Bathymetry and shelf-break depth with the 175 mbsl lowstand contour. Triangles point to surface expression of the Queen Charlotte Fault. (B) Gradient of channel networks overlain on a slope map for the same area. Knickpoints are marked with open circles and black arrows point to channels plotted in Figure 5.10. Refer to Figure 5.6 E for location.

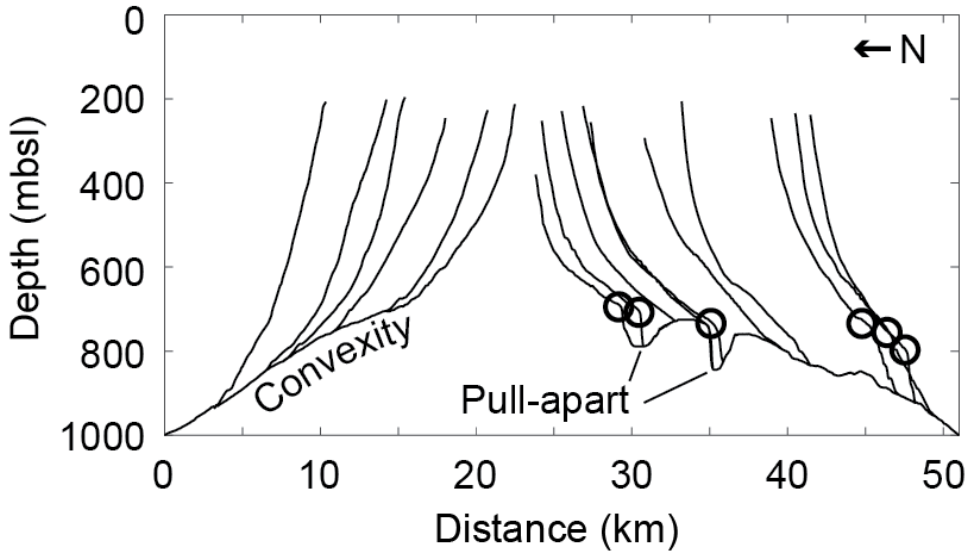

Figure 5.11: Longitudinal profile of channel networks that bypass the Queen Charlotte Terrace offshore southern Graham Island, Haida Gwaii. Knickpoints are marked with open circles.

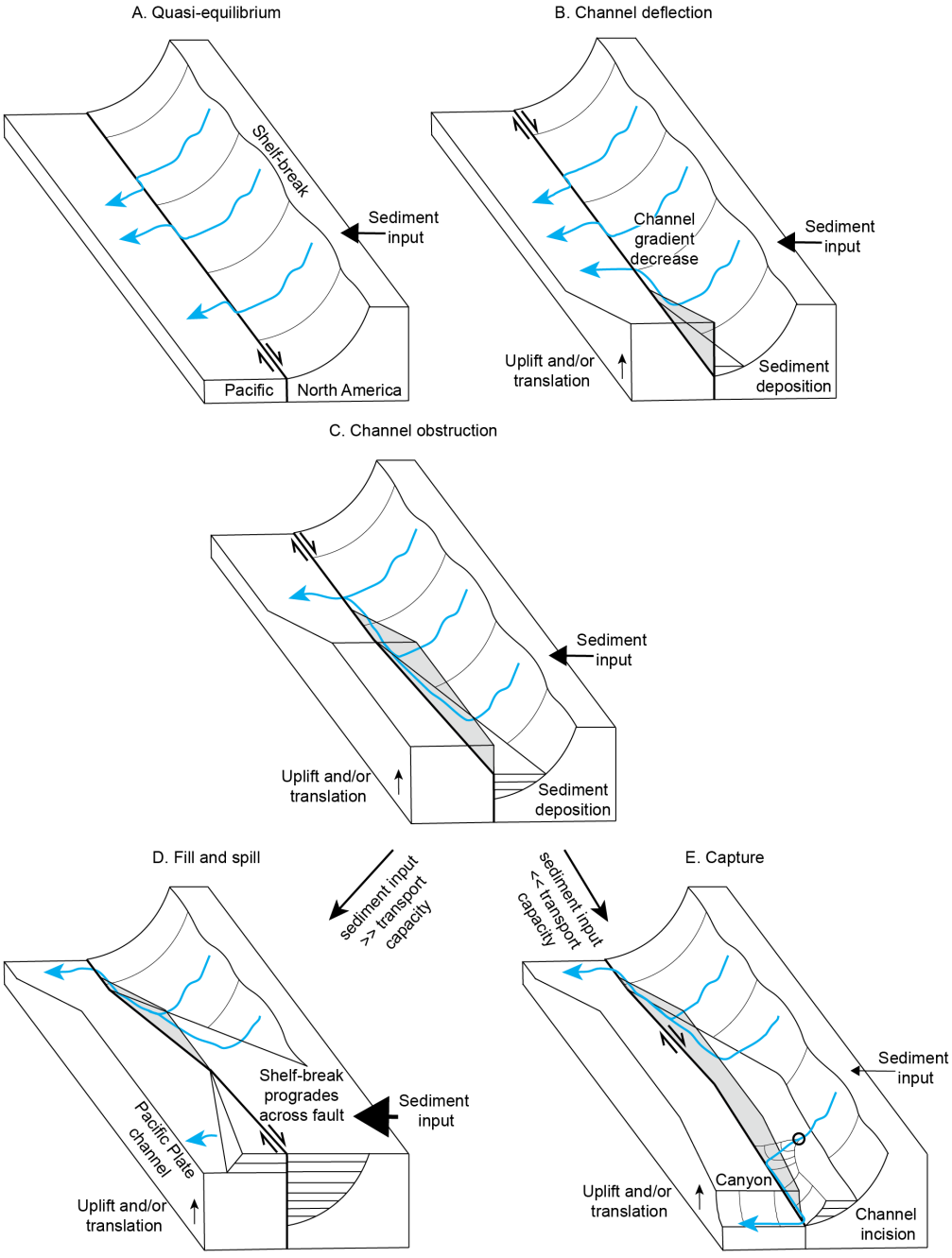

Figure 5.12: Cartoon depicting a model for the geomorphic development of the continental shelf and slope in response to barriers to flow along the Queen Charlotte Fault. Knickpoint location is marked with an open circle.

REFERENCES

Adams, E. W., & Schlager, W. (2000). Basic Types of Submarine Slope Curvature. *Journal of Sedimentary Research*, *70*(4), 814–828.

Addison, J. A., Beget, J. E., Ager, T. A., & Finney, B. P. (2010). Marine tephrochronology of the Mt. Edgecumbe Volcanic Field, Southeast Alaska, USA. *Quaternary Research*, *73*(2), 277–292.

Allen, J. (1991). The case of the inverted auriferous paleotorrent – exotic quartzite gravels on Wallowa Mountain peaks. *Oregon Geology*, *53*(5), 104–107.

Anderson, R., Densmore, A., & Ellis, M. (1999). The generation and degradation of marine terraces. *Basin Research*, *11*(1), 7–19.

Ault, A. K., Flowers, R. M., & Bowring, S. A. (2013). Phanerozoic surface history of the Slave craton. *Tectonics*, *32*(5), 1066–1083.

Ault, A. K., Gautheron, C., & King, G. E. (2019). Innovations in (U–Th)/He, Fission Track, and Trapped Charge Thermochronometry with Applications to Earthquakes, Weathering, Surface-Mantle Connections, and the Growth and Decay of Mountains. *Tectonics*, *38*(11), 3705–3739.

Barrie, J. V., & Conway, K. W. (2002). Rapid sea-level change and coastal evolution on the Pacific margin of Canada. *Sedimentary Geology*, *150*(1-2), 171–183.

Barrie, J. V., & Conway, K. W. (2013). Palaeogeographic Reconstruction of Hecate Strait British Columbia: Changing Sea Levels and Sedimentary Processes Reshape a Glaciated Shelf. In M. Z. Li, C. R. Sherwood, & P. R. Hill (Eds.), *Sediments, Morphology and Sedimentary Processes on Continental Shelves* (pp. 29–46). Chichester, West Sussex, UK: John Wiley & Sons, Ltd.

Barrie, J. V., Greene, H. G., Conway, K. W., & Brothers, D. S. (2021). Late Quaternary

sea level, isostatic response, and sediment dispersal along the Queen Charlotte fault. *Geosphere*, *17*(2), 375–388.

Beeson, M. H., & Tolan, T. L. (1990). The Columbia River Basalt Group in the Cascade Range: A Middle Miocene reference datum for structural analysis. *Journal of Geophysical Research*, *95*(B12), 19547.

Bindeman, I. N., Greber, N. D., Melnik, O. E., Artyomova, A. S., Utkin, I. S., Karlstrom, L., & Colón, D. P. (2020). Pervasive Hydrothermal Events Associated with Large Igneous Provinces Documented by the Columbia River Basaltic Province. *Scientific Reports*, *10*(1), 10206.

Bird, P. (1979). Continental delamination and the Colorado Plateau. *Journal of Geophysical Research: Solid Earth*, *84*(B13), 7561–7571.

Blackwell, D. D., Steele, J. L., Kelley, S., & Korosec, M. A. (1990). Heat flow in the state of Washington and thermal conditions in the Cascade Range. *Journal of Geophysical Research*, *95*(B12), 19495.

Blakely, R. J., Sherrod, B. L., Weaver, C. S., Wells, R. E., & Rohay, A. C. (2014). The Wallula fault and tectonic framework of south-central Washington, as interpreted from magnetic and gravity anomalies. *Tectonophysics*, *624-625*, 32–45.

Blakely, R. J., Sherrod, B. L., Weaver, C. S., Wells, R. E., Rohay, A. C., Barnett, E. A., & Knepprath, N. E. (2011). Connecting the Yakima fold and thrust belt to active faults in the Puget Lowland, Washington. *Journal of Geophysical Research: Solid Earth*, *116*(B7).

Botros, M., & Johnson, H. P. (1988). Tectonic evolution of the Explorer-Northern Juan de Fuca Region from 8 Ma to the present. *Journal of Geophysical Research: Solid Earth*, *93*(B9), 10421–10437.

Brandon, M. (2002). DECOMPOSITION OF MIXED GRAIN AGE DISTRIBUTIONS USING BINOMFIT. *On Track*, 6.

Braudy, N., Gaschnig, R. M., Wilford, D., Vervoort, J. D., Nelson, C. L., Davidson, C., ... Tikoff, B. (2017). Timing and deformation conditions of the western Idaho shear zone,

West Mountain, west-central Idaho. *Lithosphere*, *9*(2), 157–183.

Braun, J. (2002). Estimating exhumation rate and relief evolution by spectral analysis of age-elevation datasets. *Terra Nova*, *14*(3), 210–214.

Braun, J., Robert, X., & Simon-Labric, T. (2013). Eroding dynamic topography. *Geophysical Research Letters*, *40*(8), 1494–1499.

Braun, J., Simon-Labric, T., Murray, K. E., & Reiners, P. W. (2014). Topographic relief driven by variations in surface rock density. *Nature Geoscience*, *7*(7), 534–540.

Bringhurst, R. (2000). *A story as sharp as a knife: The classical Haida mythtellers and their world*. Douglas and McIntryre.

Brocher, T. M., Wells, R. E., Lamb, A. P., & Weaver, C. S. (2017). Evidence for distributed clockwise rotation of the crust in the northwestern United States from fault geometries and focal mechanisms: Clockwise Rotation in the NW US. *Tectonics*, *36*(5), 787–818.

Brothers, D. S., Andrews, B. D., Walton, M. A. L., Greene, H. G., Barrie, J. V., Miller, N. C., ... Conrad, J. E. (2019). Slope failure and mass transport processes along the Queen Charlotte Fault, southeastern Alaska. *Geological Society, London, Special Publications*, *477*(1), 69–83.

Brothers, D. S., Miller, N. C., Barrie, J. V., Haeussler, P. J., Greene, H. G., Andrews, B. D., ... Dartnell, P. (2020). Plate boundary localization, slip-rates and rupture segmentation of the Queen Charlotte Fault based on submarine tectonic geomorphology. *Earth and Planetary Science Letters*, *530*, 115882.

Brothers, D. S., ten Brink, U. S., Andrews, B. D., Chaytor, J. D., & Twichell, D. C. (2013). Geomorphic process fingerprints in submarine canyons. *Marine Geology*, *337*, 53–66.

Bruns, T. R. (1988). *Petroleum geology and hydrocarbon plays of the Gulf of Alaska onshore province: A report for the National Hydrocarbon assesment program* (Tech. Rep. No. 88-450J). USGS.

Bruns, T. R., Stevenson, A., & Dobson, M. (1992). *Gloria investigation of the exclusive economic zone in the Gulf of Alaska and off Southeast Alaska: M/V Farnella cruise F7-89-GA, June 14-July 13, 1989* (Open-File Report No. 92-317).

Burbank, D., & Anderson, R. S. (2011). Introduction to Tectonic Geomorphology. In *Tectonic Geomorphology* (pp. 1–16). John Wiley & Sons, Ltd.

Burbank, D., Meigs, A., & Brozović, N. (1996). Interactions of growing folds and coeval depositional systems. *Basin Research*, *8*(3), 199–223.

Burkett, E., & Gurnis, M. (2013). Stalled slab dynamics. *Lithosphere*, *5*(1), 92–97.

Burns, E., Morgan, D., Peavler, R., & Kahle, S. (2011). *Three-dimensional model of the geologic framework for the Columbia Plateau regional aquifer system, Idaho, Oregon, and Washington* (USGS Scientific Investigations Report).

Burns, E., Williams, C. F., Ingebritsen, S. E., Voss, C. I., Spane, F. A., & Deangelo, J. (2015). Understanding heat and groundwater flow through continental flood basalt provinces: Insights gained from alternative models of permeability/depth relationships for the Columbia Plateau, USA. , 19.

Camp, V. (1995). Mid-Miocene propagation of the Yellowstone mantle plume head beneath the Columbia River basalt source region. , 4.

Camp, V., & Hanan, B. B. (2008). A plume-triggered delamination origin for the Columbia River Basalt Group. *Geosphere*, *4*(3), 480.

Camp, V., & Hooper, P. R. (1981). Geologic studies of the Columbia Plateau: Part I. Late Cenozoic evolution of the southeast part of the Columbia River Basalt Province. *GSA Bulletin*, *92*(9), 659–668.

Campbell, N. P. (1989). Structural and stratigraphic interpretation of rocks under the Yakima fold belt, Columbia Basin, based on recent surface mapping and well data. In *Volcanism and Tectonism in the Columbia River Flood-Basalt Province* (Vol. 239).

Carlson, R. J., & Baichtal, J. F. (2015). A Predictive Model for Locating Early Holocene Archaeological Sites Based on Raised Shell-Bearing Strata in Southeast Alaska, USA. *Geoarchaeology*, *30*(2), 120–138.

Carrara, P. E., Ager, T. A., & Baichtal, J. F. (2007). Possible refugia in the Alexander Archipelago of southeastern Alaska during the late Wisconsin glaciation. *Canadian Journal of Earth Sciences*, *44*(2), 229–244.

Castellanos, J. C., Perry-Houts, J., Clayton, R. W., Kim, Y., Stanciu, A. C., Niday, B., & Humphreys, E. (2020). Seismic anisotropy reveals crustal flow driven by mantle vertical loading in the Pacific NW. *Science Advances*, *6*(28), eabb0476.

Catchings, R. D., & Mooney, W. D. (1988). Crustal structure of the Columbia Plateau: Evidence for continental rifting. *Journal of Geophysical Research: Solid Earth*, *93*(B1), 459–474.

Chetel, L. M., Janecke, S. U., Carroll, A. R., Beard, B. L., Johnson, C. M., & Singer, B. S. (2011). Paleogeographic reconstruction of the Eocene Idaho River, North American Cordillera. *Geological Society of America Bulletin*, *123*(1-2), 71–88.

Clark, I. R., & Cartwright, J. A. (2009). Interactions between submarine channel systems and deformation in deepwater fold belts: Examples from the Levant Basin, Eastern Mediterranean sea. *Marine and Petroleum Geology*, *26*(8), 1465–1482.

Clark, I. R., & Cartwright, J. A. (2011). Key controls on submarine channel development in structurally active settings. *Marine and Petroleum Geology*, *28*(7), 1333–1349.

Clark, M. K., Farley, K. A., Zheng, D., Wang, Z., & Duvall, A. R. (2010). Early Cenozoic faulting of the northern Tibetan Plateau margin from apatite (U–Th)/He ages. *Earth and Planetary Science Letters*, 11.

Darold, A., & Humphreys, E. (2013). Upper mantle seismic structure beneath the Pacific Northwest: A plume-triggered delamination origin for the Columbia River flood basalt eruptions. *Earth and Planetary Science Letters*, *365*, 232–242.

Davies, J., & von Blanckenburg, F. (1995). Slab breakoff: A model of lithosphere detachment and its test in the magmatism and deformation of collisional orogens. *Earth and Planetary Science Letters*, *129*(1-4), 85–102.

DeCelles, P. G. (2004). Late Jurassic to Eocene evolution of the Cordilleran thrust belt and foreland basin system, western U.S.A. *American Journal of Science*, *304*(2), 105–168.

DeCelles, P. G., Ducea, M. N., Kapp, P., & Zandt, G. (2009). Cyclicity in Cordilleran orogenic systems. *Nature Geoscience*, *2*(4), 251–257.

DeMets, C., & Merkouriev, S. (2016). High-resolution reconstructions of Pacific–North

America plate motion: 20 Ma to present. *Geophysical Journal International*, *207*, 741–773.

Dietz, R. S., & Menard, H. W. (1951). Origin of Abrupt Change in Slope at Continental Shelf Margin. *AAPG Bulletin*, *35*(9), 1994–2016.

Divins, D. (2003). *Total Sediment Thickness of the World's Oceans & Marginal Seas.* NOAA National Geophysical Data Center.

Dobbs, S. C., McHargue, T., Malkowski, M. A., Gooley, J. T., Jaikla, C., White, C. J., & Hilley, G. E. (2019). Are submarine and subaerial drainages morphologically distinct? *Geology*, *47*(11), 1093–1097.

Dobson, M. R., O'Leary, D., & Veart, M. (1998). Sediment delivery to the Gulf of Alaska: Source mechanisms along a glaciated transform margin. *Geological Society, London, Special Publications*, *129*(1), 43–66.

Doubrovine, P. V., & Tarduno, J. A. (2008). A revised kinematic model for the relative motion between Pacific oceanic plates and North America since the Late Cretaceous. *Journal of Geophysical Research*, *113*(B12), B12101.

Ducea, M., & Saleeby, J. (1998). A Case for Delamination of the Deep Batholithic Crust beneath the Sierra Nevada, California. *International Geology Review*, *40*(1), 78–93.

Dumitru, T. A. (1993). A new computer-automated microscope stage system for fission-track analysis. *Nuclear Tracks and Radiation Measurements*, *21*(4), 575–580.

Dumitru, T. A., Ernst, W., Wright, J. E., Wooden, J. L., Wells, R. E., Farmer, L. P., ... Graham, S. A. (2013). Eocene extension in Idaho generated massive sediment floods into the Franciscan trench and into the Tyee, Great Valley, and Green River basins. *Geology*, *41*(2), 187–190.

Duvall, A. R., & Tucker, G. E. (2015). Dynamic Ridges and Valleys in a Strike-Slip Environment. *Journal of Geophysical Research: Earth Surface*, *120*(10), 2016–2026.

Dziak, R. P. (2006). Explorer deformation zone: Evidence of a large shear zone and reorganization of the Pacific–Juan de Fuca–North American triple junction. *Geology*, *34*(3), 213.

Elliott, J. L., & Freymueller, J. T. (2020). A Block Model of Present-Day Kinematics of Alaska and Western Canada. *Journal of Geophysical Research: Solid Earth*, *125*(7).

Elliott, J. L., Larsen, C. F., Freymueller, J. T., & Motyka, R. J. (2010). Tectonic block motion and glacial isostatic adjustment in southeast Alaska and adjacent Canada constrained by GPS measurements. *Journal of Geophysical Research*, *115*(B9), B09407.

Farley, K. A. (2000). Helium diffusion from apatite: General behavior as illustrated by Durango fluorapatite. *Journal of Geophysical Research: Solid Earth*, *105*(B2), 2903–2914.

Farley, K. A., Rusmore, M. E., & Bogue, S. W. (2001). Post–10 Ma uplift and exhumation of the northern Coast Mountains, British Columbia. , 4.

Fayon, A., Tikoff, B., Kahn, M., & Gaschnig, R. (2017). Cooling and exhumation of the southern Idaho batholith. *Lithosphere*, *9*(2), 299–314.

Ferns, M. L., & McClaughry, J. D. (2013). Stratigraphy and volcanic evolution of the middle Miocene to Pliocene La Grande–Owyhee eruptive axis in eastern Oregon. In *The Columbia River Flood Basalt Province.* Geological Society of America.

Ferns, M. L., McConnell, V. S., Madin, I. P., & Johnson, J. A. (2010). *Geology of the upper Grande Ronde River basin, Union county, Oregon* (DOGAMI Bulletin No. 107).

Finley, T., Morell, K., Leonard, L., Regalla, C., Johnston, S. T., & Zhang, W. (2019). Ongoing oroclinal bending in the Cascadia forearc and its relation to concave-outboard plate margin geometry. *Geology*, *47*(2), 155–158.

Fitzgerald, J. F. (1982). Geology and Basalt Stratigraphy of the Weiser Embayment, West-Central Idaho. , 26.

Flowers, R., Ketcham, R. A., Shuster, D. L., & Farley, K. A. (2009). Apatite (U–Th)/He thermochronometry using a radiation damage accumulation and annealing model. *Geochimica et Cosmochimica Acta*, *73*(8), 2347–2365.

Flowers, R., Shuster, D., Wernicke, B., & Farley, K. (2007). Radiation damage control on apatite (U-Th)/He dates from the Grand Canyon region, Colorado Plateau. *Geology*, *35*(5), 447.

Foster, D. A., & Raza, A. (2002). Low-temperature thermochronological record of exhumation of the Bitterroot metamorphic core complex, northern Cordilleran Orogen. *Tectonophysics*, *349*(1-4), 23–36.

Fraccascia, S., Chiocci, F. L., Scrocca, D., & Falese, F. (2013). Very high-resolution seismic stratigraphy of Pleistocene eustatic minima markers as a tool to reconstruct the tectonic evolution of the northern Latium shelf (Tyrrhenian Sea, Italy). *Geology*, *41*(3), 375–378.

Galbraith, R. F. (1981). On statistical models for fission track counts. *Journal of the International Association for Mathematical Geology*, *13*(6), 471–478.

Gallagher, K. (2012). Transdimensional inverse thermal history modeling for quantitative thermochronology. *Journal of Geophysical Research: Solid Earth*, *117*(B2), n/a-n/a.

Gao, H. (2015). Crustal seismic structure beneath the source area of the Columbia River flood basalt: Bifurcation of the Moho driven by lithosphere delamination. *Geophysical Research Letters*, *42*(22), 9764–9771.

Gao, H., Humphreys, E. D., Yao, H., & van der Hilst, R. D. (2011). Crust and lithosphere structure of the northwestern U.S. with ambient noise tomography: Terrane accretion and Cascade arc development. *Earth and Planetary Science Letters*, *304*(1-2), 202–211.

Gaschnig, R., Macho, A., Fayon, A., Schmitz, M., Ware, B., Vervoort, J., ... Tikoff, B. (2017). Intrusive and depositional constraints on the Cretaceous tectonic history of the southern Blue Mountains, eastern Oregon. *Lithosphere*, *9*(2), 265–282.

Gaschnig, R., Vervoort, J. D., Lewis, R. S., & McClelland, W. C. (2010). Migrating magmatism in the northern US Cordillera: In situ U–Pb geochronology of the Idaho batholith. *Contributions to Mineralogy and Petrology*, *159*(6), 863–883.

Gaschnig, R., Vervoort, J. D., Lewis, R. S., & Tikoff, B. (2011). Isotopic Evolution of the Idaho Batholith and Challis Intrusive Province, Northern US Cordillera. *Journal of Petrology*, *52*(12), 2397–2429.

Gautheron, C., Barbarand, J., Ketcham, R. A., Tassan-Got, L., van der Beek, P., Pagel, M.,

... Fialin, M. (2013). Chemical influence on α-recoil damage annealing in apatite: Implications for (U–Th)/He dating. *Chemical Geology*, *351*, 257–267.

Gehrels, G., Rusmore, M., Woodsworth, G., Crawford, M., Andronicos, C., Hollister, L., ... Girardi, J. (2009). U-Th-Pb geochronology of the Coast Mountains batholith in north-coastal British Columbia: Constraints on age and tectonic evolution. *Geological Society of America Bulletin*, *121*(9-10), 1341–1361.

Georgiopoulou, A., & Cartwright, J. A. (2013). A critical test of the concept of submarine equilibrium profile. *Marine and Petroleum Geology*, *41*, 35–47.

Giorgis, S., Tikoff, B., & McClelland, W. (2005). Missing Idaho arc: Transpressional modification of the 87Sr/86Sr transition on the western edge of the Idaho batholith. *Geology*, *33*(6), 469.

Gomberg, J., Sherrod, B., Trautman, M., Burns, E., & Snyder, D. (2012). Contemporary Seismicity in and around the Yakima Fold-and-Thrust Belt in Eastern Washington. *Bulletin of the Seismological Society of America*, *102*(1), 309–320.

Goren, L., Willett, S. D., Herman, F., & Braun, J. (2014). Coupled numerical–analytical approach to landscape evolution modeling. *Earth Surface Processes and Landforms*, *39*(4), 522–545.

Gosselin, J. M., Cassidy, J. F., & Dosso, S. E. (2015). Shear-Wave Velocity Structure in the Vicinity of the 2012 Mw 7.8 Haida Gwaii Earthquake from Receiver Function Inversion. *Bulletin of the Seismological Society of America*, *105*(2B), 1106–1113.

Green, P. F. (1981). A new look at statistics in fission-track dating. *Nuclear Tracks*, *5*(1), 77–86.

Greene, H. G., Barrie, J. V., Brothers, D. S., Conrad, J. E., Conway, K., East, A. E., ... Rohr, K. M. M. (2019). Slope failure and mass transport processes along the Queen Charlotte Fault Zone, western British Columbia. *Geological Society, London, Special Publications*, *477*(1), 85–106.

Gromme, C. S., Beck, M. E., Wells, R. E., & Engebretson, D. C. (1986). Paleomagnetism of the Tertiary Clarno Formation of central Oregon and its significance for the tectonic

history of the Pacific Northwest. *Journal of Geophysical Research*, *91*(B14), 14089.

Guenthner, W. R., Reiners, P. W., Ketcham, R. A., Nasdala, L., & Giester, G. (2013). Helium diffusion in natural zircon: Radiation damage, anisotropy, and the interpretation of zircon (U-Th)/He thermochronology. *American Journal of Science*, *313*(3), 145–198.

Gurnis, M., Hall, C., & Lavier, L. (2004). Evolving force balance during incipient subduction. *Geochemistry, Geophysics, Geosystems*, *5*(7).

Gurnis, M., Van Avendonk, H., Gulick, S. P., Stock, J., Sutherland, R., Hightower, E., ... Carrington, L. (2019). Incipient subduction at the contact with stretched continental crust: The Puysegur Trench. *Earth and Planetary Science Letters*, *520*, 212–219.

Hage, S., Cartigny, M. J., Clare, M. A., Sumner, E. J., Vendettuoli, D., Hughes Clarke, J. E., ... Vellinga, A. J. (2018). How to recognize crescentic bedforms formed by supercritical turbidity currents in the geologic record: Insights from active submarine channels. *Geology*, *46*(6), 563–566.

Hales, T. C., Abt, D. L., Humphreys, E. D., & Roering, J. J. (2005). A lithospheric instability origin for Columbia River flood basalts and Wallowa Mountains uplift in northeast Oregon. *Nature*, *438*(7069), 842–845.

Harbert, S. A., Duvall, A. R., & Tucker, G. E. (2018). The Role of Near-Fault Relief Elements in Creating and Maintaining a Strike-Slip Landscape. *Geophysical Research Letters*, *45*(21), 11,683–11,692.

Harris, P. T., Barrie, J. V., Conway, K. W., & Greene, H. G. (2014). Hanging canyons of Haida Gwaii, British Columbia, Canada: Fault-control on submarine canyon geomorphology along active continental margins. *Deep Sea Research Part II: Topical Studies in Oceanography*, *104*, 83–92.

Harris, P. T., & Whiteway, T. (2011). Global distribution of large submarine canyons: Geomorphic differences between active and passive continental margins. *Marine Geology*, *285*(1), 69–86.

Hatem, A. E., Cooke, M. L., & Madden, E. H. (2005). Evolving efficiency of restraining

bends within wet kaolin analog experiments. *Journal of Geophysical Research: Solid Earth*, *120*(3), 1975–1992.

Heijnen, M. S., Clare, M. A., Cartigny, M. J. B., Talling, P. J., Hage, S., Lintern, D. G., ... Hughes Clarke, J. E. (2020). Rapidly-migrating and internally-generated knickpoints can control submarine channel evolution. *Nature Communications*, *11*(1), 3129.

Heiniö, P., & Davies, R. J. (2007). Knickpoint migration in submarine channels in response to fold growth, western Niger Delta. *Marine and Petroleum Geology*, *24*(6-9), 434–449.

Helland-Hansen, W., Steel, R. J., & Somme, T. O. (2012). Shelf genesis revisited. *Journal of Sedimentary Research*, *82*(3), 133–148.

Hetherington, R., Barrie, J., Reid, R. G., MacLeod, R., & Smith, D. J. (2004). Paleogeography, glacially induced crustal displacement, and Late Quaternary coastlines on the continental shelf of British Columbia, Canada. *Quaternary Science Reviews*, *23*(3-4), 295–318.

Hilley, G., Sare, R., Aron, F., Baden, C., Caress, D., Castillo, C., ... Young, H. (2020). Coexisting seismic behavior of transform faults revealed by high-resolution bathymetry. *Geology*, *48*(4), 379–384.

Ho, A. M., & Cashman, K. V. (1997). Temperature constraints on the Ginkgo flow of the Columbia River Basalt Group. *Geology*, *25*(5), 4.

Hooper, P. R., & Camp, V. (1981). Deformation of the southeast part of the Columbia Plateau. *Geology*, *9*, 323–328.

Hooper, P. R., Kleck, W. D., Knowles, C. R., Reidel, S. P., & Thiessen, R. L. (1984). Imnaha Basalt, Columbia River Basalt Group. *Journal of Petrology*, *25*(2), 473–500.

House, M. A. (2002). Uplift in the Fiordland Region, New Zealand: Implications for Incipient Subduction. *Science*, *297*(5589), 2038–2041.

Housen, B. A. (2005). Paleomagnetism and tectonic significance of Albian and Cenomanian turbidites, Ochoco Basin, Mitchell Inlier, central Oregon. *Journal of Geophysical Research*, *110*(B7), B07102.

Housen, B. A. (2018). Paleomagnetism and rotation history of the Blue Mountains, Oregon,

USA.

Humphreys, E. D. (1995). Post-Laramide removal of the Farallon slab, western United States. *Geology*, *23*(11), 4.

Hurford, A. J., & Green, P. F. (1983). The zeta age calibration of fission-track dating. *Chemical Geology*, *41*, 285–317.

Huyghe, P., Foata, M., Deville, E., Mascle, G., & Group, C. W. (2004). Channel profiles through the active thrust front of the southern Barbados prism. *Geology*, *32*(5), 429–432.

Hyndman, R. D. (2005). Subduction zone backarcs, mobile belts, and orogenic heat. *GSA TODAY*, 7.

Hyndman, R. D. (2015). Tectonics and Structure of the Queen Charlotte Fault Zone, Haida Gwaii, and Large Thrust Earthquakes. *Bulletin of the Seismological Society of America*, *105*(2B), 1058–1075.

Hyndman, R. D., & Hamilton, T. S. (1993). Queen Charlotte Area Cenozoic tectonics and volcanism and their association with relative plate motions along the northeastern Pacific Margin. *Journal of Geophysical Research: Solid Earth*, *98*(B8), 14257–14277.

Iwasaki, T., & Parker, G. (2020). The role of saltwater and waves in continental shelf formation with seaward migrating clinoform. *Proceedings of the National Academy of Sciences*, *117*(3), 1266–1273.

Janecke, S. U., & Hammond, B. F. (1997). Rapid extension in an Eocene volcanic arc: Structure and paleogeography of an intra-arc half graben in central Idaho. *Geological Society of America Bulletin*, 15.

Janecke, S. U., & Snee, L. W. (1993). Timing and Episodicity of Middle Eocene Volcanism and Onset of Conglomerate Deposition, Idaho. *The Journal of Geology*, *101*(5), 603–621.

Jijina, A. P., Currano, E. D., & Constenius, K. (2019). The paleobotany and paleoecology of the Eocene Herren beds of north-central Oregon, USA. *PALAIOS*, *34*(9), 424–436.

Johnson, S. Y., Watt, J. T., Hartwell, S. R., & Kluesner, J. W. (2018). Neotectonics of

the Big Sur Bend, San Gregorio-Hosgri Fault System, Central California. *Tectonics*, *37*(7), 1930–1954.

Kahn, M., Fayon, A. K., & Tikoff, B. (2020). Constraints on the post-orogenic tectonic history along the Salmon River suture zone from low-temperature thermochronology, western Idaho and eastern Oregon. *Rocky Mountain Geology*, *55*(1), 27–54.

Karlstrom, L., Murray, K. E., & Reiners, P. W. (2019). Bayesian Markov-Chain Monte Carlo Inversion of Low-Temperature Thermochronology Around Two 8 - 10 m Wide Columbia River Flood Basalt Dikes. *Frontiers in Earth Science*, *7*.

Kasbohm, J., & Schoene, B. (2018). Rapid eruption of the Columbia River flood basalt and correlation with the mid-Miocene climate optimum. *Science Advances*, *4*(9), eaat8223.

Kelsey, H. M., Ladinsky, T. C., Staisch, L., Sherrod, B. L., Blakely, R. J., Pratt, T. L., ... Wan, E. (2017). The Story of a Yakima Fold and How It Informs Late Neogene and Quaternary Backarc Deformation in the Cascadia Subduction Zone, Manastash Anticline, Washington, USA. *Tectonics*, *36*(10), 2085–2107.

Ketcham, R. A. (2005). Forward and Inverse Modeling of Low-Temperature Thermochronometry Data. *Reviews in Mineralogy and Geochemistry*, *58*(1), 275–314.

Kirby, E., & Whipple, K. X. (2012). Expression of active tectonics in erosional landscapes. *Journal of Structural Geology*, *44*, 54–75.

Kneller, B. (2003). The influence of flow parameters on turbidite slope channel architecture. *Marine and Petroleum Geology*, *20*(6), 901–910.

Lai, S. Y. J., Gerber, T. P., & Amblas, D. (2016). An experimental approach to submarine canyon evolution. *Geophysical Research Letters*, *43*(6), 2741–2747.

LaMaskin, T. A., Vervoort, J. D., Dorsey, R. J., & Wright, J. E. (2011). Early Mesozoic paleogeography and tectonic evolution of the western United States: Insights from detrital zircon U-Pb geochronology, Blue Mountains Province, northeastern Oregon. *Geological Society of America Bulletin*, *123*(9-10), 1939–1965.

Lay, T., Ye, L., Kanamori, H., Yamazaki, Y., Cheung, K. F., Kwong, K., & Koper, K. D. (2013). The October 28, 2012 Mw 7.8 Haida Gwaii underthrusting earthquake and

tsunami: Slip partitioning along the Queen Charlotte Fault transpressional plate boundary. *Earth and Planetary Science Letters*, *375*, 57–70.

Lecours, V., Dolan, M. F. J., Micallef, A., & Lucieer, V. L. (2016). A review of marine geomorphometry, the quantitative study of the seafloor. *Hydrology and Earth System Sciences*, *20*(8), 3207–3244.

Leopold, L., & Miller, J. (1962). *Ephemeral streams- Hydraulic factors and their relation to the drainage net* (USGS Professional Paper No. 282-A).

Lewis, P. D., Haggart, J. W., Anderson, R. G., Hickson, C. J., Thompson, R. I., Dietrich, J. R., & Rohr, K. M. M. (1991). Triassic to Neogene geologic evolution of the Queen Charlotte region. *Canadian Journal of Earth Sciences*, *28*(6), 854–869.

Lingley, W. (1995). *Petroleum potential and probability of renewed mineral-rights leasing in the Columbia Basin, Washington* (Tech. Rep.). Wa. DNR.

Liu, L., & Stegman, D. R. (2011). Segmentation of the Farallon slab. *Earth and Planetary Science Letters*, *311*(1-2), 1–10.

Lund, K., Aleinikoff, J. N., Yacob, E. Y., Unruh, D. M., & Fanning, C. M. (2008). Coolwater culmination: Sensitive high-resolution ion microprobe (SHRIMP) U-Pb and isotopic evidence for continental delamination in the Syringa Embayment, Salmon River suture, Idaho. *Tectonics*, *27*(2), n/a-n/a.

Lund, K., Box, S., Holm-Denoma, C., San Juan, C., Blakely, R., Saltus, R., ... DeWitt, E. (2015). *Basement domain map of the conterminous United States and Alaska* [Map]. USGS.

Lund, K., & Snee, L. (1988). Metamorphism, structural development and age of the continent-island juncture west-central Idaho. In *Metamorphism and crustal evolution of the Western United States* (Vol. 7). Prentice-Hall.

Ma, X., & Lowry, A. R. (2017). USArray Imaging of Continental Crust in the Conterminous United States. *Tectonics*, *36*(12), 2882–2902.

Maier, K. L., Brothers, D. S., Paull, C. K., McGann, M., Caress, D. W., & Conrad, J. E. (2017). Records of continental slope sediment flow morphodynamic responses to gra-

dient and active faulting from integrated AUV and ROV data, offshore Palos Verdes, southern California Borderland. *Marine Geology*, *393*, 47–66.

Malatesta, L. C., Bruhat, L., Finnegan, N. J., & Olive, J.-A. L. (2021). Co-location of the Downdip End of Seismic Coupling and the Continental Shelf Break. *Journal of Geophysical Research: Solid Earth*, *126*(1).

Mao, X., Gurnis, M., & May, D. A. (2017). Subduction Initiation With Vertical Lithospheric Heterogeneities and New Fault Formation. *Geophysical Research Letters*, *44*(22), 11,349–11,356.

Matmon, A., Bierman, P. R., Larsen, J., Southworth, S., & Pavich, M. (2003). Temporally and spatially uniform rates of erosion in the southern Appalachian Great Smoky Mountains. , 5.

Mayall, M., Lonergan, L., Bowman, A., James, S., Mills, K., Primmer, T., ... Skeene, R. (2010). The response of turbidite slope channels to growth-induced seabed topography. *AAPG Bulletin*, *94*(7), 1011–1030.

Mazzotti, S., Hyndman, R. D., Flück, P., Smith, A. J., & Schmidt, M. (2003). Distribution of the Pacific/North America motion in the Queen Charlotte Islands-S. Alaska plate boundary zone. *Geophysical Research Letters*, *30*(14).

McCaffrey, R., King, R. W., Payne, S. J., & Lancaster, M. (2013). Active tectonics of northwestern U.S. inferred from GPS-derived surface velocities. *Journal of Geophysical Research: Solid Earth*, *118*(2), 709–723.

McCaffrey, R., King, R. W., Wells, R. E., Lancaster, M., & Miller, M. M. (2016). Contemporary deformation in the Yakima fold and thrust belt estimated with GPS. *Geophysical Journal International*, *207*(1), 1–11.

McCaffrey, R., Qamar, A. I., King, R. W., Wells, R., Khazaradze, G., Williams, C. A., ... Zwick, P. C. (2007). Fault locking, block rotation and crustal deformation in the Pacific Northwest. *Geophysical Journal International*, *169*(3), 1315–1340.

McKay, M. P., Bollen, E. M., Gray, K. D., Stowell, H. H., & Schwartz, J. J. (2017). Prolonged metamorphism during long-lived terrane accretion: Sm-Nd garnet and U-Pb zircon

geochronology and pressure-temperature paths from the Salmon River suture zone, west-central Idaho, USA. *Lithosphere*, *9*(5), 683–701.

McKeon, R. E., Zeitler, P. K., Pazzaglia, F. J., Idleman, B. D., & Enkelmann, E. (2014). Decay of an old orogen: Inferences about Appalachian landscape evolution from low-temperature thermochronology. *GSA Bulletin*, *126*(1-2), 31–46.

McLing, T. L., Smith, R. P., Smith, R. W., Blackwell, D. D., Roback, R. C., & Sondrup, A. J. (2016). Wellbore and groundwater temperature distribution eastern Snake River Plain, Idaho: Implications for groundwater flow and geothermal potential. *Journal of Volcanology and Geothermal Research*, *320*, 144–155.

Micallef, A., Mountjoy, J. J., Barnes, P. M., Canals, M., & Lastras, G. (2014). Geomorphic response of submarine canyons to tectonic activity: Insights from the Cook Strait canyon system, New Zealand. *Geosphere*, *10*(5), 905–929.

Mitchell, N. C. (2004). Form of submarine erosion from confluences in Atlantic USA continental slope Canyons. *American Journal of Science*, *304*(7), 590–611.

Mitchell, N. C. (2005). Interpreting long-profiles of canyons in the USA Atlantic continental slope. *Marine Geology*, *214*(1-3), 75–99.

Mitchell, N. C. (2008). Summary of progress in geomorphologic modelling of continental slope canyons. *Geological Society, London, Special Publications*, *296*(1), 183–194.

Mitchell, S. G., & Montgomery, D. R. (2006). Polygenetic topography of the Cascade Range, Washington State, USA. *American Journal of Science*, *306*(9), 736–768.

Mitchell, S. G., & Reiners, P. W. (2003). Influence of wildfires on apatite and zircon (U-Th)/He ages. *Geology*, *31*(12), 1025–1028.

Montgomery, D. R., & Foufoula-Georgiou, E. (1993). Channel network source representation using digital elevation models. *Water Resources Research*, *29*(12), 3925–3934.

Morriss, M. C., Karlstrom, L., Nasholds, M. W., & Wolff, J. A. (2020). The Chief Joseph dike swarm of the Columbia River flood basalts, and the legacy data set of William H. Taubeneck. *Geosphere*, *16*(4), 1082–1106.

Müller, R. D., Cannon, J., Qin, X., Watson, R. J., Gurnis, M., Williams, S., ... Zahirovic,

S. (2018). GPlates: Building a Virtual Earth Through Deep Time. *Geochemistry, Geophysics, Geosystems*, *19*(7), 2243–2261.

Mustoe, G. E., & Leopold, E. B. (2014). Paleobotanical evidence for the post-Miocene uplift of the Cascade Range. *Canadian Journal of Earth Sciences*, *51*(8), 809–824.

Naeser, C. W. (1979). Fission-Track Dating and Geologic Annealing of Fission Tracks. In E. Jäger & J. C. Hunziker (Eds.), *Lectures in Isotope Geology* (pp. 154–169). Berlin, Heidelberg: Springer.

Nykolaishen, L., Dragert, H., Wang, K., James, T. S., & Schmidt, M. (2015). GPS Observations of Crustal Deformation Associated with the 2012 Mw 7.8 Haida Gwaii Earthquake. *Bulletin of the Seismological Society of America*, *105*(2B), 1241–1252.

Olariu, C., & Steel, R. J. (2009). Influence of point-source sediment-supply on modern shelf-slope morphology: Implications for interpretation of ancient shelf margins. *Basin Research*, *21*(5), 484–501.

Orme, D. A., Guenthner, W. R., Laskowski, A. K., & Reiners, P. W. (2016). Long-term tectonothermal history of Laramide basement from zircon–He age-eU correlations. *Earth and Planetary Science Letters*, *453*, 119–130.

Paris, P. J., Walsh, J. P., & Corbett, D. R. (2016). Where the Continent Ends. *Geophysical Research Letters*, *43*(23), 12,208–12,216.

Parrish, R. R., Carr, S. D., & Parkinson, D. L. (1988). Eocene extensional tectonics and geochronology of the Southern Omineca Belt, British Columbia and Washington. *Tectonics*, *7*(2), 181–212.

Paull, C. K., Talling, P. J., Maier, K. L., Parsons, D., Xu, J., Caress, D. W., ... Cartigny, M. J. (2018). Powerful turbidity currents driven by dense basal layers. *Nature Communications*, *9*(1), 4114.

Paull, C. K., Ussler, W., Greene, H. G., Keaten, R., Mitts, P., & Barry, J. (2002). Caught in the act: The 20 December 2001 gravity flow event in Monterey Canyon. *Geo-Marine Letters*, *22*(4), 227–232.

Perrin, C., Manighetti, I., Ampuero, J.-P., Cappa, F., & Gaudemer, Y. (2016). Location

of largest earthquake slip and fast rupture controlled by along-strike change in fault structural maturity due to fault growth. *Journal of Geophysical Research: Solid Earth*, *121*(5), 3666–3685.

Perry-Houts, J., & Humphreys, E. (2018). Eclogite-driven subsidence of the Columbia Basin (Washington State, USA) caused by deposition of Columbia River Basalt. *Geology*, *46*(7), 651–654.

Perry-Houts, J., & Karlstrom, L. (2019). Anisotropic viscosity and time-evolving lithospheric instabilities due to aligned igneous intrusions. *Geophysical Journal International*, *216*(2), 794–802.

Petcovic, H. L. (2003). Textural and Thermal History of Partial Melting in Tonalitic Wallrock at the Margin of a Basalt Dike, Wallowa Mountains, Oregon. *Journal of Petrology*, *44*(12), 2287–2312.

Plafker, G. (1987). Regional geology and petroleum potential of the northern Gulf of Alaska continental margin. In *Geology and resource potential of the continental margin of western North America and Adjacent Ocean Basins, Beaufort Sea to Baja California* (Vol. 6, pp. 229–268). Circum-Pacific Council for Energy and Mineral Resources.

Pohl, F., Eggenhuisen, J., Cartigny, M., Tilston, M., de Leeuw, J., & Hermidas, N. (2020). The influence of a slope break on turbidite deposits: An experimental investigation. *Marine Geology*, *424*, 106160.

Porter, R. C., van der Lee, S., & Whitmeyer, S. J. (2019). Synthesizing EarthScope data to constrain the thermal evolution of the continental U.S. lithosphere. *Geosphere*, *15*(6), 1722–1737.

Prather, B. E., Pirmez, C., Sylvester, Z., & Prather, D. S. (2012). Stratigraphic Response to Evolving Geomorphology in a Submarine Apron Perched On the Upper Niger Delta Slope.

Pratson, L. F., & Coakley, B. J. (1996). A model for the headward erosion of submarine canyons induced by downslope-eroding sediment flows. *Geological Society of America Bulletin*, 10.

Pratt, T. L. (2012). Large-scale splay faults on a strike-slip fault system: The Yakima Folds, Washington State. *Geochemistry, Geophysics, Geosystems*, *13*(11).

Prouty, N. G., Brothers, D. S., Kluesner, J. W., Barrie, J. V., Andrews, B. D., Lauer, R. M., ... Dartnell, P. (2020). Focused fluid flow and methane venting along the Queen Charlotte fault, offshore Alaska (USA) and British Columbia (Canada). *Geosphere*, *16*(6), 1336–1357.

Raisz, E. (1945). The Olympic-Wallowa lineament. *American Journal of Science*, *243*, 479–485.

Ramsey, L. A., Hovius, N., Lague, D., & Liu, C.-S. (2006). Topographic characteristics of the submarine Taiwan orogen. *Journal of Geophysical Research*, *111*(F2), F02009.

Reidel, S. P., Camp, V. E., Tolan, T. L., Kauffman, J. D., & Garwood, D. L. (2013). Tectonic evolution of the Columbia River flood basalt province. In *The Columbia River Flood Basalt Province* (Vol. 497). Geological Society of America.

Reidel, S. P., Camp, V. E., Tolan, T. L., & Martin, B. S. (2013). The Columbia River flood basalt province: Stratigraphy, areal extent, volume, and physical volcanology. In *The Columbia River Flood Basalt Province* (Vol. 497). Geological Society of America.

Reidel, S. P., Fecht, K. R., Hutter (Harrold), I. L., Tolan, T. L., & Chamness, M. A. (2020). The Olympic-Wallowa lineament: A new look at an old controversy. *GSA Bulletin*, *133*(1-2), 115–133.

Reidel, S. P., Kauffman, J. D., Garwood, D. L., & Bush, J. W. M. (2006). *What lies below the Columbia River Basalt?* [Poster]. Washington, D.C..

Reidel, S. P., Spane, F. A., & Johnson, V. G. (2002). *Natural Gas Storage in Basalt Aquifers of the Columbia Basin, Pacific Northwest USA: A Guide to Site Characterization* (Tech. Rep. Nos. PNNL-13962, 15020781).

Reidel, S. P., Tolan, T. L., Hooper, P. R., Beeson, M. H., Fecht, K. R., Bentley, R. D., & Anderson, J. L. (1989). The Grande Ronde Basalt, Columbia River Basalt Group; Stratigraphic descriptions and correlations in Washington, Oregon, and Idaho. In *Geological Society of America Special Papers* (Vol. 239, pp. 21–54). Geological Society

of America.

Reiners, P. W. (2003). Post-orogenic evolution of the Dabie Shan, eastern China, from (U-Th)/He and fission-track thermochronology. *American Journal of Science*, *303*(6), 489–518.

Reiners, P. W. (2005a). (U-Th)/(He-Pb) double dating of detrital zircons. *American Journal of Science*, *305*(4), 259–311.

Reiners, P. W. (2005b). Zircon (U-Th)/He Thermochronometry. *Reviews in Mineralogy and Geochemistry*, *58*(1), 151–179.

Reiners, P. W., Ehlers, T. A., Garver, J. I., Mitchell, S. G., Montgomery, D. R., Vance, J. A., & Nicolescu, S. (2002). Late Miocene exhumation and uplift of the Washington Cascade Range. , 4.

Reiners, P. W., Farley, K. A., & Hickes, H. J. (2002). He diffusion and (U–Th)/He thermochronometry of zircon: Initial results from Fish Canyon Tuff and Gold Butte. *Tectonophysics*, *349*(1), 297–308.

Reitman, N. G., Mueller, K. J., Tucker, G. E., Gold, R. D., Briggs, R. W., & Barnhart, K. R. (2019). Offset Channels May Not Accurately Record Strike-Slip Fault Displacement: Evidence From Landscape Evolution Models. *Journal of Geophysical Research: Solid Earth*, *124*(12), 13427–13451.

Retallack, G., Bestland, E., & Fremd, T. (2000). Eocene and Oligocene Paleosols of Central Oregon. *Geological Society, London, Special Publications*(344).

Riddihough, R., Finn, C., & Couch, R. (1986). Klamath-Blue Mountain lineament, Oregon. *Geology*, *14*(6), 528–531.

Rogers, G. (1986). Seismic gaps along the Queen Charlotte Fault. *Earthquake Prediction Research*, *4*, 1–11.

Rohr, K. M. M. (2015). Plate Boundary Adjustments of the Southernmost Queen Charlotte Fault. *Bulletin of the Seismological Society of America*, *105*(2B), 1076–1089.

Rohr, K. M. M., & Dietrich, J. R. (1992). Strike-slip tectonics and development of the Tertiary Queen Charlotte Basin, offshore western Canada: Evidence from seismic re-

flection data. *Basin Research*, *4*(1), 1–20.

Rohr, K. M. M., Scheidhauer, M., & Trehu, A. M. (2000). Transpression between two warm mafic plates: The Queen Charlotte Fault revisited. *Journal of Geophysical Research: Solid Earth*, *105*(B4), 8147–8172.

Rohr, K. M. M., & Tryon, A. J. (2010). Pacific-North America plate boundary reorganization in response to a change in relative plate motion: Offshore Canada. *Geochemistry, Geophysics, Geosystems*, *11*(6), n/a-n/a.

Ross, S. M. (2003). Peirce's criterion for the elimination of suspect experimental data. , 12.

Sánchez-Montes, M. L., McClymont, E. L., Lloyd, J. M., Müller, J., Cowan, E. A., & Zorzi, C. (2020). Late Pliocene Cordilleran Ice Sheet development with warm northeast Pacific sea surface temperatures. *Climate of the Past*, *16*(1), 299–313.

Schlager, W., & Adams, E. W. (2001). Model for the sigmoidal curvature of submarine slopes. *Geology*, *29*(10), 883–886.

Schmandt, B., & Humphreys, E. (2011). Seismically imaged relict slab from the 55 Ma Siletzia accretion to the northwest United States. *Geology*, *39*(2), 175–178.

Schmandt, B., Lin, F.-C., & Karlstrom, K. E. (2015). Distinct crustal isostasy trends east and west of the Rocky Mountain Front. *Geophysical Research Letters*, *42*(23), 10,290–10,298.

Schmidt, K. L., Lewis, R. S., Vervoort, J. D., Stetson-Lee, T. A., Michels, Z. D., & Tikoff, B. (2017). Tectonic evolution of the Syringa embayment in the central North American Cordilleran accretionary boundary. *Lithosphere*, *9*(2), 184–204.

Schoettle-Greene, P., Duvall, A. R., Blythe, A., Morley, E., Matthews, W., & LaHusen, S. R. (2020). Uplift and exhumation in Haida Gwaii driven by terrane translation and transpression along the southern Queen Charlotte fault, Canada. *Geology*, *48*(9), 908–912.

Schumann, T. K., Rohr, K. M. M., & Whiticar, M. J. (2013). 2D petroleum systems modeling of Queen Charlotte Basin, offshore British Columbia, Canada. *Bulletin of Canadian Petroleum Geology*, *61*(1), 65–82.

Schutt, D. L., Lowry, A. R., & Buehler, J. S. (2018). Moho temperature and mobility of lower crust in the western United States. *Geology*, *46*(3), 219–222.

Schwanghart, W., & Scherler, D. (2014). Short Communication: TopoToolbox 2 – MATLAB-based software for topographic analysis and modeling in Earth surface sciences. *Earth Surface Dynamics*, *2*(1), 1–7.

Schwartz, J. J., Johnson, K., Mueller, P., Valley, J., Strickland, A., & Wooden, J. L. (2014). Time scales and processes of Cordilleran batholith construction and high-Sr/Y magmatic pulses: Evidence from the Bald Mountain batholith, northeastern Oregon. *Geosphere*, *10*(6), 1456–1481.

Schwartz, J. J., Snoke, A. W., Cordey, F., Johnson, K., Frost, C. D., Barnes, C. G., ... Wooden, J. L. (2011). Late Jurassic magmatism, metamorphism, and deformation in the Blue Mountains Province, northeast Oregon. *Geological Society of America Bulletin*, *123*(9-10), 2083–2111.

Seligman, A. N., Bindeman, I. N., McClaughry, J., Stern, R. A., & Fisher, C. (2014). The earliest low and high 18O caldera-forming eruptions of the Yellowstone plume: Implications for the 30-40 Ma Oregon calderas and speculations on plume-triggered delaminations. *Frontiers in Earth Science*, *2*.

Seton, M., Flament, N., Whittaker, J., Müller, R. D., Gurnis, M., & Bower, D. J. (2015). Ridge subduction sparked reorganization of the Pacific plate-mantle system 60–50 million years ago. *Geophysical Research Letters*, *42*(6), 1732–1740.

Shen, W., & Ritzwoller, M. H. (2016). Crustal and uppermost mantle structure beneath the United States. *Journal of Geophysical Research: Solid Earth*, *121*(6), 4306–4342.

Shepard, F. P. (1981). Submarine Canyons: Multiple Causes and Long-Time Persistence. *AAPG Bulletin*, *65*(6), 1062–1077.

Sherrod, B., Blakely, R., Lasher, J., Lamb, A., Mahan, S., Foit, F., & Barnett, E. (2016). Active faulting on the Wallula fault zone within the Olympic-Wallowa lineament, Washington State, USA. *Geological Society of America Bulletin*, *128*(11-12), 1636–1659.

Shugar, D. H., Walker, I. J., Lian, O. B., Eamer, J. B., Neudorf, C., McLaren, D., & Fedje,

D. (2014). Post-glacial sea-level change along the Pacific coast of North America. *Quaternary Science Reviews*, *97*, 170–192.

Shuster, D. L., Flowers, R. M., & Farley, K. A. (2006). The influence of natural radiation damage on helium diffusion kinetics in apatite. *Earth and Planetary Science Letters*, *249*(3-4), 148–161.

Sinclair, H., & Tomasso, M. (2002). Depositional Evolution of Confined Turbidite Basins. *Journal of Sedimentary Research*, *72*(4), 451–456.

Smith, A. J. (2003). Structure, seismicity, and thermal regime of the Queen Charlotte Transform Margin. *Journal of Geophysical Research*, *108*(B11), 2539.

Smith, G. A., & Ashwill, M. (1998). Late Eocene–early Oligocene tectonism, volcanism, and floristic change near Gray Butte, central Oregon. *Geological Society of America Bulletin*, 20.

Smith, S. (2005). *Distribution, paleodrainage, and paleoclimate of the Miocene Columbia River Basalt Group and associated sedimentary interbeds in the Clearwater Embayment of west-central Idaho and southeastern Washington* (PhD Thesis). Washington State University.

S. Serra, C., Martínez-Loriente, S., Gràcia, E., Urgeles, R., Vizcaino, A., Perea, H., ... Zitellini, N. (2020). Tectonic evolution, geomorphology and influence of bottom currents along a large submarine canyon system: The São Vicente Canyon (SW Iberian margin). *Marine Geology*, *426*, 106219.

Staisch, L., Blakely, R., Kelsey, H., Styron, R., & Sherrod, B. (2018). Crustal Structure and Quaternary Acceleration of Deformation Rates in Central Washington Revealed by Stream Profile Inversion, Potential Field Geophysics, and Structural Geology of the Yakima Folds. *Tectonics*, *37*(6), 1750–1770.

Stanciu, C., & Humphreys, E. D. (2020). Upper mantle tomography beneath the Pacific Northwest interior. *Earth and Planetary Science Letters*, *539*, 116214.

Stanciu, C., Russo, R. M., Mocanu, V. I., Bremner, P. M., Hongsresawat, S., Torpey, M. E., ... Hole, J. A. (2016). Crustal structure beneath the Blue Mountains terranes and

cratonic North America, eastern Oregon, and Idaho, from teleseismic receiver functions: Moho Beneath Eastern Oregon and Idaho. *Journal of Geophysical Research: Solid Earth*, *121*(7), 5049–5067.

Stern, R. J., & Dumitru, T. A. (2019). Eocene initiation of the Cascadia subduction zone: A second example of plume-induced subduction initiation? *Geosphere*, *15*(3), 659–681.

Stevenson, C. J., Jackson, C. A.-L., Hodgson, D. M., Hubbard, S. M., & Eggenhuisen, J. T. (2015). Deep-Water Sediment Bypass. *Journal of Sedimentary Research*, *85*(9), 1058–1081.

Strahler, A. N. (1957). Quantitative analysis of watershed geomorphology. *Eos, Transactions American Geophysical Union*, *38*(6), 913–920.

Stüwe, K., White, L., & Brown, R. (1994). The influence of eroding topography on steady-state isotherms. Application to fission track analysis. *Earth and Planetary Science Letters*, *124*(1), 63–74.

Summerhayes, C. P., Sestini, G., Misdorp, R., & Marks, N. (1978). Nile Delta: Nature and evolution of continental shelf sediments. *Marine Geology*, *27*(1), 43–65.

Surpless, K. D., & Beverly, E. J. (2013). Understanding a critical basinal link in Cretaceous Cordilleran paleogeography: Detailed provenance of the Hornbrook Formation, Oregon and California. *Geological Society of America Bulletin*, *125*(5-6), 709–727.

Survey, Y. G. (2020). *A digital atlas of terranes for the northern Cordillera* [Map]. Yukon Geological Survey.

Susanth, S., Kurian, P. J., Bijesh, C. M., Twinkle, D., Tyagi, A., & Rajan, S. (2021). Controls on the evolution of submarine canyons in steep continental slopes: Geomorphological insights from Palar Basin, southeastern margin of India. *Geo-Marine Letters*, *41*(1), 14.

Sutherland, R., Gurnis, M., & Kamp, P. J. J. (2009). Regional exhumation history of brittle crust during subduction initiation, Fiordland, southwest New Zealand, and implications for thermochronologic sampling and analysis strategies. *New Zealand*, 17.

Sutherland Brown, A. (1968). *Geology of the Queen Charlotte Islands*.

Swanson, D., Anderson, J., Camp, V., Hooper, P., Taubeneck, W., & Wright, T. (1981). *Reconnaissance geologic map of the Columbia River basalt group, northern Oregon and western Idaho.* USGS.

Swanson, D., Wright, T., & Helz, R. (1975). Linear vent systems and esitmated rates of magma production and eruption for the Yakima Basalt on the Columbia Plateau. *American Journal of Science*, *275*, 877–905.

Sweetkind, D. S., & Blackwell, D. D. (1989). Fission-track evidence of the Cenozoic thermal history of the Idaho batholith. *Tectonophysics*, *157*(4), 241–250.

Szeliga, W. (2013). 2012 Haida Gwaii Quake: Insight Into Cascadia's Subduction Extent. *Eos, Transactions American Geophysical Union*, *94*(9), 85–86.

ten Brink, U. S., Miller, N. C., Andrews, B. D., Brothers, D. S., & Haeussler, P. J. (2018). Deformation of the Pacific/North America Plate Boundary at Queen Charlotte Fault: The Possible Role of Rheology. *Journal of Geophysical Research: Solid Earth*, *123*(5), 4223–4242.

Tikoff, B., Kelso, P., Manduca, C., Markley, M. J., & Gillaspy, J. (2001). Lithospheric and crustal reactivation of an ancient plate boundary: The assembly and disassembly of the Salmon River suture zone, Idaho, USA. *Geological Society, London, Special Publications*, *186*(1), 213–231.

Tikoff, B., Kelso, P. R., & Kobayashi, D. (2019). The Precambrian rift-transform geometry of western Laurentian, 30 clockwise rotation of central Idaho, and implications for Yellowstone hotspot magmatism. *AGU Fall Meeting Abstracts*, *13*.

Toraman, E. (2014). *Late stage exhumation of metamorphic core complexes and landscape development during orogenic collapse of the North American Cordillera* (PhD Thesis). University of Minnesota.

Trabant, C., Hutko, A. R., Bahavar, M., Karstens, R., Ahern, T., & Aster, R. (2012). Data Products at the IRIS DMC: Stepping Stones for Research and Other Applications. *Seismological Research Letters*, *83*(5), 846–854.

Trehu, A. M., Scheidhauer, M., Rohr, K. M. M., Tikoff, B., Walton, M. A. L., Gulick,

S. P. S., & Roland, E. C. (2015). An Abrupt Transition in the Mechanical Response of the Upper Crust to Transpression along the Queen Charlotte Fault. *Bulletin of the Seismological Society of America*, *105*(2B), 1114–1128.

Valera, J. L., Negredo, A. M., & Jiménez-Munt, I. (2011). Deep and near-surface consequences of root removal by asymmetric continental delamination. *Tectonophysics*, *502*(1), 257–265.

Vanney, J.-R., & Stanley, D. J. (1983). Shelfbreak Physiography: An Overview.

VanTassell, J., Ferns, M., McConnell, V., & Smith, G. R. (2001). The mid-Pliocene Imbler fish fossils, Grande Ronde Valley, Union County, Oregon, and the connection between Lake Idaho and the Columbia River. *Oregon Geology*, *63*(3).

Walker, F., & Allen, M. B. (2012). Offset rivers, drainage spacing and the record of strike-slip faulting: The Kuh Banan Fault, Iran. *Tectonophysics*, *530-531*, 251–263.

Walton, M. A. L., Brothers, D., Miller, N. C., Kluesner, J., Haeussler, P., Barrie, J. V., & Greene, H. G. (2018). *Distribution of secondary faulting and deformation patterns along the Queen Charlotte Fault, southeastern Alaska* [T51G-0259].

Walton, M. A. L., Gulick, S. P., Reece, R. S., Barth, G. A., Christeson, G. L., & Van Avendonk, H. J. (2014). Dynamic response to strike-slip tectonic control on the deposition and evolution of the Baranof Fan, Gulf of Alaska. *Geosphere*, *10*(4), 680–691.

Walton, M. A. L., Gulick, S. P. S., Haeussler, P. J., Roland, E. C., & Trehu, A. M. (2015). Basement and Regional Structure Along Strike of the Queen Charlotte Fault in the Context of Modern and Historical Earthquake Ruptures. *Bulletin of the Seismological Society of America*, *105*(2B), 1090–1105.

Walton, M. A. L., Roland, E. C., Walter, J. I., Gulick, S. P., & Dotray, P. J. (2019). Seismic velocity structure across the 2013 Craig, Alaska rupture from aftershock tomography: Implications for seismogenic conditions. *Earth and Planetary Science Letters*, *507*, 94–104.

Waters, A. C. (1961). Stratigraphic and lithologic variations in the Columbia River basalt. *American Journal of Science*, *259*(8), 583–611.

Wells, R., Bukry, D., Friedman, R., Pyle, D., Duncan, R., Haeussler, P., & Wooden, J. (2014). Geologic history of Siletzia, a large igneous province in the Oregon and Washington Coast Range: Correlation to the geomagnetic polarity time scale and implications for a long-lived Yellowstone hotspot. *Geosphere*, *10*(4), 692–719.

Wells, R., & McCaffrey, R. (2013). Steady rotation of the Cascade arc. *Geology*, *41*(9), 1027–1030.

Wells, R., Weaver, C. S., & Blakely, R. J. (1998). Fore-arc migration in Cascadia and its neotectonic significance. *Geology*, *26*(8), 759–762.

Whipple, K. X., & Tucker, G. E. (1999). Dynamics of the stream-power river incision model: Implications for height limits of mountain ranges, landscape response timescales, and research needs. *Journal of Geophysical Research: Solid Earth*, *104*(B8), 17661–17674.

Wilson, D. (2002). The Juan de Fuca plate and slab: Isochron structure and Cenozoic plate motions. In *The Cascadia Subduction Zone and related subduction systems: Seismic structure, intraslab earthquakes and processes, and earthquake hazards.*

Wilson, D., & Cox, A. (1980). Paleomagnetic evidence for tectonic rotation of Jurassic plutons in Blue Mountains, eastern Oregon. *Journal of Geophysical Research: Solid Earth*, *85*(B7), 3681–3689.

Wolf, R. A., Farley, K. A., & Kass, D. M. (1998). Modeling of the temperature sensitivity of the apatite U–Th/ rHe thermochronometer. *Chemical Geology*, 10.

Wyld, S. J., Umhoefer, P. J., & Wright, J. E. (2006). Reconstructing northern Cordilleran terranes along known Cretaceous and Cenozoic strike-slip faults: Implications for the Baja British Columbia hypothesis and other models. , 22.

Yorath, C. J., & Hyndman, R. D. (1983). Subsidence and thermal history of Queen Charlotte Basin. *Canadian Journal of Earth Sciences*, *20*(1), 135–159.

Žák, J., Verner, K., Tomek, F., Holub, F. V., Johnson, K., & Schwartz, J. J. (2015). Simultaneous batholith emplacement, terrane/continent collision, and oroclinal bending in the Blue Mountains Province, North American Cordillera: Oroclinal bending in the Blue Mountains. *Tectonics*, *34*(6), 1107–1128.

Zapata, S., Sobel, E. R., del Papa, C., Jelinek, A. R., & Glodny, J. (2019). Using a Paleosurface to Constrain Low-Temperature Thermochronological Data: Tectonic Evolution of the Cuevas Range, Central Andes. *Tectonics*, *38*(11), 3939–3958.

Zhang, J., & Gulick, S. P. (2020). Sequence stratigraphy and depositional history of the Baranof Fan: Insights for Cordilleran Ice Sheet outflow to the Gulf of Alaska. *GSA Bulletin*, *132*(1-2), 353–372.

Appendix A

SUPPLEMENTAL FIGURES

A.1 Chapter 2 Supplemental Figures

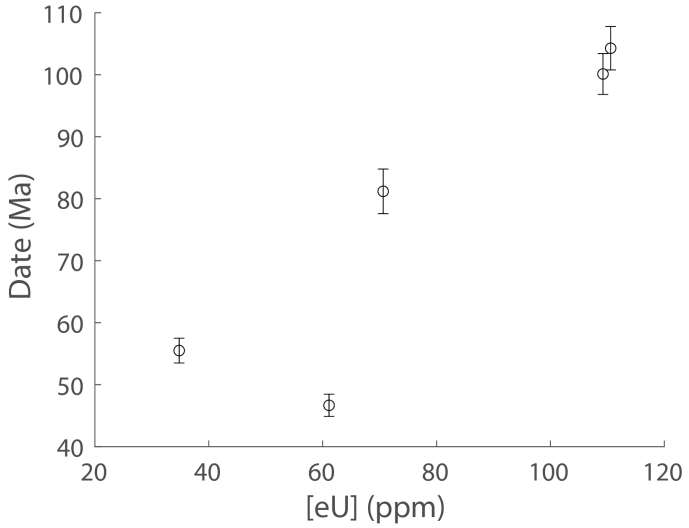

Figure A.1: Date-eU plot for sample WM08 from the Bald Mountain Batholith.

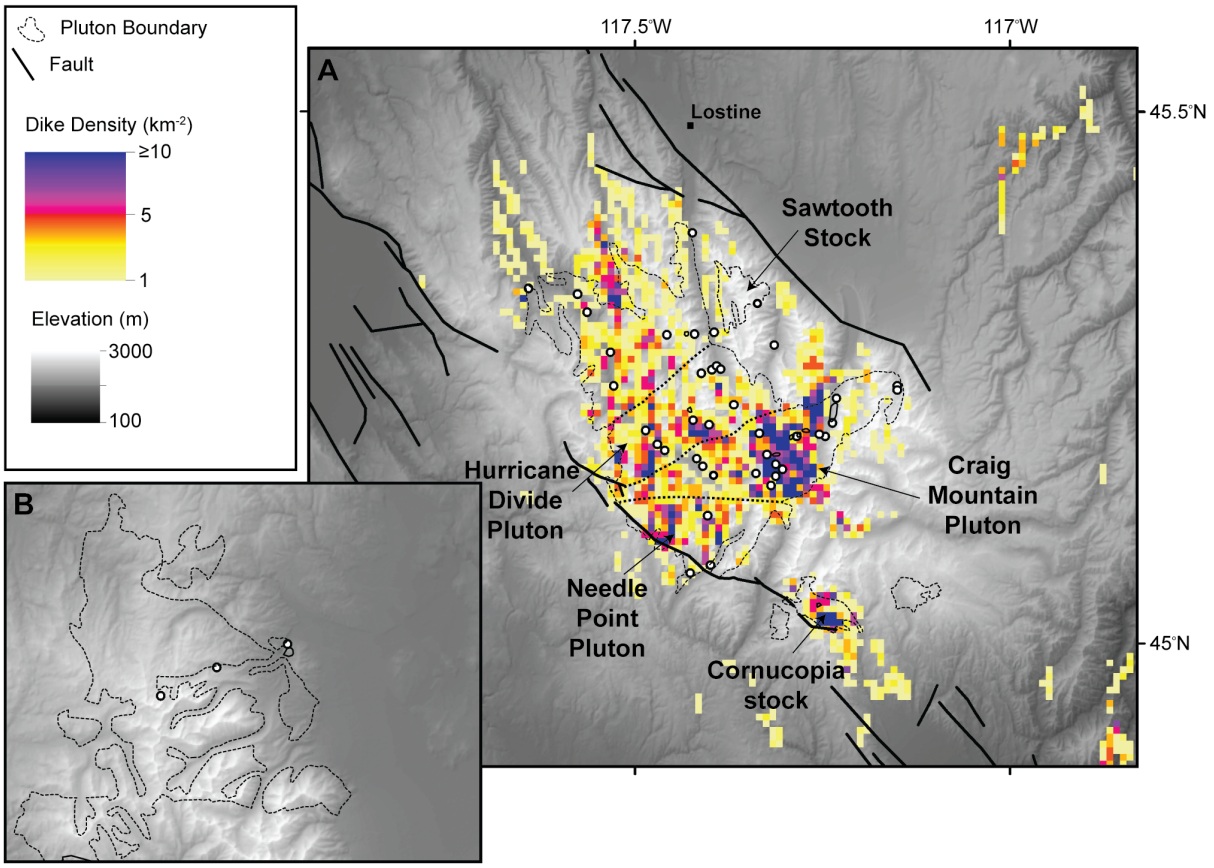

Figure A.2: Density of dikes in the Wallowa Mountains and surroundings

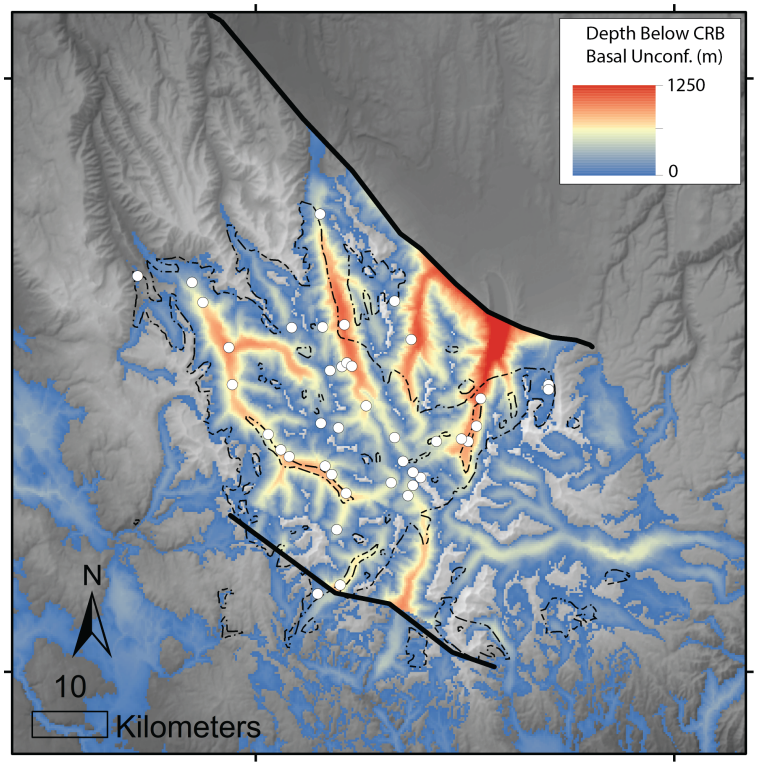

Figure A.3: Estimated incision depth below the CRB basal unconformity with barriers used to constrain surface interpolation drawn as thick black lines, dashed outline of Wallowa Batholith, and sample locations marked with white circles.

A.2 Chapter 3 Supplemental Figures

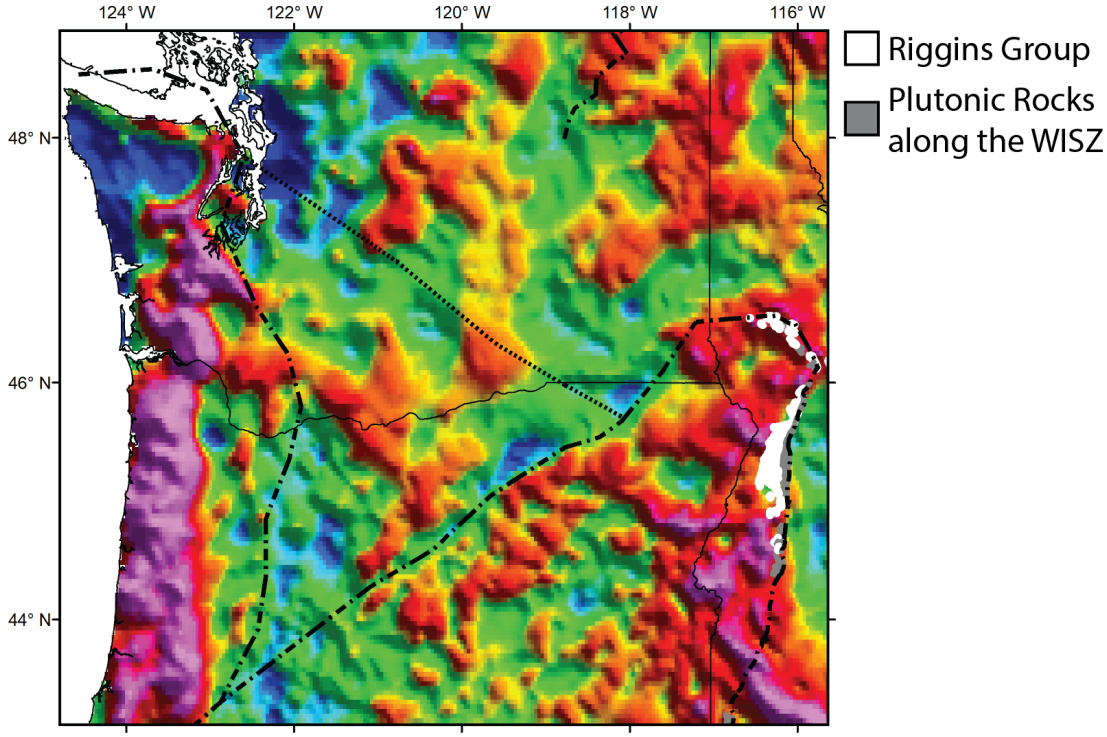

Figure A.4: Isostatic gravity map and bedrock units used to map terrane boundaries. Hotter colors are increasingly positive isostatic gravity anomalies. Isostatic gravity downloaded from https://mrdata.usgs.gov/gravity/isostatic/.

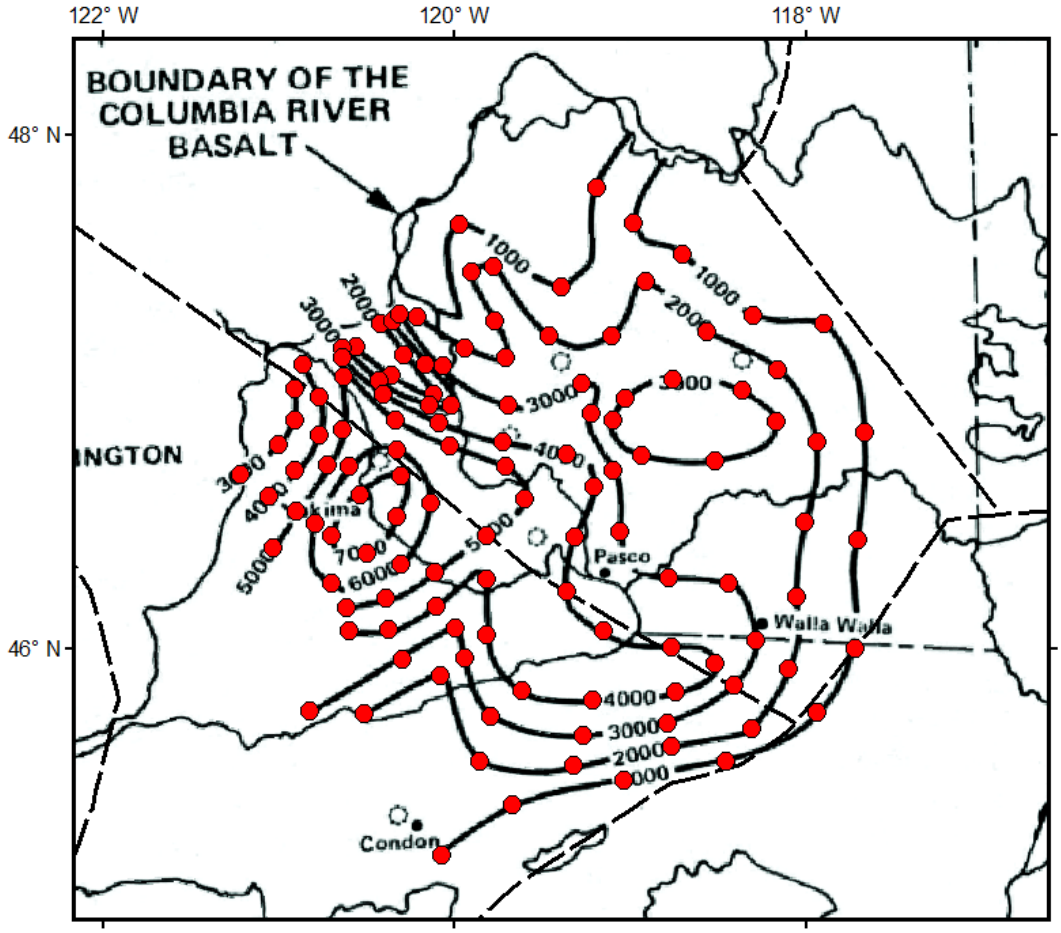

Figure A.5: Isopach of pre-CRB sediments in the Columbia Basin with points used to constrain interpolation. Isopach from (Campbell, 1989).

A.3 Chapter 4 Supplemental Figures

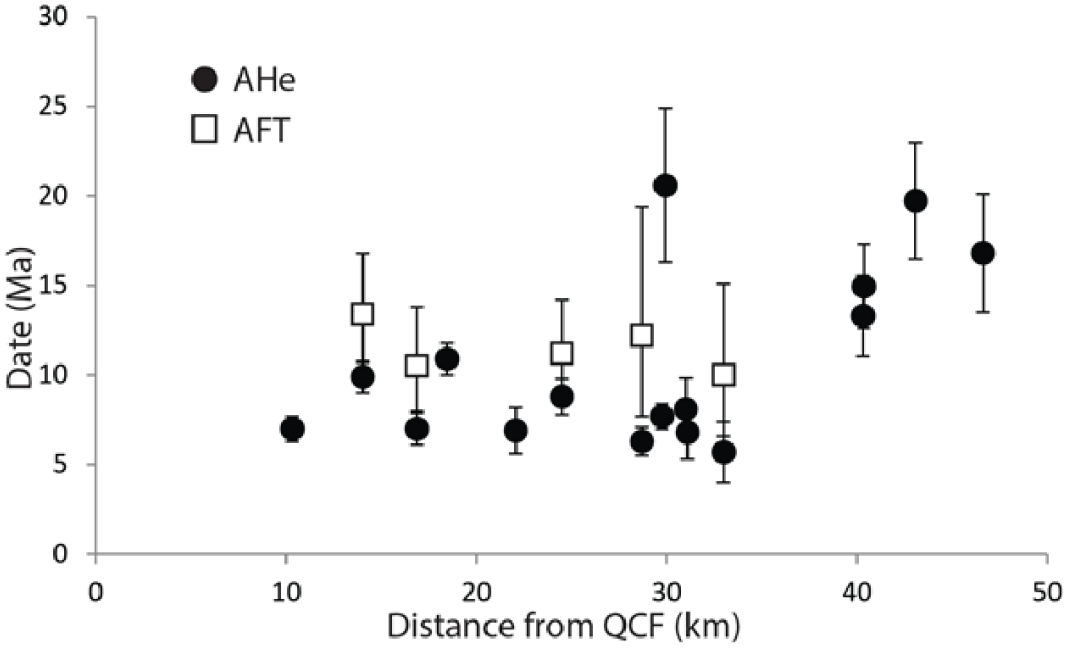

Figure A.6: AHe and AFT dates from Haida Gwaii plotted relative to the plate boundary as defined by the Queen Charlotte Fault.

A.4 Chapter 5 Supplemental Figures

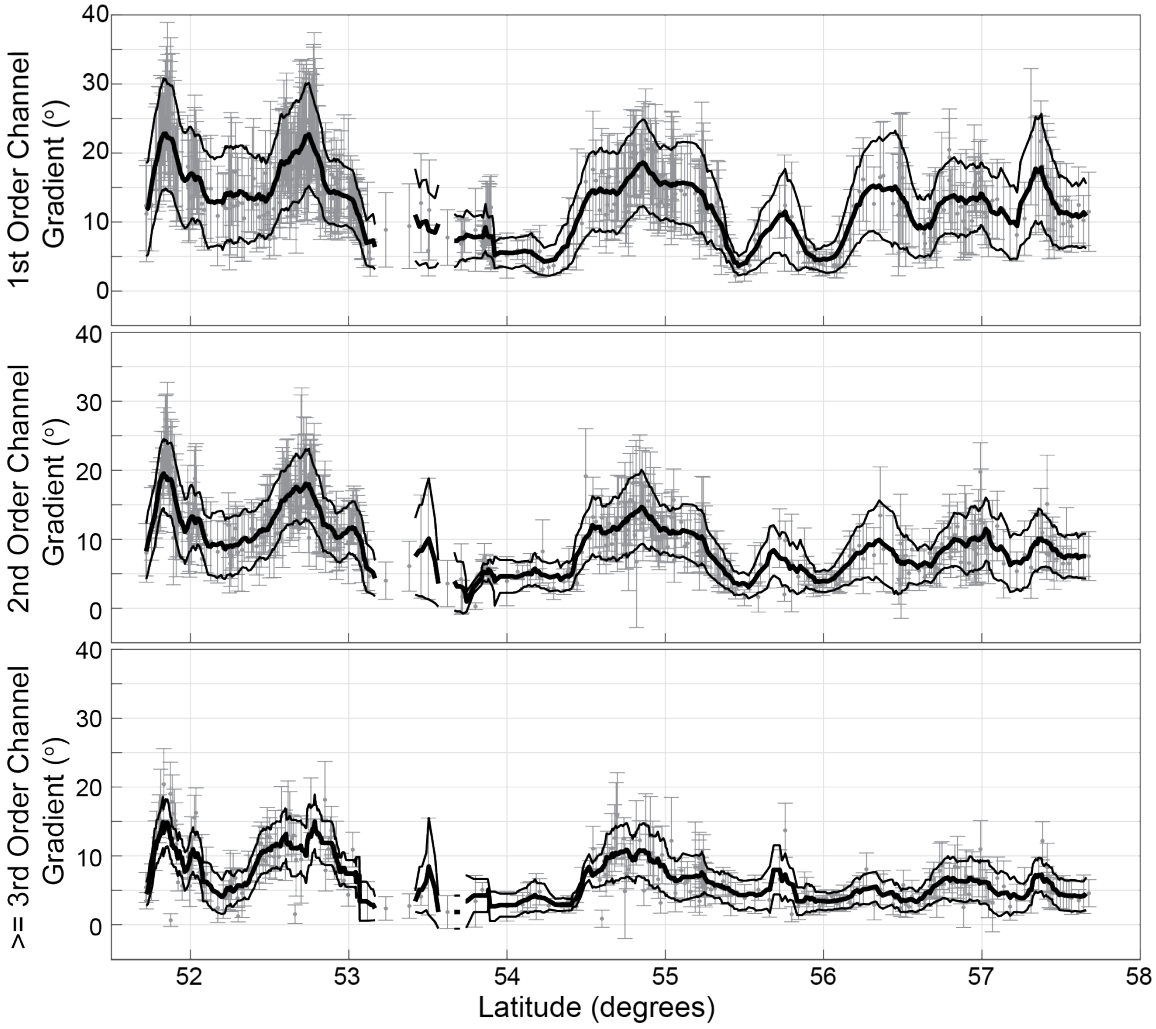

Figure A.7: Average gradient of first, second, and third or greater order submarine channels. 1σ error bars applied to all measurements.

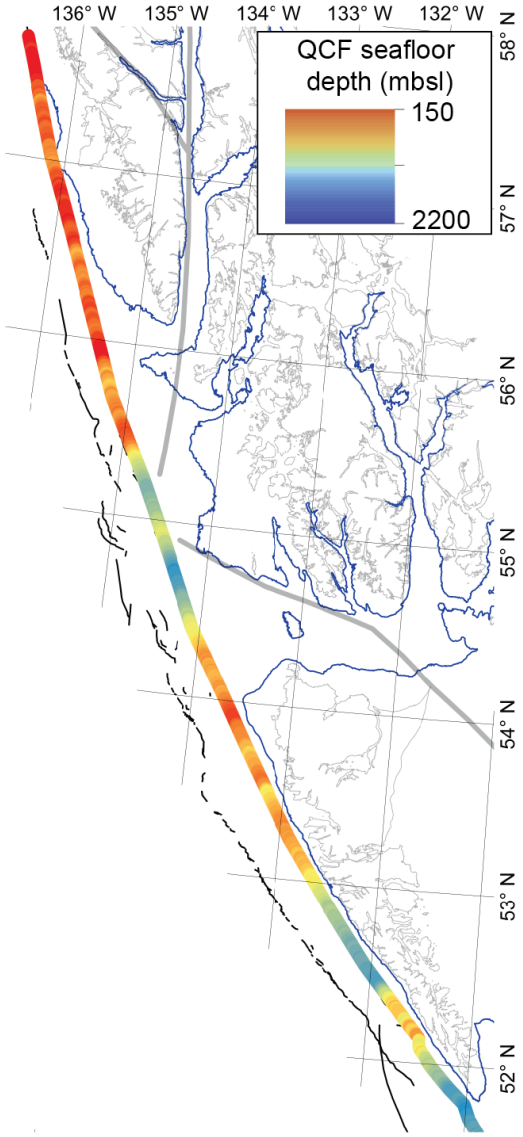

Figure A.8: Depth of the Queen Charlotte Fault overlain on simplified tectonic and geographic map. Thick grey line marks terrane boundaries. Black lines mark faults mapped from bathymetry.

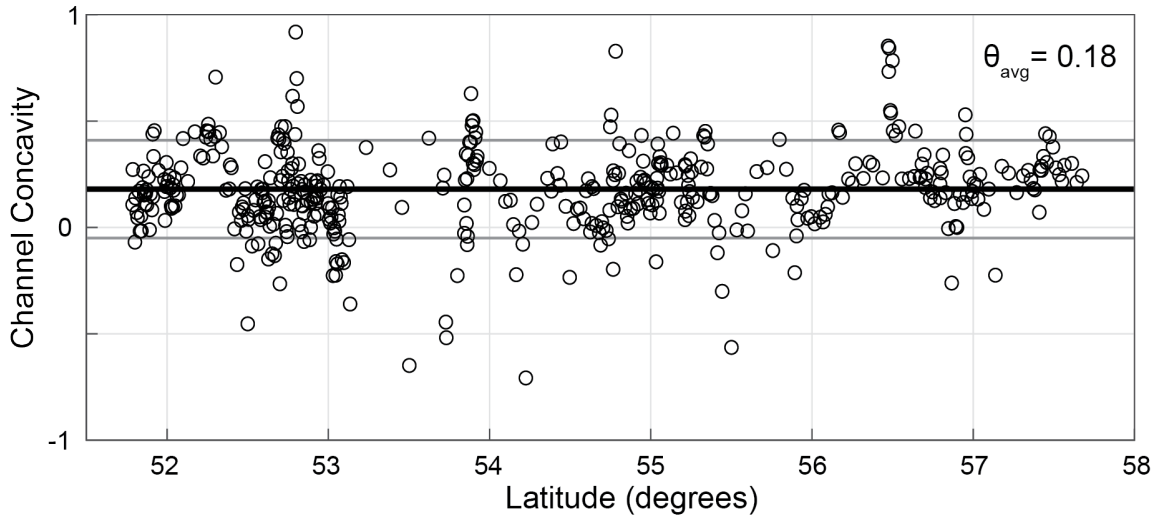

Figure A.9: Submarine channel concavity. Average and 1σ shown as horizontal bars.

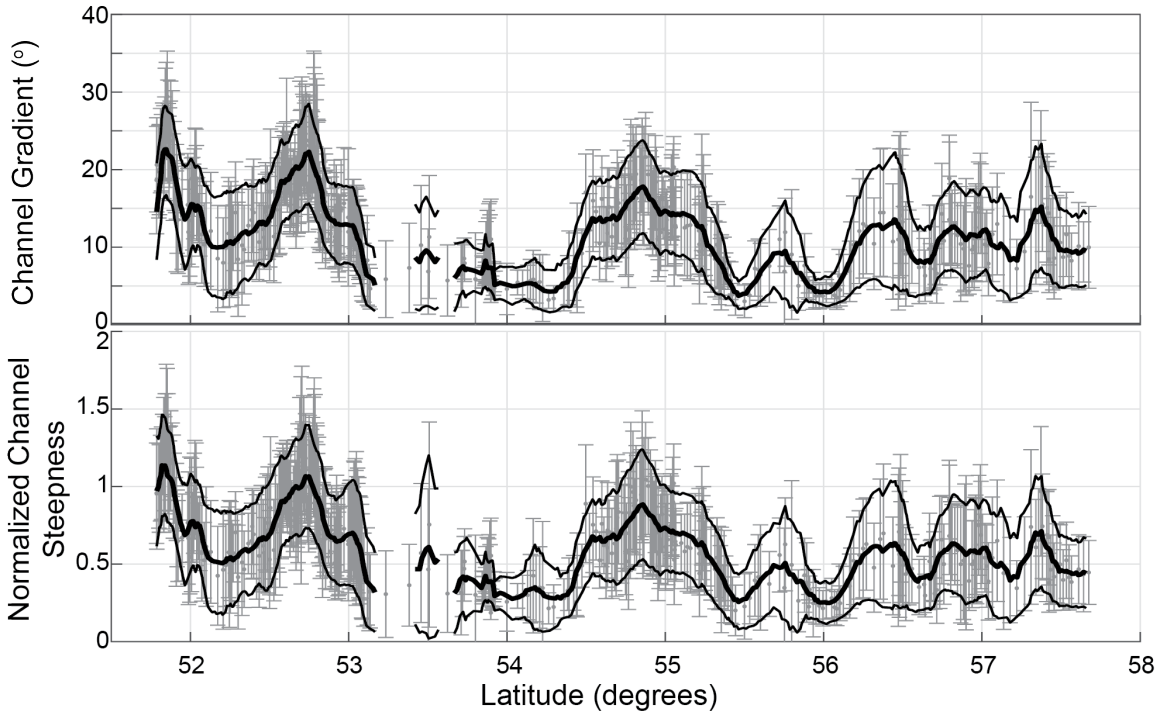

Figure A.10: Comparison between average channel gradient and average normalized channel steepness for submarine channels. 1σ error bars applied to all measurements.

Appendix B

APATITE (U-TH)/HE THERMOCHRONOMETRY DATA

B.1 Apatite (U-Th)/He Thermochronometry data from the Wallowa and Elkhorn Mountains

Table B.1: Apatite (U-Th)/He thermochronometry data from the Wallowa and Elkhorn Mountains. [a] equivalent spherical radius; [b] Number of grain termini. 0 – Both tips broken; 1 – One tip broken; 2 – Whole grain; [c] Effective uranium concentration, calculated as U+0.235*Th; [d] alpha-ejection correction of (Farley, 2000); [e] Analytically uncertainty based on U, Th, He, Sm, and grain length measurements. Grains in italics were excluded from means, plots, and models. They were excluded because either [f] Ft <0.6, [g] Re-extraction <98%, or [h] failure of the Peirce outlier test (Ross, 2003).

Sample	Grain	Mass (μg)	r[a] (μm)	T[b]	He (nmol/g)	U (ppm)	Th (ppm)	Sm (ppm)	eU[c] (ppm)	Raw (Ma)	Date	Ft[d]	Date (Ma)	1σ [e]
WM06														
	a[h]	*1.56*	*55.3*	*2*	*10.40*	*17.75*	*24.17*	*257.97*	*23.41*	*80.10*		*0.72*	*110.24*	*4.3*
	b[h]	*2.16*	*58.5*	*2*	*8.98*	*17.96*	*27.04*	*216.55*	*24.29*	*66.87*		*0.74*	*90.09*	*3.2*
	c	2.88	50.0	2	4.10	15.45	18.14	236.38	19.69	37.58		0.73	51.01	1.8
	d	1.27	66.3	2	3.29	15.62	26.90	274.86	21.92	27.09		0.77	34.94	1.5
	e	2.16	53.4	2	3.11	10.84	16.89	189.92	14.79	37.98		0.72	52.30	2.2
WM07														
	a	1.15	50.4	2	5.88	27.48	26.64	171.93	33.72	31.79		0.71	44.70	1.8
	b	1.85	49.9	2	4.67	24.54	28.29	244.72	31.16	27.21		0.74	36.85	1.3
	c	1.15	58.1	2	7.83	26.23	30.78	284.32	33.43	42.49		0.71	59.73	2.4
	d	0.84	49.0	2	6.45	29.99	34.68	317.50	38.11	30.75		0.69	44.56	1.9
	e	3.67	66.3	2	4.89	14.47	18.43	189.56	18.78	47.06		0.77	60.77	2.0
WM08														
	a	1.46	51.3	2	7.85	29.50	22.66	409.24	34.80	40.75		0.73	55.50	2.0
	b	0.82	44.7	2	11.07	50.32	46.18	510.41	61.12	32.88		0.70	46.67	1.8
	c	0.44	48.0	2	20.73	60.44	43.57	597.43	70.63	53.19		0.65	81.19	3.6
	d	1.10	39.0	2	40.87	81.66	117.84	577.21	109.23	67.97		0.67	100.12	3.3
	e	1.04	47.0	2	43.16	87.37	99.16	492.86	110.58	70.95		0.68	104.27	3.5
WM21														
	a	1.17	53.2	2	2.75	17.74	32.54	252.39	25.36	19.64		0.71	27.48	1.3
	b	1.73	55.4	2	2.31	14.62	28.32	153.60	21.25	19.76		0.72	27.36	1.2
	c	1.32	51.1	2	1.56	14.96	27.15	236.08	21.31	13.23		0.71	18.59	1.0

	d	1.34	49.5	2	1.87	14.82	33.72	132.75	22.71	15.01	0.69	21.64	1.1
	e	0.82	46.1	2	1.99	19.57	34.72	267.85	27.69	13.03	0.69	18.84	1.2
WM22													
	a	1.58	54.4	2	23.72	44.73	96.32	411.83	67.27	63.99	0.72	88.65	2.8
	b	1.71	52.6	2	29.52	55.87	86.59	401.88	76.13	70.41	0.71	99.14	3.1
	c	2.70	56.5	2	20.90	40.64	65.99	308.03	56.09	67.67	0.73	92.67	2.8
	d	1.90	58.1	2	29.30	55.67	86.33	451.95	75.87	70.08	0.74	94.05	2.8
	e	3.17	61.4	2	20.36	37.21	50.76	252.02	49.09	75.28	0.76	98.90	2.8
WM23													
	a	1.65	47.9	2	27.42	54.76	68.01	264.37	70.68	70.58	0.69	101.43	3.3
	b	2.83	58.8	2	37.73	75.47	91.78	328.23	96.95	70.83	0.74	94.84	2.6
	c	0.76	43.9	2	44.05	98.73	126.19	454.93	128.26	62.54	0.66	93.61	3.2
	d	1.05	47.7	2	35.28	74.54	96.95	409.72	97.22	66.01	0.69	95.44	3.2
	e	0.61	44.5	2	46.26	104.85	132.45	617.68	135.84	61.94	0.68	90.34	3.1
WM24													
	a	1.26	50.5	2	74.62	156.60	139.14	424.10	189.16	71.88	0.71	100.98	2.9
	b	0.47	38.2	2	72.77	174.89	221.61	528.03	226.75	58.54	0.64	91.51	3.3
	c	0.77	41.6	1	66.27	192.98	109.80	379.34	218.67	55.35	0.65	84.42	2.8
	d	1.49	45.6	2	59.25	142.92	92.15	278.48	164.48	65.72	0.69	95.55	2.9
	e	0.61	40.1	2	80.29	213.77	138.08	380.14	246.08	59.57	0.65	91.64	3.1
WM25													
	a	1.45	49.4	2	4.81	57.66	72.38	385.07	74.60	11.77	0.71	16.62	0.6
	b	1.51	49.6	1	4.83	55.00	67.13	403.23	70.71	12.46	0.70	17.63	0.6
	c	1.01	46.4	2	7.61	95.90	99.35	430.09	119.15	11.68	0.69	16.85	0.6
	d	1.76	50.5	2	4.11	47.25	60.36	247.38	61.37	12.25	0.71	17.27	0.6
	e	1.27	47.8	2	3.96	47.34	58.43	335.66	61.02	11.84	0.69	17.01	0.6
WM27													
	a	2.42	51.3	2	8.70	21.94	30.00	290.82	28.96	54.30	0.72	74.74	2.5
	b^h	*1.06*	*49.4*	*2*	*23.52*	*42.09*	*58.38*	*611.91*	*55.75*	*76.06*	*0.70*	*108.04*	*3.9*
	c	0.88	45.4	2	24.30	83.71	71.31	349.02	100.40	44.15	0.69	63.31	2.1
	d	0.91	47.6	1	16.06	46.14	68.22	624.42	62.11	46.78	0.68	68.58	2.6
	e	2.70	57.0	2	13.63	34.06	53.71	534.26	46.63	52.76	0.75	70.02	2.1
WM28													
	a	2.35	56.5	2	4.40	13.97	14.64	265.04	17.39	45.55	0.73	62.00	2.4
	b	1.23	47.0	2	6.84	40.92	29.07	589.29	47.72	25.91	0.69	37.06	1.4
	c	2.58	55.7	2	2.16	18.26	16.06	455.87	22.02	17.54	0.74	23.50	0.9
	d	0.82	44.4	2	2.86	6.24	20.45	787.00	11.03	43.76	0.66	63.34	4.6
	e	0.96	41.6	2	3.97	23.43	20.81	345.74	28.30	25.37	0.65	38.60	1.9
WM29													
	a	0.97	46.0	1	64.83	128.60	164.11	480.07	167.01	70.69	0.68	103.81	3.3
	b	2.24	47.5	2	29.81	53.78	80.32	203.93	72.58	74.78	0.69	107.56	3.4
	c	2.02	51.3	1	93.91	195.09	225.27	384.98	247.81	69.13	0.73	94.80	2.5
	d	1.12	50.1	1	69.49	184.69	160.50	489.52	222.24	57.06	0.70	80.78	2.3
	e	0.64	43.4	2	88.33	234.48	164.28	597.68	272.92	59.05	0.67	87.60	2.8
WM30													
	a	2.36	52.7	2	9.23	19.24	38.72	380.31	28.30	58.70	0.72	80.74	2.7
	b	1.35	49.7	2	12.28	29.52	26.96	453.46	35.83	61.75	0.70	86.88	3.2
	c	0.99	48.1	2	15.50	36.24	28.99	403.92	43.03	65.13	0.70	92.17	3.6

	d	0.68	45.7	2	13.43	31.67	34.35	793.29	39.71	60.41	0.67	89.46	4.0
	e[h]	*0.89*	*42.4*	*2*	*15.08*	*49.99*	*32.73*	*430.51*	*57.65*	*47.46*	*0.67*	*70.62*	*2.7*
WM31													
	a	6.30	72.7	2	1.87	17.02	18.34	301.71	21.31	15.81	0.79	19.96	0.6
	b	3.72	65.1	2	2.47	27.37	26.93	322.89	33.67	13.34	0.77	17.23	0.5
	c	4.23	67.0	2	2.47	28.12	24.40	308.69	33.83	13.29	0.77	17.16	0.5
	d	3.22	54.0	2	2.68	30.90	21.67	248.55	35.97	13.60	0.75	18.07	0.6
	e	2.14	55.5	2	3.52	37.85	44.38	431.64	48.24	13.27	0.74	17.88	0.6
WM35													
	a	1.51	46.8	2	19.24	39.71	65.70	534.92	55.08	63.13	0.69	90.50	3.1
	b	2.41	61.8	1	14.12	27.13	62.25	440.84	41.70	61.17	0.75	81.52	2.5
	c	1.71	52.4	2	22.33	49.61	64.18	504.26	64.63	62.60	0.73	84.98	2.6
	d[g]	*1.12*	*46.4*	*2*	*20.53*	*32.05*	*59.85*	*586.09*	*46.05*	*80.19*	*0.69*	*115.36*	*4.3*
	e	5.64	69.3	2	15.71	31.19	42.29	313.79	41.08	69.25	0.76	90.41	2.4
WM39													
	a	3.52	57.1	2	2.26	25.80	27.34	364.15	32.20	12.70	0.75	16.85	0.5
	b	3.44	61.5	2	1.47	16.11	20.67	333.74	20.95	12.63	0.75	16.73	0.6
	c	3.35	62.4	2	2.23	24.67	31.45	486.31	32.03	12.57	0.76	16.45	0.5
	d	2.21	59.8	1	1.57	17.32	27.55	384.38	23.77	11.92	0.74	15.99	0.7
	e	1.70	53.8	2	1.94	24.34	26.71	279.62	30.59	11.52	0.72	15.97	0.7
WM42													
	a	1.77	45.3	2	47.31	108.99	63.57	223.36	123.87	69.64	0.67	103.12	3.2
	b	1.24	50.1	2	64.06	156.20	94.69	429.52	178.36	65.47	0.70	92.68	2.7
	c	1.50	52.5	2	68.39	145.96	93.65	292.72	167.87	74.25	0.71	103.95	3.0
	d	2.10	54.1	2	80.09	193.77	104.75	424.94	218.28	66.91	0.74	90.04	2.3
	e	2.50	58.5	2	57.62	124.25	66.16	214.88	139.73	75.18	0.74	100.73	2.6
WM51													
	a	1.99	52.9	2	22.75	68.02	85.77	411.00	88.09	47.03	0.72	65.53	1.9
	b	1.49	51.2	2	27.40	69.15	95.34	485.97	91.46	54.47	0.72	75.68	2.3
	c	1.70	53.2	1	26.49	71.79	105.21	450.74	96.41	50.03	0.73	68.39	2.0
	d[h]	*2.01*	*57.5*	*2*	*24.75*	*101.03*	*90.97*	*378.34*	*122.31*	*36.95*	*0.73*	*50.17*	*1.4*
	e	1.93	53.5	2	27.24	66.77	96.55	494.65	89.36	55.42	0.73	75.20	2.2
WM52													
	a	1.94	54.3	2	31.60	73.12	96.84	372.48	95.78	60.06	0.73	82.29	2.4
	b	0.98	44.5	1	49.33	121.43	132.16	294.38	152.35	59.09	0.68	86.06	2.7
	c	2.31	54.0	1	25.82	60.33	75.53	244.53	78.00	60.33	0.72	83.20	2.4
	d[g]	*3.63*	*64.2*	*2*	*0.12*	*51.12*	*83.98*	*302.32*	*70.77*	*0.31*	*0.76*	*0.40*	*0.1*
WM53													
	a	1.38	54.6	0	45.86	119.17	9.10	342.80	121.30	68.85	0.73	94.20	2.8
	b	0.52	42.6	1	30.75	105.99	115.58	507.60	133.04	42.15	0.66	63.93	2.4
	c	1.12	42.9	1	28.91	86.91	82.76	236.33	106.27	49.68	0.67	74.26	2.5
	d	0.44	43.1	1	71.84	192.18	52.98	621.55	204.58	63.97	0.65	97.50	3.5
WM54													
	a	0.91	48.9	1	25.42	36.45	62.22	401.20	51.01	90.08	0.69	129.11	4.9
	b	1.19	50.4	2	15.38	22.76	37.87	379.36	31.62	87.47	0.70	123.13	4.8
	c[h]	*1.13*	*43.2*	*2*	*11.56*	*13.00*	*20.14*	*193.13*	*17.71*	*117.23*	*0.68*	*171.38*	*8.1*
	d	0.71	44.7	1	30.98	60.63	85.81	356.22	80.71	69.79	0.66	104.38	3.9
	e[g]	*6.09*	*70.7*	*1*	*12.96*	*21.19*	*25.23*	*277.14*	*27.09*	*86.27*	*0.79*	*109.09*	*3.0*

WB005												
	a	71.00	65.5	-	159.58	19.67	19.90	-	24.34	54.03	0.77	70.30	0.7
WB009												
	a	46.15	66.1	-	40.49	11.52	13.12	-	14.60	22.91	0.77	29.70	0.3
	b	52.88	80.0	-	37.08	9.30	12.32	-	12.19	25.12	0.81	31.00	0.4
WB010												
	a	28.18	56.6	-	424.69	49.30	34.71	-	57.45	60.92	0.73	83.10	1.0
WB017												
	a	18.76	46.6	-	258.06	25.50	16.98	-	29.49	72.05	0.68	106.40	1.2
WB034												
	a	31.37	53.0	-	100.18	55.94	84.79	-	75.85	10.91	0.71	15.30	0.1
WB101												
	a	27.06	68.3	-	462.37	31.78	66.19	-	47.34	80.26	0.78	103.10	1.0
	b	15.89	77.2	-	514.57	29.95	90.50	-	51.22	82.48	0.80	102.60	1.0
	c	5.88	35.6	-	303.37	27.20	67.04	-	42.96	58.10	0.58	99.90	1.2
WB104												
	a	76.81	89.4	-	89.41	46.35	53.06	-	58.81	12.43	0.83	15.00	0.1
	b	19.04	43.1	-	75.41	43.43	60.53	-	57.65	10.81	0.65	16.60	0.2
WB109												
	a	27.83	55.4	-	242.60	25.04	35.23	-	33.32	59.95	0.72	82.50	0.8
	b	7.36	41.5	-	263.86	28.12	38.67	-	37.21	58.40	0.64	91.40	1.1
WB112												
	a	11.42	38.6	-	122.09	33.78	39.07	-	42.96	23.48	0.61	38.40	0.5
WB118												
	a	26.31	54.4	-	64.63	34.90	35.16	-	43.16	12.38	0.72	17.20	0.1
	b	42.52	55.5	-	52.83	26.60	32.00	-	34.12	12.80	0.73	17.60	0.1
WB121												
	a	50.91	49.8	-	207.90	40.30	43.33	-	50.48	34.00	0.70	48.80	0.4
	b	32.68	68.2	-	241.54	39.61	36.89	-	48.28	41.29	0.78	53.10	0.5
WB130												
	a	161	82.8	-	139.97	15.02	13.32	-	18.15	63.53	0.82	77.80	0.7
WB131												
	a	66.16	65.6	-	57.06	6.65	7.60	-	8.43	55.77	0.77	72.50	0.8
WB139												
	a	-	52.0	-	276.51	35.11	28.19	-	41.74	53.92	0.71	76.00	1.0
	b	42.06	72.9	-	295.42	32.97	29.98	-	40.02	60.82	0.79	76.80	0.9
WB141												
	a	23.60	47.7	-	128.35	20.41	16.95	-	24.40	43.41	0.68	63.50	0.7
	b	19.45	53.1	-	127.57	17.71	14.10	-	21.02	50.05	0.72	70.00	0.7
WB143												

a	37.47	61.1	-	155.83	15.84	17.90	-	20.50	64.00	0.75	85.10	0.9
WB146												
a	64.20	60.9	-	61.58	13.15	13.00	-	16.21	31.38	0.75	41.80	0.4
WB149												
a	128	75.2	-	34.55	16.00	14.58	-	19.43	14.70	0.80	18.40	0.1
b	47.94	68.7	-	26.78	12.68	13.16	-	15.77	14.04	0.78	18.00	0.1
WB152												
a	66.44	65.3	-	212.56	20.32	23.85	-	25.93	67.49	0.77	87.90	0.9
b	46.97	63.8	-	181.18	17.60	22.24	-	22.83	65.33	0.76	85.70	0.8
WB154												
a	81.29	70.9	-	117.04	12.62	14.75	-	16.08	59.95	0.79	76.30	0.8
WB158												
a	151.89	85.8	-	91.53	11.88	14.38	-	15.26	49.45	0.82	60.10	0.6
b	40.71	63.0	-	91.00	12.15	16.06	-	15.92	47.12	0.76	62.10	0.7
WB166												
a	25.25	45.3	-	515.91	46.65	59.34	-	60.59	70.07	0.67	104.90	0.9
WB250												
a	88.39	71.9	-	740.90	66.71	41.79	-	76.53	79.67	0.79	100.90	1.1
b	55.37	60.5	-	715.86	65.58	44.53	-	76.05	77.48	0.75	103.30	0.9
WB267												
a	23.08	54.0	-	109.70	13.83	12.91	-	16.86	53.63	0.72	74.50	0.8
b	11.11	79.0	-	78.22	8.71	10.48	-	11.17	57.67	0.81	71.40	1.6
c	9.03	38.2	-	80.37	10.87	11.68	-	13.61	48.68	0.61	80.00	1.2

B.2 Apatite (U-Th)/He Thermochronometry data from Haida Gwaii

Table B.2: Apatite (U-Th)/He thermochronometry data from Haida Gwaii. [a] equivalent spherical radius; [b] Number of grain termini. 0 – Both tips broken; 1 – One tip broken; 2 – Whole grain; [c] Effective uranium concentration, calculated as U+0.235*Th; [d] alpha-ejection correction of (Farley, 2000); [e] Analytically uncertainty based on U, Th, He, Sm, and grain length measurements. Grains in italics were excluded from means, plots, and models. They were excluded because either [f] Ft <0.6, [g] Re-extraction <98% or, [h] failure of the Peirce outlier test (Ross, 2003)

Sample	Grain	Mass (μg)	r[a] (μm)	T[b]	He (nmol/g)	U (ppm)	Th (ppm)	Sm (ppm)	eU[c] (ppm)	Raw Date (Ma)	Ft[d]	Date (Ma)	1σ [e]
BARRY													
	a	1.0	39.0	2	7.15	145.5	167.2	15.5	184.8	7.16	0.64	11.16	0.24
	b[f]	*0.7*	*33.3*	*2*	*4.8*	*111.7*	*137.1*	*12.6*	*143.9*	*6.16*	0.58	*10.61*	*0.31*
	c	0.8	35.7	2	5.0	114.4	132.7	11.8	145.6	6.38	0.609	10.45	0.44
	d	1.4	43.3	2	5.53	114.6	142.9	18.9	148.1	6.90	0.676	10.20	0.28

HG02												
	a	1.9	46.8	2	0.36	20.8	31.6	11.5	28.2	2.38	0.693	3.43	0.22
	b	0.8	34.2	2	0.3	11.3	5.8	9.8	12.7	3.83	0.596	6.40	0.78
	c	2.5	45.8	1	0.4	11.8	13.5	7.4	14.9	4.97	0.689	7.21	0.37
	d	1.8	44.0	1	0.59	19.0	15.1	9.8	22.6	4.82	0.684	7.04	0.40
	e	2.3	45.1	1	0.4	20.9	29.4	10.3	27.8	2.91	0.683	4.25	0.3
HG03													
	a	3.4	50.9	2	1.21	41.8	21.5	11.5	46.8	4.80	0.722	6.63	0.27
	b	3.6	53.9	1	1.3	40.2	25.2	7.1	46.1	5.40	0.739	7.30	0.28
	c	1.4	43.3	2	1.8	51.7	25.4	8.5	57.7	5.63	0.68	8.26	0.25
	d	1.9	45.9	2	1.59	46.5	27.2	10.0	52.9	5.58	0.695	8.02	0.40
	e	1.1	36.7	2	1.7	54.7	28.0	12.9	61.2	5.08	0.621	8.16	0.5
HG04													
	a	1.0	39.5	2	2.45	63.1	69.5	18.3	79.4	5.70	0.645	8.82	0.50
	b	2.1	44.1	2	2.4	47.7	67.1	15.8	63.5	6.88	0.676	10.17	0.27
	c	1.5	44.1	2	2.0	47.9	54.9	14.6	60.8	6.16	0.679	9.05	0.31
	d	1.9	45.0	1	1.52	42.9	51.7	12.1	55.0	5.11	0.687	7.42	0.31
	e	1.5	40.7	2	1.7	43.8	50.6	15.1	55.7	5.69	0.651	8.72	0.5
HG05													
	a[g]	*2.8*	*53.9*	*2*	*2.45*	*44.2*	*69.5*	*11.5*	*60.5*	*5.99*	*0.733*	*8.17*	*0.31*
	b	1.0	39.4	2	2.4	66.2	108.6	16.7	91.7	5.64	0.64	8.80	0.49
	c	1.1	38.0	2	2.0	93.9	147.3	21.0	128.5	5.33	0.624	8.53	0.30
	d[g]	*1.2*	*40.7*	*2*	*1.52*	*77.7*	*123.1*	*15.9*	*106.6*	*4.29*	*0.652*	*6.57*	*0.22*
	e	1.3	41.9	2	1.7	57.2	87.9	14.5	77.8	5.32	0.661	8.03	0.3
HG06													
	a	1.1	37.8	1	4.62	131.0	164.4	14.0	169.6	5.04	0.633	7.95	0.29
	b	1.0	37.7	2	5.8	157.2	166.7	15.4	196.3	5.46	0.629	8.66	0.37
	c	1.5	44.6	2	5.6	188.9	236.2	12.6	244.5	4.23	0.684	6.18	0.18
	d	3.5	57.3	2	2.15	76.3	95.5	7.6	98.7	4.02	0.749	5.37	0.16
	e	1.7	45.7	2	3.6	118.6	132.1	15.0	149.7	4.45	0.69	6.44	0.2
HG09													
	a	2.5	47.9	1	0.59	6.4	13.5	35.8	9.6	11.07	0.699	15.69	0.94
	b[h]	*1.6*	*42.5*	*1*	*7.0*	*11.4*	*63.1*	*36.0*	*26.2*	*48.63*	*0.651*	*74.21*	*2.66*
	c	1.2	37.6	1	0.7	6.4	10.0	51.8	8.7	14.10	0.626	22.09	1.77
	d[f]	*0.7*	*33.3*	*1*	*6.21*	*10.8*	*30.4*	*58.9*	*18.0*	*61.91*	*0.58*	*104.99*	*9.45*
	e	1.0	38.1	2	0.8	7.3	10.3	56.0	9.7	15.33	0.628	23.92	3.5
HG10													
	a	1.3	41.7	2	2.231	68.7	33.26	12.93	76.5	5.40	0.667	8.08	0.28
	b	2.9	51.3	1	1.411	49.1	30.07	9.57	56.1	4.65	0.728	6.39	0.25
	c	0.9	36.5	2	2.063	80.7	41.57	12.99	90.5	4.22	0.622	6.78	0.36
	d	0.8	35.6	2	2.608	92.2	52.16	15.86	104.4	4.62	0.616	7.50	0.49
	e	2.1	46.7	1	1.336	48.2	29.50	10.44	55.1	4.49	0.704	6.37	0.16
HG12													
	a	2.69	49.46	2	0.865	21.47	21.34	19.73	26.5	6.02	0.711	8.44	0.45
	b	1.98	45.58	2	1.345	28.00	30.43	29.12	35.1	7.04	0.688	10.20	0.30
	c	1.72	44.50	2	1.268	24.87	28.09	30.48	31.5	7.40	0.681	10.83	0.87
	d	3.65	52.73	1	0.797	15.37	19.76	18.30	20.0	7.32	0.728	10.02	0.42
	e	3.19	51.48	1	1.100	21.99	28.28	21.78	28.6	7.07	0.723	9.76	0.45

HG15												
	a[g]	*3.81*	*50.83*	*0*	*0.529*	*7.53*	*12.15*	*28.57*	*10.4*	*9.21*	*0.72*	*12.71*	*0.75*
	b	2.82	49.01	1	0.503	12.75	20.46	37.19	17.6	5.21	0.707	7.33	0.29
	c[g]	*6.31*	*63.73*	*0*	*0.834*	*13.95*	*17.98*	*24.79*	*18.2*	*8.40*	*0.776*	*10.79*	*0.41*
	d[g]	*8.49*	*68.81*	*0*	*0.602*	*7.09*	*12.24*	*21.60*	*10.0*	*10.98*	*0.789*	*13.86*	*0.50*
	e	2.28	45.67	1	0.589	15.09	18.97	46.57	19.6	5.47	0.69	7.88	0.45
HG17													
	a[f]	*1.15*	*37.13*	*0*	*3.322*	*25.55*	*45.01*	*68.18*	*36.1*	*16.74*	*0.627*	*26.52*	*1.20*
	b[f]	*2.35*	*44.37*	*0*	*0.839*	*6.70*	*7.29*	*40.09*	*8.4*	*17.75*	*0.683*	*25.65*	*2.52*
	c[f]	*1.57*	*39.98*	*0*	*2.330*	*19.49*	*32.37*	*68.52*	*27.1*	*15.58*	*0.648*	*23.82*	*1.38*
HG19													
	a	3.14	57.36	2	2.883	25.35	36.90	42.09	34.0	15.52	0.75	20.61	0.77
	b	2.90	52.62	2	0.740	9.94	16.50	16.18	13.8	9.81	0.725	13.50	0.70
	c	3.32	54.75	1	1.062	12.31	24.22	11.13	18.0	10.85	0.737	14.70	0.71
	d	1.20	41.27	2	2.023	23.51	29.28	45.10	30.4	12.17	0.658	18.38	1.88
HG28													
	a	3.95	56.20	1	0.696	21.13	14.43	19.71	24.5	5.22	0.749	6.96	0.26
	b[f]	*1.23*	*40.33*	*2*	*0.195*	*6.28*	*8.12*	*26.81*	*8.2*	*4.29*	*0.648*	*6.55*	*1.14*
	c	2.10	50.03	2	0.234	7.64	9.33	26.58	9.8	4.32	0.716	5.99	0.69
	d	3.13	56.57	2	0.204	5.34	6.92	26.02	7.0	5.25	0.747	6.98	0.52
	e	1.24	41.70	2	0.271	11.10	12.55	27.30	14.1	3.51	0.663	5.26	0.38
HG29													
	a	1.22	40.07	2	0.220	10.44	8.05	34.83	12.3	3.24	0.651	4.93	0.67
	b	1.51	43.17	2	0.436	10.57	13.77	40.40	13.8	5.71	0.67	8.44	0.68
	c	1.39	41.26	2	0.356	12.55	12.31	43.94	15.4	4.17	0.658	6.28	0.63
	d	2.30	47.35	1	0.239	6.29	7.40	30.77	8.0	5.34	0.701	7.54	0.70
HG32													
	a	1.89	46.21	2	0.940	15.35	38.84	8.77	24.5	7.08	0.684	10.32	0.61
	b[f]	*1.90*	*45.62*	*2*	*0.939*	*24.99*	*42.38*	*13.85*	*35.0*	*4.95*	*0.684*	*7.23*	*0.33*
	c	1.60	44.26	2	1.188	19.49	36.36	9.39	28.0	7.82	0.675	11.56	0.31
	d[f]	*1.59*	*45.44*	*2*	*1.282*	*31.16*	*62.88*	*10.79*	*45.9*	*5.15*	*0.684*	*7.52*	*0.26*
HG34													
	a	1.25	41.11	2	1.570	46.83	32.92	30.66	54.6	5.31	0.66	8.02	0.41
	b	2.69	51.52	1	1.311	47.05	13.91	13.24	50.3	4.82	0.733	6.57	0.43
	c[f]	*2.22*	*48.15*	*1*	*1.359*	*42.48*	*18.73*	*16.71*	*46.9*	*5.36*	*0.715*	*7.49*	*0.36*
	d	1.14	40.20	2	1.253	49.00	25.22	21.39	54.9	4.22	0.656	6.42	0.41
	e[f]	*1.20*	*39.88*	*2*	*1.079*	*35.59*	*25.15*	*16.78*	*41.5*	*4.80*	*0.65*	*7.38*	*0.63*
06CD16													
	a	6.2	58.3	2	0.43	3.5	11.6	-	6.3	12.63	0.76	17	1.1
	b	2.4	42.5	2	0.46	5.9	11.4	-	8.5	10.08	0.68	15	1.0
	c	1.3	34.8	2	1.55	20.0	44.3	-	30.4	9.51	0.617	15	0.8
	d	1.4	36.0	2	0.36	4.3	14.8	-	7.7	8.60	0.629	14	1.1
	e	1.2	33.7	2	0.46	8.6	18.9	-	13.1	6.60	0.606	11	0.8
	f	4.3	53.4	2	0.49	5.4	12.0	-	8.3	10.98	0.74	15	1.0
	g	2.7	44.0	2	0.48	8.5	11.0	-	11.9	7.97	0.69	12	0.7
	h	2.8	44.3	2	0.81	13.8	20.4	-	18.6	8.08	0.691	12	0.7
	i	3.2	45.0	2	0.31	5.8	10.0	-	8.1	7.18	0.695	10	0.7

07CD16												
a	2.2	36.1	2	0.07	0.8	2.9	-	1.5	9.50	0.626	16	3.0
b	6.0	53.8	2	0.12	0.8	2.7	-	1.4	15.19	0.741	21	1.7
c	2.0	39.3	2	0.08	0.8	2.3	-	1.3	11.31	0.654	17	3.6
d	4.7	51.7	2	0.10	0.8	2.3	-	1.4	13.20	0.731	18	1.8
e[h]	*3.1*	*47.6*	*2*	*0.10*	*0.5*	*1.8*	-	1.0	*20.39*	*0.712*	*29*	*3.5*
f	3.2	45.0	2	0.09	0.7	1.7	-	1.1	15.29	0.695	22	3.0
g	2.8	42.7	2	0.09	0.8	2.7	-	1.5	10.98	0.68	16	2.4
h	7.6	61.9	2	0.09	0.7	1.8	-	1.1	15.05	0.773	19	1.7
i	2.3	41.1	2	0.12	0.7	2.3	-	1.3	16.96	0.669	25	3.4
j	23.0	88.7	2	0.12	0.7	2.0	-	1.2	19.24	0.838	23	1.6
21CD16												
a	1.47	37.00	2	0.500	10.24	23.4	-	15.7	5.95	0.638	9	0.6
b	0.97	31.40	2	0.660	25.63	22.5	-	30.9	3.99	0.58	7	0.5
29CD16												
a[h]	*2.17*	*42.30*	*2*	*0.49*	*2.19*	*5.9*	-	3.6	*25.36*	*0.678*	*37*	*2.4*
b[h]	*1.45*	*35.50*	*2*	*0.98*	*3.65*	*14.2*	-	7.0	*26.23*	*0.624*	*42*	*2.4*
c	1.14	33.50	2	2.27	35.16	45.9	-	45.9	9.18	0.606	15	0.8
d	*1.65*	*37.90*	*2*	*0.85*	*4.76*	*17.0*	-	8.8	*17.99*	*0.645*	*28*	*1.6*
e	1.72	36.70	2	0.25	3.21	11.3	-	5.9	7.96	0.634	13	1.1
f	*2.31*	*39.10*	*2*	*0.53*	*3.59*	*18.4*	-	7.9	*12.35*	*0.653*	*19*	*1.2*
g	1.6	38.1	2	0.19	2.8	8.3	-	4.8	7.50	0.647	12	1.4
h[h]	*7.5*	*62.9*	*2*	*0.29*	*14.7*	*30.8*	-	21.9	*2.46*	*0.776*	*3*	*0.2*
i	1.7	36.5	2	0.22	1.8	8.6	-	3.8	10.97	0.632	17	1.7
j	2.0	39.9	2	0.30	3.1	8.2	-	5.0	10.99	0.661	17	1.3
k[h]	*6.5*	*61.7*	*2*	*0.98*	*7.2*	*17.6*	-	11.4	*15.98*	*0.774*	*21*	*1.3*
l	5.3	53.2	2	0.47	4.0	14.1	-	7.3	12.05	0.738	16	1.0

Appendix C

APATITE FISSION TRACK THERMOCHRONOMETRY DATA

C.1 Apatite Fission Track Thermochronometry data from Haida Gwaii

Table C.1: Apatite Fission Track thermochronometry data from Haida Gwaii.

Sample	no. grains	Standard track density x10^6cm^{-2} (no. counted)	Fossil track density x 10^5cm^{-2} (no. counted)	Induced track density x 10^6cm^{-2} (no. counted)	Chi square prob. %	Dpar in μm	Central age (Ma) (95% CI)	Mean length in μm (no. measured)
BARRY	16	1.44 (2315)	3.34 (66)	6.82 (1348)	99	-	12.9 (+3.7/-2.9)	13.53±1.1(9)
HG02	20	1.53 (2465)	0.43 (24)	1.17 (660)	95	-	10(+5.1/-3.4)	-
HG04	20	1.5(2425)	1.41 (77)	3.38 (1854)	97	2.3	11.2(+3.0/-2.4)	14.9±0.9(4)
HG12	20	1.5(2415)	1.35(84)	2.7(1683)	95	2.6	13.4(+3.4/-2.7)	15±0.8(4)
HG28	30	1.47(2365)	0.21(19)	0.44(409)	92	-	12.2(+7.2/-4.5)	13.1±1.5(4)
HG34	20	1.47(2365)	1.67(56)	4.18(1405)	99	2.2	10.5(+3.3/-2.5)	14.7±1(5)

Appendix D

ZIRCON (U-TH)/HE THERMOCHRONOMETRY DATA

D.1 Zircon (U-Th)/He Thermochronometry data from the Wallowa and Elkhorn Mountains

Table D.1: Zircon (U-Th)/He thermochronometry data from the Wallowa and Elkhorn Mountains. [a] equivalent spherical radius; [b] Number of grain termini. 0 – Both tips broken; 1 – One tip broken; 2 – Whole grain; [c] Effective uranium concentration, calculated as U+0.235*Th; [d] alpha-ejection correction of (Farley, 2000); [e] Analytically uncertainty based on U, Th, He, Sm, and grain length measurements.

Sample	Grain	Mass (μg)	r[a] (μm)	T[b]	He (nmol/g)	U (ppm)	Th (ppm)	Sm (ppm)	eU[c] (ppm)	Raw Date (Ma)	Ft[d]	Date (Ma)	1σ [e]
WB034													
	a	40.70	66.3	-	510.20	74.70	35.20	-	82.97	50.70	0.81	62.60	0.6
WB101													
	a	33.00	52.0	-	3974.20	296.30	111.60	-	322.53	101.30	0.76	133.40	1.3
WB104													
	a	11.00	47.0	-	314.00	149.90	65.40	-	165.27	15.70	0.73	21.40	0.1
WB118													
	a	33.00	72.0	-	1957.60	164.90	31.90	-	172.40	93.40	0.83	113.10	1.1
WB130													
	a	17	41.0	-	2220.50	230.90	78.30	-	249.30	73.40	0.70	105.50	1.0
WB149													
	a	52	90.0	-	493.50	44.00	12.90	-	47.03	86.30	0.86	100.30	1.0
WB152													
	a	38.00	65.0	-	3407.20	318.60	48.70	-	330.04	85.00	0.81	105.30	1.0

D.2 Zircon (U-Th)/He Thermochronometry data from Haida Gwaii

Table D.2: Zircon (U-Th)/He thermochronometry data from Haida Gwaii. [a] equivalent spherical radius; [b] Number of grain termini. 0 – Both tips broken; 1 – One tip broken; 2 – Whole grain; [c] Effective uranium concentration, calculated as U+0235*Th; [d] alpha-ejection correction of (Farley, 2000); [e] Analytically uncertainty based on U, Th, He, Sm, and grain length measurements. Grains in italics were excluded from means, plots, and models. They were excluded because of [h] failure of the Peirce outlier test (Ross, 2003).

Sample	Grain	Mass (μg)	r[a] (μm)	T[b]	He (nmol/g)	U (ppm)	Th (ppm)	Sm (ppm)	eU[c] (ppm)	Raw Date (Ma)	Ft[d]	Date (Ma)	1σ [e]
HG04													
	a	5.7	57.0	2	15.83	119.8	37.6	0.1	1.149	7.16	0.801	28.44	0.66
	b[h]	*5.5*	*56.1*	*2*	*31.8*	*447.2*	*75.1*	*0.7*	*464.8*	*6.16*	*0.799*	*15.88*	*0.94*
	c	6.0	56.3	2	19.2	160.6	55.4	0.1	173.6	6.38	0.798	25.60	0.81
HG12													
	a	5.21	53.93	2	25.751	182.13	62.88	0.46	196.9	24.21	0.790	30.63	0.84
	b	3.85	48.18	2	20.975	141.30	48.09	0.04	152.6	25.45	0.766	33.19	1.49
	c	5.75	57.34	2	18.975	114.90	37.39	0.15	123.7	28.40	0.802	35.38	0.85
HG28													
	a	5.98	54.75	2	19.396	60.63	26.61	0.42	66.9	53.55	0.792	67.52	4.45
	b	11.75	70.69	2	18.706	66.85	24.48	0.45	72.6	47.60	0.838	56.77	2.79
	c	4.16	52.07	2	18.445	75.33	28.86	0.54	82.1	41.53	0.783	52.99	1.78

Appendix E

ONLINE DATA REPOSITORY

A digital data repository accompanies this dissertation and contains:

1. Thermochronometry data tables for Chapters 2 and 4

2. QTQt model results for analysis described in Chapters 2 and 4

3. A table of Columbia River Basalt contact elevations presented in Chapter 3

4. Supplemental videos for Chapter 4

Some content may be updated after the publication of this dissertation. Updates can be accessed at https://github.com/PSGreene.

VITA

Philip Schoettle Greene

Education:

2015- PhD. Earth and Space Sciences, University of Washington, Seattle, USA. Thesis: "Tectonics as recorded by thermochronometry, deformed datums, and submarine landscapes in western North America."
Advisor: Alison Duvall

2012-13 M.Sc. Earth Sciences, University of Toronto, Toronto, Canada. Thesis: "Passive margin subduction and the dynamics of collisional orogenesis."
Advisor: Russell Pysklywec

2006-11 B.Sc. Biology & Earth and Planetary Sciences McGill University, Montreal, Canada. Thesis: "Fluvial geomorphology of the Andean pre-Cordillera, Peru."
Advisor: Sarah Hall

Awards & Fellowships:

2019 Dorothy G. Stevens Fellowship, Department of Earth and Space Sciences, University of Washington
2018 AGU Outstanding Student Presentation Award, Tectonophysics Section
2016 NSF GRFP Honorable Mention
2015 Top Scholar Award, University of Washington
2011 Student Undergraduate Research Award, McGill University